General Relativistic Radiative Transfer in Black Hole Systems

Ziri Younsi

Mullard Space Science Laboratory
Department of Space and Climate Physics
University College London

A thesis submitted to University College London
for the degree of Doctor of Philosophy

October 2013

I, Ziri Younsi, confirm that the work presented in this thesis is my own. Where information has been derived from other sources, I confirm that this has been indicated in the thesis.

_____

_____

Abstract

Accretion onto compact objects plays a central role in high-energy astrophysics. The presence of a compact object considerably alters the structure and dynamics of the accreting plasma, as well as its radiative emissions. For accreting black holes in Active Galactic Nuclei (AGN) this is especially true. A significant fraction of the emission may originate or pass near the event horizon. Strong gravity modifies the radiation from an emission source. Photons no longer propagate in straight lines and experience frequency shifts. Gravitational lensing creates multiple images of an emission source, further modifying its temporal and spectral properties. Addressing these effects, the first part of this thesis formulates the equations of radiative transfer for particles with and without mass in a manifestly covariant form. Using ray-tracing, the observed images and line emission from accretion disks and tori are calculated. The effects of absorption, emission and optical depth gradients are investigated.

The second part of this thesis examines scattering in general relativity. The general relativistic Compton scattering kernel and its angular moments are expressed in closed-form for the first time, in terms of hypergeometric functions. This has the advantage of being fast, accurate and not restricted by specific energy ranges. The results are in perfect agreement with semi-analytic calculations and Monte-Carlo simulations of Compton scattering of monochromatic emission lines.

Finally, I investigate the effects of variability in the accretion flow. Two models are considered: a plasmoid on a Keplerian orbit around a black hole and a magnetically-driven plasmoid ejection from the disk corona. Deriving a new time-dependent radiative transfer formulation, I calculate this variable emission, presenting the results in the form of spectrograms and lightcurves.

Acknowledgements

Foremost, I would like to express my sincere gratitude to my supervisor, Professor Kinwah Wu, whose generosity, kindness and encouragement have kept me going through the most difficult of times. His wisdom and his passion have inspired me to strive to be the best I can possibly be. I am forever in his debt.

Secondly, I would like to thank Dr Curtis Saxton, for his tireless scientific and technical counsel, without which I would never have come this far. I also thank him for taking the time to carefully proof-read my thesis. Special thanks go to Professor Mark Cropper, for his kindness and encouragement, and for being so supportive during my time as a seminar organiser. I also thank Dr Roberto Mignani, for being such a supportive colleague, and from whose example I have learnt so much.

I extend my gratitude to my friends at MSSL, for making my time here so enjoyable. In particular, I thank Awat Rahimi, Ehsan Pedram, Missagh Mehdipour, Yudish Ramanjooloo and David Barnes, for not only driving me from London to MSSL all of these years, but for also being such wonderful company on all of these journeys.

My sincere thanks to David Kirby and Inderjeet Kalsi for their generosity, kindness and patience these last ten years. I thank them both, together with Thomas Richardson, for their friendship, as well as for their camaraderie throughout our many gym sessions, helping me grow in both body and mind.

I would also like to thank Janet, John, Tim and Jayne, who have treated me as family all these years. I thank them for their generosity and their love, and for always being so thoughtful.

I thank my parents for all of their love and support, and for enabling me to be so independent. I especially thank my younger sisters, Tanina and Baya,

and my younger brother, Menad, for making my visits home so enjoyable.

Finally, I dedicate this work to Lottie, who has given me her love and her friendship these past eight years, helping me grow into who I am today. Words cannot express how much she has done for me, and how much she means to me.

Contents

List of Variables

List of Figures

List of Tables

Chapter 1

Introduction

1.1 Overview

In this thesis I investigate general relativistic radiative transfer and apply it to calculate the emission from AGN. The supermassive black holes (SMBHs) which reside in the centres of AGN provide an opportunity to probe the nature of matter and radiation under the most extreme of conditions. The intense gravity in the vicinity of a black hole affects the hydrodynamics of the accretion flow and significantly alters the manner in which radiation is emitted and transferred in the flow.

I derive a general relativistic radiative transfer formulation. This formulation incorporates emission, absorption, and relativistic, geometrical and optical depth effects, as well as particle mass self-consistently. The formulation is derived in a covariant manner, expressing all physical quantities as relativistic invariants. This avoids the need to Lorentz-transform between frames of reference until the very end of calculations, meaning all relativistic effects (including Doppler boosts and frequency shifts, beaming, gravitational redshifts, lensing and formation of multiple images) are implicit in my calculations.

In solving the general relativistic radiative transfer equations, I employ a ray-tracing method. I include particle time delay effects in my formulation, considering situations where variability and outflows are present. For the case where the opacity is high and Compton scattering dominates, I present a new method for calculating the scattering kernel for Compton scattering in general relativistic environments.

The core focus of this thesis is the radiative transfer of radiation in accretion and outflows around black holes. Whilst general relativistic magnetohydrodynamic (GRMHD) and general relativistic particle-in-cell (GRPIC) simulations of the flow from which the radiation is emitted are now quite sophisticated (e.g. Fuerst et al. 2007; Drappeau et al. 2013), my primary concern is with the details of radiation transport around black holes. The formulation I present can accurately and self-consistently calculate emission from arbitrary matter distributions. The numerical results from GRMHD and GRPIC simulations may be used to obtain this matter distribution, along with its associated magnetic, thermodynamic and kinematic properties, upon which the general relativistic radiative transfer formulation developed in this thesis may then be applied.

Throughout I have adopted a modular approach, enabling continuous refinement of the treatment of radiative processes with the minimum of computational overhead. Calculations of the emission from geometrically thin, optically thick accretion disks are now ubiquitous. I begin in Chapter 4 by applying the formulation to emission from an optically thick accretion torus, and comparing with emission from disks. Geometrical effects on the observed emission are discussed. Next, I introduce opacity gradient effects in the form a transparent three-dimensional emitting volume, modelled as a thermodynamic torus with density-driven emission. I then include emission and absorption in the form of thermal free-free emission and electron scattering. In Chapter 5, I derive the Compton scattering kernel in general relativity, the first such closed-form calculation. Finally, In Chapter 6, I investigate relativistic outflows in the form of plasmon ejecta, applying the time-dependent part of my code to calculate the observed lightcurves and spectrograms.

1.2 Active Galactic Nuclei

An AGN is a compact region at the centre of a galaxy (the nucleus), characterised by exceptionally bright observed luminosities across the entire electromagnetic spectrum far in excess of what can produced by the host galaxy's stars alone. AGN were first detected in the 1940s as point-like sources with

powerful optical emission spectra showing very broad, strong and redshifted emission lines (Seyfert 1943). They were also found to exhibit variability in the optical waveband over periods of several months, with the emitting source being completely unresolved. However, strong X-ray variability was observed in detail in AGN over periods of a few hours to a few days (see McHardy and Czerny 1987; Lawrence et al. 1987). Such observations imply an extremely compact emission region. AGN are the dominant sources of cosmic X-rays, which are generated in their nuclei down to distances of a few gravitational radii of the central black hole. Emission at other wavelengths is generated at distances several orders of magnitude further out. Moreover, X-rays are the most direct probe of AGN and their underlying accretion processes and prodigious energy liberation (10^{42}–10^{46} erg s^{-1}) as they can penetrate through the vast columns of obscuring gas and dust associated with accreting matter around the central SMBH. The corresponding power of an AGN in the X-ray alone is between 10^{9}–10^{13} $L_{\odot}$ (bolometric solar luminosity), sufficiently powerful to rival an entire galaxy.

There exist many different classes of AGN with different observational properties (see Krolik 1999; Beckmann and Shrader 2012). These classes exhibit different ratios of radio, optical/UV and X-ray flux, dissimilar amounts of variability and the presence or absence of broad and narrow emission lines in their optical spectra. Multi-wavelength studies of AGN and their corresponding results have lead to the unification model of AGN (Antonucci 1993), which attempts to explain these different classes in terms of observer inclination angles to the central black hole and the accretion rate.

In a generic AGN model (Figure 1.1) the central engine is assumed to be a SMBH ($\sim 10^{6}M_{\odot}$–$10^{10}M_{\odot}$), surrounded by a geometrically thin, optically thick accretion disk. At very high mass accretion rates (e.g. Abramowicz et al. 1988) the radiation pressure force becomes so great that the inner disk expands vertically and can no longer be treated as geometrically thin (see Abramowicz et al. 1978; Kozlowski et al. 1978). In accretion onto the black hole there are also collimated outflows in the form of a pair of large scale relativistic jets which are directed along the spin axis of the accretion disk. These relativistic

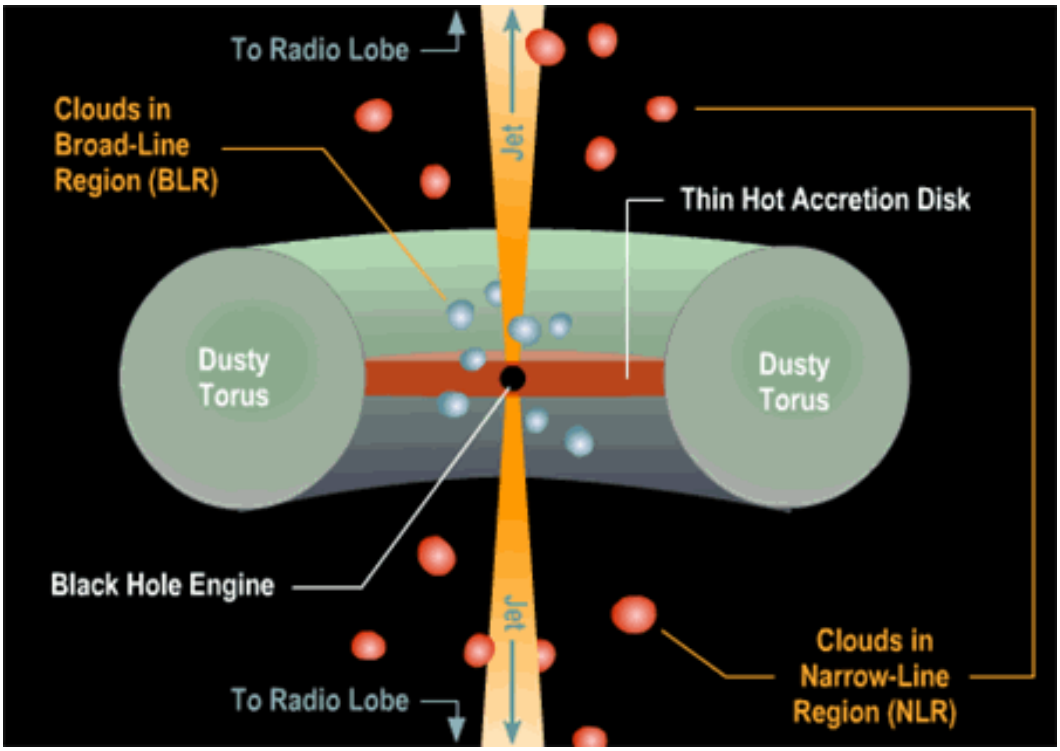

Fig. 1.1: Schematic view of an AGN through the equatorial plane. The black hole in the central engine is surrounded by a thin accretion disk, which may have an inner thick disk/torus. The accretion disk lies within the optically thick torus of molecular gas and dust. Broad emission line and narrow emission line clouds lie outside of the equatorial plane, above the accretion disk. Narrow emission line clouds are much further from the black hole than the broad emission line clouds. A pair of relativistic jets may also be launched from within the vicinity of the black hole event horizon into their corresponding radio lobes. Credit: Brooks/Cole Thomson Learning

jets feed into large scale radio-emitting lobes, which are roughly ellipsoidal in structure (Blandford and Rees 1974). These radio lobes are powered by beams of ultra-relativistic particles and magnetic field in their respective relativistic jets, which are launched from very close to the central engine (see Boettcher et al. 2012, for a review of jet launching models).

Above the accretion disk there are broad emission line gas clouds, at a few fractions of a pc from the central black hole, which are heated by radiation from the disk, giving rise to broad optical/UV emission lines. Observations of these broad emission lines in Seyfert-1 galaxies imply velocities at full-width-half-maximum (FWHM) $\sim$ 1000–5000 km s^{-1} very close to the black hole. If

the observer's view is uninterrupted by the dusty torus then this is classed as a Type-1 AGN. This optically thick torus of molecular gas and dust is located at roughly from one to a few pc from the central black hole, reprocessing radiation from the accretion disk and re-emitting it mainly in the infrared. Even further out are the narrow emission line gas clouds, between approximately 30 pc and 300 pc, which also interact with radiation from the accretion disk. Although this model contains the essence of the components, their linear dimension and the distance to the central black hole are approximate, depending greatly on the luminosity of the AGN (see Krolik 1999). If an observer's line-of-sight passes directly through the dusty torus, whereby only the narrow emission line clouds are observable, this AGN is classed as Type-2. Observations of the narrow optical/UV emission line region in Seyfert-2 galaxies suggest gas velocities at FWHM $\sim$ 500–1000 km s^{-1}. Seyfert-1 and Seyfert-2 galaxies are radio-quiet Type-1 and Type-2 AGN, respectively, and exhibit only small, sub-parsec scale versions of the large-scale relativistic jets and radio lobes seen in extragalactic radio sources (see Wilson and Ulvestad 1982, 1983; Pedlar et al. 1993). Radio-loud Type-1 and Type-2 AGN are divided into broad-line radio galaxies (BLRGs) and narrow-line radio galaxies (NLRGs), respectively.

Radio-loud AGN often exhibit relativistic jets of plasma being emitted from the nucleus. The axis of these relativistic jets is assumed to be aligned with the spin axis of the accretion disk. Relativistic jets are thought to be responsible for the synchrotron radio emission from the nucleus and the radio lobes where the relativistic jets terminate. The appearance of a radio-loud AGN also depends on the viewing angle relative to the jet. If viewed almost directly along the jet axis, relativistic Doppler boosting causes the jet emission to be beamed forward, significantly enhancing the observed emission, and leading to observed superluminal motion along the line of sight. Such radio-loud AGN are classified as blazars. However, if viewed at angles away from the jet axis towards the equatorial plane, then the radio-loud AGN is classified as a radio galaxy, with an associated pair of radio lobes either side of the nucleus.

Blazars are themselves divided into two main catagories: BL Lacertae (BL Lac) objects and flat spectrum radio quasars (FSRQs) (see Penston and Can-

non 1970; Strittmatter et al. 1972). FSRQs are also known as optically violent variable (OVV) quasars, since the majority of FSRQs tend to show rapid variability, high polarization, and radio structures dominated by compact radio cores.

Sources of radio emission other than radio galaxies first appeared star-like in optical images, possessing neither a galaxy nor a nebula. These objects were named quasars (quasi-stellar radio sources) and are characterised by their extremely luminous and rapidly varying continuum emission, as well as unusually broad emission lines in their optical spectra. This rapid variability is observed at all frequencies from radio to γ-rays (Urry and Padovani 1995). It was originally thought that quasars were nearby stars with very unusual properties. Spectral studies of 3C 273 identified well-known broad emission lines at a then remarkable redshift of $z = 0.158$ (Schmidt 1963). Quasars were originally thought to be accretion-powered "super-stars" of a million solar masses or more, with just a minor contribution coming from fusion (Hoyle and Fowler 1963; Fowler 1964, 1966). One of the early suggestions for the origin of the redshifts of quasar emission lines was gravitational redshift caused by extremely high density Galactic stars. Shortly thereafter it was found that the observed emission line widths required the emitting gas to be confined to a region within a small fractional radius around the quasar. Such an object was shown to be unstable (Chandrasekhar 1964). In addition to this, the observed symmetry of the quasar emission lines could not be accounted for by gravitational redshift (Greenstein and Schmidt 1964). A consensus quickly emerged and it became clear that quasars were in fact extragalactic in origin, with their redshifted emission lines a consequence of cosmological redshift from the expansion of the Universe.

For many years the question as to what was fuelling the central SMBH in AGN was an open debate (Schmidt 1972; Hills 1975; Frank and Rees 1976; Adams 1977; Dahari 1984). It was from the accumulation of many theoretical and observational arguments that the presence of tidal forces which remove angular momentum from matter in the vicinity of the SMBH and enable it to accrete was acknowledged. Thereafter the notion of a SMBH coupled with a

rotating disk became widely accepted (Rees 1984) and the vast cosmological distances of quasars became accepted by the astronomical community as a whole. The host galaxies of quasars were eventually resolved with the advent of charged-coupled devices (CCDs) and more sophisticated imaging detectors, confirming quasars as AGN at high cosmological redshift. The most distant quasar detected so far, at $z = 7.085$, is ULAS J1120+0641 (Mortlock et al. 2011), only 0.77 billion years after the Big Bang.

Quasar-like objects without strong radio emission called quasi-stellar objects (QSOs) were also discovered (e.g. Sandage 1965), although the terms quasar and QSO are used interchangeably. It was later found that only roughly 10% of quasars are radio-loud. Strictly speaking, QSOs refer to radio-quiet quasi-stellar sources. Although FSRQs and BL Lac objects share the properties associated with a non-thermal continuum, FSRQs have strong and broad optical emission lines, while in BL Lacs the optical lines are weak or absent altogether. Bolometric luminosities are higher in FSRQs than BL Lacs (Sambruna et al. 1996), exhibiting thermal activity perhaps related to an accretion disk in their optical and ultraviolet (UV) spectra. This is in contrast to BL Lacs, which have smooth continua. At these inclinations the accretion disk cannot be seen.

Moving further away from the relativistic jet axis, emission from the accretion disk is unobscured. In many systems this thermal disk emission is revealed as the "big-blue-bump" in the optical/UV part of spectra (Shields 1978). Emission lines from both the broad line region and narrow line region may now be observed in the optical spectra. Objects viewed at such inclinations are Seyferts-1s and steep-spectrum radio quasars (SSRQs). The spectra of Type-1 Seyfert galaxies show broad emission lines in the UV and X-ray, as well as visible light from their cores. SSRQs are normally radio lobe-dominated radio quasars. Their lobe emission dominates their core emission, since beaming effects are less severe as their relativistic jets are viewed at larger inclination angles.

At even higher inclinations the line-of-sight view of the accretion disk and central black hole is interrupted by the dusty torus. Consequently, only

light scattered from the nucleus is observable. At these inclinations even the broad line emission region may be obscured, but the narrow emission line region remains unobscured. These objects are Seyfert-2s and are predominantly radio-quiet. In practice, Seyfert-1 galaxies that show intermediate properties (ratio of broad line to narrow line components) are divided into sub-classes (Osterbrock and Ferland 2006). For example, a Seyfert-1.9 is a Seyfert-1 in which only broad Hα (653 nm) emission lines are seen, whereas a Seyfert-1.5 has similar broad and narrow Hβ (486 nm) emission line components.

For radio galaxies not observed face-on, the relativistic jet is projected onto the sky. These radio galaxies are divided into two separate classes: Fanaroff and Riley (1974) Class-I (FR-I) and Class-II (FR-II) objects. These sources are classified using the ratio of the distance between the regions of highest surface brightness on opposite sides of the central galaxy or quasar, to the total extent of the source up to the lowest brightness contour in the radio map. Those sources whose distance ratio is less than 0.5 are FR-I objects, whereas sources with ratios greater than 0.5 are FR-II objects. FR-I radio lobes are edge-dim and centrally bright, with a relativistic jet which gradually widens into the lobe. FR-II radio lobes are edge-bright and centrally dimmer, with a relativistic jet which maintains its narrow cross-section until the lobe. In addition, FR-II radio jets also tend to have a hot spot on the side furthest from the galaxy. This hot-spot is the strong shock where the relativistic jet terminates, colliding with a wall of ambient thermal gas.

Upper limits to AGN size may be obtained from observations of AGN structure in the optical and radio, as well as through measuring the widths of their spectral lines in various wavebands. However, more stringent constraints may in some cases be set through observation of the variability timescale of the AGN luminosity. In nearby AGN (e.g. NGC 4395), optical observations place an upper-limit on the linear size of the nucleus at $\sim$ 1 pc (Ho et al. 1992). Very-long-baseline interferometry (VLBI) measurements of the radio cores of AGN enable upper-limits to be placed on the size of the compact core (see Falcke and Biermann 1999; Ulvestad and Ho 2001; Anderson et al. 2004).

Structure is present on all observed scales, with the length scale of observed structure depending on the observed frequency. Measurements of absorption lines and line variability (the reverberation technique) may also be used to estimate the distance of the broad emission line region.

The variability timescale of a system is $t_{\rm var} = l/c$, where l is the length-scale of the system and c is the speed of light. In general, significant changes in the structure of a system cannot be observed over timescales shorter than this timescale. Due to the size of the system, different photons arrive at Earth at different times, smearing out the changes in the observed structure. Consequently, the size of the system is constrained by $l \leq ct_{\rm var}$. This variability-size argument is the basis of the reverberation mapping technique using iron lines, whereby following changes in the continuum, the lines change and through the measured lag the distance may be inferred (see Blandford and McKee 1982; Reynolds et al. 1999). This technique is used to probe the inner structure of AGN accretion disks. This is complicated by reflecting boundaries and intrinsic source motion. Reflection of the observed emission will lead to over-estimation of the system size. However, as has been observed in superluminal expansion, the observed $t_{\rm var}$ is shorter than the corresponding timescale in the source rest frame. This inevitably leads to an underestimate of size for rapidly varying sources.

Essentially AGN may be categorised based on their viewing inclination angle and whether they are radio-quiet or radio-loud. Despite this taxonomy, AGN are complex systems and do not always readily lend themselves to fixed classifications. Obscuration of AGN by dust lanes and the interstellar medium (ISM) makes optical distinction between starburst galaxies and low-luminosity AGN difficult due to new star formation along the line-of-sight (e.g. Treister et al. 2009). However, X-ray observations of AGN show a distinct emission signature, enabling them to be clearly distinguished from galaxies without an AGN.

1.3 Accretion Disks

Accretion disks are an ubiquitous phenomenon in astrophysics, often giving rise to bipolar relativistic jets. The strong gravitational field of black holes, coupled with the high angular momentum of accreting matter, enables an accretion disk to form. Frictional heating from relativistic matter in the inner region of black hole accretion disks can generate temperatures in excess of 10^5K, emitting optical and UV photons. These photons are then up-scattered to X-ray energies by a corona of hot electrons above and below the accretion disk. The liberation of gravitational potential energy from matter accreting onto black holes is widely believed to be the primary power source in AGN. Accretion onto black holes is a natural and powerful mechanism to produce the observed high-energy radiation from AGN.

1.3.1 Thin disks

In most cases the accretion flow is so closely confined to the equatorial plane that the disk may be regarded as a two-dimensional flow. The most successful formulation to-date is the α-viscosity prescription (Shakura and Sunyaev 1973). The accretion disk is assumed to be geometrically thin and the underlying subsonic turbulence is the source of viscosity. In this prescription the largest eddies in the flow are negligible in comparison to the vertical extent of the disk, and so the viscosity, ν, may be expressed as

$$\nu = \alpha c_{\rm s} H \ , \tag{1.1}$$

where $c_{\rm s}$ is the sound speed, H is the disk thickness, and α is a dimensionless parameter ($\alpha < 1$). All information about the disk viscosity is encapsulated in this parameter. The presence of a free parameter does not hinder the prescription, since most physical quantities only depend weakly on α. However, since observable quantities depend weakly on α, it is difficult to constrain.

This prescription may be extended to include the disk vertical structure (see Frank et al. 2002). For thin disks, the disk radius is much greater than the disk height: radial and vertical dependencies are separable. Working in cylindrical polar coordinates, the disk structure is most easily considered first in the z-direction. The flow is negligible in this direction, and the momentum

conservation equation gives

$$\frac{1}{\rho}\frac{\partial P}{\partial z} = \frac{\partial}{\partial z}\left(\frac{GM}{\sqrt{R^2+z^2}}\right) , \tag{1.2}$$

where R is the radius of a disk element, ρ and P are the density and pressure of the accreting matter, M is the mass of the accretor and G is the gravitational constant. Since $z \ll R$, equation (1.2) immediately becomes

$$\frac{1}{\rho}\frac{\partial P}{\partial z} = -\frac{GMz}{R^3} . \tag{1.3}$$

Since the typical disk scaleheight is H, $z \sim H$ and $\partial P/\partial z \sim P/H$, where $z \sim H$. Assuming an equation of state for the disk of the form

$$P = \rho c_{\rm s}^2 , \tag{1.4}$$

the disk scaleheight may be expressed as

$$\frac{H}{R} \simeq c_{\rm s}\sqrt{\frac{R}{GM}} , \tag{1.5}$$

which yields, given $H \ll R$, the condition

$$c_{\rm s} \ll \sqrt{\frac{GM}{R}} . \tag{1.6}$$

Therefore, for the thin disk prescription to be valid, the local Keplerian velocity must be highly supersonic. Neglecting time-dependence, the mass conservation for the disk (see Frank et al. 2002) is

$$\frac{\partial}{\partial R}\left(R\Sigma v_R\right) = 0 , \tag{1.7}$$

where $\Sigma \equiv \Sigma(R) = \int \mathrm{d}z\, \rho(z)$ is the disk surface density and v_R is the radial drift velocity. Clearly $R\Sigma v_R$ is a conserved quantity in the mass conservation equation, representing the constant inflow of mass through each fluid element in the disk. It therefore follows that the mass accretion rate is

$$\dot{M} = -2\pi R\Sigma v_R , \tag{1.8}$$

the minus sign indicating that the total mass within the disk is decreasing. From conservation of angular momentum, integration yields

$$-\nu\Sigma\Omega = -\Sigma v_R\Omega + \frac{C}{2\pi R^3} , \tag{1.9}$$

where $\Omega \equiv \Omega(R)$ is the angular velocity of a disk fluid element and C is an integration constant determined by the disk inner boundary condition ($\Omega'(R) = 0$). For simplicity, it is assumed that the disk truncates at the surface of the accretor ($R = R_*$). The disk angular velocity remains Keplerian at this radius and therefore

$$\Sigma v_R \sqrt{\frac{GM}{R_*^3}} = \frac{C}{2\pi R_*^3} \ . \tag{1.10}$$

The constant C may now be found as

$$C = -\dot{M}\sqrt{R_* GM} \ . \tag{1.11}$$

Substituting equation (1.11) into equation (1.9) yields

$$\nu\Sigma = \frac{\dot{M}}{3\pi}\left(1 - \sqrt{\frac{R_*}{R}}\right) \ , \tag{1.12}$$

and

$$v_R = -\frac{3\nu}{2R}\left(1 - \sqrt{\frac{R_*}{R}}\right)^{-1} \ . \tag{1.13}$$

The viscous dissipation rate per unit disk area $D(R)$ within the disk is given by (see Frank et al. 2002) the following expression

$$D(R) = \frac{1}{2}\nu\Sigma\left(R\Omega'(R)\right)^2 \ . \tag{1.14}$$

Substituting $\Omega = \Omega_{\rm K}$, the dissipation rate follows as

$$D(R) = \frac{3GM\dot{M}}{8\pi R^3}\left[1 - \sqrt{\frac{R_*}{R}}\right] \ . \tag{1.15}$$

It is immediately evident that the dissipation rate through a thin accretion disk is independent of the viscosity. If the disk is assumed optically thick in the z-direction, then the radiation from each disk fluid element is roughly a blackbody with temperature $T(R)$ given by

$$\sigma T^4(R) = D(R) \ , \tag{1.16}$$

where $\sigma = \pi^2 k_{\rm B}^4/60\hbar^3 c^2$ is the black-body emittance constant, $k_{\rm B}$ is the Boltzmann constant and $\hbar$ is the reduced Planck constant. Now the radial temperature profile for a steady-state geometrically thin, optically thick Shakura-Sunyaev accretion disk (Shakura and Sunyaev 1973) is given by

$$T(R) = \left[\frac{3GM\dot{M}}{8\pi R^3\sigma}\left(1 - \sqrt{\frac{R_*}{R}}\right)\right]^{1/4} \ . \tag{1.17}$$

The spectrum from the disk may be approximated as a black-body and integrated over the disk to determine the observed flux at a given frequency, ν, yielding

$$F_\nu \propto \nu^3 \int_{R_*}^{R_{\rm out}} {\rm d}R \, \frac{R}{e^{h\nu/k_{\rm B}T(R)} - 1} \ , \tag{1.18}$$

where $R_{\rm out}$ is the disk outer radius, h is the Planck constant, and the constant of proportionality, which is equal to $4\pi h \cos i / c^2 d^2$, depends on the observer inclination angle, i, and the distance to the source, d.

All of the previous equations may now be combined to obtain the radial dependence of all variables (see Frank et al. 2002). As an example, the disk scale height, density and central temperature may be expressed as

$$H = 1.7 \times 10^8 \alpha^{-1/10} \dot{M}_{16}^{3/20} m_1^{-3/8} R_{10}^{9/8} f^{3/5} \ {\rm cm} \ , \tag{1.19}$$

$$\rho = 3.1^{-8} \alpha^{-7/10} \dot{M}_{16}^{11/20} m_1^{5/8} R_{10}^{-15/8} f^{11/5} \ {\rm g \ cm^{-3}} \ , \tag{1.20}$$

$$T_{\rm c} = 1.4 \times 10^4 \alpha^{-1/5} \dot{M}_{16}^{3/10} m_1^{1/4} R_{10}^{-3/4} f^{6/5} \ {\rm K} \ , \tag{1.21}$$

where $\dot{M}_{16} = \dot{M} / \left(10^{16} \, {\rm g \ s^{-1}}\right)$, $m_1 = M/M_\odot$, $R_{10} = R/(10^{10}{\rm cm})$, and

$$f^4 = 1 - \sqrt{\frac{R_*}{R}} \ . \tag{1.22}$$

From equation (1.19) it follows that

$$\frac{H}{R} = 1.7 \times 10^{-2} \alpha^{-1/10} \dot{M}_{16}^{3/20} m_1^{-3/8} R_{10}^{1/8} f^{3/5} \ , \tag{1.23}$$

i.e. $H \ll R$ and the disk is indeed thin. As noted previously, the dependence of all physical quantities on the parameter α is very weak.

1.3.2 Thick disks

The thin disk solution breaks down when the accretion rate, $\dot{M}$, exceeds a threshold, known as the Eddington accretion rate (Eddington 1926). This is given by

$$\dot{M}_{\rm Edd} = \frac{4\pi G M m_{\rm p}}{\eta \, c \, \sigma_{\rm T}} \ , \tag{1.24}$$

where $m_{\rm p}$ is the proton mass, η is the accretion efficiency (the ratio of the observed luminosity, L, to rest mass energy of the accreting material, $\dot{M}c^2$), and $\sigma_{\rm T}$ is the Thomson cross-section (Thomson 1906). When this happens the

radiation pressure within the disk balances the gravitational force. The disk scale height may now be defined as

$$H \simeq \frac{3R_*}{4}\frac{\dot{M}}{\dot{M}_{\rm Edd}}\left(1-\sqrt{\frac{R_*}{R}}\right) \ . \tag{1.25}$$

As $\dot{M}$ increases, the disk scaleheight, particularly in the inner regions where R is small, is no longer negligible. Consequently, it is expected that in accreting systems like AGN the accretion disk will become thick in the inner region.

Like the stellar case in which the Eddington approximation was originally derived, disk accretion may be limited by radiation pressure, counteracting gravity and viscous dissipation. Unlike the stellar case, the different geometry of the accretion disk can potentially complicate the situation considerably. In applying this limit to disk models the following assumptions (see Heinzeller and Duschl 2007) are inherent: (i) spherical symmetry; (ii) isotropic radiation; (iii) homogeneous degree of ionisation and (iv) stationarity. It is clear none of these approximations apply for the accretion disk. In addition to these, the Eddington approximation, irrespective of the stellar or disk case, makes the following approximations: (1) opacity is from Thomson scattering alone; (2) gas pressure is negligible compared to radiation pressure and (3) no relativistic effects are considered. As a consequence of this many research efforts have been focused on the applicability of the Eddington limit to the disk case (e.g. Jaroszynski et al. 1980; Abramowicz et al. 1980). In addition to standard radiative cooling, these models considered advective flows which permit the critical accretion rate to rise without increasing the radiative flux.

In the inner disk region $H \simeq R$ and the assumption of a geometrically thin disk is no longer applicable. The system of equations governing the properties of the accretion disk becomes unclosed. This problem may be overcome by parameterising the angular velocity or angular momentum of the thick disk, instead of the viscosity. Equilibrium figures of steady thick disks are toroidal in shape and internally stratified: a special case of the shape and structure of a rotating relativistic fluid. This is discussed at length in Chapter 4, where the relevant equilibrium figures, including internal thermodynamic properties, are derived. For now a simple prescription is adopted to illustrate more general

properties of thick disks.

Assuming fluid particles are rotating in circular orbits, with no radial or vertical displacements, then in cylindrical polar coordinates $(v_R, v_\phi, v_z) = (0, R\Omega, 0)$. The equations of hydrostatic equilibrium in the radial and vertical directions yield

$$\frac{1}{\rho}\frac{\partial P}{\partial R} = -\frac{\partial \Phi}{\partial R} + \Omega^2 R \,, \tag{1.26}$$

$$\frac{1}{\rho}\frac{\partial P}{\partial z} = -\frac{\partial \Phi}{\partial z} \,, \tag{1.27}$$

where Φ is the gravitational potential. These equations, representing the balance of forces on a fluid element, may be written in vector form (see Kozlowski et al. 1978; Frank et al. 2002) as

$$\frac{1}{\rho}\nabla P = -\nabla\Phi + \Omega^2 R = \mathbf{g}_{\text{eff}} \,, \tag{1.28}$$

where $\mathbf{g}_{\text{eff}}$ is the effective gravitational acceleration, encompassing gravitational and centrifugal accelerations. This effective gravity is orthogonal to isobaric surfaces in the fluid. For a polytropic equation of state, the isopycnic and isobaric surfaces coincide, and are orthogonal to the effective acceleration. This important property is used in Chapter 4 to derive the structure of relativistic accretion tori. The condition for a polytropic equation of state to hold is found by taking the curl of equation (1.28), yielding

$$\begin{aligned} \nabla\left(\frac{1}{\rho}\right) \times \nabla P &= 2\Omega\nabla\Omega \times R \\ &= 2\frac{\partial\Omega}{\partial z}\mathbf{v} \,, \end{aligned} \tag{1.29}$$

where $\mathbf{v}$ is the fluid velocity field. It is now clear in equation (1.29) that isopycnic and isobaric surfaces coincide when $\partial\Omega/\partial z = 0$, i.e. $\Omega \equiv \Omega(R)$.

In certain cases, the analytic form of $\Omega\,(R)$ is simple enough that equation (1.28) may be integrated analytically to obtain $\rho\,(R, z)$ and $P\,(R, z)$ (see Kozlowski et al. 1978). In this instance Ω is essentially a free parameter, implying a lack of constraint for the fluid. In reality the fluid is permeated by a magnetic field and GRMHD effects govern the flow. In Chapter 4 the form of Ω is chosen to closely approximate the geometrical properties of relativistic accretion tori in numerical GRMHD simulations.

1.4 Relativistic Jets in AGN

Relativistic jets in AGN are highly collimated plasma outflows. They are linear features originating from, and associated with, the central SMBH. Although some believe that these relativistic jets are powered by the accretion disk around the black hole itself, it is now widely accepted that AGN jets are powered primarily by black holes. Relativistic jets transport tremendous amounts of power away from the central region, necessitating them to be coupled with processes involving a SMBH. Therefore potential energy and rotation of the central SMBH are the main power sources for these jets.

Approximately 1% of AGN are radio galaxies which accrete enough matter to become luminous enough to overpower the emission from the ensemble of stars in the entire galaxy. AGN in spiral galaxies are weak radio sources, which may involve small-scale jets or may only lead to uncollimated core sources. Only about 10% of radio galaxies, i.e. $\sim 0.1\%$ of all AGN, are able to launch relativistic jets (see Begelman et al. 1984; Bridle and Perley 1984). These jets exhibit structural dimensions far greater than their host galaxies.

The first recorded observation of a jet was in 1918 within the elliptical galaxy M87 (Curtis 1918). The commonly accepted model of jets consists of two oppositely directed jets, although in many cases only one side is easily detected. Radio depolarisation measurements are used to determine which jet is pointing towards Earth, with the side with the stronger jet closer to Earth showing less depolarisation since it is viewed through a smaller amount of material along the line-of-sight. This is the so-called "Laing-Garrington effect" (Laing 1988; Garrington et al. 1988).

VLBI observations display superluminal motions within the jets themselves, now understood as bulk relativistic motions (i.e. Doppler boosting) of emitting plasma closely inclined to the observer line-of-sight. Jets transport energy, momentum and angular momentum from the black hole far away from the central region (Rees 1971; Scheuer 1974). In the case of FR galaxies these jets dissipate their energy and momentum within radio lobes up to a megaparsec away from the central region. Thus studies of jets must consider scales varying by over ten orders of magnitude. It is still an open question as to

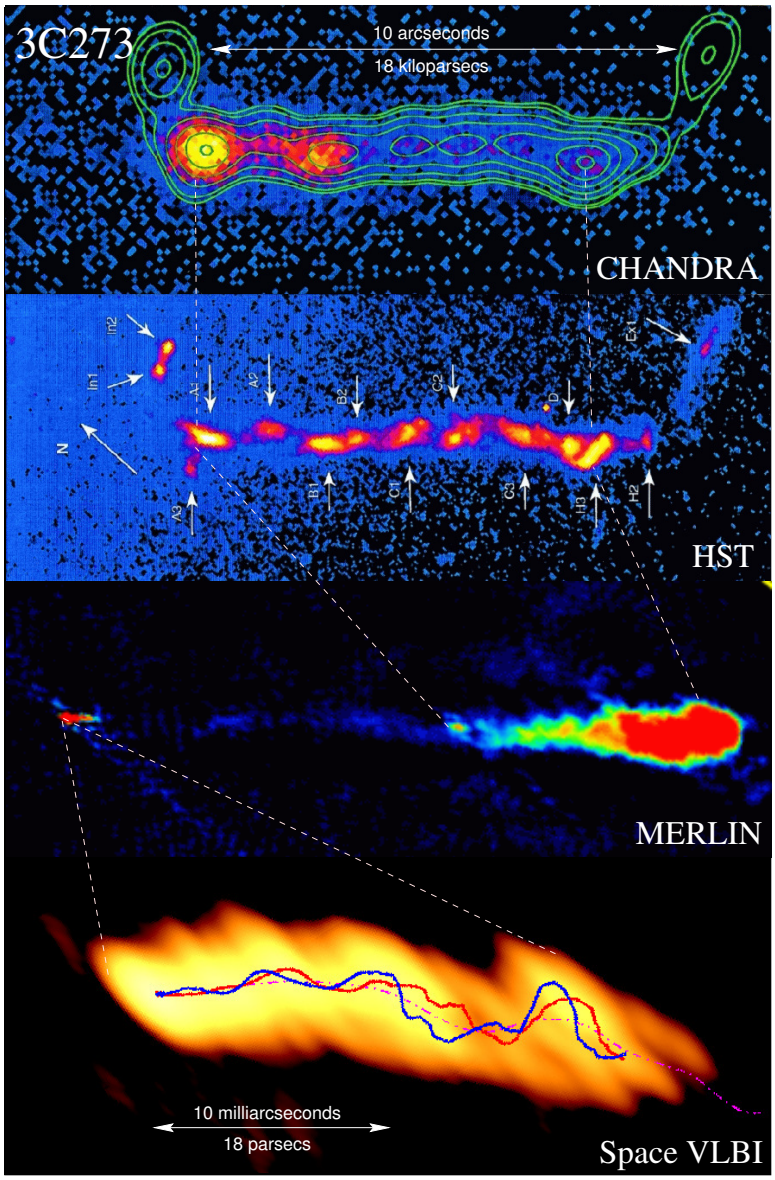

Fig. 1.2: Multiband collage in X-ray, optical, large-scale radio and VSOP survey images of the jet in the quasar 3C273. Bottom: Linear perturbation analysis of Kelvin-Helmholtz instability to model the observed double helical structure of the jet (outlined with red and blue lines) describes well the intrinsic structure of the jet on scales of up to 300 parsecs. Credit: Andrei Lobanov and Anton Zensus (MPIfR).

what constitutes a jet: are they baryonic or leptonic in content? The principal species responsible for transporting energy and momentum (electrons, positrons, protons, nuclei, Poynting flux) is still unknown (Nishikawa et al. 2011). Consequently, the mechanism by which jets manifest and accelerate also remains an open question.

Prior to the *Hubble* space telescope (HST) observations of jets were poorly resolved in the optical/UV due to the limited angular resolutions available. HST data of 3C273 were the first detailed morphological and degree-of-polarisation observations of a jet in the optical/UV (e.g. Uchiyama et al. 2006). The *Einstein* observatory (launched in 1978) was the first instrument to detect X-ray knots in FR II radio galaxies and quasars, as well as hot spots associated with jets (e.g. Lea et al. 1982). Later *ROSAT* (1990) detected several more jets (e.g. Birkinshaw and Worrall 1994). However, it was not until the launch of *Chandra* with its exquisite angular resolution that many more jets were discovered (e.g. Chartas et al. 2000). X-ray observations of knots and jet hot spots have provided key insights into jet physics. From a large-scale dynamics perspective these knots appear as shocks propagating upstream/downstream in the jet plasma. Radio galaxy-scale knots may stand still as decollimation shocks i.e. standing shock waves. These knots are also interpreted by some as separate ejection events (e.g. Jester 2008). It is not yet a settled matter as to what determines the motions of knots in jets. The Lorentz factors of radiating electrons within these jets must be of the order of 10^7–10^8 for such weak magnetic fields to produce the observed synchrotron emission in X-rays. Such ultra-relativistic electrons have extremely short half-lives. Consequently, X-ray data can constrain source size much better than optical/UV data, since such electrons cannot travel very far from where they were accelerated (see Boettcher et al. 2012).

Most radio-loud AGN cores are spatially unresolved on sub-parsec scales. Gamma-ray emission is observed in those regions when the AGN jet is closely directed along the line-of-sight (i.e. blazars). Detected energies are in the MeV and TeV ranges, with extremely short time variability for increasing energy.

It is, however, gamma-ray bursts (GRBs) that are the sources of the most powerful jets in the Universe (see Boettcher et al. 2012, for a review of GRBs and jets). Observational association of GRBs with afterglows in the X-ray and optical confirm that these sources are extragalactic in origin (Fishman and

Meegan 1995; Galama et al. 1998). Calculations of GRB γ-ray flux yield energies in excess of 10^{54} erg, exceeding the radiative energy release of typical supernovae by more than three orders of magnitude. The fast flux variability of GRBs ($\sim$seconds) place lower bounds on the jet bulk Lorentz factor, Γ, of 10^2–10^3 (Rees and Meszaros 1992, 1994; Meszaros and Rees 1997; Piran 2005).

The emission in jets is highly non-thermal and associated with a power-law distribution of relativistic electrons interacting with a magnetic field and ambient photons. The two most likely emission processes in jets are therefore Synchrotron radiation and inverse Compton (IC) scattering. Synchrotron radiation results from relativistic electrons gyrating in a magnetic field (and will be discussed in Chapter 2). Most observed radio sources are powered by synchrotron emission. However, in relativistic jets, synchrotron emission is also seen in the optical and X-ray. IC emission occurs when ultra-relativistic electrons scatter off low energy photons, transferring much of their energy-momentum to the photon, resulting in a much higher-energy photon than prior to scattering.

Numerical GRMHD simulations of accreting black holes which are spinning rapidly exhibit spontaneous jet formation, suggesting that the majority of jet energy comes from the black hole itself, and not the accretion disk. In observations of accreting stellar-mass black holes it has been found that jet radio luminosity and black hole spin are correlated, implying a causal relationship between jet power and black hole spin (Narayan and McClintock 2012), with the jet power scaling roughly as the square of the black hole spin parameter. The continuum fitting method (see Zhang et al. 1997; McClintock et al. 2006) is used to determine the black hole spins in these cases.

The Penrose process around a spinning black hole allows, in principle, for energy to be extracted from infalling matter (see Misner et al. 1973). Within the ergo-region of a rotating black hole (discussed in Chapter 3), there exist negative (redshifted) energy orbits. If a particle enters (or exits) the ergo-sphere, it has positive energy. Particles with negative energy orbits must have interacted with other particles prior to this state. When two particles of positive energy interact within the ergo-region, one is propelled into a negative

energy orbit, and the other into a positive energy orbit (through conservation of energy-momentum). If the subsequent positive energy particle exits the ergo-region and escapes the black hole itself, it has extracted energy from the black hole. However, in astrophysical black holes the presence of magnetic fields in the flow necessitates an electromagnetic extension of this process (see Komissarov et al. 2007).

The generalised Penrose process is commonly known as the Blandford-Znajeck (BZ) mechanism (Blandford and Znajek 1977). This is an extension of the Penrose process to include the dynamo effects of a uniform magnetic field (see Komissarov 2004). A spinning black hole embedded in a uniform magnetic field aligned with the black hole spin axis will generate a stationary quadrupolar distribution of electric charge with a corresponding poloidal electric field. No seed electric charge is introduced, hence the BZ mechanism is a purely general relativistic phenomenon (Misner et al. 1973). The magnetic field essentially extracts angular momentum from the black hole, reducing its spin. It is plausible that the launching site of jets is in this magnetospheric region around the black hole, powered by the BZ mechanism. Numerous numerical GRMHD simulations of jets support this conclusion (e.g. Komissarov and Barkov 2009; McKinney et al. 2012). The proposed scenarios in these simulations produce results consistent with observations.

Chapter 2

Radiation Processes

2.1 Classical Radiative Transfer

Radiative transfer is the study of how radiation propagates through a medium. As radiation passes through matter it may undergo absorption, emission and scattering before finally reaching a distant observer. This interaction modifies the radiation, leaving an imprint of the material the radiation has traversed. This is applicable to all types of radiation flux, including flux in the form of neutrinos and even gravitational waves. As such, radiative transfer is a powerful tool for extracting information about matter from observations of its radiative emissions. The classical radiative transfer equation and its general relativistic covariant analog are derived and discussed in detail in Chapter 3.

2.1.1 Geometric optics limit

Throughout this thesis I investigate radiative transfer in the limit where the wavelength of radiation is small in comparison to other characteristic length scales of objects and the emitting environment itself. For example, the wavelength of X-rays is negligible compared to the gravitational radius of an AGN. As such, the effects of diffraction may be neglected and the refractive index of the medium is unity.

In standard descriptions of radiative transfer theory the specific intensity is used as a fundamental variable, with radiation in the form of rays. However, the quantum properties of light assumed in the theory of radiative transfer also impose certain restrictions. The specific intensity, I_ν, is defined (e.g.

Rybicki and Lightman 1979) as

$$\mathrm{d}E = I_\nu \, \mathrm{d}A \, \mathrm{d}\Omega \, \mathrm{d}\nu \, \mathrm{d}t \ , \tag{2.1}$$

i.e. the energy $\mathrm{d}E$ crossing an area $\mathrm{d}A$ in time $\mathrm{d}t$, within a solid angle $\mathrm{d}\Omega$ in a frequency range $\mathrm{d}\nu$. In this description it is assumed that $\mathrm{d}A$, $\mathrm{d}\Omega$, $\mathrm{d}\nu$, and $\mathrm{d}t$ are all infinitesimal. However, due to the uncertainty principle, $\mathrm{d}A$ and $\mathrm{d}\Omega$ cannot both be made arbitrarily small, that is

$$\mathrm{d}A \, \mathrm{d}\Omega \gtrsim \lambda^2 \ , \tag{2.2}$$

where λ is the wavelength of radiation. Therefore as soon as $\mathrm{d}A \sim \lambda^2$, the ray direction cannot be defined with accuracy and the concept of rays breaks down. In addition to this, uncertainty in the energy means

$$\mathrm{d}E \ \mathrm{d}t \gtrsim \hbar \ . \tag{2.3}$$

This implies

$$\mathrm{d}\nu \, \mathrm{d}t \gtrsim 1 \ . \tag{2.4}$$

Therefore when the wavelength of light exceeds atomic distance scales the specific intensity in equation (2.1) is no longer a valid description of the interaction of light on atomic scales. However, it is still a valid macroscopic theory. To treat this more precisely requires employing the eikonal approximation, i.e. treating the radiation as a scalar field rather than a vector. In this formalism rays are defined as curves whose tangents at each point are parallel to the direction of propagation of the radiation. This condition only holds if the amplitude and direction of the electromagnetic wave remain constant over a distance λ. This is the formal definition of the geometric optics limit (see Misner et al. 1973; Gammie and Leung 2012). Consider a time-varying wave represented as a function $f(\mathbf{r}, t)$, expressed as

$$f(\mathbf{r}, t) = a(\mathbf{r}, t) \, \mathrm{e}^{\mathrm{i}\psi(\mathbf{r}, t)} \ , \tag{2.5}$$

where $\mathbf{r}$ is a spatial position vector, $a(\mathbf{r}, t)$ is the slowly varying amplitude of the wave, and $\psi(\mathbf{r}, t)$ is its rapidly varying phase. Substituting equation (2.5) into the wave equation yields

$$\Box a + \mathrm{i}a \, \Box\psi + 2\mathrm{i} \left(\nabla a \cdot \nabla\psi - \frac{1}{c^2} \partial_t\psi \, \partial_t a \right) - a \left(\nabla\psi \right)^2 + \frac{a}{c^2} \left(\partial_t\psi \right)^2 = 0 \ , \tag{2.6}$$

where the background metric signature is $[-,+,+,+]$, $\Box \equiv \nabla^2 - c^{-2}\partial_t^2$ is the D'Alembert wave operator and ∂_t denotes partial differentiation with respect to t. The geometric optics limit may now be formally defined as

$$\frac{1}{a}\left|\nabla a\right| \ll \left|\nabla\psi\right| \ , \tag{2.7}$$

$$\left|\nabla^2\psi\right| \ll \left|\nabla\psi\right|^2 \ , \tag{2.8}$$

$$\frac{1}{a}\left|\nabla^2 a\right| \ll \left|\nabla\psi\right|^2 \ , \tag{2.9}$$

$$\frac{1}{a}\left|\partial_t a\right| \ll \left|\partial_t\psi\right| \ , \tag{2.10}$$

$$\left|\partial_t^2\psi\right| \ll \left|\partial_t\psi\right|^2 \ , \tag{2.11}$$

from which it immediately follows that equation (2.6) becomes

$$\left(\nabla\psi\right)^2 - \frac{1}{c^2}\left(\partial_t\psi\right)^2 = 0 \ , \tag{2.12}$$

which is precisely the eikonal equation. The wave vector $\mathbf{k} = -i\nabla\psi$ and the local frequency $\omega = -\partial_t\psi$, which reduce the eikonal equation to

$$\left|\mathbf{k}\right|^2 - \frac{\omega^2}{c^2} = 0 \ , \tag{2.13}$$

which is simply the dispersion relation for electromagnetic waves in vacuum.

In a refractive medium with refractive index n, by defining a total path length derivative $\mathrm{d}/\mathrm{d}s$, where s is the path length, the radiative transfer equation, in the absence of scattering, may be written (see Pomraning 1972) as

$$\frac{\mathrm{d}}{\mathrm{d}s}\left(\frac{I_\nu}{n^2}\right) + \frac{3}{c}\partial_t n\left(\frac{I_\nu}{n^2}\right) = 0 \ . \tag{2.14}$$

If the refractive index is not time-varying then

$$\frac{\mathrm{d}}{\mathrm{d}s}\left(\frac{I_\nu}{n^2}\right) = 0 \ , \tag{2.15}$$

implying I_ν/n^2 is a conserved quantity. In this manner, the radiative transfer formulation in Chapter 3 may be extended to included the effects of a dispersive medium. Details may be found in Pomraning (1972).

2.1.2 Scattering in radiative transfer

In flat space the equation of radiative transfer through a stationary medium, in the presence of isotropic scattering, may be written as

$$\frac{\mathrm{d}I_\nu}{\mathrm{d}s} = -\alpha_\nu I_\nu + j_\nu + \iint \mathrm{d}\Omega'\, d\nu'\, \sigma\left(\nu,\nu'\right) I_\nu\left(\Omega'\right) \ , \tag{2.16}$$

where α_ν is the frequency-dependent absorption coefficient of the medium (which is contributed to in the presence of scattering), j_ν the frequency-dependent emission coefficient, and σ the scattering kernel for the assumed radiation process. Equation (2.16) is an integro-differential equation and is very difficult to solve analytically. The spatially non-local nature of the scattering term means even radiation that is outside of the line-of-sight may be scattered into it. To calculate the intensity variation along any particular ray, the entire radiation field through all space (and for time-dependent radiative transfer, time also) must be solved for. This is highly non-trivial and requires proper accounting of the energy-momentum redistribution and correct specification of both spatial and energy boundary conditions. The case where scattering is negligible is formulated in Chapter 3 and studied in Chapter 4. Radiative transfer with scattering, including relativistic effects and strong gravity, is discussed in detail in Chapter 5.

In the vicinity of astrophysical black holes in AGN, accretion material may be optically thick. In this regime electron scattering dominates and radiative transfer calculations which omit scattering do not correctly approximate the physics. In this case the intensity is non-local and does not separate out into individual spatial and energy components.

There exist several methods to solve the radiative transfer equation with scattering. One such method is employing Monte-Carlo simulations to follow rays from the observer to the source, and at each time-step scatter the rays with a probability which is weighted by the scattering kernel. This method requires many rays in order to obtain a good sample of the scattering medium. Unfortunately, as opacity increases the number of scatterings per ray becomes quadratic in optical depth and the numerical scheme requires many more evaluations per time-step, inevitably failing.

Other methods employ spectral techniques, i.e. expanding the radiation field in a series of moments, as a function of position, momentum and energy. If the moment expansion is truncated at an appropriate point then a good approximation for the distribution of the radiation field is obtained. Given sufficient symmetry, the above equation can be reduced to a one-dimensional

form. This occurs in the plane-parallel case, where the radiation field only depends on the z coordinate. It is common to calculate angular moments of the intensity in terms of $\mu = \cos\theta$, where θ is the angle between the ray and the z-direction. Expanding moments to order n yields n equations in n+1 unknowns, i.e. the problem is under-determined.

The Eddington approximation applies a closure equation for the system, reducing the problem to the solution of n equations in n unknowns, which may be solved algebraically. The Eddington approximation is most easily illustrated in the plane-parallel case. By assuming that the intensity may be written as a series of increasing powers in μ, the intensity may be expanded as

$$I_\nu(\mu, z) = \sum_{n=0}^{\mathrm{N}} a_n(z)\,\mu^n \ , \tag{2.17}$$

where a_n are coefficients in the expansion and N is the maximum order of the moment expansion. The i-th radiative moment (M_i) of the radiation field may now be written as

$$\begin{aligned} M_i &= \frac{1}{2}\int_{-1}^{1} \mathrm{d}\mu\, I_\nu(\mu, z)\,\mu^i \\ &= \sum_{n=0}^{N} \frac{1+(-1)^{n+i}}{n+i+1} a_n(z) \ , \end{aligned} \tag{2.18}$$

where $i_{\max} = N + 1$ for the system to remain closed.

As a simple example of the Eddington approximation, consider the case $N = 1$, i.e.

$$I_\nu(\mu, z) = a_0(z) + a_1(z)\,\mu \ , \tag{2.19}$$

with $i_{\max} = 2$. The first three moments are given by

$$M_0 = a_0 \ , \tag{2.20}$$

$$M_1 = \frac{a_1}{3} \ , \tag{2.21}$$

$$M_2 = \frac{a_0}{3} \ . \tag{2.22}$$

It immediately follows that

$$M_0 = 3M_2 \ , \tag{2.23}$$

i.e. the Eddington approximation. In local thermodynamic equilibrium (LTE) the radiative transfer equation in an isotropic scattering medium reads

$$\mu \frac{\mathrm{d}I_\nu}{\mathrm{d}z} = -\alpha_\nu \left(I_\nu - \mathcal{B}_\nu\right) + \sigma_\nu (J_\nu - I_\nu) \ , \tag{2.24}$$

where $\mathcal{B}_\nu$ is the black body emissivity and J_ν ($\equiv M_{0,\nu}$) is the isotropic intensity. Integrating at zeroth and first order in μ over all angles yields

$$\frac{\mathrm{d}M_{1,\nu}}{\mathrm{d}z} = \alpha_\nu \left(\mathcal{B}_\nu - M_{0,\nu}\right) \ , \tag{2.25}$$

$$\frac{\mathrm{d}M_{2,\nu}}{\mathrm{d}z} = -\left(\alpha_\nu + \sigma_\nu\right) M_{1,\nu} \ . \tag{2.26}$$

Using equation (2.23), equations (2.25) and (2.26) may be combined, yielding the following second order ODE

$$\frac{\mathrm{d}^2 M_{0,\nu}}{\mathrm{d}z^2} = 3\alpha_\nu \left(\alpha_\nu + \sigma_\nu\right) \left(M_{0,\nu} - \mathcal{B}_\nu\right) \ , \tag{2.27}$$

the radiative diffusion equation. By solving this equation with suitable boundary conditions, the distribution of radiation may be obtained. Increasing the number of moments in the method increases the accuracy of the obtained radiation distribution. The method presented here does not work in general relativity. In this instance a generalised moment expansion of the flux in terms of tensors may be used (Thorne 1980; Fuerst 2006). In Chapter 5, I derive the scattering kernel for Compton scattering in general relativity, and discuss its inclusion into a generalised moment expansion.

2.2 Radiation Processes

Radiation arises from three types of process: bound-bound, free-bound and free-free radiative transitions. These terms refer to the state of electrons prior to and immediately after an atomic transition. In a bound-bound process an atom or ion is agitated into an excited state, and subsequently decays through the emission of a photon. This is the basis of spectral line formation. From quantum mechanics it is known that these states are quantised, therefore radiation of a specific frequency is emitted.

In free-free radiative transitions, e.g. Bremsstrahlung emission, the incident electron is free prior to and after its interaction with the Coulomb field of

a nearby ion. However, in a free-bound transition, or recombination radiation, the electron is captured in a bound stable orbit around the ion, emitting a photon which carries off the excess energy. The capture cross-section of ions is proportional to Z^4 (where Z is the atomic number). Therefore a free-bound transition for an iron ion is $\sim 4.6 \times 10^5$ times more likely than for a hydrogen ion.

Free-free spectra are a continuum, extending from the electron energy down to zero. Free-bound spectra cover a relatively narrow energy range above the electron kinetic energy. This is because the photon energy from free-bound interactions is the sum of the kinetic energy of the incident electron *and* the binding energy of the state into which it recombines. The photon energy is greater than the electron kinetic energy, in contrast to the situation with free-free interactions where it must be less.

It is important to note that photons with energies of up to $\sim$ 8 keV can be produced by electrons with zero kinetic energy, if they are captured by a fully ionised iron nucleus. Consequently, the free-bound continuum is very sensitive to the electron spectrum down to very low energies. This is in contrast to free-free radiation, which is not. In spite of this, and even with the huge increase in the probability of free-bound interactions with iron nuclei compared to other nuclei, free-free interactions still dominate at hard X-ray energies, since protons are so much more abundant than iron nuclei. In the following subsections the properties of Bremsstrahlung, synchrotron radiation and Compton scattering are introduced, all being free-free emission mechanisms and the dominant radiation processes close to a black hole.

2.2.1 Bremsstrahlung radiation

Radiation due to acceleration of a charged particle in the Coulomb field of another charged particle (e.g. an ion or nucleus) is Bremsstrahlung (literally "braking") or free-free emission (see Jackson 1975; Tucker 1975; Rybicki and Lightman 1979; Longair 1992). In hot dense plasmas in the accretion flow around black holes there exist multiple charged species and Bremsstrahlung is an important radiation process. Bremsstrahlung due to the collision of like particles (e.g. electron-electron, proton-proton) is zero in the dipole ap-

proximation, since the dipole moment is simply proportional to the centre of mass of the two particles, which is a constant of motion. However, at electron and photon energies above $\sim$ 300keV (i.e. hard X-rays) electron-electron Bremsstrahlung (i.e. quadrupolar radiation) becomes important and can even explain, for example, the observed hard spectral cut-off in solar flares (e.g. Kontar et al. 2007).

Throughout this thesis I neglect quadrupolar and other higher order effects. The electron is assumed to be travelling in a straight line and the effect of radiation on its orbit is not considered.

It is assumed that the emission comes from electron-ion Bremsstrahlung, with the ion having a rest mass far greater than the electron. In this regime the electron may be considered as moving in a fixed Coulomb field. It is assumed that the electron is moving rapidly enough that the angle through which it is deflected by the ion is small. Bremsstrahlung is the dominant continuum emission mechanism in thermal plasmas, where the electrons and ions are in thermal equilibrium. Consequently, it is an important cooling mechanism for astrophysical plasmas and very efficient at producing X-rays in black hole accretion.

However, accelerated electrons often have a power law distribution of energies. Power law distributions of particles may also be produced in shock waves. This means that non-thermal Bremsstrahlung can be produced in objects such as AGN and their associated jets. In FR-II radio galaxies the hot-spots in strong shocks where the jet terminates can emit inverse Bremsstrahlung radiation. This is characterised by the emission of photons by fast suprathermal ions in collisions with ambient electrons possessing relatively low velocities, as is found in jet termination regions. Therefore, the particular importance of thermal or non-thermal state, and the corresponding electron-ion Bremsstrahlung or inverse (ion-electron) Bremsstrahlung depends on the underlying velocity distributions of the interacting species. Hereafter, the term Bremsstrahlung refers specifically to thermal Bremsstrahlung radiation from a population of relativistic electrons with an underlying Maxwellian velocity distribution.

The Bremsstrahlung radiation spectrum covers a broad range of the elec-

tromagnetic spectrum as it is not an oscillatory process. The total power in the process is dominated by the distance of closest approach (impact parameter), b, of the electron, where it is most strongly accelerated.

For a single non-relativistic electron of charge e at a distance d from an ion of charge Ze, its acceleration is given, as in Jackson (1975), by

$$\begin{aligned} \mathbf{a} &= \frac{Z\mathrm{e}^2}{m_\mathrm{e} d^2}\widehat{\mathbf{d}} \\ &= \frac{Z\mathrm{e}^2}{m_\mathrm{e}\left(b^2+v^2t^2\right)}\widehat{\mathbf{d}}\ , \end{aligned} \tag{2.28}$$

where $t = 0$ is taken as the time of closest approach, m_e is the electron mass and v is the electron velocity. The dipole electric field at a radial distance r from the electron is given by

$$\begin{aligned} |\mathbf{E}| &= \frac{\mathrm{e}a}{c^2 r}\sin^2\theta \\ &= \frac{Z\mathrm{e}^3\sin\theta}{m_\mathrm{e}c^2 r\left(b^2+v^2t^2\right)}\ . \end{aligned} \tag{2.29}$$

In order to obtain the spectrum radiated by a single electron, first the Fourier transform of the electric field must be calculated

$$\begin{aligned} \widetilde{E}_\nu &= \int_{-\infty}^{\infty}\mathrm{d}t\, E(t)\mathrm{e}^{2i\pi\nu t} \\ &= \frac{Ze^3\sin\theta}{m_\mathrm{e}c^2 r}\int_{-\infty}^{\infty}\mathrm{d}t\,\frac{\mathrm{e}^{2i\pi\nu t}}{b^2+v^2t^2} \\ &= \frac{Ze^3\sin\theta}{m_\mathrm{e}c^2 r}\frac{\pi}{bv}\mathrm{e}^{-2\pi\nu b/v}\ . \end{aligned} \tag{2.30}$$

The radiated spectrum of a single electron is therefore

$$\begin{aligned} \frac{\mathrm{d}W}{\mathrm{d}\nu} &= \frac{c}{2\pi}\int \mathrm{d}\omega\, r^2\left|\widetilde{E}_\nu\right|^2 \\ &= \frac{4\pi^2}{3}\frac{Z^2\mathrm{e}^6}{m_\mathrm{e}^2 c^3 b^2 v^2}\mathrm{e}^{-4\pi\nu b/v}\ , \end{aligned} \tag{2.31}$$

which is a flat spectrum for $\nu \ll v/b$ and an exponential cutoff in its tail for $\nu \gg v/b$. For simplicity, assuming all electrons have the same velocity, v, then the number of electrons passing through an annulus of thickness $\mathrm{d}b$ of possible impact parameters of a single ion per unit time is $n_\mathrm{e} v\, 2\pi b\,\mathrm{d}b$, where n_e is the number density of electrons. To calculate the radiated power per unit volume

requires multiplying by the number density of ions, $n_{\rm i}$, yielding

$$\begin{aligned}\frac{{\rm d}W}{{\rm d}\nu{\rm d}V{\rm d}t} &= 2\pi n_{\rm e} n_{\rm i} v \int_{b_{\rm min}}^{\infty} {\rm d}b\, b \frac{{\rm d}W(b)}{{\rm d}b} \\ &\approx \frac{8\pi^3}{3}\frac{Z^2{\rm e}^6}{m_{\rm e}^2 c^3 v}\int_{b_{\rm min}}^{b_{\rm max}}\frac{{\rm d}b}{b}\,, \end{aligned} \tag{2.32}$$

where the fact that the spectrum has an exponential cutoff for $\nu \gg v/b$ allows the exponential to be approximated by a step function which changes from 1 to 0 at $\nu \sim v/b$. In essence this sets a maximum impact parameter $b_{\rm max} \sim v/\nu$. The value of $b_{\rm min}$ may be set in one of two different ways. The first is through quantum mechanical considerations. Because of the uncertainty principle, the electron cannot approach closer than $b \sim \hbar/m_{\rm e}v$. The second is where the small angle approximation for the electron trajectory breaks down, i.e. $b_{\rm min} \sim Z{\rm e}^2/m_{\rm e}v^2$. In high velocity regions, like in the accretion flow near the black hole event horizon, the uncertainty principle sets $b_{\rm min}$.

To find the emission coefficient for Bremsstrahlung, the radiated power per unit volume must be integrated over the velocity distribution for electrons (assumed Maxwellian). The lower limit of this integration is set by the minimum allowed energy of the electron, which is $m_{\rm e}v^2/2 = h\nu$ in order to emit a photon of energy ν. So the minimum electron velocity is quantised by the discreteness of photon energies. Performing this integration yields

$$\begin{aligned} j_\nu^{\rm ff} &= \frac{32\pi}{3}\left(\frac{2\pi}{3}\right)^{1/2}\frac{Z^2{\rm e}^6}{m_{\rm e}^2c^3}\left(\frac{m_{\rm e}}{k_{\rm B}T}\right)^{1/2} n_{\rm e}n_{\rm i}{\rm e}^{-h\nu/k_{\rm B}T}\bar{g}_{\rm ff} \\ &= 6.8\times10^{-38}Z^2 n_{\rm e}n_{\rm i}T_{\rm e}^{-1/2}{\rm e}^{-h\nu/k_{\rm B}T_{\rm e}}\bar{g}_{\rm ff}\ {\rm erg\ s^{-1}\ cm^{-3}\ Hz^{-1}}\,, \end{aligned} \tag{2.33}$$

where Z is the atomic number, $n_{\rm e}$ and $n_{\rm i}$ the densities of electrons and ions respectively, $k_{\rm B}$ is the Boltzmann constant, $T_{\rm e}$ the temperature of electrons and $\bar{g}_{\rm ff}(T_{\rm e},\nu)$ is the velocity-averaged Gaunt factor. The exponential cutoff is a result of the quantisation of photon energies and the exponentially small number of extremely high-energy electrons in the Maxwellian distribution function. The $T_{\rm e}^{-1/2}$ term is from the fact that the power emitted by an electron is proportional to v^{-1} and scales as $v^{-1} \propto T_{\rm e}^{-1/2}$. Free-free emission is an electron-ion process, with emissivity proportional to $n_{\rm e}n_{\rm i}$, i.e. density squared, and is hence a dominant process in dense plasmas. The exact temperature and frequency dependence of the Gaunt factor depends on the regime

being considered, and lies in the range of 1.1 to 1.5. Tabulated values of the Gaunt factor and its explicit functional dependencies may be found in e.g. Itoh et al. (2002). The total integrated emissivity may be obtained by integrating over all frequencies, yielding

$$j^{\rm ff} = 1.4 \times 10^{-27} T_{\rm e}^{1/2} n_{\rm e} n_{\rm i} Z^2 \bar{g}_{\rm B}(T_{\rm e}) \text{ erg s}^{-1} \text{ cm}^{-3} \, , \tag{2.34}$$

where $\bar{g}_{\rm B}(T_{\rm e})$ is a frequency average over $\bar{g}_{ff}$. Choosing the Gaunt factor to be 1.2 is a good approximation and is always correct to within $\sim 20\%$. For a thermalised distribution of highly relativistic electrons the total integrated emissivity is now given by

$$j^{\rm ff} = 1.4 \times 10^{-27} T_{\rm e}^{1/2} Z^2 n_{\rm e} n_{\rm i} \bar{g}_B \left(1 + 4.4 \times 10^{-10} T_{\rm e}\right) \text{ erg s}^{-1} \text{ cm}^{-3} \, , \tag{2.35}$$

which is identical to equation (2.34), except for the bracketed temperature-dependent relativistic correction term. The effects of thermal Bremsstrahlung radiation in relativistic accretion tori are investigated in Chapter 4.

2.2.2 Synchrotron radiation

It is well-known that accelerated charges emit electromagnetic radiation. Synchrotron radiation arises from the emissions of relativistic and ultra-relativistic particles gyrating in a magnetic field (see Ginzburg and Syrovatskii 1965; Jackson 1975; Rybicki and Lightman 1979). Magnetic fields are now known to be ubiquitous in the Universe with synchrotron radiation dominating much of high energy astrophysics. It is responsible for the radio emission in the relativistic jets of black holes ($\nu < 300$GHz), and is most likely the origin of the optical and X-ray continuum emission in quasars.

Synchrotron emission is a non-thermal process, which in the present context means that the radiation is from the continuum emission by particles with a non-Maxwellian distribution of velocities.

From the Liénard-Wiechert potentials and fields for a point charge (see Jackson 1975), upon differentiation the electric and magnetic fields of the point charge are given by

$$\mathbf{E}(\mathbf{r},t) = \frac{q}{c}\left[\frac{(\mathbf{n}-\boldsymbol{\beta})\,(1-\beta^2)}{\kappa^3 R^2}\right] + \frac{q}{c}\left[\frac{\mathbf{n}\times\left\{(\mathbf{n}-\boldsymbol{\beta})\times\dot{\boldsymbol{\beta}}\right\}}{\kappa^3 R}\right] \, , \tag{2.36}$$

$$\mathbf{B}(\mathbf{r},t) = \mathbf{n}\times\mathbf{E}(\mathbf{r},t) \, , \tag{2.37}$$

where $\boldsymbol{\beta} \equiv \mathbf{u}/c$, $\kappa \equiv 1 - \mathbf{n}\cdot\boldsymbol{\beta}$, $\mathbf{n}$ is a unit vector, q is the charge of the particle and R is the distance of the particle from the origin, including both present and retarded positions of the charge, where

$$\left[(1-\mathbf{n}\cdot\boldsymbol{\beta})^2 R\right] = \frac{1}{\gamma^2}\left(b^2 + \gamma^2 v^2 t^2\right) \ . \tag{2.38}$$

Here b is the distance of closest approach to the origin of the particle, as in Bremsstrahlung emission, and $\gamma = (1-\beta^2)^{-1/2}$ is the Lorentz factor of the particle. The fields are written in this way since in order to determine the position of the particle at time t, the retarded position and time of the particle must be calculated. Retarded time and present time are related via $t = t' + R/c$.

It is clear that the magnetic field is perpendicular to both $\mathbf{E}$ and $\mathbf{n}$. The first term in equation (2.36) is the velocity field of the particle, which is proportional to $1/R^2$ and arises from the Coulomb law for moving point charges. The second term is the acceleration field of the particle, is perpendicular to $\mathbf{n}$, and constitutes the radiation field of the particle, along with $\mathbf{E}$. Since the radiation field is of interest in this study, the radiation field of the particle is therefore

$$\mathbf{E}_{\rm rad}(\mathbf{r},t) = \frac{q}{c}\left[\frac{\mathbf{n}\times\left\{(\mathbf{n}-\boldsymbol{\beta})\times\dot{\boldsymbol{\beta}}\right\}}{\kappa^3 R}\right] \ , \tag{2.39}$$

$$\mathbf{B}_{\rm rad}(\mathbf{r},t) = \mathbf{n}\times\mathbf{E}_{\rm rad} \ . \tag{2.40}$$

From this the energy per unit frequency per unit solid angle may be calculated as

$$\frac{\mathrm{d}W}{\mathrm{d}\nu\,\mathrm{d}\Omega} = \frac{q^2}{4\pi^2 c}\left|\int \mathrm{d}t\,\left\{\left[\mathbf{n}\times(\mathbf{n}-\boldsymbol{\beta})\times\dot{\boldsymbol{\beta}}\right]\kappa^{-3}\right\}e^{i\nu t}\right|^2 \ . \tag{2.41}$$

To solve this integral requires changing variable to the present time $t' = t - R(t')/c$. In astrophysical settings the radiation source is located far from the observer, so $R \approx R_0 - \mathbf{n}\cdot\mathbf{r}(t')$, resulting in the following relation between the retarded time and present time

$$\begin{aligned} \mathrm{d}t &= \mathrm{d}t'(1-\mathbf{n}\cdot\boldsymbol{\beta}) \\ &= \kappa \mathrm{d}t' \ . \end{aligned} \tag{2.42}$$

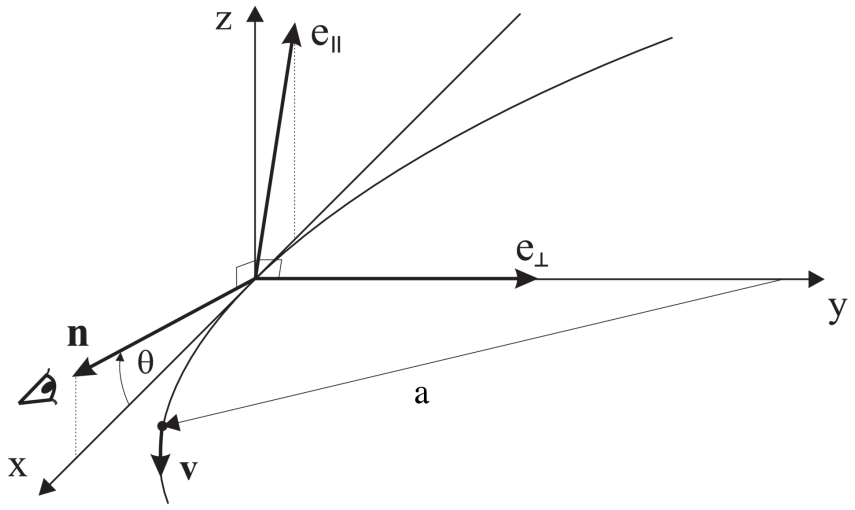

Fig. 2.1: Polarisation of Synchrotron radiation. The orbital plane of the particle is instantaneously in the $x-y$ plane at $t=0$. The vector $\mathbf{n}$ points towards the observer. The orthogonal axes $\mathbf{e}_{\parallel}$ and $\mathbf{e}_{\perp}$ are introduced to discuss the polarisation of the emission.

Using the following identity

$$\frac{\mathrm{d}}{\mathrm{d}t'}\left[\frac{\mathbf{n}\times(\mathbf{n}\times\boldsymbol{\beta})}{1-\mathbf{n}\cdot\boldsymbol{\beta}}\right]=\frac{\mathbf{n}\times(\mathbf{n}-\boldsymbol{\beta})\times\dot{\boldsymbol{\beta}}}{(1-\mathbf{n}\cdot\boldsymbol{\beta})^2}\ , \tag{2.43}$$

equation (2.41) may be integrated by parts to yield

$$\frac{\mathrm{d}W}{\mathrm{d}\nu\,\mathrm{d}\Omega}=\frac{q^2}{4\pi^2 c}\left|\int \mathrm{d}t'\,e^{i\nu(t'-\mathbf{n}\cdot\mathbf{r}/c)}\mathbf{n}\times(\mathbf{n}\times\boldsymbol{\beta})\right|^2\ , \tag{2.44}$$

which is now independent of the particle acceleration. From Figure 2.1 the vector product may be expressed as

$$\mathbf{n}\times(\mathbf{n}\times\boldsymbol{\beta})=-\mathbf{e}_{\perp}\sin\left(\frac{vt'}{a}\right)+\mathbf{e}_{\parallel}\cos\left(\frac{vt'}{a}\right)\sin\theta\ , \tag{2.45}$$

where $\beta=1$ has been taken, θ is the opening angle of the Synchrotron emission cone, and $\mathbf{e}_{\parallel}$ and $\mathbf{e}_{\perp}$ are polarisation basis vectors parallel and perpendicular to the direction of motion, respectively. The exponent in the exponential term in equation (2.44) may be expanded as

$$\begin{aligned} t'-\frac{\mathbf{n}\cdot\mathbf{r}(t')}{c} &= t'-\frac{a}{c}\cos\theta\sin\left(\frac{vt'}{a}\right) \\ &\approx \frac{1}{2\gamma^2}\left[\left(1+\gamma^2\theta^2\right)t'+\frac{c^2\gamma^2t'^3}{3a^2}\right]\ , \end{aligned} \tag{2.46}$$

where the fact that the opening angle of the emission cone is very narrow at ultra-relativistic velocities has been used. Except when $\theta<1/\gamma$ and $ct'<a/\gamma$,

the exponent oscillates rapidly so its contribution to the integral vanishes. Integrating over the full particle path requires only the contribution from small angles. Expressions for the spectrum in the two polarisation states may be obtained along $\mathbf{e}_{\parallel}$ and $\mathbf{e}_{\perp}$. Applying the same techniques as previously, the following expressions are obtained

$$\frac{\mathrm{d}W}{\mathrm{d}\nu\,\mathrm{d}\Omega} = \frac{\mathrm{d}W_{\parallel}}{\mathrm{d}\nu\,\mathrm{d}\Omega} + \frac{\mathrm{d}W_{\perp}}{\mathrm{d}\nu\,\mathrm{d}\Omega}\ , \tag{2.47}$$

$$\frac{\mathrm{d}W_{\parallel}}{\mathrm{d}\nu\,\mathrm{d}\Omega} = \frac{q^2\nu^2\theta^2}{4\pi^2 c}\left|\int \mathrm{d}t'\,\exp\left\{\frac{i\nu}{2\gamma^2}\left[\left(1+\gamma^2\theta^2\right)t' + \frac{c^2\gamma^2 t'^3}{3a^2}\right]\right\}\right|^2\ , \tag{2.48}$$

$$\frac{\mathrm{d}W_{\perp}}{\mathrm{d}\nu\,\mathrm{d}\Omega} = \frac{q^2\nu^2}{4\pi^2 c}\left|\int \mathrm{d}t'\,\frac{ct'}{a}\exp\left\{\frac{i\nu}{2\gamma^2}\left[\left(1+\gamma^2\theta^2\right)t' + \frac{c^2\gamma^2 t'^3}{3a^2}\right]\right\}\right|^2\ . \tag{2.49}$$

The limits of integration may be extended from $-\infty$ to ∞ since the integrands decay rapidly for $t' > a/\gamma c$. Upon changing variable and integrating the following expressions are obtained

$$\frac{\mathrm{d}W_{\parallel}}{\mathrm{d}\nu\,\mathrm{d}\Omega} = \frac{\sqrt{3}\,q^2\gamma\sin\alpha}{2c}\left[F(x) - G(x)\right]\ , \tag{2.50}$$

$$\frac{\mathrm{d}W_{\perp}}{\mathrm{d}\nu\,\mathrm{d}\Omega} = \frac{\sqrt{3}\,q^2\gamma\sin\alpha}{2c}\left[F(x) + G(x)\right]\ , \tag{2.51}$$

where

$$F(x) \equiv x\int_x^{\infty} d\zeta\, K_{5/3}(\zeta)\ , \tag{2.52}$$

$$G(x) \equiv xK_{2/3}(x)\ , \tag{2.53}$$

where $x \equiv \nu/\nu_{\mathrm{c}}$ and $K_n(x)$ is the modified Bessel function of the second kind of order n. Here ν_{c} is the critical frequency, above which the effects of synchrotron radiation become negligible, and is defined as

$$\nu_{\mathrm{c}} = \frac{3\gamma^2 qB\sin\alpha}{2mc}\ , \tag{2.54}$$

where α is the pitch angle of the Synchrotron radiation and m is the mass of the charged particle. The frequency-dependent power in each polarisation mode is found by simply dividing the above expressions by the orbital period of the particle. The sum of these yields the frequency-dependent total emitted power

$$P(\nu) = \frac{\sqrt{3}\,q^3 B\sin\alpha}{2\pi mc^2}F(x)\ . \tag{2.55}$$

From this the emission coefficient for Synchrotron radiation may be expressed as

$$j_\nu = \frac{\sqrt{3}\, q^3 B \sin\alpha}{8\pi^2 mc^2} F(x) \text{ erg s}^{-1} \text{ cm}^{-3} \text{ Hz}^{-1} \ , \tag{2.56}$$

where $j_\nu = P(\nu)/4\pi$. Integrating this over a power-law distribution of electrons of the form $N(\gamma)\mathrm{d}\gamma = C\gamma^{-p}\mathrm{d}\gamma$ with $\gamma_1 < \gamma < \gamma_2$, where C is a constant of proportionality and p is the power-law index. The total power per unit volume per unit frequency may be obtained as

$$P_{\text{total}}(\nu) = \frac{\sqrt{3}\, q^3 C B \sin\alpha}{2\pi mc^2(p+1)} \Gamma\left(\frac{3p+19}{12}\right) \Gamma\left(\frac{3p-1}{12}\right) \left(\frac{mc\nu}{3qB\sin\alpha}\right)^{(1-p)/2} \ , \tag{2.57}$$

where $\Gamma(p)$ denotes the gamma function. From the equations of motion of a relativistic particle in a magnetic field it may be shown that the total emitted power is given by

$$P_{\text{synch}} = \frac{4}{3}\sigma_{\text{T}} c \beta^2 \gamma^2 U_{\text{B}} \ , \tag{2.58}$$

where $U_{\text{B}} = B^2/8\pi$ is the magnetic energy density.

One of the distinguishing features of synchrotron radiation is that it is strongly polarised. Synchrotron radiation is only observable when the particle is moving within $\sim 1/\gamma$ towards the observer. Such an observer sees strong linear polarisation, the dominant component coming from the polarisation perpendicular to **B**. For the power-law distribution of electrons assumed here, the degree of polarisation (see Rybicki and Lightman 1979) is

$$\Pi = \frac{p+1}{p+\frac{7}{3}} \ . \tag{2.59}$$

It can be shown that the degree of linear polarisation of mono-energetic particles is 75%, which is very high indeed. It follows that synchrotron emission is highly polarised. For a single electron, seven times more power is radiated in the perpendicular rather than the parallel polarisation direction. This method is used to map the magnetic fields in spiral galaxies (e.g. Beck 2005).

By detailed balance, for every emission process there is an associated absorption process. For synchrotron radiation this is termed synchrotron self-absorption. An emitted photon interacts with a charge within the magnetic field and is absorbed. However, stimulated emission may also occur. To treat

this quantitatively requires using the Einstein coefficients for synchrotron radiation. Details may be found in Westfold (1959). The important result is the absorption coefficient for this process, which is found as

$$\begin{aligned}\alpha_\nu &= \frac{\sqrt{3}\,q^3}{8\pi m}\left(\frac{3q}{2\pi m^3 c^5}\right)^{p/2} C\left(B\sin\alpha\right)^{(p+2)/2} \\ &\quad \times \Gamma\left(\frac{3p+12}{12}\right)\Gamma\left(\frac{3p+22}{12}\right)\nu^{-(p+4)/2}\,. \end{aligned} \tag{2.60}$$

IC emission occurs when ultra-relativistic electrons scatter off of low energy photons, transferring much of their energy-momentum to the photon, resulting in a photon of much higher energy than prior to scattering.

2.2.3 Compton scattering

The thin accretion disk model in Chapter 1 is sufficient to explain the observed optical and UV continuum emission in AGN. However, AGN also emit radiation in the form of X-rays, which cannot be accounted for by thermal disk models. This necessitates the existence of another radiating medium. This is known as the corona: a cloud of hot electrons which up-scatters lower energy optical and UV photons (emitted from the accretion disk) into the X-ray band.

The scattering of photons by electrons is known as Compton scattering (e.g. Compton 1923; Tolhoek 1956; Rybicki and Lightman 1979; Pozdnyakov et al. 1983; Longair 1992). When the photons lose energy to the electrons in the scattering event the process is generally referred to as Compton scattering. When low energy photons scatter off ultra-relativistic electrons the photons gain energy and this is referred to specifically as IC scattering (e.g. Krawczynski 2012). In the case of photons of energy much less than the electron rest mass energy being scattered by non-relativistic electrons the problem may be treated classically in the Thomson regime ($\beta \ll 1$ and $h\nu \ll m_\mathrm{e}c^2$). Relativistic effects are negligible and the problem may be considered as that of electromagnetic plane waves scattering off of an oscillating electron — i.e. dipole radiation. The process is elastic. Of course, this is just an approximation and energy and momentum are exchanged between the photon and the electron. To investigate the physics of this in detail requires a relativistic treatment.

In the photon-electron scattering process, conservation of energy-momentum implies

$$k^\mu + p^\mu = k'^\mu + p'^\mu \ , \tag{2.61}$$

where k^μ is the 4-momentum of the photon, and p^μ the 4-momentum of the electron. Primed variables indicate post-collisional quantities. Taking the square of both sides of equation (2.61) yields

$$\cancelto{0}{k^\mu k_\mu} + \cancelto{-m_\mathrm{e}^2}{p^\mu p_\mu} + 2k^\mu p_\mu = \cancelto{0}{k'^\mu k'_\mu} + \cancelto{-m_\mathrm{e}^2}{p'^\mu p'_\mu} + 2k'^\mu p'_\mu \ ,$$

from which the following equation is obtained

$$k^\mu p_\mu = k'^\mu p'_\mu \ . \tag{2.62}$$

Contracting both sides of equation (2.61) with k'_μ gives

$$k^\mu k'_\mu + p^\mu k'_\mu - p^\mu k_\mu = 0 \ , \tag{2.63}$$

where equation (2.62) has been employed. From quantum mechanics and special relativity the photon and electron 4-momenta may be written as

$$k^\mu = h\nu \left[1, \widehat{\mathbf{\Omega}}/c\right] , \tag{2.64}$$

$$p^\mu = \gamma m_\mathrm{e} c \left[c, \boldsymbol{\beta}\right] , \tag{2.65}$$

where $\widehat{\mathbf{\Omega}}$ is a directional unit vector. Inserting these momenta into equation (2.63) yields the following formula

$$\frac{\nu'}{\nu} = \frac{1 - \boldsymbol{\beta}\cdot\widehat{\mathbf{\Omega}}}{\left(1 - \boldsymbol{\beta}\cdot\widehat{\mathbf{\Omega}}'\right) + \frac{h\nu}{\gamma m_\mathrm{e} c^2}\left(1 - \widehat{\mathbf{\Omega}}\cdot\widehat{\mathbf{\Omega}}'\right)} \ . \tag{2.66}$$

The angle between incident and scattered photons is θ, and therefore $\widehat{\mathbf{\Omega}}\cdot\widehat{\mathbf{\Omega}}' = \cos\theta$. If the incident photon energy is much less than that of the electron ($h\nu \ll m_\mathrm{e}c^2$), then $\nu = \nu'$ and the incident and scattered photons have the same energy. This is Thomson scattering. However, if the electron is highly relativistic ($\beta \to 1$ and $\gamma m_\mathrm{e} c^2 \gg h\nu$), after introducing the auxiliary angles $\boldsymbol{\beta}\cdot\widehat{\mathbf{\Omega}} = \beta\mu$ and $\boldsymbol{\beta}\cdot\widehat{\mathbf{\Omega}}' = \beta\mu'$, where $\mu \equiv \cos\alpha$, then the energy change becomes

$$\begin{aligned} \frac{\nu'}{\nu} &\simeq \frac{1-\beta\mu}{1-\beta\mu'} \\ &\simeq 1 + \beta(\mu'-\mu) + (\beta\mu')^2 + (\beta\mu')^3 + \ldots \ , \end{aligned} \tag{2.67}$$

which may be written as

$$\frac{\Delta\nu}{\nu} \simeq (\mu' - \mu)\,\beta + \mathcal{O}\left(\beta^2\right) \ . \tag{2.68}$$

The angle α is simply the incoming angle with respect to the electron 4-velocity. However, in the case of extreme beaming the angle α' is strongly beamed in the direction of the electron 4-velocity and $\alpha' \sim 1/\gamma \ll 1$ and hence $\mu' \approx 1$, which gives

$$\frac{\Delta\nu}{\nu} \simeq (1 - \mu)\,\beta \ . \tag{2.69}$$

Averaging over all angles μ yields

$$\begin{aligned} \left\langle \frac{\Delta\nu}{\nu} \right\rangle &\simeq \frac{\beta \int_{-1}^{1} \mathrm{d}\mu\ (1-\mu)}{\int_{-1}^{1} \mathrm{d}\mu} \\ &= \beta \ , \end{aligned}$$

which is the familiar Doppler shift formula

$$\frac{\Delta\nu}{\nu} \sim \beta \ . \tag{2.70}$$

The full Compton scattering case is far more complicated and has its roots in quantum electrodynamics. The differential cross-section for unpolarised radiation is given by the Klein-Nishina (Klein and Nishina 1929) formula

$$\frac{\mathrm{d}\sigma_{\mathrm{KN}}}{\mathrm{d}\Omega} = \frac{r_0^2}{2}\left(\frac{\nu'}{\nu}\right)^2\left(\frac{\nu}{\nu'} + \frac{\nu'}{\nu} - \sin^2\theta\right) \ , \tag{2.71}$$

where $r_0 = \mathrm{e}^2/m_{\mathrm{e}}c^2$ is the classical electron radius. This formula reduces the Compton scattering cross-section from its classical value as photon energies become large, so Compton scattering becomes less efficient at higher energies. The total cross-section is given by

$$\sigma_{\mathrm{KN}} = \frac{3}{4}\sigma_{\mathrm{T}}\left[\frac{1+x}{x^2}\left\{\frac{2x(1+x)}{1+2x} - \ln(1+2x)\right\} + \frac{1}{2x}\ln(1+2x) - \frac{1+3x}{(1+2x)^2}\right] \ , \tag{2.72}$$

where $x \equiv h\nu/m_{\mathrm{e}}c^2$. For an isotropic distribution of photons scattering off an isotropic distribution of electrons, the net power (averaged over all angles) radiated by an electron in an IC scattering event is given by Rybicki and Lightman (1979) as

$$P_{\mathrm{Comp}} = \frac{4}{3}\sigma_{\mathrm{T}}c\gamma^2\beta^2 U_{\mathrm{ph}} \ , \tag{2.73}$$

where $U_{\rm ph}$ is the photon energy density prior to scattering and is defined as

$$\begin{aligned} U_{\rm ph} &= \int \mathrm{d}^3 p \, \nu \, n\left(p\right) \\ &= \int \mathrm{d}\nu \, v\nu \ , \end{aligned} \tag{2.74}$$

where $n\left(p\right)\mathrm{d}^3 p = v\,\mathrm{d}\nu$ is the density of photons having energy in the range $\mathrm{d}\nu$, and $n\left(p\right)$ is the photon phase space distribution function. This derivation assumes isotropy in both the photon and electron distributions, as well as $\gamma h\nu \ll m_{\rm e}c^2$ and $\nu' \gg \nu$, and is only applicable in the Thomson regime. Corrections to equation (2.73) to include the Klein-Nishina regime ($x \ll 1$) and the effects of energy transfer in the electron rest frame may be included (see Blumenthal and Gould 1970; Rybicki and Lightman 1979).

The total Compton power may be calculated by integrating equation (2.73) over a power-law distribution of electrons. Taking $N(\gamma)\mathrm{d}\gamma$ as the number of electrons per unit volume with γ in the range γ to $\gamma + \mathrm{d}\gamma$, then the total power is

$$P_{\rm tot} = \frac{4}{3}\sigma_{\rm T} c \, U_{\rm ph} C \times \begin{cases} \ln\left(\frac{\gamma_{\rm max}}{\gamma_{\rm min}}\right), & \text{if } p = 3 \\ \left(3-p\right)^{-1}\left(\gamma_{\rm max}^{3-p} - \gamma_{\rm min}^{3-p}\right), & \text{otherwise} \end{cases} \tag{2.75}$$

There is a similarity between the power due to Compton scattering (2.73) and the power due to synchrotron radiation (2.58). They are related via

$$\frac{P_{\rm synch}}{P_{\rm Comp}} = \frac{U_{\rm B}}{U_{\rm ph}} \ . \tag{2.76}$$

Therefore losses due to synchrotron and Compton processes are in the ratio of the magnetic field energy density to the photon field energy density, and are independent of γ. The scattered photons may be produced in the source from Synchrotron radiation, and if these electrons are subsequently boosted in energy through IC scattering then the resultant emission is said to be synchrotron self-Compton (SSC).

If the spectrum of a radiation source is primarily determined by Compton processes then it is referred to as Comptonised. This requires that the medium in which this is occurring be sufficiently transparent that other processes (e.g. Bremsstrahlung) do not dominate the spectrum instead. Comptonisation becomes more likely the hotter the gas is.

For simplicity, first consider an ensemble of photons and non-relativistic electrons, where $h\nu \ll m_{\rm e}c^2$. From equation (2.66) the relative change in photon energy may be written

$$\frac{\Delta\nu}{\nu} = \frac{h\nu}{m_{\rm e}c^2}(1-\cos\theta) \ . \tag{2.77}$$

Averaging this over all angles yields

$$\frac{\Delta\nu}{\nu} = \frac{h\nu}{m_{\rm e}c^2} \ , \tag{2.78}$$

which satisfies $\Delta\nu/\nu \ll 1$. Therefore $\nu' \simeq \nu$ and the photon energy gain after scattering is negligible. The radiated power of these non-relativistic electrons ($\gamma \approx 1$) is given by

$$P_{\rm Comp} = \frac{4}{3}\sigma_{\rm T}c\left(\frac{v}{c}\right)^2 \ , \tag{2.79}$$

where v is the linear electron velocity. The number of scattered photons per unit time is the number of photons encountered per unit time by an electron, denoted by the photon number density $N_{\rm phot}c\sigma_{\rm T}$, where $N_{\rm phot}$ is the total number of photons. Thus, the photon number density is simply

$$N_{\rm phot} = \frac{U_{\rm rad}}{h\nu} \ , \tag{2.80}$$

hence

$$\sigma_{\rm T}N_{\rm phot}c = \frac{\sigma_{\rm T}U_{\rm rad}c}{h\nu} \ . \tag{2.81}$$

Therefore

$$\frac{\Delta\nu}{\nu} = \frac{4}{3}\left(\frac{v}{c}\right)^2 \ , \tag{2.82}$$

for $h\nu \gg m_{\rm e}c^2$. Therefore, if the photon energy is much smaller than the electron rest mass energy then the electrons gain energy in the scattering event. Conversely, if the photon energy is far greater than the electron rest mass energy then the photons gain energy.

In reality some of the electrons are thermalised. Consider a thermal distribution of electrons with temperature $T_{\rm e}$. It follows that

$$\frac{3}{2}k_{\rm B}T_{\rm e} = \frac{1}{2}m_{\rm e}v^2 \ , \tag{2.83}$$

which implies $(v/c)^2 = 3k_{\rm B}T_{\rm e}/m_{\rm e}c^2$. Thus for photons which satisfy $h\nu \ll m_{\rm e}c^2$ the following relation may be obtained

$$\frac{\Delta\nu}{\nu} = \frac{4k_{\rm B}T_{\rm e}}{m_{\rm e}c^2} \tag{2.84}$$

Combining this result with equation (2.78) an expression for the energy loss or gain in both energy regimes may be written as

$$\frac{\Delta\nu}{\nu} = \frac{1}{m_{\rm e}c^2}\left(4k_{\rm B}T_{\rm e} - h\nu\right) \ . \tag{2.85}$$

This is the expression for energy transfer per scattering event for non relativistic electrons in thermal equilibrium. Thus if $h\nu > 4k_{\rm B}T_{\rm e}$ then energy is transferred to the electron (i.e. the photon loses energy due to electron recoil). Conversely, if $h\nu < 4k_{\rm B}T_{\rm e}$ then the photons may gain energy and this is IC scattering. Around black holes and most other cases of astrophysical interest $h\nu < 4k_{\rm B}T_{\rm e}$ and IC scattering is dominant. Therefore photons gain or lose energy in a random walk process as they move through a plasma cloud. The photon energy gain per unit time due to the Doppler effect along a random path is given by the Compton y-parameter

$$y = \frac{k_{\rm B}T_{\rm e}}{m_{\rm e}c^2} c\sigma_{\rm T} n_{\rm e} \ . \tag{2.86}$$

If the plasma region has a characteristic length l, then the optical depth for scattering is given by

$$\tau = n_{\rm e}\sigma_{\rm T} l \ , \tag{2.87}$$

and the associated probability for scattering is $e^{-\tau}$. In regions of high optical depth it may be shown that the number of scatterings $N \approx \tau^2$, whereas for regions of low optical depth $N = 1 - e^{-\tau} \simeq \tau$. In most estimates it is reasonable to use $N \approx \tau^2 + \tau$ or, more commonly, $N \approx \max(\tau, \tau^2)$ for all optical depths.

The above analysis considers strong and weak Comptonisation in a non-relativistic medium. It is natural to ask what happens in intermediate cases. This was considered and first solved by Kompaneets in 1949. The derivation of this result is non-trivial and omitted for the sake of brevity. The time evolution of a Comptonised radiation spectrum is governed by the evolution of the photon phase space density due to scattering from electrons. This may be found by solving the Boltzmann equation for this process. Solving this to second order yields the Kompaneets equation, which describes the evolution of the photon distribution function (in the non-relativistic regieme) for multiple

IC scatterings

$$\frac{\partial n}{\partial y} = \frac{1}{x^2}\frac{\partial}{\partial x}\left[x^4\left(n + n^2 + \frac{\partial n}{\partial x}\right)\right] \ . \tag{2.88}$$

In the Kompaneets equation the first term in brackets, n, describes the cooling of photons (i.e. electron recoil). The second term, n^2 describes cooling due to induced Compton scattering. The final term, $\partial n/\partial x$, describes the increase/decrease in photon numbers in frequency space. In this instance the Compton y-parameter is generalised to an integral along the photon path

$$y = \int \mathrm{d}l \, \frac{k_\mathrm{B} T_\mathrm{e}}{m_\mathrm{e} c^2} \sigma_\mathrm{T} n_\mathrm{e} \ . \tag{2.89}$$

A good approximate solution for the flux density F_ν found by Sunyaev and Zel'dovich (1980), and applied to accretion disks by Sunyaev and Titarchuk (1985), is given by

$$F_\nu(x) \propto \begin{cases} x^{\alpha+3}, & x \ll x_0 \\ x^{-\alpha}, & x_0 \ll x \ll 1 \\ x^3 e^{-x}, & x \gg 1 \end{cases} \tag{2.90}$$

where the spectral index α is given by

$$\alpha = \sqrt{\frac{9}{4} + \frac{1}{y}} - \frac{3}{2} \ , \tag{2.91}$$

and $x_0 = h\nu_0/k_\mathrm{B}T_\mathrm{e}$, where ν_0 is the frequency of seed photons. For $h\nu \ll k_\mathrm{B}T_\mathrm{e}$ the spectrum is power-law in profile. At high photon energies ($h\nu \gg k_\mathrm{B}T_\mathrm{e}$) electron recoil effects dominate and the spectrum assumes a Wien law profile.

2.3 Line Formation

The emission lines in AGN X-ray spectra are a key diagnostic of physical processes occurring near the event horizon of the central black hole. These broadened lines arise as a consequence of classical line broadening and relativistic line broadening (e.g. Griem 1974; Fabian et al. 2000). Classical broadening includes the natural line width due to uncertainty in the electron energy levels, as well as thermal broadening and potentially turbulent broadening (see Novotny 1973). Macroscopic motions of the medium may introduce Doppler shifts which can further increase the observed line width. Relativistic

line broadening incorporates special relativistic transverse Doppler shifts and beaming, as well as gravitational redshift, which is a purely general relativistic effect.

2.3.1 Classical line formation

A non-relativistic line profile is essentially a delta function at the emission line rest frequency. However, many effects serve to broaden this line. On a quantum level, natural line broadening occurs from bound-bound transitions. A photon incident upon an atom with a bound electron may be considered as an oscillating electric field. The electron will radiate a quantised amount of radiation when it undergoes a bound-bound transition. When the electron emits, it experiences a force from its own radiation, damping its oscillatory motion (see Rybicki and Lightman 1979). This damping is related to uncertainty in the energy levels.

Assuming the incident photon is propagating in the x-direction, the electron will experience an oscillation in the y-direction. The electron is a harmonic oscillator of the form

$$\ddot{y} + \Gamma\dot{y} + \omega_0^2 y = \frac{\mathrm{e}}{m_\mathrm{e}} E_0 \mathrm{e}^{\mathrm{i}\omega t} \ , \tag{2.92}$$

where an overdot denotes differentiation with respect to time, Γ is the damping constant for the electron, $\omega \equiv 2\pi c/\lambda$ is the incident photon oscillation frequency, E_0 is the electric field energy and $\omega_0 = (E_\mathrm{upper} - E_\mathrm{lower})/2\pi\hbar$ is defined in terms of the upper and lower energy levels, denoted respectively by E_upper and E_lower. Equation (2.92) may be solved, yielding

$$y(t) = \left(\frac{\mathrm{e}}{m_\mathrm{e}}\right) \frac{E_0 \mathrm{e}^{\mathrm{i}\omega t}}{\omega_0^2 - \omega^2 + \mathrm{i}\Gamma\omega} \ . \tag{2.93}$$

This is the classical equation for the amplitude of dipole oscillations in a photon field. Resonance occurs when the photon frequency matches the difference in energy levels ($\omega = \omega_0$). It may be shown that the natural absorption coefficient per atom is given by

$$\alpha_\mathrm{natural} = \frac{\pi \mathrm{e}^2}{m_\mathrm{e} c} \frac{\Gamma/2}{(\Delta\omega)^2 + (\Gamma/2)^2} \ , \tag{2.94}$$

where $\Delta\omega = (\omega_0 - \omega)$. This is a Lorentzian profile. A more detailed treatment requires deriving the damping constant from the Einstein coefficients. There

is in fact a damping constant associated with both the lower and upper energy levels, with the damping constant being related to the uncertainty in each level via

$$\Delta E_{\rm upper} = \frac{h}{2\pi\Gamma_{\rm upper}} , \tag{2.95}$$

$$\Delta E_{\rm lower} = \frac{h}{2\pi\Gamma_{\rm lower}} , \tag{2.96}$$

where $\Gamma = \Gamma_{\rm upper} + \Gamma_{\rm lower}$. It is the probability distribution of this spread of photon energies due to uncertainty in the energy levels that results in the Lorentzian profile. This is the natural width of a line.

In reality, lines are always broader than their natural widths. Additional broadening, particularly in AGN, arises from thermal and turbulence effects (see Griem 1974). In an isothermal gas each atom has an observable radial component of velocity, $v_{\rm rad}$. Bound-bound transitions in atoms moving towards/away from the observer will absorb photons with wavelengths shorter/longer than the rest-frame transition wavelength ($\lambda_{\rm rest}$), by an amount

$$\lambda = \lambda_{\rm rest}\left(1 \mp \frac{v_{\rm rad}}{c}\right) . \tag{2.97}$$

In terms of the most probable velocity, $v_{\rm p}$, for an atom in a gas with temperature T, the Doppler shift is given by

$$\begin{aligned} \Delta\lambda_{\rm D} &= \frac{v_{\rm p}}{c}\lambda_{\rm rest} \\ &= \frac{\lambda_{\rm rest}}{c}\left(\frac{2k_{\rm B}T}{m}\right)^{1/2} , \end{aligned} \tag{2.98}$$

where m is the mass of the atom and T is the gas temperature. These Doppler shifts spread the absorption over a wider range of wavelengths, modifying the observed line profile into a Voigt profile (Voigt 1912). At each radial velocity the absorbing atoms form a natural absorption profile, with the amplitude modulated by the number of atoms at that velocity. The probability that an atom will have a velocity $v_{\rm rad}$ is

$$f(v_{\rm rad}) = \frac{1}{\sqrt{\pi}\,v_{\rm p}} {\rm e}^{-(v_{\rm rad}/v_{\rm p})^2} {\rm d}v_{\rm rad} . \tag{2.99}$$

Therefore, from the Doppler shift in equation (2.98), the distribution of $\Delta\lambda$ removed from a ray is given by

$$f(\Delta\lambda)\mathrm{d}\lambda = \frac{1}{\sqrt{\pi}\Delta\lambda_\mathrm{D}}\mathrm{e}^{-(\Delta\lambda/\Delta\lambda_\mathrm{D})^2}\mathrm{d}\lambda \ . \tag{2.100}$$

Since $\Delta\lambda_\mathrm{D}$ is proportional to $T^{1/2}$, the absorption increases with increasing temperature. It is straightforward to show that the effects of redshift, z, are easily included, resulting in the following relation

$$f(\Delta\lambda_\mathrm{obs})\mathrm{d}\lambda_\mathrm{obs} = f(\Delta\lambda)\mathrm{d}\lambda \ , \tag{2.101}$$

where $\Delta\lambda_\mathrm{obs} = \Delta\lambda(1+z)$. Therefore, the observed broadening of a line is increased in a redshifted medium, but the distribution of velocities is an invariant quantity. As such, equation (2.100) may be applied for all redshifts.

The Voigt profile gives the distribution of absorption as a function of wavelength (Voigt 1912; Olivero and Longbothum 1977). This applies when the natural absorption coefficient per atom for natural broadening is convolved with the thermal distribution of atoms. In this instance the optical depth, τ_λ, takes the form of a Voigt profile

$$\begin{aligned}
\tau_\lambda &= \int_{-\infty}^{\infty}\mathrm{d}\lambda' \, N\alpha_\mathrm{natural}(\lambda')f(\lambda'-\lambda) \\
&= N\frac{\mathrm{e}^2\lambda_\mathrm{rest}^2}{m_\mathrm{e}c^2}f\frac{\widetilde{\Gamma}}{(\lambda-\lambda_\mathrm{rest})^2+\widetilde{\Gamma}^2} * \frac{1}{\sqrt{\pi}\Delta\lambda_\mathrm{D}}\mathrm{e}^{-(\Delta\lambda/\Delta\lambda_\mathrm{D})^2} \\
&= N\frac{\pi\mathrm{e}^2\lambda_\mathrm{rest}^2}{m_\mathrm{e}c^2}\frac{f}{\sqrt{\pi}\Delta\lambda_\mathrm{D}}H(x,y) \ ,
\end{aligned} \tag{2.102}$$

where $\widetilde{\Gamma} \equiv \Gamma\lambda_\mathrm{rest}^2/4\pi c$, $N = \int \mathrm{d}s \, n$ is the column density, and $H(x,y)$ is the Hjerting function

$$H(x,y) = \frac{y}{\pi}\int_{-\infty}^{\infty}\mathrm{d}t \, \frac{\mathrm{e}^{-t^2}}{(x-t)^2+y^2} \ , \tag{2.103}$$

where

$$x = \frac{\Delta\lambda}{\Delta\lambda_\mathrm{D}} \ , \tag{2.104}$$

$$y = \frac{\Gamma\lambda_\mathrm{rest}^2}{4\pi c}\frac{1}{\Delta\lambda_\mathrm{D}} \ . \tag{2.105}$$

The Hjerting function may be written analytically as

$$H(x,y) = e^{-(x^2-y^2)}\left\{\cos 2xy + \mathrm{Im}\left[\mathrm{i}\,\mathrm{Erf}(\mathrm{i}z)\mathrm{e}^{-2\mathrm{i}xy}\right]\right\} \ , \tag{2.106}$$

where $\mathrm{Erf}(z)$ is the error function. In this instance x is the independent variable, being the difference between the wavelength along the profile and the line center, in units of the Doppler width. The parameter y is not a function of $\Delta\lambda$, and so does not vary across the absorption profile. However y is a function of the damping constant Γ, the wavelength of the line center λ_{rest} and the Doppler width $\Delta\lambda_{\mathrm{D}}$.

Consequently, the absorption profile will have the form

$$I_\lambda = I_{\lambda,0}\, \mathrm{e}^{-\tau_\lambda} \ , \tag{2.107}$$

where I_λ is the observed flux and $I_{\lambda,0}$ is the continuum flux in the absence of the absorption line.

In principle, a given observed line shape may be fitted to equation (2.107) to obtain the column density and Doppler width. In practice this approach only works with high resolution data with good signal-to-noise. Additionally, when looking at high-resolution spectra, absorption lines often have multiple components, constituting a complex, blended profile.

In practice Doppler widths are written in terms of the Doppler b parameter

$$\begin{aligned} b &= \frac{c}{\lambda}\Delta\lambda_{\mathrm{D}} \\ &= \left(\frac{2k_{\mathrm{B}}T}{m_{\mathrm{i}}}\right)^{1/2} \ , \end{aligned} \tag{2.108}$$

where m_{i} is the mass of the atomic species in which the transition occurs. Equations (2.104) and (2.105) may be re-expressed as

$$x = \frac{v_{\mathrm{rad}}}{c} \ , \tag{2.109}$$

$$y = \frac{\Gamma\lambda_{\mathrm{rest}}^2}{4\pi b} \ , \tag{2.110}$$

whereby the optical depth may be re-expressed in terms of a single component as

$$\tau_\lambda = N\frac{\sqrt{\pi}\,\mathrm{e}^2}{m_{\mathrm{e}}b^2} f\, H(x,y) \ . \tag{2.111}$$

By inserting this expression into equation (2.107), individual velocity components may be measured in complex absorption profiles. If such an absorption

line is viewed at a redshift z, then the transformation between the observer frame and the rest frame is given by

$$\frac{v_{\rm rad}}{c} = \frac{\lambda}{(1+z)\lambda_{\rm rest}} - 1 \ . \tag{2.112}$$

In principle, with a given redshifted multiple-component absorption profile, it is possible to determine the redshifts, Doppler b parameters and column densities for each component. This requires statistical fitting of Voigt profiles (e.g. Outram et al. 2000).

As mentioned earlier, if the emitting plasma is turbulent then line broadening may also arise. Consider two absorption lines in the same isothermal cloud of gas. For two atoms of masses m_1 and m_2 the ratio of their Doppler b parameters is given by

$$\left(\frac{b_1}{b_2}\right) = \left(\frac{m_2}{m_1}\right)^{1/2} \ . \tag{2.113}$$

Heavier atoms have smaller Doppler b parameters, which follows intuitively. By considering the turbulence as a Gaussian, although unphysical, the Voigt profile is conserved in the total absorption coefficient. Gaussian functions may be convolved by linearly adding the squares of their respective dispersions. As such, the Doppler b parameters may be written as

$$\begin{aligned} b^2 &= b_{\rm therm}^2 + b_{\rm turb}^2 \\ &= \frac{2k_{\rm B}T}{m} + b_{\rm turb}^2 \ , \end{aligned} \tag{2.114}$$

where the turbulent component is independent of mass. In a given gas cloud, if turbulence dominates over thermal processes then the value of the Doppler b parameter is roughly constant over all observed absorption lines.

It may be shown, using equation (2.114) for each component, that the turbulent component may be written in terms of both components as

$$b_{\rm turb}^2 = \frac{b_2^2 - (m_1/m_2)b_1^2}{1-(m_1/m_2)} \ . \tag{2.115}$$

If more than two atomic species are present, more constraints may be placed on T, as well as the relative contribution of $b_{\rm turb}$. The higher the mass ratio of the atomic species, the better the constraints.

Additional macroscopic motions of the medium may introduce Doppler shifts which can further increase the line width when the observed emission is integrated over a large region with an inhomogeneous velocity, e.g. rotational broadening of stellar absorption lines (Shajn and Struve 1929).

2.3.2 Relativistic line formation (and distortions)

The X-ray emission observed in active galactic nuclei (AGN) and black hole binaries is believed to be powered by accretion of material onto black holes (Salpeter 1964; Lynden-Bell 1969; Shakura and Sunyaev 1973). Generally speaking, the term 'iron line' refers to the neutral Fe Kα line (at 6.4 keV). The accreting hot plasmas rotating around the black hole form a disk or a torus. It has been suggested that dense remnant neutron tori can also be formed around compact objects, which could be a very massive neutron star or a black hole, after two neutron stars merge (see Shibata et al. 2003; Baiotti et al. 2008; Rezzolla et al. 2010). In such systems, the influence of curved space-time is significant. It affects the radiative transport of particles in the accretion flow as well as the hydrodynamics of the flow itself (see Novikov and Thorne 1973).

Emission from accretion disks around compact objects has been investigated for several decades now. Emission lines from geometrically thin accretion disks around gravitating objects are expected to have two peaks (Smak 1969). The peaks correspond to emission from the two parts of the disk, which have opposite projected line-of-sight velocities. Double-peaked optical lines have been observed in a variety of binary systems (e.g. black hole X-ray binaries, Johnston et al. 1989; Marsh et al. 1994; Soria et al. 1999; Wu et al. 2001). Double-peaked optical lines are also seen in a small fraction of AGN (Puchnarewicz et al. 1996; Eracleous and Halpern 2003; Strateva et al. 2006). These double-peaked lines can be explained in a Newtonian framework as described in Smak (1969) (see also Horne and Marsh 1986). Double-peaked lines have also been observed in the X-ray spectra of accreting black holes. Broad asymmetric double-peaked Fe Kα lines were found in the spectra of a number of AGN (e.g. MCG–6-30-15, Tanaka et al. 1995). The X-rays of AGN are believed to originate from regions very close to the central black hole, where the

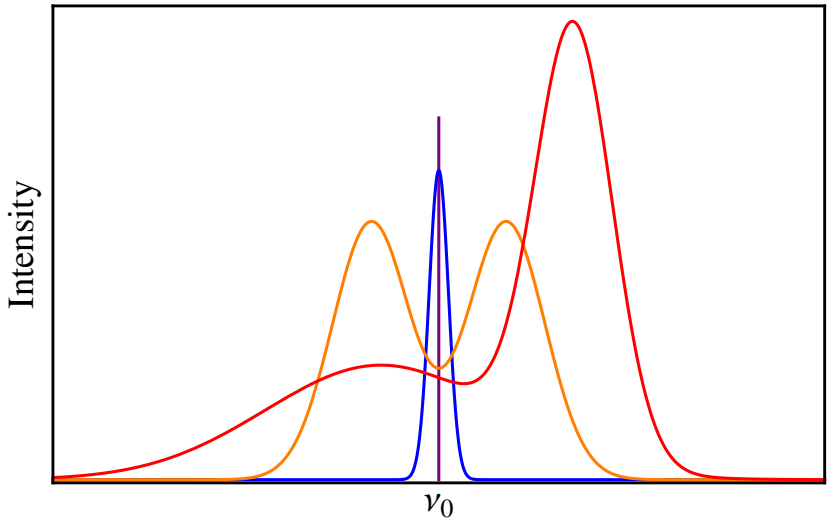

Fig. 2.2: Illustration (not to scale) of how a line profile from an accretion disk is formed. The intrinsic line is a delta function (purple) centred about the line rest frequency ν_0. Due to natural line broadening, thermal broadening, turbulent broadening and macroscopic Doppler motions the line assumes a Voigt profile (blue). Keplerian rotational motion of the disk shifts the line to higher and lower energies (orange) due to opposite line of sight motions. Finally, special relativistic and space-time curvature effects broaden and shift the line, causing it to become asymmetric (red).

accretion flow is highly relativistic and the gravity is strong. The emissions from different parts of the accretion flow are therefore boosted differentially. Various relativistic effects also cause additional differential broadening and distortion of any line emission. As such, the emission lines from the inner regions of relativistic accretion disks around black holes have a very broad profile, with an extended red wing and a pronounced blue peak (Cunningham 1975; Reynolds et al. 1999; Fabian et al. 2000). These different effects are illustrated in Figure 2.2. Black holes with faster spins would give rise to relativistic accretion lines with a broader red wing, because the inner boundary of an accretion disk around a maximally rotating black hole can extend very close to the black hole event horizon.

The emission from accreting gas and outflows in the vicinity of black holes is subject to Doppler shifts, lensing, gravitational time-dilation, and other relativistic dynamical effects. There have been numerous calculations

of relativistic (photon) lines from accretion disks and tori around black holes (e.g. Cunningham 1975; Gerbal and Pelat 1981; Fabian et al. 1989; Stella 1990; Kojima 1991; Bao 1992; Fanton et al. 1997; Reynolds et al. 1999; Fabian et al. 2000; Fuerst and Wu 2004; Beckwith and Done 2004a, 2005; Čadež and Calvani 2006; Schnittman and Rezzolla 2006; Fuerst and Wu 2007; Dexter and Agol 2009; Sochora et al. 2011; Vincent et al. 2011; Wang and Li 2012).

The three most common methods for calculating relativistic line profiles are (i) the transfer function method (e.g. Cunningham 1975; Fabian et al. 2000), (ii) the elliptic function method (e.g. Dexter and Agol 2009) and (iii) the direct geodesic integration method (e.g. Fuerst and Wu 2004; Schnittman and Rezzolla 2006; Fuerst and Wu 2007; Anderson et al. 2010; Vincent et al. 2011; Younsi et al. 2012; Yang and Wang 2013). The transfer function method and the elliptic function method are efficient for the calculation of emission from thin axisymmetric optically thick accretion disks but are not applicable to systems that lack the appropriate geometry and symmetry. The elliptic function method computes all co-ordinates in the Kerr metric semi-analytically. This has the advantage of being very fast since integration step size is no longer an issue, working well in simple observer emitter problems for relativistic line profiles. However, this method is limited by its inability to handle radial turning points in the geodesics, as well as the more general case of particle geodesics. Moreover, it cannot handle emission structures without sharply defined boundaries, i.e. three-dimensional structures with opacity. The direct geodesic integration method is a brute force approach, and less restrictive in this context, compared to the other two methods. It works well with any three-dimensional accretion flow, e.g. time-dependent accretion flows from numerical relativistic hydrodynamic simulations, and can also handle opacity variations within the system.

In most of these relativistic calculations, the focus was on the investigation of line broadening due to relativistic effects. While relativistic ray-tracing of photons in strong gravity and the corresponding calculations of emission line profile broadening have been investigated in various astrophysical settings for decades, there have been only a few studies, often in restricted settings, of the

opacity effects due to self-absorption, emission and scattering within the accretion flows and along the line of sight (e.g. Zane et al. 1996; Fuerst 2006; Wu et al. 2006, 2008; Dolence et al. 2009). Covariant radiative transfer calculations of emission from accretion flows in more general settings with an explicit treatment of absorption, emission and scattering are lacking. There is also no corresponding covariant radiative transport formulation applicable to both relativistic particles without mass (photons) and with mass (e.g. neutrinos), in a general astrophysical setting in the present literature. (Note that particles with mass do not follow null geodesics, and the relativistic formulation and the corresponding ray-tracing need to be modified.) In Chapter 3, I derive a covariant radiative transfer formulation to do just this.

Various aspects of the emission, e.g. reverberation and reflection (Reynolds et al. 1999), and effects of higher-order images (e.g. Viergutz 1993; Bao et al. 1994; Beckwith and Done 2005), have been investigated using the methods mentioned above. These studies have shown how the intrinsic emission line profiles are shaped by the accretion flow dynamics and by the spacetime near the black hole. They have provided a framework to interpret the observations qualitatively, in particular, the Fe lines in X-ray spectra. Absorption by line-of-sight material, as well as emission and the effects of electron scattering have only been addressed in recent studies by Fuerst and Wu (2004) and Younsi et al. (2012), the results of which will be discussed in Chapter 4. Absorption and scattering are important in the line formation process. They must be properly considered in spectral models in order to obtain results that are useful for interpreting observations.

Chapter 3

General Relativistic Radiative Transfer and Ray-Tracing

In order to perform practical radiative transport calculations in full general relativity, the geodesic motion of both photons and particles with mass must be determined. However, in the strong gravitational field of a rotating black hole, space-time is no longer flat, and the motions of both massive and massless particles (such as photons) follow curved trajectories. Moreover, in the vicinity of a rotating black hole, even space-time itself is affected by the black hole's rotation, giving rise to the dragging of inertial frames. This has a very strong influence on the angular velocity of orbiting particles.

This Chapter introduces the mathematical techniques for computing geodesics and performing radiative transport calculations in the strong gravitational field of a rotating black hole. The properties of the space-time of the rotating black hole are introduced and the equations of motion of both photons and particles with mass are derived through the Lagrangian formalism. The motion of particles under the influence of external forces, such as in the flow of a relativistic accretion torus, is also determined and the ray-tracing setup is outlined in detail. Finally, the general relativistic radiative transfer formalism is introduced.

3.1 Kerr Black Hole

It is widely acknowledged that most stellar objects that undergo gravitational collapse are in possession of some angular momentum. Upon collapse the

resultant object must also possess some angular momentum. It thus follows that black holes must have some intrinsic angular momentum inherited from their progenitor. Therefore a complete treatment of radiative processes around black holes must account for the black hole angular momentum, or spin. Herein, unless explicitly stated otherwise, the geometrical unit convention (with $G = c = h = 1$) and the metric signature $(-, +, +, +)$ are adopted throughout this thesis. The black hole spin parameter, or angular momentum per unit mass, is defined as

$$a \equiv \frac{J}{M} \ ,$$

where M is the mass of the black hole and J is its total angular momentum. The black hole spin parameter satisfies $|a| < 1$, with the case $a > 1$ corresponding to a type of "naked singularity", namely the non-existence of an event horizon, which is generally considered unphysical due to violation of causality, and led to the proposition of the "Cosmic Censorship" theorem (see Wald 1998). Taking dynamical and evolutionary properties into account, black holes may be in possession of spins as high as 0.998, as calculated by Thorne (1974). The black hole "no-hair theorem" states that black holes can be wholly characterised in terms of their mass, angular momentum and charge (see Misner et al. 1973). However, it is highly unlikely that any black hole can possess a significant amount of charge as any net charge it possesses would be rapidly neutralised by the surrounding ISM or accretion flow. The rotating black hole is therefore assumed to be uncharged.

With this in mind, the most general solution of the Einstein Field Equations describing a rotating black hole is given by the Kerr (1963) solution. The Kerr metric, written in Boyer-Lindquist (BL) co-ordinates (oblate spheroidal co-ordinates), is given by

$$\mathrm{d}s^2 = g_{tt}\mathrm{d}t^2 + 2g_{t\phi}\mathrm{d}t\mathrm{d}\phi + g_{rr}\mathrm{d}r^2 + g_{\theta\theta}\mathrm{d}\theta^2 + g_{\phi\phi}\mathrm{d}\phi^2 \ , \tag{3.1}$$

where the covariant metric coefficients $g_{\mu\nu}$ are given by

$$g_{tt} = -\left(1 - \frac{2Mr}{\Sigma}\right) , \tag{3.2}$$

$$g_{t\phi} = -\frac{2aMr\sin^2\theta}{\Sigma} , \tag{3.3}$$

$$g_{rr} = \frac{\Sigma}{\Delta} , \tag{3.4}$$

$$g_{\theta\theta} = \Sigma , \tag{3.5}$$

$$g_{\phi\phi} = \frac{\sin^2\theta}{\Sigma}\left[\left(r^2 + a^2\right)^2 - \Delta\, a^2 \sin^2\theta\right] , \tag{3.6}$$

and

$$\Sigma(r,\theta) = r^2 + a^2\cos^2\theta , \tag{3.7}$$

$$\Delta(r) = r^2 - 2Mr + a^2 , \tag{3.8}$$

where the three-vector (r, θ, ϕ) corresponds to spherical polar zenith and azimuthal co-ordinates respectively, and r is a modified radial co-ordinate variable which does not coincide with the usual spherical polar radius. Note that the Kerr metric, equation (3.1), is independent of both t and ϕ, implying that the Kerr space-time is both stationary and axisymmetric. For completeness, the contravariant components of the Kerr metric are also stated, which will be useful in later calculations. These are given by

$$g^{tt} = -\frac{g_{\phi\phi}}{\Delta\sin^2\theta} , \tag{3.9}$$

$$g^{t\phi} = \frac{g_{t\phi}}{\Delta\sin^2\theta} , \tag{3.10}$$

$$g^{rr} = \frac{1}{g_{rr}} , \tag{3.11}$$

$$g^{\theta\theta} = \frac{1}{g_{\theta\theta}} , \tag{3.12}$$

$$g^{\phi\phi} = -\frac{g_{tt}}{\Delta\sin^2\theta} . \tag{3.13}$$

From these equations a discussion of the important properties and regions of the Kerr space-time naturally follows. In the case of a non-rotating black hole, setting $a = 0$ reduces equation (3.1) to

$$\mathrm{d}s^2 = -\left(1 - \frac{2M}{r}\right)\mathrm{d}t^2 + \left(1 - \frac{2M}{r}\right)^{-1}\mathrm{d}r^2 + r^2\mathrm{d}\theta^2 + r^2\sin^2\theta\,\mathrm{d}\phi^2, \tag{3.14}$$

which is precisely the Schwarzschild solution describing the exterior gravitational field of a non-rotating compact object. When the black hole mass is zero, equation (3.1) reduces to

$$\mathrm{d}s^2 = -\mathrm{d}t^2 + \frac{\Sigma}{r^2+a^2}\,\mathrm{d}r^2 + \Sigma\,\mathrm{d}\theta^2 + (r^2+a^2)\sin^2\theta\,\mathrm{d}\phi^2 \ , \tag{3.15}$$

which is the metric for flat Euclidean space

$$\mathrm{d}s^2 = -\mathrm{d}t^2 + \mathrm{d}x^2 + \mathrm{d}y^2 + \mathrm{d}z^2 \ , \tag{3.16}$$

in oblate spheroidal co-ordinates. From this the transformation between rectangular co-ordinates and BL co-ordinates is readily obtained as

$$x = \sqrt{r^2+a^2}\,\sin\theta\cos\phi \ , \tag{3.17}$$

$$y = \sqrt{r^2+a^2}\,\sin\theta\sin\phi \ , \tag{3.18}$$

$$z = r\cos\theta \ . \tag{3.19}$$

The inverse transformation, from rectangular to BL co-ordinates, follows algebraically and is given by

$$r = \sqrt{\frac{\sigma+\sqrt{\sigma^2+4a^2z'^2}}{2}} \ , \tag{3.20}$$

$$\theta = \arccos\left(\frac{z'}{r}\right) \ , \tag{3.21}$$

$$\phi = \mathrm{atan2}(y',x') \ , \tag{3.22}$$

where $\sigma \equiv x'^2 + y'^2 + z'^2 - a^2$.

It is clear from equations (3.2)–(3.6) that there exist two singular regions, one at $\Sigma(r,\theta) = 0$ and the other at $\Delta(r) = 0$. The former is satisfied when $(r,\theta) = (0,\pi/2)$, which has no physical meaning in BL co-ordinates. However, substitution into equations (3.17)–(3.19) yields $(x,y,z) = (a\cos\phi, a\sin\phi, 0)$. Hence the singularity at $\Sigma(r,\theta) = 0$ corresponds to a ring of radius a, located in the equatorial plane of the black hole. In the limit $a = 0$ this singularity degenerates to a point, as is the case in the Schwarzschild space-time. The second singular region, $\Delta(r) = 0$, may be re-expressed as $(r-r_+)(r-r_-) = 0$, where

$$r_\pm = M \pm \sqrt{M^2-a^2} \ , \tag{3.23}$$

giving rise to two singularities. The first singularity, r_+, corresponds to the "Event Horizon" of the black hole: the surface upon which the escape velocity of a particle is locally the speed of light. The second, inner horizon, is also known as the Cauchy Horizon, and is more a mathematical curiosity than a physically relevant horizon since it is interior to the conventional event horizon. A particle which passes into the region $r < r_+$ must by necessity follow geodesics along decreasing values of r until entering the region $r < r_-$ (see Chandrasekhar 1983). Therefore r_+ is a one-way membrane where once crossed escape is impossible, hence the term "event horizon", the boundary of the black hole region. Thus, anything that happens within $r = r_-$ will not affect physics outside of it, i.e in the rest of the Universe, since particles in the region $r < r_-$ may never enter the region $r > r_-$. For this reason r_- is referred to as a Cauchy Horizon. Note that in the limit $a = 0$, the event horizon is located at $r = 2M$, which is precisely the Schwarzschild radius. The Cauchy Horizon in this case is located at $r = 0$, coinciding with the ring singularity, namely the singularity of the black hole.

Naturally the question arises as to what is the difference between a horizon and a singularity, since the metric is singular at both. True singularities are curvature singularities of the space-time itself, and may be computed from curvature invariants like the Kretschmann scalar, which is the contraction of the Riemann curvature tensor and is defined as

$$\begin{aligned} K &\equiv R^{\mu\nu\alpha\beta} R_{\mu\nu\alpha\beta} \\ &= \frac{48M^2\left(2r^2 - \Sigma\right)\left(\Sigma^2 - 16r^2a^2\cos^2\theta\right)}{\Sigma^6} \,. \end{aligned} \tag{3.24}$$

It immediately follows that the only true singularity corresponds to $\Sigma(r, \theta) = 0$, namely the ring singularity. The event horizon (as well as the Cauchy horizon) is thus a co-ordinate singularity and not a true physical singularity, and can in principle be removed through a suitable co-ordinate transformation. For the Kerr space-time such a transformation exists and is given by writing the metric in Kerr-Schild form, as it was originally derived by Kerr (1963). The

resultant co-ordinate transformation is given by

$$\mathrm{d}\tilde{t} = \mathrm{d}t \pm \frac{r^2 + a^2}{\Delta}\mathrm{d}r \ , \tag{3.25}$$

$$\mathrm{d}\tilde{\phi} = \mathrm{d}\phi \pm \frac{a}{\Delta}\mathrm{d}r \ , \tag{3.26}$$

which may be integrated to yield

$$\tilde{t} = t \pm \left[r + M\log\Delta + \frac{2M^2}{r_+ - r_-}\log\left(\frac{r - r_+}{r - r_-}\right)\right] \ , \tag{3.27}$$

$$\tilde{\phi} = \phi \pm \frac{a}{r_+ - r_-}\log\left(\frac{r - r_+}{r - r_-}\right) \ , \tag{3.28}$$

where the $\pm$ sign corresponds to outgoing (ingoing) null geodesics. Of course transforming from Kerr-Schild co-ordinates to BL co-ordinates is physically meaningless when the geodesic is interior to the event horizon since in reality everything within r_+ is causally disconnected from the rest of the Universe. However, the use of "horizon penetrating" Kerr-Schild co-ordinates has important applications in many areas of numerical Astrophysics, such as GRMHD simulations where physical quantities like the topology of the magnetic field must not be abruptly truncated at the event horizon (e.g. Gammie et al. 2003).

An important phenomenon caused by the rotation of a Kerr black hole is the dragging of inertial frames. To understand this, consider a zero angular momentum observer (ZAMO). ZAMO's are defined as a set of local observers 'hovering' with fixed spatial coordinates, whose world lines are orthogonal to surfaces of constant time. In the Schwarzschild case this is simply $(u^\mu)_{\mathrm{ZAMO}} = (u^t, 0, 0, 0)$. However, in the Kerr metric, even for a stationary observer with $L_z = u_\phi = 0$, surfaces of constant BL time, t, are not orthogonal to the observer's world line. Since $u^\phi = g^{t\phi}u_t + g^{\phi\phi}u_\phi \neq 0$, even when $u_\phi = 0$, then the geodesic of a ZAMO has a non-zero angular velocity

$$\Omega = \frac{\mathrm{d}\phi}{\mathrm{d}t} = \frac{u^\phi}{u^t} \ . \tag{3.29}$$

It follows from the metric that a ZAMO satisfies $u_\phi = 0 = g_{t\phi}u^t + g_{\phi\phi}u^\phi$, from

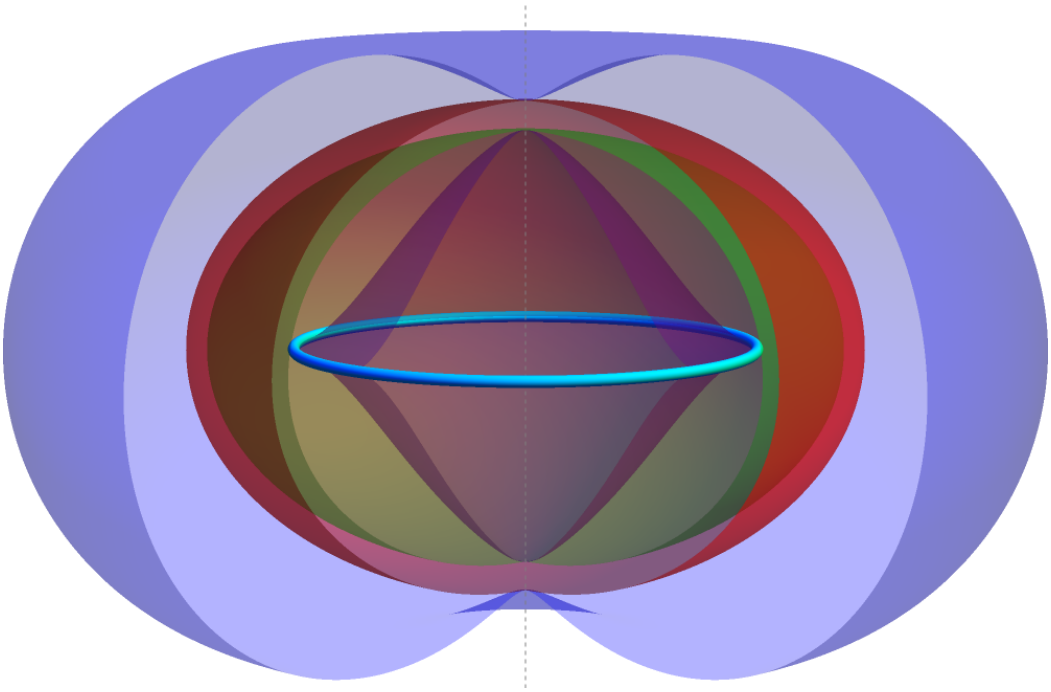

Fig. 3.1: Cut-through view in 3D of the key surfaces of a Kerr black hole with spin parameter $a = 0.998$. From outside to inside: Static Limit (blue), Event Horizon (red), Cauchy Horizon (green), Inner Static Limit (purple) and the ring singularity (blue equatorial ring). The grey dotted line is the spin axis of the black hole.

whence it follows that

$$\begin{aligned} \Omega &= -\frac{g_{t\phi}}{g_{\phi\phi}} \\ &= \frac{2aMr}{(r^2+a^2)^2 - \Delta a^2 \sin^2\theta} \ , \end{aligned} \tag{3.30}$$

where $\Omega/aM > 0$, i.e. the ZAMO's angular velocity has the same sign as that of the black hole and hence co-rotates with the black hole. It follows that the 4-velocity of the ZAMO is given by

$$\begin{aligned} (u^\mu)_{\text{ZAMO}} &= \left(u^t, 0, 0, u^\phi\right) \\ &= u^t \left(1, 0, 0, \Omega\right) \ . \end{aligned} \tag{3.31}$$

In the Kerr metric $u_t = g_{tt}u^t + g_{t\phi}u^\phi$, which upon inserting u^ϕ for the ZAMO yields

$$u_t = \left[g_{tt} - \frac{(g_{t\phi})^2}{g_{\phi\phi}} \right] u^t \ . \tag{3.32}$$

Using the identity $u^\alpha u_\alpha = -1$, equation (3.32) becomes

$$\begin{aligned} \left(u^t\right)^2 &= \frac{g_{\phi\phi}}{\left(g_{t\phi}\right)^2 - g_{tt}g_{\phi\phi}} \\ &= \frac{g_{\phi\phi}}{\Delta \sin^2\theta} \ , \end{aligned} \tag{3.33}$$

hence

$$(u^\mu)_{\mathrm{ZAMO}} = \sqrt{\frac{g_{\phi\phi}}{\Delta \sin^2\theta}}\,(1,0,0,\Omega) \ . \tag{3.34}$$

Another region of physical interest of the Kerr black hole is the region where g_{tt} (equation 3.2), which is usually negative, changes sign. This surface is termed the "Static Limit" and the region located between the static limit and the event horizon is known as the ergo-region or ergosphere (in reality it is not a sphere, but rather an oblate spheroid). The static limit is obtained by solving for $g_{tt} = 0$, yielding

$$r_{\mathrm{SL}\pm} = M \pm \sqrt{M^2 - a^2\cos^2\theta} \ . \tag{3.35}$$

The static limit, $r_{\mathrm{SL}+}$, and the event horizon, r_+, coincide at the poles of the black hole spin axis (i.e. $\theta = 0,\, \pi$). For a Schwarzschild black hole the static limit and the event horizon coincide, i.e. the static limit is the event horizon and there does not exist an ergo region for a non-rotating black hole. The "Inner Static Limit" is given by $r_{\mathrm{SL}-}$ and defines the inner boundary, beyond which g_{tt} again changes sign and an observer can once more remain static. For a Schwarzschild black hole the inner static limit reduces to a point and coincides with the singularity at the centre. A static observer is defined as a timelike geodesic with a tangent vector proportional to the killing vector $k^\mu = (1,0,0,0)$, hence a zero 3-velocity. Consider $k^\mu k^\nu g_{\mu\nu} = g_{tt}$ for our static observer, which must be negative for the static observer to remain timelike. As already noted, g_{tt} changes sign at the static limit and becomes positive, and hence spacelike. That is to say a stationary observer cannot exist there. This implies an observer cannot remain static in this region and must therefore move with the rotation of the black hole in order to remain timelike. The inner static limit, $r_{\mathrm{SL}-}$, although defining the inner edge of the ergo region, lies within the event horizon of the black hole and is thus causally disconnected

from the outside Universe. These regions of physical interest are illustrated in Figure 3.1.

3.2 Particle Motion in the Kerr Space-time

The equations of motion of free particles in the Kerr space-time are readily found from the geodesic equations of motion. This requires prior knowledge of the Christoffel symbols. It is simpler, and more symmetric, to formulate the equations of motion from the Lagrangian

$$\mathcal{L} = \frac{1}{2}\left(g_{tt}\dot{t}^2 + 2g_{t\phi}\dot{t}\dot{\phi} + g_{rr}\dot{r}^2 + g_{\theta\theta}\dot{\theta}^2 + g_{\phi\phi}\dot{\phi}^2\right) \ , \tag{3.36}$$

where $\dot{x}^\mu \equiv \mathrm{d}x^\mu/\mathrm{d}\lambda$. Note that, as with the metric itself, the Lagrangian is not dependent on t and ϕ co-ordinates, which naturally gives rise to conserved quantities. From the Euler-Lagrange equations of motion

$$\frac{\mathrm{d}}{\mathrm{d}\lambda}\left(\frac{\partial\mathcal{L}}{\partial\dot{x}^\mu}\right) - \frac{\partial\mathcal{L}}{\partial x^\mu} = 0 \ , \tag{3.37}$$

where λ is an affine parameter for the geodesic path and x^μ is a position 4-vector. Stationarity and axisymmetry immediately imply the following conserved quantities

$$\frac{\partial\mathcal{L}}{\partial\dot{t}} = -E \ , \tag{3.38}$$

$$\frac{\partial\mathcal{L}}{\partial\dot{\phi}} = L_z \ , \tag{3.39}$$

where E and L_z are respectively the total energy of the particle and the projection of its angular momentum along the black hole spin axis. The covariant 4-momentum components thus follow as $(p_t,\, p_r,\, p_\theta,\, p_\phi) = (-E,\, \Sigma\dot{r}/\Delta,\, \Sigma\dot{\theta},\, L_z)$. The Euler-Lagrange equations now simplify considerably, yielding

$$\dot{t} = E + \frac{2Mr}{\Sigma\Delta}\left[(r^2+a^2)E - aL_z\right] \ , \tag{3.40}$$

$$\dot{r}^2 = \frac{\Delta}{\Sigma}\left(\mu + E\dot{t} - L_z\dot{\phi} - \Sigma\dot{\theta}^2\right) \ , \tag{3.41}$$

$$\dot{\theta}^2 = \frac{1}{\Sigma^2}\left[\mathcal{Q} + \left(E^2+\mu\right)a^2\cos^2\theta - L_z^2\cot^2\theta\right] \ , \tag{3.42}$$

$$\dot{\phi} = \frac{2aMrE + (\Sigma - 2Mr)\,L_z\mathrm{cosec}^2\theta}{\Sigma\Delta} \ , \tag{3.43}$$

where the trivial constant of motion, μ, is the rest mass of the particle (equal to 0 for massless particles and -1 for particles with non-zero mass), and $\mathcal{Q}$ is a

fourth constant of motion called the Carter constant (Carter 1968). With this the set of equations (3.40)-(3.43) may reduced to a problem of quadratures. However, equations (3.41)-(3.42) contain square terms in $\dot{r}$ and $\dot{\theta}$, potentially making the determination of the signs of $\dot{r}$ and $\dot{\theta}$, particularly at turning points, numerically challenging. This problem may be circumvented by calculating the second derivatives of r and θ from the Euler-Lagrange equations, yielding

$$\begin{aligned}
\ddot{r} &= \frac{\Delta}{\Sigma}\Bigg\{\frac{M(\Sigma-2r^2)}{\Sigma^2}\dot{t}^2+\frac{(r-M)\,\Sigma-r\Delta}{\Delta^2}\dot{r}^2 \\
&+ r\dot{\theta}^2+\left[r+\left(\frac{\Sigma-2r^2}{\Sigma^2}\right)a^2M\sin^2\theta\right]\sin^2\theta\,\dot{\phi}^2 \\
&- 2aM\sin^2\theta\left(\frac{\Sigma-2r^2}{\Sigma^2}\right)\dot{t}\dot{\phi}+\frac{a^2\sin 2\theta}{\Delta}\dot{r}\dot{\theta}\Bigg\}\,, \qquad (3.44)\\
\ddot{\theta} &= \frac{1}{2\Sigma}\Bigg(\sin 2\theta\Bigg\{\frac{2a^2Mr}{\Sigma^2}\dot{t}^2-\frac{4aMr\left(r^2+a^2\right)^2}{\Sigma^2}\dot{t}\dot{\phi}-\frac{a^2}{\Delta}\dot{\phi}^2 \\
&+ a^2\dot{\theta}^2+\left[\Delta+\frac{2Mr\left(r^2+a^2\right)^2}{\Sigma^2}\right]\dot{\phi}^2\Bigg\}-4r\dot{r}\dot{\theta}\Bigg)\,. \qquad (3.45)
\end{aligned}$$

Thus equations (3.40), (3.43), (3.44) and (3.45) are a system of six coupled ordinary differential equations (ODEs) which must be solved at each point λ along a geodesic, yielding (t, r, $\dot{r}$, θ, $\dot{\theta}$, ϕ), given appropriate initial conditions for these six variables. This is illustrated in Figure 3.2. The initial conditions are determined at the observer's image plane prior to the computation of the geodesic.

Since emission from accreting material around a Kerr black hole is of primary concern, the particle motion in the accretion flow must be considered. This motion will be subject to the presence of non-gravitational external forces acting on the particle, which must be specified beforehand to determine the particle kinematics. However, for simplicity an implicit treatment of the external force applicable to accretion flows around black holes is considered. Consider a simple model in which $\dot{\theta} \ll \dot{r} \ll \dot{\phi} < \dot{t}$, thus allowing $\dot{r}$ and $\dot{\theta}$, given their negligibility compared to other quantities, to be neglected as a first approximation. The equation of motion of particles under the influence of an external force reads (see Misner et al. 1973)

$$\ddot{x}^\alpha+\Gamma^\alpha{}_{\mu\nu}\dot{x}^\mu\dot{x}^\nu=a^\alpha\,, \qquad (3.46)$$

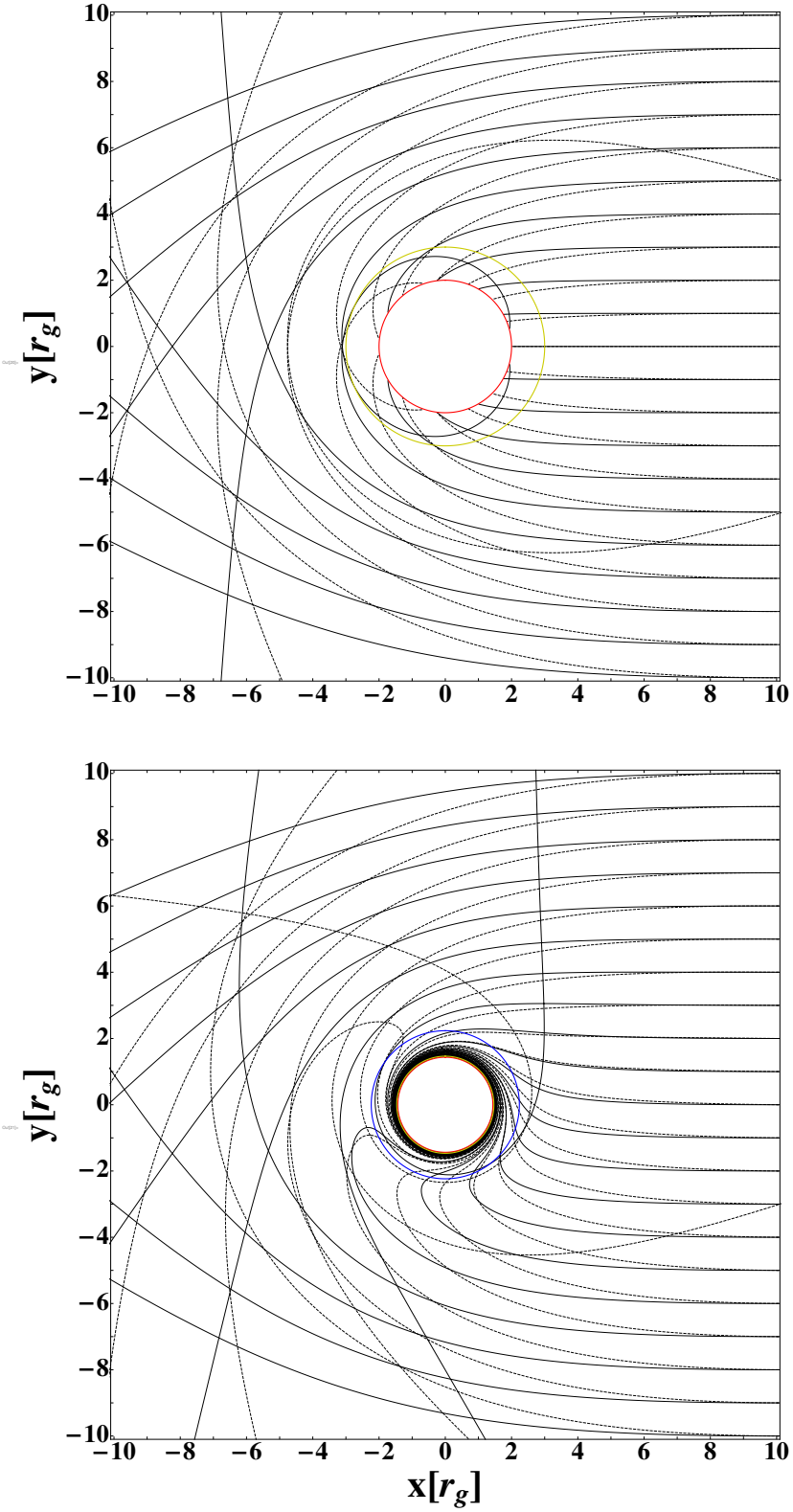

Fig. 3.2: Equatorial orbits around Schwarzschild ($a = 0$, top) and Kerr ($a = 0.998$, bottom) black holes. Solid and dotted lines indicate photon and particle geodesics respectively. Geodesics originate from the right hand side of the panels. The red circle indicates the black hole event horizon, the yellow circle the light circularisation radius and the blue circle the static limit. Note the top-bottom symmetry in the Schwarzschild case and the effect of frame-dragging on retrograde orbits in the extreme Kerr case. In the Kerr case the black hole is rotating anticlockwise.

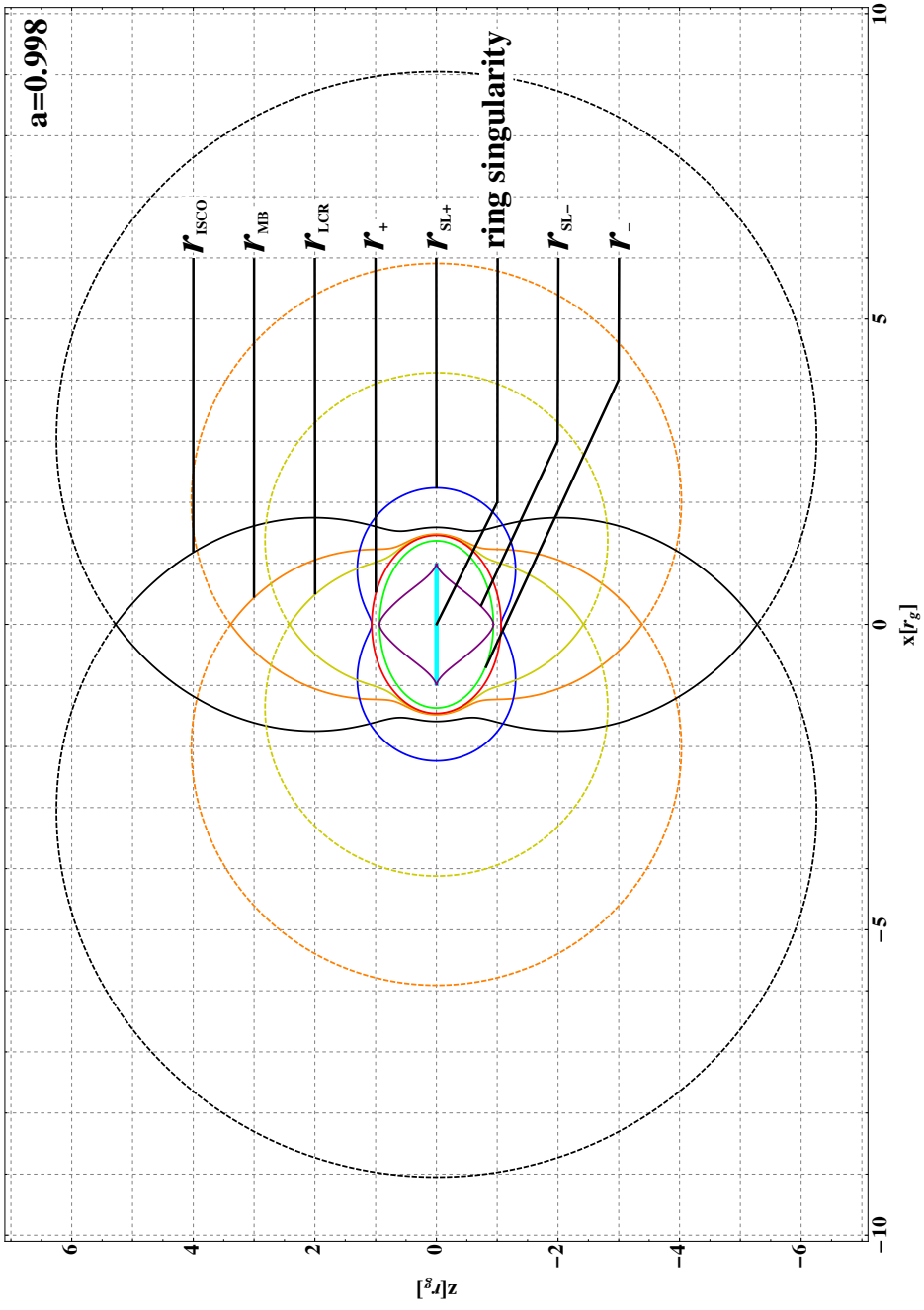

Fig. 3.3: Cross-sectional view of the major critical surfaces of the Kerr black hole ($a = 0.998$). Solid and dotted lines denote prograde and retrograde surfaces respectively.

where a^α is the 4-acceleration per unit mass due to an external force and $\Gamma^\alpha{}_{\mu\nu}$ is the Christoffel symbol. The assumption of stationarity implies $a^\phi = 0$. Given the 4-velocity is everywhere orthogonal to the 4-acceleration ($a^\nu u_\nu = 0$), since $\dot{r} = \dot{\theta} = 0$, i.e. particles remain in circular orbits, then it follows that $a^t = 0$. For simplicity $a^r = 0$ is prescribed, which implies a rotationally-supported flow. From $u^\nu u_\nu = -1$, a^θ may be determined self-consistently under the assumption $\dot{\theta} = 0$. This solution corresponds to a flow rotationally supported in the $\hat{r}$ direction and pressure supported in the $\hat{\theta}$ direction. Inserting the Christoffel symbol components (Appendix A) into equation (3.46) yields only one non-trivial equation in the radial direction, which may be simplified to yield

$$\dot{t} = \left(\frac{\Sigma\sqrt{r}\sin\theta}{\sqrt{M\left(2r^2 - \Sigma\right)}} + a\sin^2\theta \right) \dot{\phi} \ . \tag{3.47}$$

The metric also gives the condition $g_{tt}\dot{t}^2 + 2g_{t\phi}\dot{t}\dot{\phi} + g_{\phi\phi}\dot{\phi}^2 = -1$. Although the motion derived for these 'forced' particles is not geodesic, the approximation that the (non-gravitational) external force, in the observer's frame, does not overpower the local gravitational force is employed, allowing the motion to be considered geodesic to zeroth order. Inserting equation (3.47) into the aforementioned metric condition yields, after algebraic simplifications

$$\dot{t} = \frac{1}{\xi}\left[\Sigma\sqrt{r} + a\sin\theta\sqrt{M\left(2r^2 - \Sigma\right)}\right] \ , \tag{3.48}$$

$$\dot{\phi} = \frac{\sqrt{M\left(2r^2 - \Sigma\right)}}{\xi\sin\theta} \ , \tag{3.49}$$

with $\dot{r} = 0$, $\dot{\theta} = 0$, where

$$\xi^2 = \Sigma\left[\Sigma\left(r + M\right) - 4Mr^2 + 2a\sin\theta\sqrt{Mr\left(2r^2 - \Sigma\right)}\right] \ . \tag{3.50}$$

Equating equations (3.48) and (3.49) with equations (3.40) and (3.43) respectively gives the energy and z-component of the angular momentum of the particle as

$$E = \frac{1}{\zeta}\left[\left(\Sigma - 2Mr\right)\sqrt{r} + a\sin\theta\sqrt{M\left(2r^2 - \Sigma\right)}\right] \ , \tag{3.51}$$

$$L_z = \frac{\sin\theta}{\zeta}\left[\left(r^2 + a^2\right)\sqrt{M\left(2r^2 - \Sigma\right)} - 2aMr^{3/2}\sin\theta\right] \ . \tag{3.52}$$

The marginally stable orbit, or innermost stable circular orbit (ISCO), for material particles is determined by the surface where $\partial E/\partial r = 0$, which upon differentiation of equation (3.51) and simplification yields

$$\Delta\Sigma^2 - 4r\left(2r^2 - \Sigma\right)\left(\sqrt{2r^2 - \Sigma} - a\sin\theta\sqrt{r}\right)^2 = 0 \ , \tag{3.53}$$

the solution of which determines $r_{\rm ISCO}$ as a function of θ. From equation (3.51), the solution to $E = 1$ yields the radius of marginally bound parabolic orbits, $r_{\rm MB}$, as a function of θ. The underlying assumptions used to derive the particle velocities break down when $\xi^2 \leq 0$. The boundary surface $\xi = 0$ is the light circularisation radius, $r_{\rm LCR}$. These are all illustrated in Figure 3.3. For orbits in the equatorial plane, relevant to calculations for geometrically thin accretion disks, the expressions for the ISCO, marginally bound orbits and the light circularisation radius simplify to those given in Bardeen et al. (1972). Although black hole mass is retained in all of the preceding expressions, in practical calculations it is set to unity, which is equivalent to normalising the length scale to the gravitational radius of the black hole, i.e. $r_{\rm g} = GM/c^2 = 1$.

3.3 Ray-Tracing Initialisation

In determining the geodesic for a particle or photon, the initial conditions for such a geodesic must be specified. Since the Kerr metric and consequently the geodesic equations of motion are independent of time, the geodesic may be traced backwards in time, from the observer to the point of emission. This is reverse ray-tracing. If the ray is not captured by the black hole, then it is taken to have originated either from the vicinity of the black hole, such as the accretion flow, or from the background.

An observer is constructed as in Figure 3.4, represented by green axes. The observer image plane is the x-y plane and the z-axis of the observer is directed towards the black hole centre, with the x-y plane being perpendicular to the z-axis. The orientation of the x and y axes is arbitrary and does not affect the physics. In all calculations in this thesis the orientation of the x and y axes is as shown in Figure 3.4. The centre of the image plane is located a distance $r_{\rm obs}$ (in BL co-ordinates) from the centre of the black hole, at an

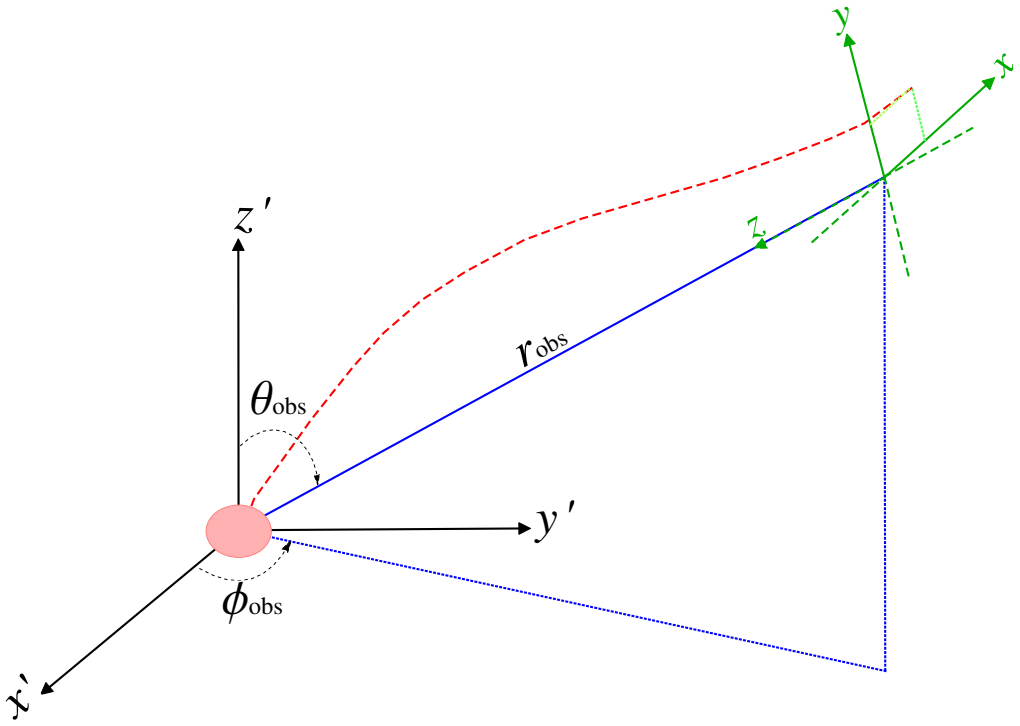

Fig. 3.4: Ray-tracing setup. An observer (green axes) is located some distance from the black hole (blue axes). The observer grid (image plane) is the $x-y$ plane. An example photon trajectory is indicated by the red dashed line.

angle $\theta_{\rm obs}$ with respect to the black hole spin axis. The black hole axes are (x', y', z') and the spin axis of the black hole and the z'-axis are assumed to coincide. The observer is located at a position $\phi_{\rm obs}$ with respect to the black hole x-axis. In practical calculations $\phi_{\rm obs}$ is set to zero by default, by virtue of the Kerr metric being axisymmetric. However, there are instances (e.g. time-dependent radiative transfer) where it is sometimes useful to specify the azimuthal location of the observer. Thus the observer is specified by the BL co-ordinates $(r_{\rm obs}, \theta_{\rm obs}, \phi_{\rm obs})$ and each individual photon or particle the observer receives by (x, y, z).

Close to the black hole, space-time curvature becomes significant and the observer image plane is curved, introducing a curvature-dependent distortion of the observed image. To remove this effect, in all calculations in this thesis the observer is located at a distance of $10^4 r_{\rm g}$ from the centre of the black

hole. At this distance numerical calculations of the geodesics yield a deviation from Euclidean geometry of less than one part in 10^{10}, which is smaller than the numerical precision of the integration of the geodesic itself. Space-time is assumed flat at this distance and the curvature of the observer image plane is considered negligible, enabling the assumption of orthogonality of rays arriving at its surface and the application of the ray-tracing method.

First the observer co-ordinate system, $\overline{\mathbf{x}} \equiv (x, y, z)^{\mathbf{T}}$, must be transformed into the black hole co-ordinate system, $\overline{\mathbf{x}}' \equiv (x', y', z')^{\mathbf{T}}$. This may be achieved by rotating and translating the observer's axes onto the black hole's axes. First rotate clockwise by $(\pi - \theta_{\rm obs})$ about the x-axis, then clockwise by $(2\pi - \phi_{\rm obs})$ about the z-axis, followed by a reflection in the plane $y = x$ and then a translation of (x, y, z) using (3.17) to (3.19). Upon simplification of the resultant matrix algebra this yields

$$\begin{aligned} \mathbf{x}' &= \mathbf{A}_{y=x}\,\mathbf{R}_z(2\pi - \phi_{\rm obs})\mathbf{R}_x(\pi - \theta_{\rm obs})\mathbf{x} + \mathbf{T}_{\mathbf{x}\to\mathbf{x}'} \\ &= \begin{pmatrix} \mathcal{D}(y,z)\cos\phi_{\rm obs} - x\sin\phi_{\rm obs} \\ \mathcal{D}(y,z)\sin\phi_{\rm obs} + x\cos\phi_{\rm obs} \\ (r_{\rm obs} - z)\cos\theta_{\rm obs} + y\sin\theta_{obs} \end{pmatrix}, \end{aligned} \tag{3.54}$$

where

$$\mathcal{D}(y,z) = \left(\sqrt{r_{\rm obs}^2 + a^2} - z\right)\sin\theta_{\rm obs} - y\cos\theta_{\rm obs}\ . \tag{3.55}$$

After employing equations (3.20)–(3.22), the initial position of a ray on the image plane in BL co-ordinates can be determined. Next the initial velocities of the ray must be determined. Differentiating equation (3.54) with respect to the affine parameter yields

$$\dot{\mathbf{x}}' = \begin{pmatrix} -\dot{x}\sin\phi_{\rm obs} - (\dot{y}\cos\theta_{\rm obs} + \dot{z}\sin\theta_{\rm obs})\cos\phi_{\rm obs} \\ \dot{x}\cos\phi_{\rm obs} - (\dot{y}\cos\theta_{\rm obs} + \dot{z}\sin\theta_{\rm obs})\sin\phi_{\rm obs} \\ \dot{y}\sin\theta_{\rm obs} - \dot{z}\cos\theta_{\rm obs} \end{pmatrix}\ . \tag{3.56}$$

Each ray received arrives perpendicular to the image plane, moving parallel to the z-axis, hence setting $(\dot{x}, \dot{y}, \dot{z}) = (0, 0, 1)$, yields the rectangular components

of the ray's velocity in black hole co-ordinates as

$$\dot{x}' = \begin{pmatrix} -\sin\theta_{\rm obs}\cos\phi_{\rm obs} \\ -\sin\theta_{\rm obs}\sin\phi_{\rm obs} \\ -\cos\theta_{\rm obs} \end{pmatrix} . \tag{3.57}$$

Finally, differentiating equations (3.17) to (3.19) with respect to the affine parameter, solving for $\dot{r}, \dot{\theta}, \dot{\phi}$, and inserting equation (3.57) yields the initial conditions for the velocity of the ray's geodesic as

$$\dot{r} = -\frac{r\mathcal{R}\sin\theta\sin\theta_{\rm obs}\cos\Phi + \mathcal{R}^2\cos\theta\cos\theta_{\rm obs}}{\Sigma} , \tag{3.58}$$

$$\dot{\theta} = \frac{r\sin\theta\cos\theta_{\rm obs} - \mathcal{R}\cos\theta\sin\theta_{\rm obs}\cos\Phi}{\Sigma} , \tag{3.59}$$

$$\dot{\phi} = \frac{\sin\theta_{\rm obs}\sin\Phi}{\mathcal{R}\sin\theta} , \tag{3.60}$$

where $\mathcal{R} \equiv \sqrt{r^2 + a^2}$ and $\Phi \equiv (\phi - \phi_{\rm obs})$. However, the initial values for $\left(L_z, E, \dot{t}\right)$ must still be determined. An expression for L_z in terms of E and $\dot{\phi}$ may be obtained by eliminating $\dot{t}$ between equations (3.40) and (3.43). Similarly, E may be obtained by expressing equation (3.41) in terms of $\dot{t}$, equating with equation (3.40), and eliminating L_z using the previously obtained expression. After some algebra the resultant expressions are

$$E^2 = \left(\frac{\Sigma - 2Mr}{\Sigma\Delta}\right)\left(\Sigma\dot{r}^2 + \Sigma\Delta\,\dot{\theta}^2 - \Delta\mu\right) + \Delta\sin^2\theta\,\dot{\phi}^2 , \tag{3.61}$$

$$L_z = \frac{\left(\Sigma\Delta\dot{\phi} - 2aMrE\right)\sin^2\theta}{\Sigma - 2Mr} , \tag{3.62}$$

$$\dot{t} = \left[1 + \frac{2Mr(r^2 + a^2)}{\Sigma\Delta}\right]E - \left(\frac{2aMr}{\Sigma\Delta}\right)L_z . \tag{3.63}$$

Hence equations (3.20)–(3.22) and (3.58)–(3.63) define $(t, r, \theta, \phi, \dot{t}, \dot{r}, \dot{\theta}, \dot{\phi}, E, L_z)$ completely in terms of the position of the centre of the image plane $(r_{\rm obs}, \theta_{\rm obs}, \phi_{\rm obs})$ and the position of the ray on the image plane $(x, y, 0)$, with the initial time $t = t_{\rm obs}$ set to zero.

Although the above method appears more complicated as the BL co-ordinate system has been dealt with explicitly, it affords greater generality in allowing the observer to be positioned any finite distance (excluding the ergo-region) from the black hole. These expressions provide analytic results and

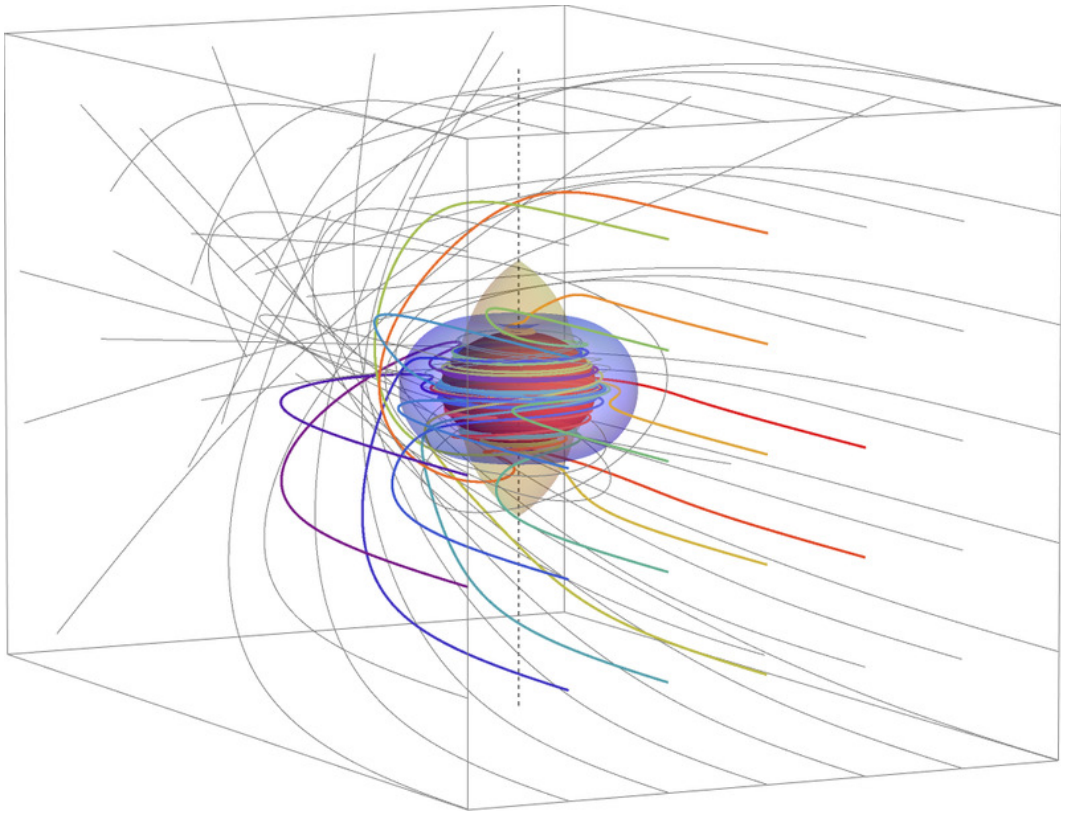

Fig. 3.5: Ray-tracing a grid of 49 photon geodesics from an observer located in the equatorial plane ($r_{\rm obs} = 10\,{\rm r_g}$, $\theta_{\rm obs} = \pi/2$, $a = 0.998$). Grey lines indicate geodesics which are not captured by the black hole. Coloured lines indicate geodesics captured by the black hole. Yellow, blue and red translucent surfaces represent the LCR, Static Limit and Event Horizon respectively. The grey dotted line is the spin axis of the black hole, with the black hole rotating anticlockwise as viewed from above.

mean the observer need not be located at infinity, where space-time is asymptotically flat. This saves significant computational time. The application of the aforementioned procedures to ray-tracing a grid of photons is illustrated in Figure 3.5.

Furthermore, since it has not been used in specifying the initial conditions of the geodesic, the Carter constant

$$\mathcal{Q} = \Sigma^2\dot{\theta}^2 + \left[L_{\rm z}^2{\rm csc}^2\theta - a^2\left(E^2+\mu\right)\right]\cos^2\theta, \tag{3.64}$$

may be used as an independent check of the accuracy of the numerical integration. By computing $\mathcal{Q}$ using equation (3.64) at each step in the numerical integration of the geodesic, $\Delta\mathcal{Q}_{i\rightarrow i+1} = |\mathcal{Q}_{i+1} - \mathcal{Q}_i|$ is calculated between suc-

cessive steps. If $\Delta\mathcal{Q}_{i\rightarrow i+1} > 10^{-9}$ then the integration step is repeated at half the previous step size until this condition is satisfied.

3.4 General Relativistic Radiative Transfer

In the previous sub-section the method to solve the geodesics for particles around the Kerr black hole was detailed. An initial intensity for the ray is assigned and its evolution through the material it traverses between its point of emission in the accretion flow and the observer is computed. The absorption and emission properties of the medium from point to point must be known, and the whole method must be performed in a covariant manner, given that the space-time is curved.

The emission and absorption processes may be considered as sources and sinks which the ray bundle traverses. In vacuum the number of particles along a ray bundle is conserved. In the presence of emission and absorption, the radiative transfer equation can be expressed as

$$\frac{\mathrm{d}I_\nu}{\mathrm{d}s} = -\alpha_\nu I_\nu + j_\nu \ , \tag{3.65}$$

(Chandrasekhar 1960; Rybicki and Lightman 1979) where $I_\nu \equiv I_\nu(s)$ is the specific intensity of the ray at a frequency ν, and α_ν and j_ν are, respectively, the absorption and emission coefficients at a frequency ν. By introducing the variable

$$\tau_\nu(s) = \int_{s_0}^{s} \mathrm{d}s'\, \alpha_\nu(s') \ , \tag{3.66}$$

which is the optical depth (optical thickness of the medium between s and s_0), the radiative transfer equation may be rewritten as

$$\frac{\mathrm{d}I_\nu}{\mathrm{d}\tau_\nu} = -I_\nu + \frac{j_\nu}{\alpha_\nu} = -I_\nu + S_\nu \ , \tag{3.67}$$

where $S_\nu = j_\nu/\alpha_\nu$ is the source function. Direct integration of the equation yields

$$\begin{aligned} I_\nu(s) &= I_\nu(s_0)\ \mathrm{e}^{-\tau_\nu} + \int_{s_0}^{s} \mathrm{d}s'\, j_\nu(s')\ \mathrm{e}^{-(\tau_\nu(s)-\tau_\nu(s'))} \\ &= I_\nu(0)\ \mathrm{e}^{-\tau_\nu} + \int_0^{\tau_\nu} \mathrm{d}\tau'_\nu\, S_\nu(\tau'_\nu)\ \mathrm{e}^{-(\tau_\nu-\tau'_\nu)} \ , \end{aligned} \tag{3.68}$$

where the constant $I_\nu(s_0)$ $(= I_\nu(0))$ is the initial value of the specific intensity. While optical depth, which is a scalar quantity, is invariant under

Lorentz transformations, the radiative transfer equations in the conventional form (equations (3.65) and (3.67)) are not.

It is now shown that a covariant formulation for radiative transfer can be derived from the conservation of phase space volume and the conservation of particle number. Construct a phase space volume $\mathcal{V}$ threaded with a small bundle of particles. In the co-moving frame, these particles occupy a spatial volume element $\mathrm{d}^3\vec{x} = \mathrm{d}x\,\mathrm{d}y\,\mathrm{d}z$ and a momentum volume element $\mathrm{d}^3\vec{p} = \mathrm{d}p_x\,\mathrm{d}p_y\,\mathrm{d}p_z$. Liouville's theorem ensures that the phase space volume, given by $\mathrm{d}\mathcal{V} = \mathrm{d}^3\vec{x}\mathrm{d}^3\vec{p}$, is unchanged along the affine parameter λ, i.e.

$$\frac{\mathrm{d}\mathcal{V}}{\mathrm{d}\lambda} = 0 \tag{3.69}$$

(Misner et al. 1973). This together with the conservation of the number of particles dN within the phase space volume element implies that the phase space density

$$f(x^i, p^i) = \frac{\mathrm{d}N}{\mathrm{d}\mathcal{V}}\ , \tag{3.70}$$

is invariant along λ.

For relativistic particles, $|\vec{p}| = E$, and $\mathrm{d}^3\vec{p} = E^2\mathrm{d}E\,\mathrm{d}\Omega$. The volume element of a bundle of relativistic particles is also given by $\mathrm{d}^3\vec{x} = \mathrm{d}A\,\mathrm{d}t$, where $\mathrm{d}A$ is the area element of the bundle. Thus, the phase space density of a bundle of relativistic particles may be expressed as

$$f(x^i, p^i) = \frac{\mathrm{d}N}{E^2\mathrm{d}A\,\mathrm{d}t\,\mathrm{d}E\,\mathrm{d}\Omega}\ . \tag{3.71}$$

The specific intensity of a ray (bundle of photons) is simply

$$I_E = \frac{E\,\mathrm{d}N}{\mathrm{d}A\,\mathrm{d}t\,\mathrm{d}E\,\mathrm{d}\Omega} \tag{3.72}$$

(see Rybicki and Lightman 1979). It follows that

$$\mathcal{I} \equiv \frac{I_\nu}{\nu^3} = \frac{I_E}{E^3} \tag{3.73}$$

is a Lorentz invariant quantity. The Lorentz-invariant intensity is denoted by $\mathcal{I}$, and may also be regarded as the occupation number of particles in the phase space for a particle bundle.

To find the transformation of the absorption coefficient, consider material in a reference frame K streaming with velocity v between two planes parallel

to the x-axis, separated by a distance l. In this frame the ray traverses the material at an angle θ to the x-axis. Now let K' be the rest frame of the material. In the rest frame the distance between the two planes is l' and the ray now makes an angle θ' with respect to the x-axis. This is illustrated in Rybicki and Lightman (1979) (Chapter 4).

The optical depth along the ray is an invariant, since $\mathrm{e}^{-\tau_\nu}$ gives the fraction of photons passing through the material. As such, the optical depth may be written as

$$\begin{aligned} \tau_\nu &= \frac{l}{\sin\theta}\alpha_\nu \\ &= \frac{l}{\nu\sin\theta}\nu\,\alpha_\nu \\ &\propto \frac{l}{k_y}\nu\,\alpha_\nu \ , \end{aligned} \tag{3.74}$$

where $k_y \propto \nu \sin\theta$ is the y component of the photon 4-momentum. It follows that $k_y = k_y'$ and $l = l$' in both frames, since they are perpendicular to the streaming material. Therefore it immediately follows from equation (3.74) that $\nu\,\alpha_\nu$ is a Lorentz invariant quantity and the corresponding Lorentz-invariant absorption coefficient is $\chi = \nu\,\alpha_\nu$.

The transformation for the emission coefficient may be obtained from the source function via $j_\nu = \alpha_\nu S_\nu$. From equation (3.67) it follows that S_ν/ν^3 is a Lorentz invariant quantity and therefore j_ν/ν^2 is a Lorentz invariant quantity and the Lorentz invariant emission coefficient $\eta = j_\nu/\nu^2$ may also be obtained. These absorption and emission coefficients, as seen by the observer, are related to their counterparts in the local rest frame of the medium via $\nu\,\alpha_\nu = \nu_0\,\alpha_{0,\nu}$ and $j_\nu/\nu^2 = j_{0,\nu}/\nu_0^2$ respectively, where the subscript "0" denotes variables measured in the local rest frame.

3.4.1 Photon and relativistic massless particle

For photons (or a massless relativistic particle) $k_\alpha k^\alpha = 0$, where k_α is the (covariant) 4-momentum and defined as the tangent 4-vector $\mathrm{d}/\mathrm{d}\lambda$ to the photon world-line ($k_\alpha = \mathrm{d}x_\alpha/\mathrm{d}\lambda$), where λ is the affine parameter of the world-line. Consider a photon propagating in a fluid with 4-velocity u^β. The transverse component of the photon's 4-velocity, orthogonal to u^α, in the co-

moving frame of the fluid is denoted by v^β, which may be obtained as follows

$$\begin{aligned} v^\beta &= P^{\alpha\beta}k_\alpha \\ &= k^\beta + (k_\alpha u^\alpha)u^\beta \ , \end{aligned} \tag{3.75}$$

where $P^{\alpha\beta} = g^{\alpha\beta} + u^\alpha u^\beta$ is the projection tensor and $g^{\alpha\beta}$ the space-time metric tensor. The variation in the path length s with respect to the affine parameter λ is then

$$\begin{aligned} \frac{\mathrm{d}s}{\mathrm{d}\lambda} &= -\left|\left|v^\beta\right|\right|\Big|_{\lambda_{\rm obs}} \\ &= -\sqrt{g_{\alpha\beta}(k^\alpha + (k_\beta u^\beta)u^\alpha)(k^\beta + (k_\alpha u^\alpha)u^\beta)}\ \Big|_{\lambda_{\rm obs}} \\ &= -\sqrt{k_\beta k^\beta + (k_\alpha u^\alpha)^2 u_\beta u^\beta + 2(k_\alpha u^\alpha)^2}\ \Big|_{\lambda_{\rm obs}} \\ &= -k_\alpha u^\alpha \Big|_{\lambda_{\rm obs}} , \end{aligned} \tag{3.76}$$

where the minus sign arises from the metric signature adopted, and the fact that the convention that the photon energy must be positive is such that $\mathrm{d}s/\mathrm{d}\lambda = 1$ in the co-moving frame. For a stationary observer located at infinity, $k_\beta u^\beta = -E_{\rm obs}$. The relative energy shift of the photon between the observer's frame and the comoving frame is therefore

$$\gamma^{-1} = \frac{\nu_0}{\nu} = \frac{-k_\alpha u^\alpha|_\lambda}{E_{\rm obs}} = \frac{k_\alpha u^\alpha|_\lambda}{k_\beta u^\beta|_{\lambda_{\rm obs}}}. \tag{3.77}$$

Making use of the Lorentz-invariant properties of the variables $\mathcal{I}$, χ and η, and of the optical depth τ_ν, the radiative transfer equation may be rewritten in the following form

$$\frac{\mathrm{d}\mathcal{I}}{\mathrm{d}\tau_\nu} = -\mathcal{I} + \frac{\eta}{\chi} = -\mathcal{I} + \mathcal{S} \ , \tag{3.78}$$

where $\mathcal{S} = \eta/\chi$ is the Lorentz-invariant source function. All quantities in equation (3.78) are Lorentz invariant, and hence the equation is covariant. As $\mathrm{d}\tau_\nu = \alpha_\nu \mathrm{d}s$, it follows that

$$\frac{\mathrm{d}\mathcal{I}}{\mathrm{d}s} = -\alpha_\nu \mathcal{I} + \frac{j_\nu}{\nu^3} \ . \tag{3.79}$$

It follows that

$$\frac{\mathrm{d}\mathcal{I}}{\mathrm{d}\lambda} = -k_\alpha u^\alpha|_\lambda \left(-\alpha_{0,\nu}\mathcal{I} + \frac{j_{0,\nu}}{\nu_0^3}\right) \ , \tag{3.80}$$

(see Winkler and Norman 1986; Fuerst and Wu 2004), where $\alpha_{0,\nu} \equiv \alpha_0(x^\beta, \nu)$ and $j_{0,\nu} \equiv j_0(x^\beta, \nu)$, where, as before, "0" denotes variables that are evaluated in the local fluid rest frame, for a given ν. In ray-tracing calculations an observer frequency ν is specified, all required variables at this location are determined, and how these variables change in different reference frames through the radiative transfer equation is specified. The solution to equation (3.80) is

$$\mathcal{I}(\lambda) = \mathcal{I}(\lambda_0)\mathrm{e}^{-\tau_\nu(\lambda)} - \int_{\lambda_0}^{\lambda} \mathrm{d}\lambda'' \frac{j_{0,\nu}(\lambda'')}{\nu_0^3} \exp\left(-\int_{\lambda''}^{\lambda} \mathrm{d}\lambda' \, \alpha_{0,\nu}(\lambda') k_\alpha u^\alpha|_{\lambda'}\right) k_\alpha u^\alpha|_{\lambda''} \, , \tag{3.81}$$

(cf. Baschek et al. 1997; Fuerst and Wu 2004), where the optical depth is

$$\tau_\nu(\lambda) = -\int_{\lambda_0}^{\lambda} \mathrm{d}\lambda' \, \alpha_{0,\nu}(\lambda') k_\alpha u^\alpha|_{\lambda'} \, . \tag{3.82}$$

In terms of the optical depth,

$$\mathcal{I}(\tau_\nu) = \mathcal{I}(\tau_0)\mathrm{e}^{-\tau_\nu} + \int_{\tau_0}^{\tau_\nu} \mathrm{d}\tau'_\nu \, \mathcal{S}(\tau'_\nu)\mathrm{e}^{-(\tau_\nu - \tau'_\nu)} \, . \tag{3.83}$$

For a distant observer, $-k^\alpha u_\alpha|_{\lambda_{\mathrm{obs}}} \rightarrow E$, the observed photon energy, which may be normalised to unity. The radiative transfer equation can be expressed as two decoupled differential equations

$$\frac{\mathrm{d}\tau_\nu}{\mathrm{d}\lambda} = \gamma^{-1}\alpha_{0,\nu} \, , \tag{3.84}$$

$$\frac{\mathrm{d}\mathcal{I}}{\mathrm{d}\lambda} = \gamma^{-1}\left(\frac{j_{0,\nu}}{\nu_0^3}\right)\mathrm{e}^{-\tau_\nu} \, , \tag{3.85}$$

which follow immediately from differentiation of equations (3.82) and (3.81) respectively, with respect to λ. These two equations are more useful in practical relativistic radiative transfer calculations because they allow the efficient computation, through a simple Eulerian method, of the optical depth along a ray, regardless of whether the ray-tracing is executed forward or backwards in time. This is then used to compute the intensity along the ray.

3.4.2 Relativistic particle with mass

For massless particles, contraction of the 4-momentum gives $k_\alpha k^\alpha = 0$, but for particles with a non-zero mass m, it gives $p_\alpha p^\alpha = -m^2 \equiv \mu$. Possession of mass modifies the particle's equations of motion, changing the geodesics from null to time-like (Carter 1968; Boyer and Lindquist 1967). Moreover,

a covariant particle flux is mass-dependent. The radiative transfer equations derived for massless particles (equations (3.79) and (3.80)) are therefore not applicable for particles with mass (such as neutrinos or relativistic electrons). Nevertheless, the formulation obtained for massless particles can easily be modified to include the effects of particle mass. A similar procedure is followed as in the case of massless particles in the following derivation. The variation in the path length with respect to the affine parameter may be expressed as

$$\frac{\mathrm{d}s}{\mathrm{d}\lambda} = -\sqrt{g_{\alpha\beta}(p^\alpha + (p_\beta u^\beta)u^\alpha)(p^\beta + (p_\alpha u^\alpha)u^\beta)}\,\Big|_{\lambda_{\rm obs}}, \tag{3.86}$$

(see Younsi et al. 2012), analogous to equation (3.76) in the case of massless particles. Because $p^\alpha p_\alpha \neq 0$,

$$\begin{aligned}\frac{\mathrm{d}s}{\mathrm{d}\lambda} &= -\sqrt{p_\beta p^\beta + (p_\alpha u^\alpha)^2}\,\Big|_{\lambda_{\rm obs}} \\ &= -\sqrt{(p_\alpha u^\alpha)^2 - m^2}\,\Big|_{\lambda_{\rm obs}}.\end{aligned} \tag{3.87}$$

This may be inserted into equation (3.78), which does not depend on the particle mass explicitly. After some algebra, the general covariant transfer equation for relativistic particles is obtained as

$$\frac{\mathrm{d}\mathcal{I}}{\mathrm{d}\lambda} = -\sqrt{1 - \left(\frac{m}{p_\beta u^\beta\big|_{\lambda_{\rm obs}}}\right)^2}\, p_\alpha u^\alpha\Big|_\lambda \left(-\alpha_{0,\nu}\mathcal{I} + \frac{j_{0,\nu}}{\nu^3}\right). \tag{3.88}$$

For a stationary observer located at infinity, $p_\beta u^\beta = -E$. Equation (3.88) differs from equation (3.80) by an aberration factor $\sqrt{1-(m/E)^2}$. This factor reduces the intensity gradient along the ray. Because it approaches unity when $m \to 0$, the radiative transfer equation (3.80) is the radiative transfer equation (3.88) in the zero-mass limit.

Chapter 4

Accretion Tori

As equation (3.88) reveals, the essential components of the covariant radiative transfer formulation are the emission coefficient, the absorption coefficient, the relative energy shift of the particles with respect to the medium and the aberration factor. These are all evaluated along the particle geodesics. Given the thermodynamic conditions of the medium, local values of the emission coefficient and the absorption coefficient can be calculated. Knowledge of the hydrodynamic properties of the medium enables the relative energy shift and the aberration factor to be determined.

In this Chapter the covariant radiative transfer formulation is applied and calculations of the emission from three-dimensional objects in a gravitational field are demonstrated. Accretion tori around rotating black holes are considered. They may have several emission components with different optical depths. Accretion tori are three-dimensional objects with internal structure. This is in contrast to optically thick, geometrically thin accretion disks, which are two-dimensional objects where explicit covariant radiative transfer is unnecessary in determining how the radiation propagates and is modified within the disk.

4.1 Modelling Accretion Tori

For accreting objects, the accretion luminosity $L_{\rm acc}$ roughly scales with the mass accretion rate $\dot{M}$ as $L_{\rm acc} = \varepsilon \dot{M}$. The conversion parameter $\varepsilon \sim 10^{20}$ erg g^{-1} for black holes (see Frank et al. 2002). The formation of geometrically thin accretion disks around a black hole requires that the radiation

pressure force in the accretion flow is much smaller than the local gravitational force exerted by the black hole. This condition is usually satisfied when $\dot{M}$ is sufficiently low, such that $L_{\rm acc}$ is much lower than the Eddington luminosity, which is given by $L_{\rm Edd} = 1.4 \times 10^{38}(M/M_{\odot})$ erg s^{-1}. Because $L_{\rm acc}$ increases with $\dot{M}$, a high $\dot{M}$ implies a high $L_{\rm acc}$ and hence a large radiative pressure within the disk where the radiation is liberated. When $L_{\rm acc}$ approaches $L_{\rm Edd}$, the radiation pressure force becomes comparable to the local gravitational force, and the accretion disk inflates and become a torus (see e.g. Frank et al. 2002).

In general, full knowledge of the fluid viscosity is required in determining the structure and hydrodynamics of the accretion torus. However, in accretion tori the angular momentum transport is non-local. The relevant processes cannot be parameterised with a local viscosity, as in the case of modelling geometrically thin accretion disks, where the α-viscosity prescription is often used (Shakura and Sunyaev 1973; Abramowicz et al. 1988). It is believed that the angular momentum transport in accretion disks and tori is mediated by tangled magnetic fields that permeate the flow (e.g. magneto-rotational instability (MRI) – see Hawley 2000; Balbus 2003). In principle this magnetic viscosity and the flow hydrodynamics need to be determined simultaneously and self-consistently. Nevertheless, certain phenomenological prescriptions are proposed to bypass the viscosity calculations, e.g. assuming an angular momentum distribution within the torus instead of solving for the distribution. With such prescriptions, the structure of the accretion torus can be determined by solving only the remaining hydrodynamic equations and the equation of state. This thesis takes such a phenomenological approach to construct accretion tori, assuming a specific angular velocity profile within the torus (see also Fuerst and Wu 2004, 2007; Abramowicz 2005). With the angular velocity profile specified, the density and entire flow profiles may be determined in terms of certain normalised variables. The resulting accretion torus is then rescaled, using the results from accretion tori/disks obtained by numerical MRI simulations (Hawley 2000; Balbus 2003). The torus model constructed as such is able to capture the geometrical aspects of the MRI

accretion tori and the physical conditions within the accretion flow.

The maximum energy available from an object of mass M is $E_{\max} = Mc^2$ and the minimum time in which said energy can be released is $t_{\min} = r_{\rm g}/c$. Therefore the maximum power is

$$L_{\rm Planck} = \frac{E_{\max}}{t_{\min}} = \frac{c^5}{G} \approx 10^{59} \text{erg sec}^{-1} \ , \tag{4.1}$$

which is the absolute upper limit for power of anything in the Universe. It was noted by Abramowicz et al. (1988) that the upper limit for the radiative power of an object of mass M (gravity and radiation in equilibrium) is given by the Eddington limit

$$L_{\rm Edd} = L_{\rm Planck} \frac{\Sigma_{\rm grav}}{\Sigma_{\rm rad}} \ , \tag{4.2}$$

where $\Sigma_{\rm grav}$ is the object's total effective gravitational cross-section and $\Sigma_{\rm rad}$ the total radiative cross-section. This is the most general form of the Eddington limit. The standard formula for the Eddington limit is obtained from the assumptions that a "star" is radiation pressure supported, that the radiation interacts with matter through electron scattering and that effective gravity is provided exclusively by Newtonian gravity. This results in $\Sigma_{\rm rad} = N\sigma_{\rm T}$ and $\Sigma_{\rm grav} = 4\pi r_{\rm g}^2$, where N is the number of electrons within said object. It immediately follows that for spherical accretion the corresponding Eddington luminosity is

$$L_{\rm Edd} = \frac{4\pi G M m_p c}{\sigma_{\rm T}} \approx 1.4 \times 10^{38} \, (M/M_\odot) \ \text{erg sec}^{-1} \ . \tag{4.3}$$

Beyond the Eddington limit, the radiation pressure becomes so large that the thin disk solution no longer holds, and the accretion disk puffs up into a torus.

4.2 Emission Surface of Rotationally Supported Torus

To calculate the emission from an opaque accretion torus, one need only to specify the torus' boundary surface and its physical conditions. The simplest model that enables the boundary emission surface to be defined is a rotationally supported torus. In this model, the total pressure force is balanced by the 4-acceleration in an arbitrary fluid element. The inner boundary of the torus is defined where this balance breaks down. With an appropriate parametrisation

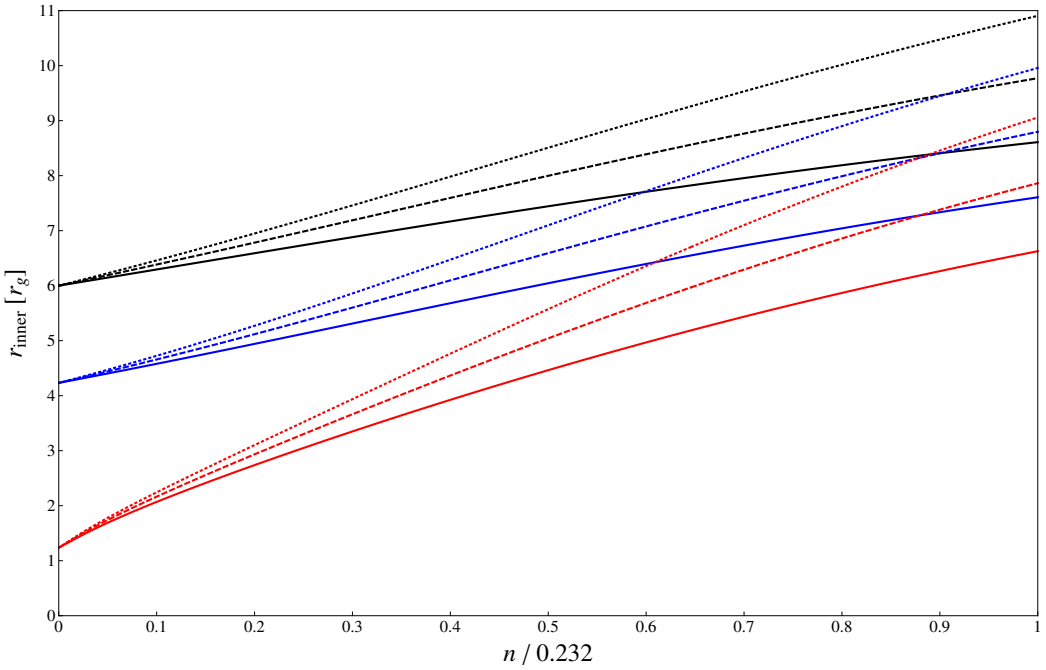

Fig. 4.1: Torus inner radius as a function of the angular velocity profile index parameter n. Red, blue and black curves correspond to black holes with spin parameters $a = 0.998$, 0.5 and 0 respectively. Solid, dashed and dotted lines correspond to Keplerian radii of $r_{\mathrm{K}} = 8\,r_{\mathrm{g}}$, $10\,r_{\mathrm{g}}$ and $12\,r_{\mathrm{g}}$ respectively. The inner edge of the torus is strongly dependent on the index n. In the case $n = 0$ the assumed angular velocity profile becomes pseudo-Keplerian ($r\,\sin\theta$ – dependence) and the inner edge is located at the ISCO. However, as n increases the inner edge of the torus quickly moves further away from the ISCO. This effect is more pronounced for higher black hole spin parameters. The black hole spin parameter a and the index parameter counteract each other. The former shifts the torus inner edge towards the ISCO (thereby increasing the torus' vertical extent and volume) and the latter shifts this inner edge away from the ISCO, consequently reducing the torus' vertical extent and volume.

of the angular velocity profile (Ω, as a function of position in the torus) the 4-acceleration may be derived, yielding the pressure force. Tracing the isobars gives the isobaric surfaces inside the torus. This process is essential in order to construct the gradient contours of the 4-acceleration in the $r-\theta$ plane (in the (t, r, θ, ϕ) spherical co-ordinate system). The torus boundary surface is simply the outermost allowed isobaric surface.

A stationary, axisymmetric, rotationally supported accretion torus is considered. The symmetry axis of the torus is aligned with the spin vector of the central black hole. The 4-acceleration of the flow is derived from the 4-velocity

$$a^{\alpha} = u^{\alpha}{}_{,\beta}\, u^{\beta} + \Gamma^{\alpha}{}_{\beta\sigma} u^{\beta} u^{\sigma} \ . \tag{4.4}$$

Because the poloidal components of the flow are dynamically unimportant, we set the 4-velocity as $u^{\alpha} = (u^t, 0, 0, u^{\phi})$. It follows that $u^{\alpha}{}_{,\beta}\, u^{\beta} = 0$ and

$$a^{\alpha} = \Gamma^{\alpha}{}_{tt} u^t u^t + 2\Gamma^{\alpha}{}_{t\phi} u^t u^{\phi} + \Gamma^{\alpha}{}_{\phi\phi} u^{\phi} u^{\phi} \ . \tag{4.5}$$

In BL co-ordinates, the covariant r and θ components of the 4-acceleration are

$$a_r = \frac{\Sigma}{\Delta} a^r = -\left[M \left(\frac{\Sigma - 2r^2}{\Sigma^2} \right) \left(\dot{t} - a \sin^2\theta \ \dot{\phi} \right)^2 + r \sin^2\theta \ \dot{\phi}^2 \right] \ , \tag{4.6}$$

$$a_{\theta} = \Sigma\, a^{\theta} = -\sin 2\theta \left\{ \frac{Mr}{\Sigma^2} \left[a\dot{t} - \left(r^2 + a^2 \right) \dot{\phi} \right]^2 + \frac{\Delta}{2} \dot{\phi}^2 \right\} . \tag{4.7}$$

Setting $a_{\alpha} u^{\alpha} = 0$ yields a set of differential equations for the isobaric surfaces. It is more convenient to express the equations as

$$\frac{\mathrm{d}r}{\mathrm{d}\xi} = \frac{\psi_2}{\sqrt{\psi_2^2 + \Delta \psi_1^2}} \ , \tag{4.8}$$

$$\frac{\mathrm{d}\theta}{\mathrm{d}\xi} = \frac{-\psi_1}{\sqrt{\psi_2^2 + \Delta \psi_1^2}} \ , \tag{4.9}$$

for the calculation and construction of the torus boundary surface. Here ξ is an auxiliary variable, and the functions ψ_1 and ψ_2 are given by

$$\psi_1 = M \left(\frac{\Sigma - 2r^2}{\Sigma^2} \right) \left(\Omega^{-1} - a \sin\theta \right)^2 + r \sin^2\theta \ , \tag{4.10}$$

$$\psi_2 = \sin 2\theta \left(\frac{Mr}{\Sigma^2} \left[a\, \Omega^{-1} - \left(r^2 + a^2 \right) \right]^2 + \frac{\Delta}{2} \right) . \tag{4.11}$$

Solving equations (4.8) and (4.9), with the inner boundary radius of the torus and the specified angular velocity profile gives the torus boundary surface.

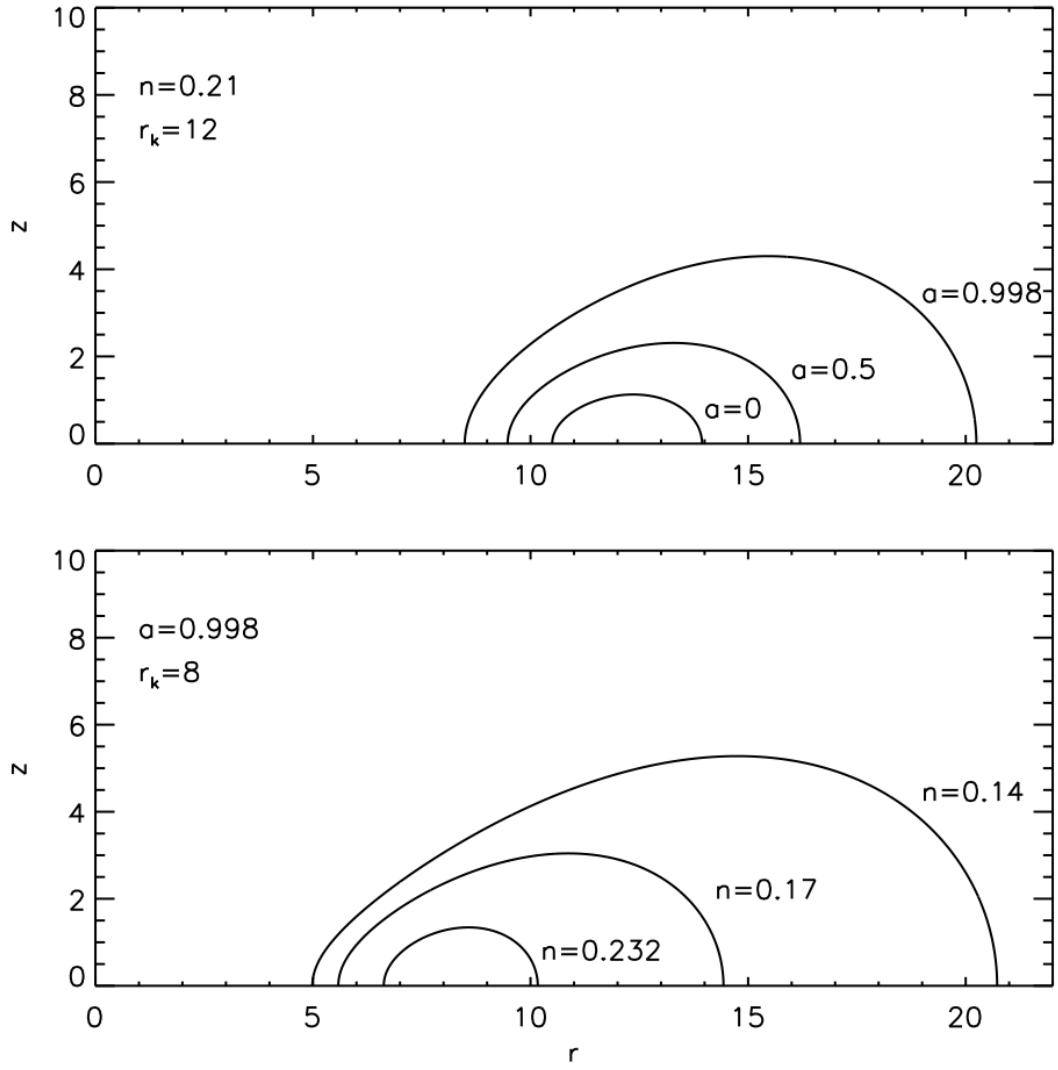

Fig. 4.2: Cross-sections of the boundary surfaces of model rotationally supported tori in cylindrical coordinates with $z = r\cos\theta$ (the equatorial plane of the tori is $z = 0$). The top panel shows the tori around Kerr black holes with spin parameters $a = 0$, 0.5 and 0.998. The angular velocity profile index of the tori $n = 0.21$, and the Kelperian radius $r_{\rm K} = 12\ r_{\rm g}$. The bottom panel shows the tori with angular velocity indices $n = 0.14$, 0.17 and 0.232. The Keplerian radius of the tori is $r_{\rm K} = 8\ r_{\rm g}$, and the black-hole spin parameter $a = 0.998$.

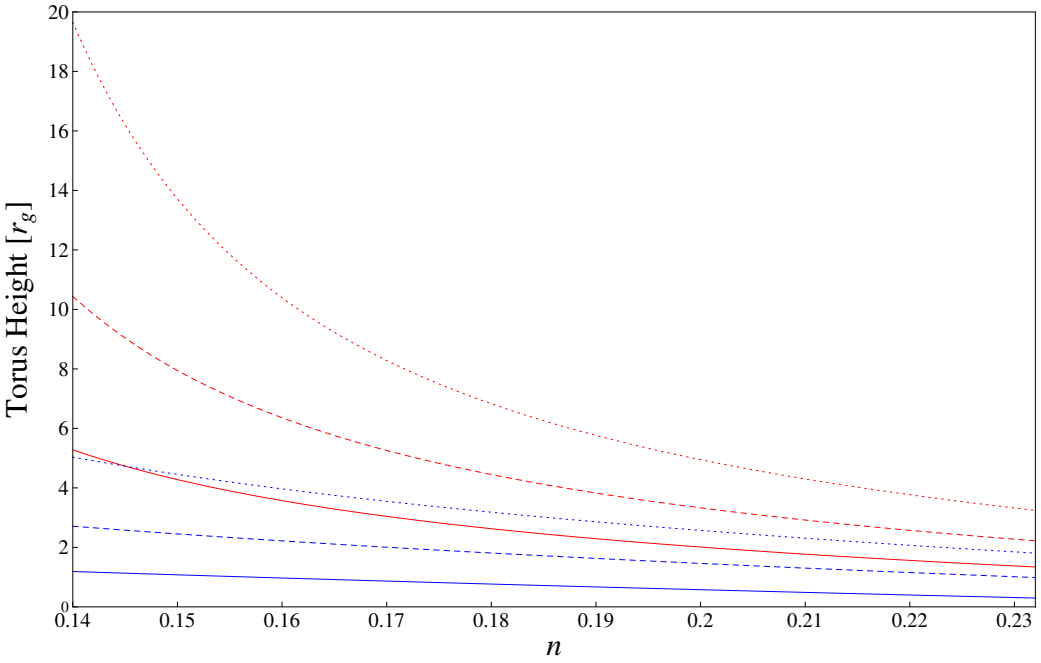

Fig. 4.3: Torus height (vertical extent) as a function of the angular velocity profile index parameter n. Same as in Figure 4.1, except the case $a = 0$ (black) is omitted. As the Keplerian radius increases, so does the torus height. However, as in Figure 4.2, the effect of n is to reduce the torus height. Thus n ultimately determines the size of the torus, as well as the extent to which it self-occludes.

As in Fuerst and Wu (2004, 2007), an angular velocity profile with the form

$$\Omega(r\sin\theta) = \frac{\sqrt{M}}{(r\sin\theta)^{3/2} + a\sqrt{M}}\left(\frac{r_{\rm K}}{r\ \sin\theta}\right)^{n}, \tag{4.12}$$

is considered, where $r_{\rm K}$ is the radius on the equatorial plane at which the material circulates with a Keplerian velocity. The differential rotational velocity gradient gives rise to an implicit pressure force, supporting the torus material above and below the equatorial plane. The parametrisation using the variable $r\ \sin\theta$ ensures the constant density and pressure surfaces coincide in the Newtonian limit and a polytropic equation of state is applicable for the flow.

The index parameter n is crucial for regulating the pressure forces, thus adjusting the torus' geometrical aspect ratio. Its property is similar to that of the q index of the von Zeipel parameter in the study of stability of accretion disks (see Chakrabarti 1985; Blaes and Hawley 1988). Generally, $n \approx q - 1.5$, with the relation being exact for Schwarzschild black holes. Tori with $q > \sqrt{3}$

are unstable. In the Newtonian limit tori with $n = 0.232$ are marginally stable (Blaes and Hawley 1988).

The angular velocity and angular momentum of the flow are $\Omega = u^\phi/u^t$ and $l = -u_\phi/u_t$ respectively, and the redshift factor is given by

$$A \;=\; u^t = \left[-(g_{tt} + 2\Omega g_{t\phi} + \Omega^2 g_{\phi\phi})\right]^{-1/2} \;, \tag{4.13}$$

and the energy per unit inertial mass of the flow material is

$$U \;=\; -u_t = -\sqrt{\frac{g_{t\phi}^2 - g_{tt}g_{\phi\phi}}{g_{\phi\phi} + 2lg_{t\phi} + l^2 g_{tt}}} \;. \tag{4.14}$$

These two quantities are related via

$$AU = \frac{1}{(1 - l\Omega)} \;. \tag{4.15}$$

Zero values for the denominators in equations (4.13) and (4.14) correspond to the locations (the photon surface) where the local flow speeds reach the speed of light.

In this model, the condition for the inner boundary radius must be specified. This is taken as the intersection of the isobaric surface with either the orbits of marginal stability or the limiting surface of photon orbits, whichever has a larger radius. Usually the photon surface is within the marginally stable orbit. The inner boundary of the torus is therefore in general determined by the orbits of marginal stability, which satisfy $\partial U/\partial r = 0$. For a particular angular velocity law $\Omega\,(r, \theta)$, solving this condition yields

$$\begin{aligned}
&2aM\sin^4\theta\left[\frac{r^2}{\Sigma} - \left(r^2 + a^2 + \frac{a^2 M r \sin^2\theta}{\Sigma}\right)\frac{\Sigma - 2r^2}{\Sigma^2}\right]\Omega^3 \\
&+\sin^2\theta\left[M\left(\frac{6Mr(r^2+a^2)}{\Sigma} + 3\Delta - \Sigma\right)\frac{\Sigma - 2r^2}{\Sigma^2} + r\left(1 - \frac{2Mr}{\Sigma}\right)\right]\Omega^2 \\
&-\frac{6aM^2 r\sin^2\theta}{\Sigma}\left(\frac{\Sigma - 2r^2}{\Sigma^2}\right)\Omega \\
&+\Delta\sin^2\theta\,\Omega\frac{\partial\Omega}{\partial r} - M\left(1 - \frac{2Mr}{\Sigma}\right)\frac{\Sigma - 2r^2}{\Sigma^2} = 0 \;,
\end{aligned} \tag{4.16}$$

which when solved for r, yields the inner edge of the torus (for a particular choice of $r_{\rm K}$ and n). The solution to equation (4.16) is plotted as a function of n in Figure 4.1 for various values of a and $r_{\rm K}$. Equations (4.8) and (4.9) for the torus surface are now readily integrated.

Figure 4.2 shows the boundary surfaces of rotationally supported tori with various system parameters. The shapes of the tori are determined by the rotational velocity index of the torus n and the black-hole spin parameter a. When $r_{\rm K}$ is fixed, the vertical thickness of the torus increases with a but decreases with n. The degree of self-occluding of an optically thick torus and hence the spectral properties of the emission depend on the aspect ratio of the torus (see Figure 4.3) and the viewing inclination. Note that the tori in Figure 4.2 are purely rotation-supported. The thermal pressure of the torus gas and the radiative pressure of the emission from the gas have not been included in their construction. The presence of gas pressure and radiation pressure will modify the aspect ratio of the tori. In the next subsection a more general situation which includes both the gas pressure and radiative pressure is considered, and tori with internal density and temperature structures are considered.

4.3 Pressure Supported Torus Structure

Accretion tori resemble stars that have an atmosphere with an optical depth gradient. While emission from an opaque torus originates from an unobscured infinitesimally thin layer on the torus surface, emission from a translucent or an optically thin accretion torus is formed by the emission contributions from all regions interior to the torus. The thermodynamic and hydrodynamic structures of the torus determine the spectral properties of its emission, and so they must be determined prior to performing the radiative transfer calculations.

To model the internal structure of the accretion tori, a prescription given by Abramowicz et al. (1978) and Kozlowski et al. (1978) is adopted. The tori are considered to be stationary and axisymmetric. They consist of a perfect fluid, and the stress-energy-momentum tensor of the flow is given by

$$T^{\alpha\beta} = (\rho + P + \epsilon)u^{\alpha}u^{\beta} + Pg^{\alpha\beta} \ , \tag{4.17}$$

where P is the pressure, ρ is the density, and ϵ is the fluid internal energy. Because $T^{\alpha\beta}{}_{;\beta} = 0$, the following continuity equation is obtained

$$(\rho + P + \epsilon)_{,\beta}u^{\alpha}u^{\beta} + (\rho + P + \epsilon)(u^{\alpha}{}_{;\beta}u^{\beta} + u^{\alpha}u^{\beta}{}_{;\beta}) + P_{,\beta}g^{\alpha\beta} = 0 \ . \tag{4.18}$$

Projecting onto the 3-surface orthogonal to the fluid velocity u^α with the projection tensor $P^{\alpha\beta} = g^{\alpha\beta} + u^\alpha u^\beta$ yields the momentum equation

$$(\rho + P + \epsilon)u^\alpha{}_{;\beta}u^\beta + P_{,\beta}g^{\alpha\beta} = 0 \ . \tag{4.19}$$

Because the torus is stationary and axisymmetric, it has negligible poloidal flow components, hence

$$u_{\alpha;\beta}u^\beta = -\Gamma^\sigma_{\alpha\beta}u_\sigma u^\beta = -\frac{1}{2}u^\sigma u^\beta g_{\sigma\beta,\alpha} \ . \tag{4.20}$$

Differentiating $u^\alpha u_\alpha = -1$ gives

$$(u^\alpha u_\alpha)_{,\delta} = g_{\alpha\beta,\delta}u^\alpha u^\beta + 2u^\alpha u_{\alpha,\delta} = 0 \ .$$

Thus,

$$u^\alpha u_{\alpha,\delta} = -\frac{1}{2}u^\alpha u^\beta g_{\alpha\beta,\delta} \ . \tag{4.21}$$

It follows that

$$u_{\alpha;\beta}u^\beta = u^\beta u_{\beta,\alpha} = u^t\partial_\alpha u_t + u^\phi\partial_\alpha u_\phi \ , \tag{4.22}$$

where ∂_α is the gradient in the x^α direction. Recall that $\Omega = u^\phi/u^t$ and $l = -u_\phi/u_t$. Therefore, it follows that

$$u^\phi u_t = \Omega(u^t u_t) = -\frac{\Omega}{1 - l\Omega} \ . \tag{4.23}$$

The gradient of l is

$$\partial_\alpha l = \frac{u_\phi}{u_t^2}\partial_\alpha u_t - \frac{1}{u_t}\partial_\alpha u_\phi \ . \tag{4.24}$$

It follows that

$$\frac{\Omega\partial_\alpha l}{1 - l\Omega} = \frac{1}{u_t}\partial_\alpha u_t + u^t\partial_\alpha u_t + u^\phi\partial_\alpha u_\phi \ . \tag{4.25}$$

Equation (4.22) can now be expressed as

$$u_{\alpha;\beta}u^\beta = \frac{\Omega\partial_\alpha l}{1 - l\Omega} - \frac{1}{u_t}\partial_\alpha u_t \ . \tag{4.26}$$

Thus,

$$\frac{\partial_\alpha P}{\rho + P + \epsilon} = \partial_\alpha \ln(u_t) - \frac{\Omega\partial_\alpha l}{1 - l\Omega} \tag{4.27}$$

(cf. equation (7) in Abramowicz et al. (1978) for the accretion torus).

An equation of state is required to close the system of equations and the gas within the torus is assumed to be barotropic. Owing to the complexity of

the Kerr metric, the solution must be computed numerically. However, in the special case of $l =$ constant, corresponding to a marginally stable torus, there is an analytic solution

$$\int_0^P \frac{dP'}{\rho + P' + \epsilon} = \ln(u_t) - \ln(u_t)_{\rm inner} \ , \tag{4.28}$$

where $\ln(u_t)_{\rm inner}$ is evaluated at the inner edge of the torus.

To know the transparency of the torus to radiation requires that the local emissivity and opacity within the torus be specified explicitly. As such, the velocity, temperature and density structure of the torus must be determined prior to the radiative transfer calculations.

The total pressure within the torus is the sum of the gas pressure and the radiation pressure, i.e. $P = P_{\rm gas} + P_{\rm rad}$, where

$$P_{\rm gas} = \frac{\rho k_{\rm B} T}{\mu m_{\rm H}} = \beta P \ , \tag{4.29}$$

$$P_{\rm rad} = \frac{4\sigma}{3c} T^4 = (1-\beta) P \ . \tag{4.30}$$

Here μ the mean molecular weight, $m_{\rm H}$ the mass of a hydrogen atom and β is the ratio of gas pressure to total pressure. Eliminating $k_{\rm B}T$ in the above equations yields

$$P = \hbar c \left[\frac{45(1-\beta)}{\pi^2 (\mu m_{\rm H} \beta)^4} \right]^{1/3} \rho^{4/3} \ . \tag{4.31}$$

For a polytropic equation of state $P = \kappa \rho^\Gamma$, the internal energy is related to the pressure by $\epsilon = P/\Gamma - 1$. Equation (4.31) implies $\Gamma = 4/3$, and $\kappa = \hbar c [45(1-\beta)/\pi^2 (\mu m_{\rm H} \beta)^4]^{1/3}$.

Combining the momentum equation (4.19) for a perfect fluid with the polytropic equation of state gives

$$\left(\rho + \frac{\Gamma}{\Gamma - 1} P \right) a^\alpha = -P_{,\beta} g^{\alpha\beta} \ . \tag{4.32}$$

Differentiating the polytropic equation of state yields

$$\partial_\alpha P = \kappa \Gamma \rho^{\Gamma - 1} (\partial_\alpha \rho) \ . \tag{4.33}$$

The density structure of the torus is then given by

$$\partial_\alpha \rho = -a_\alpha \left(\frac{\rho^{2-\Gamma}}{\kappa \Gamma} + \frac{\rho}{\Gamma - 1} \right). \tag{4.34}$$

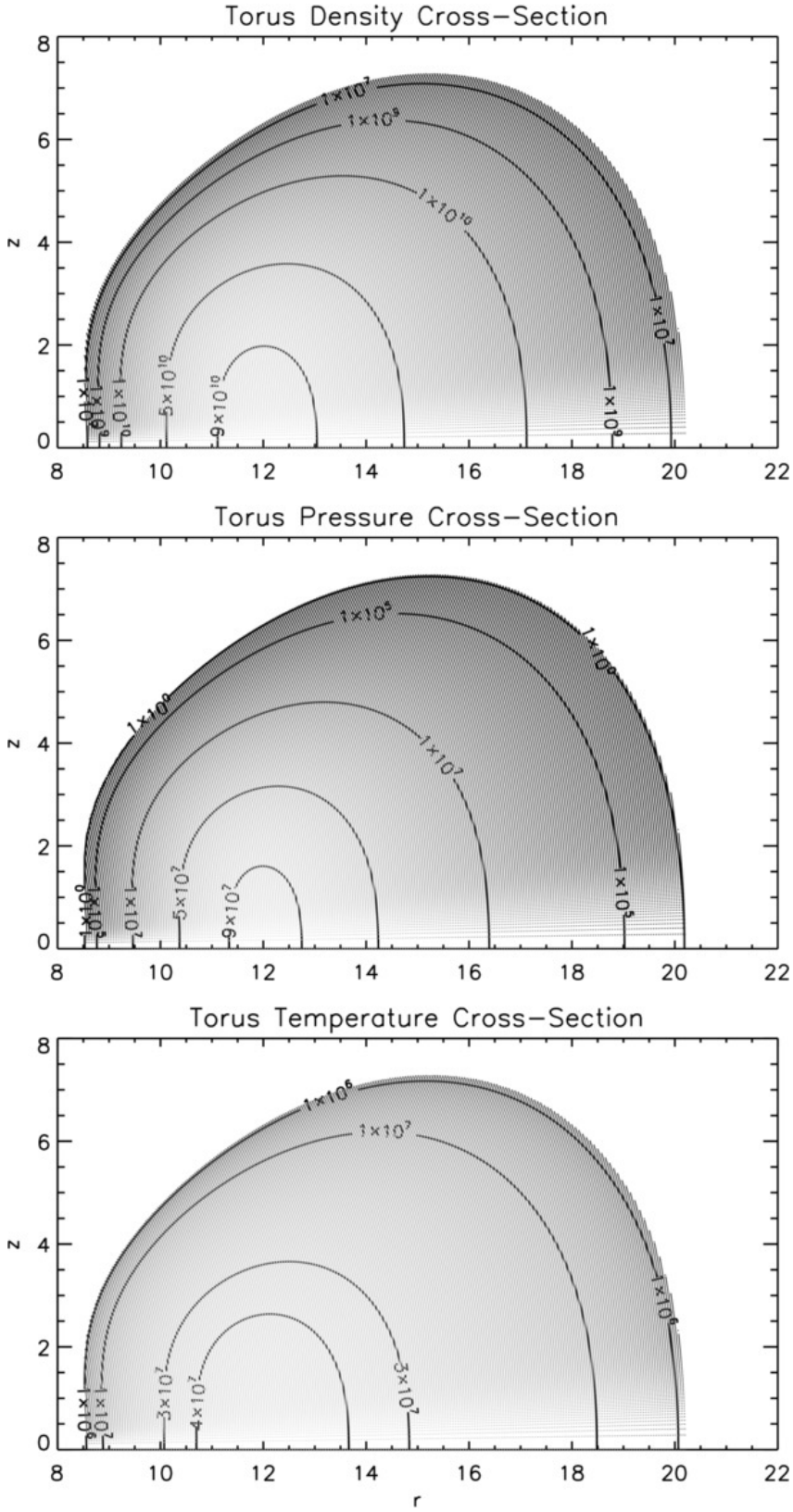

Fig. 4.4: Cross-sections show the density, pressure and temperature contours in model translucent tori (panels from top to bottom). The angular velocity profile index of the tori $n = 0.21$, the Keplarian radius $r_{\rm K} = 12\ r_{\rm g}$. The black-hole spin paramter $a = 0.998$. The central density of the torus $\rho_{\rm c} = 10^{11}$ cm^{-3}. The ratio of the gas pressure to the total pressure $\beta = 1.235 \times 10^{-5}$.

Introducing a new variable ξ (akin to logarithm of temperature), where $\xi = \ln(\Gamma - 1 + \Gamma\kappa\rho^{\Gamma-1})$, equation (4.34) simplifies to

$$\partial_\alpha \xi = -a_\alpha \ . \tag{4.35}$$

The stationarity and axisymmetry conditions imply that there are only two non-trivial components (r and θ) in the equation. By evaluating the line integral from $r = r_{\rm K}$, $\rho = \rho_{\rm c}$ at the torus centre to the required (r, θ) location, the density field $\rho(r, \theta)$ is determined. The temperature within the torus may also be derived as a function of ρ, yielding

$$k_{\rm B}T = \hbar c \left[\frac{45\,(1-\beta)}{\pi^2(\mu m_{\rm H}\beta)}\right]^{1/3} \rho^{1/3} \ . \tag{4.36}$$

With $\rho(r, \theta)$ determined, the pressure and temperature are readily calculated from equations (4.31) and (4.36).

Figure 4.4 shows the density, pressure and temperature structures of a model torus with $n = 0.21$, $r_{\rm K} = 12\ r_{\rm g}$, $\beta = 1.235 \times 10^{-5}$, and $\rho_{\rm c} = 10^{11}\ {\rm cm}^{-3}$. The spin parameter of the black hole is $a = 0.998$. There are several noticeable features in the torus. The torus is pressure supported. Its boundary is located where the density ρ and hence the pressure P vanish. The temperature T also vanishes at the torus boundary surface for the equation of state that has been adopted. As is shown in the bottom panel of Figure 4.4, the temperature $T \sim 10^7$ K in most of the torus interior, but drops off rapidly within a very short distance of $\sim 1\ r_{\rm g}$ and reaches 0 K at the torus boundary. Compared to the rotationally supported tori (Figure 4.1), the rotation and radiative pressure supported tori are larger in vertical extent. The vertical inflation of the torus is caused by the addition of radiative and thermal gas pressure forces.

4.4 Radiative Transfer Calculations for Accretion Tori

4.4.1 Emission from opaque rotationally supported tori

For an opaque torus, the emission spectrum can be calculated from the emissivity distribution on the torus' boundary surface, with corrections for the relativistic shifts with respect to the distant observer. This emissivity has a radial power-law distribution with an index of -2, i.e. $j \propto r^{-2}$. In Figure

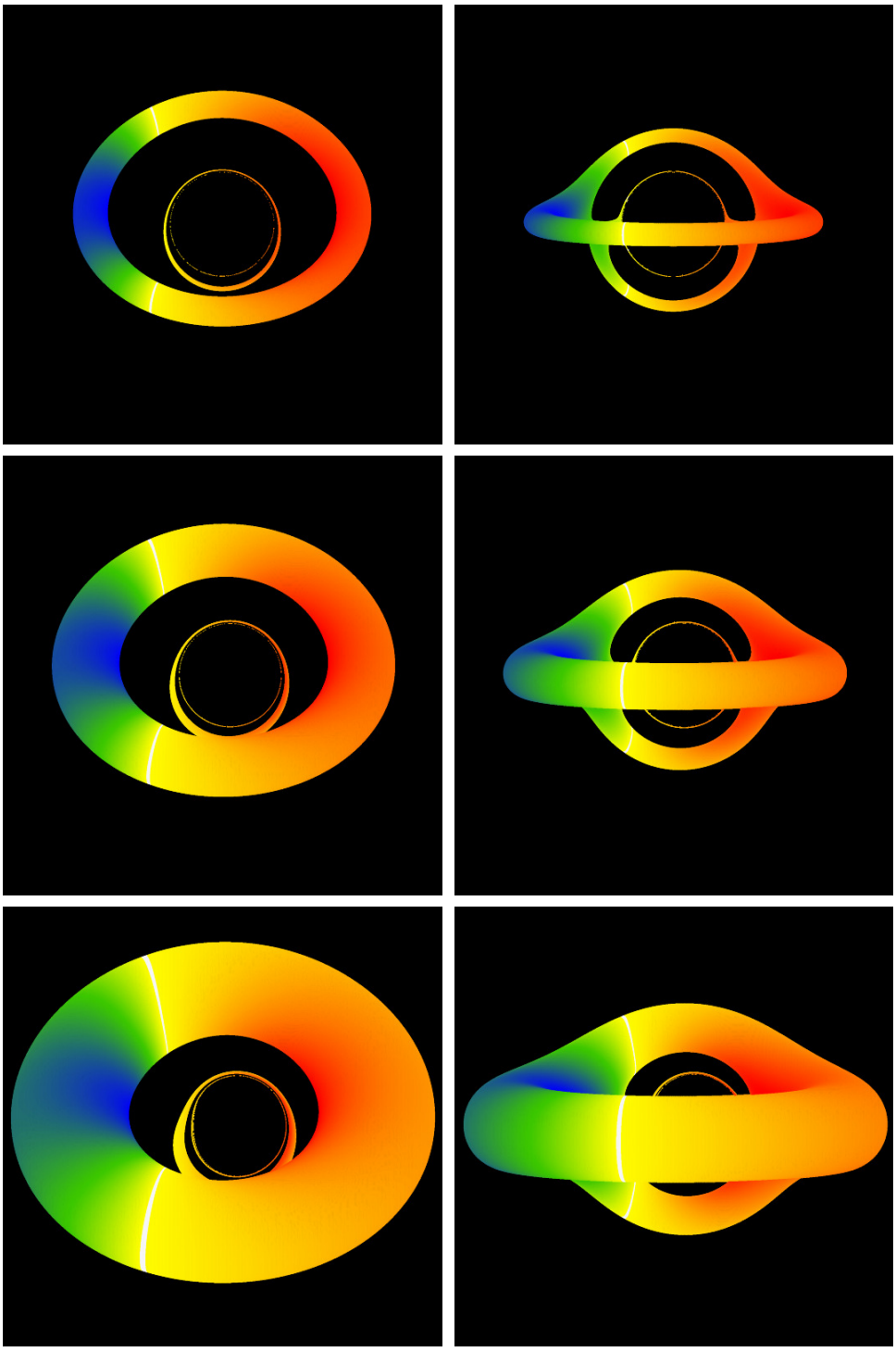

Fig. 4.5: False-colour frequency shift maps of the surface emission from opaque tori around different black holes. The torus parameters are $n = 0.232$ and $r_{\rm K} = 12\ r_{\rm g}$. The black-hole spin parameters are $a = 0$, 0.5 and 0.998 (panels from top to bottom). The viewing inclinations of the tori are 45° (left column) and 85° (right column). For $a = 0$ the range of frequency shifts $\mathrm{E/E_0}$ (where E_0 is the rest-frame line centre energy) for $i = 45°$ and $i = 85°$ are $(0.874, 1.445)$ and $(0.756, 1.560)$, respectively. Similarly, for $a = 0.5$ the frequency shift ranges are $(0.870, 1.487)$ and $(0.755, 1.591)$. Finally, for $a = 0.998$ the corresponding frequency shift ranges are $(0.864, 1.535)$ and $(0.767, 1.616)$.

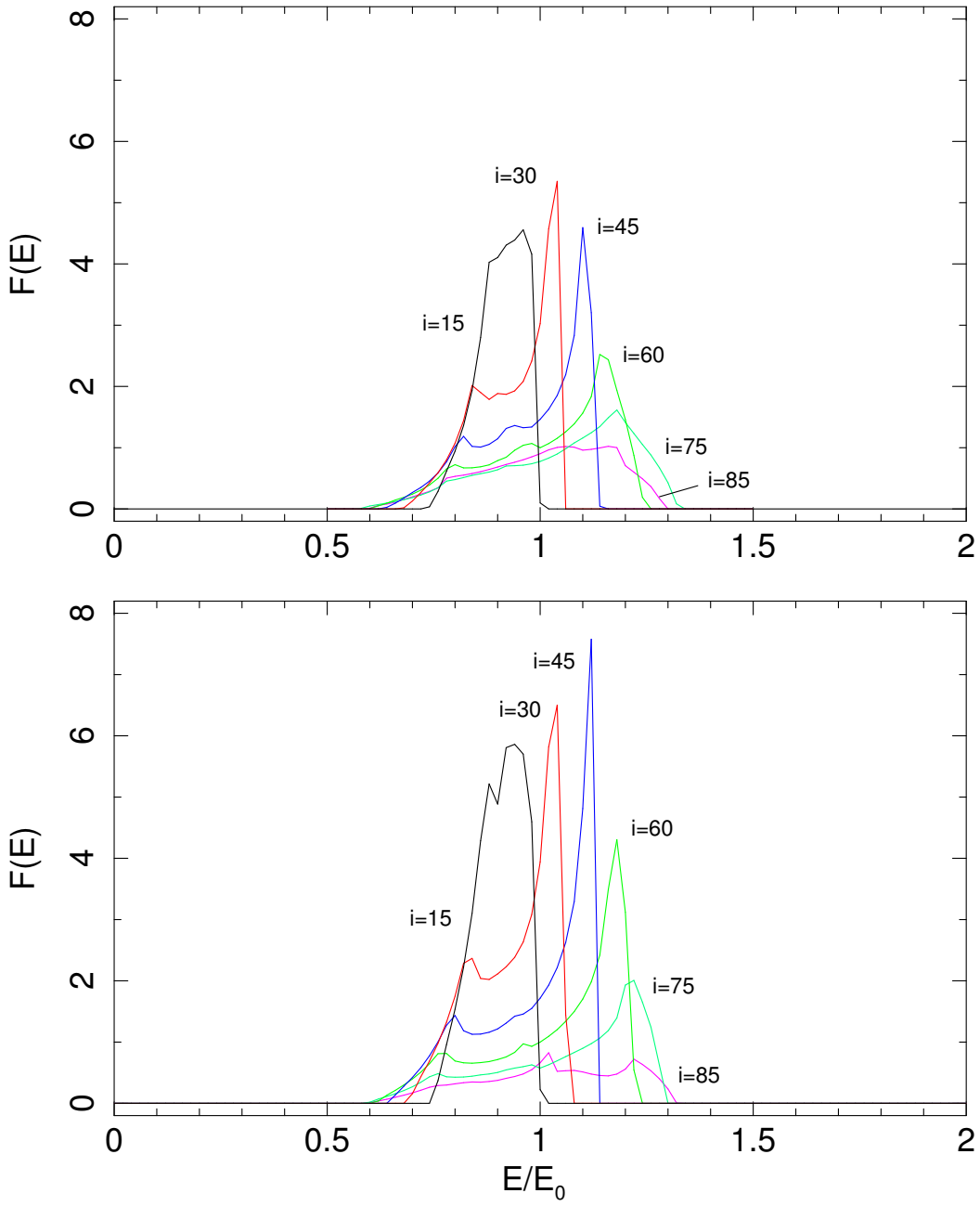

Fig. 4.6: Profiles of emission lines from an opaque rotationally supported accretion torus (top panel) and a geometrically thin optically thick accretion disk (bottom panel) viewed at different inclinations i. The torus dynamical parameters are $n = 0.21$ and $r_{\rm K} = 12\ r_{\rm g}$. The inner boundary radius of the torus $r_{\rm inner} = 8.486\ r_{\rm g}$ and the outer boundary radius $r_{\rm outer} = 20.246\ r_{\rm g}$. The disk has the same values for the inner boundary radius and the outer boundary radius as the torus. In both cases, the black-hole spin parameter $a = 0.998$. The line emissivity is proportional to r^{-2}, where r is the radial distance from the central black hole. The line profiles are normalised such that the flux $F(E_0) = 1$ at the viewing inclination angle $i = 60°$.

4.5 images of rotationally supported tori viewed at inclination angles of 45° and 85° for various black hole spin parameters are shown. The torus is left-right symmetric in shape if the black hole is not rotating. The black hole's rotation drags the surrounding space-time around the black hole, and so the torus around a Kerr black hole is asymmetric. Optically thick tori would suffer self-eclipsing at high viewing inclination angles. Each pixel in the torus images shown in Figure 4.5 has only one single value for the relative frequency shift between the emission surface element and the observer. This relative frequency shift is coded with colours in the torus images. It is clear to see that the regions with the highest redshifts and with the highest blueshifts are obscured by the front limb of the torus when the viewing inclination angle is close to 90°.

In calculating the intensity and the emission spectrum of an opaque torus, the ray-tracing formulation described in Chapter 3.3 is employed, adequately taking into account effects such as gravitational redshift, lensing, kinetic time dilation and Doppler boosting. Only propagation of radiation outside the torus is relevant, so the emission and absorption coefficients are set to zero in the radiative transfer equation along the rays emerging from the torus' boundary surface. Relativistic frequency shifts are computed at the surface boundary, which upon convolving with a specified spatial profile for the source function of the emission yields the emission spectrum.

Figure 4.6 shows the spectral profiles of emission lines from an opaque torus and a geometrically thin, optically thick disk with the same inner and outer radius. The inner radius of the model accretion disk is much larger than the minimum radius allowed, which is roughly 1.237 $r_{\rm g}$ for a maximally rotating black hole. A major difference between a torus and a thin disk is that self-obscuration can occur for the torus at high viewing inclinations, while the first-order emission from the upper disk surface is always visible by a distant observer. The emission from the inner torus regions where relativistic effects are most severe and the emission suffers the highest and lowest frequency shifts does not contribute to the emission. For a thin disk, the inner disk regions with the highest and lowest frequency shifts do contribute to the total

emission spectra. The line profiles of the torus and the disk in Figure 4.6 show little difference at low viewing inclinations. This is easily understood, because the torus and disk not only look similar when they are viewed pole-on, they show similar radial dependences in the surface emissivity distribution when the entire upper emission surface is unobscured. For viewing inclinations $i \sim 80^\circ$ or higher, the line from the torus is narrower than the line from the disk, and in particular the edge of its blue wing is at a lower energy than that of the line from the disk, because the inner torus region where the bluest emission originates is eclipsed by the front limb. The third mini-peak in spectra viewed at inclinations $i \geq 45^\circ$ is due the emission from higher-order images (photons which orbit the black hole multiple times before being received).

4.4.2 Emission from translucent pressure-supported tori

Optically thin and translucent tori do not have a sharply defined emission surface. All parts within the tori contribute to the emission, with the contribution weighted according to matter concentration (density) and to the local values of the thermodynamic variables (e.g. temperature) relevant to the radiation processes considered. A low optical depth across the torus permits the transmission of the emission from higher-order lensed images, therefore the emission spectrum of the torus is the sum of the spectra from all the orders of lensed images weighted by the optical depth of the ray. Figure 4.7 shows the intensity images of an optically thin radiative pressure dominated torus for different viewing inclination angles, and Figure 4.8 shows the intensity images of an optically thin radiative pressure dominated torus with a lower internal radiation pressure.

For the $\beta = 1.235 \times 10^{-5}$ optically thin torus model, the value of β was chosen so that the inner and outer radii of the torus very closely matched the inner and outer radii of the opaque tori and thin disks discussed in the previous section, enabling a comparison of the resulting images and emission line profiles. The second model with $\beta = 5 \times 10^{-5}$, i.e. a smaller internal radiation pressure, illustrates the dependence of the torus size on β. The dynamical parameters of the two tori are $n = 0.21$ and $r_{\rm K} = 12\ r_{\rm g}$, and the spin parameter of the central black hole is $a = 0.998$. The emissivity takes the

form $j \propto \rho$, and the light-of-sight optical depth across the tori $\tau \ll 1$. As seen in the figures, changes in the pressure ratio parameter β alter the aspect ratio of the torus, which determines to what degree self-occluding occurs for a given viewing inclination angle. In spite of this, the general emission properties in these images are qualitatively similar, because of the translucency of the torus. In both tori, the intensity of the emission is strongest at the interior of the torus, where the density is high. The rotation of the torus causes frequency shifts in the emission and Doppler boosting of the intensity. These relativistic effects are more obvious for high viewing inclination angles. The emission from the approaching limb of the torus is amplified and appears to be significantly brighter than the emission from the receding limb of the torus.

Figure 4.9 (top panel) shows the profile of an emission line from a radiative pressure dominated optically thin torus viewed at different inclination angles. The lines are broad and have an asymmetric profile, characteristic of line emission from relativistic accretion disks viewed at moderate inclination angles, $i \approx 45^\circ - 70^\circ$ (see e.g. Cunningham 1975; Fabian et al. 2000). In contrast to the lines from relativistic accretion disks, the profiles of lines from optically thin tori do not change significantly when the viewing inclination angle changes from 45° to 85° (cf. the line profiles in Figure 4.6). The asymmetric broad profiles of the lines from optically thick relativistic disks are due to the combination of a number of effects: Doppler boosting, Doppler velocity shift, gravitational time dilation and gravitational lensing. Emission from an optically thin torus does not depend on the projected area of an emission surface element, as is the case for optically thick accretion disks or optically thick accretion tori. While the emission from an optically thin torus is modified by Doppler boosting, Doppler velocity shifting and gravitational time dilation, it is less affected by gravitational lensing and the area projection effect. The transparency of the torus to the emission could complicate the process of using the emission lines to diagnose the dynamical properties an observed torus. First of all, the emission of the higher-order lensed images, which are unobscured, could severely contaminate the emission from the direct image. Secondly, two emission lines can cross-contaminate each other in the spectrum,

and because of the large relativistic shifts one line could cause absorption of another line that originates from a different region within the torus. For an optically thin torus, multiple rays corresponding to different energy shifts can hit the same pixel in the image plane. This is forbidden for ray-tracing in the case of optically thick disks or tori, where each ray originates from a single point on the emission boundary surface of the disk or the torus and each pixel in the disk or torus image corresponds to a uniquely defined relativistic energy shift.

Figure 4.9 (bottom panel) shows that two distinct lines can be blended easily and may be taken as a single emission line with a complex relativistic line profile. These two distinct lines are modelled according to the relative properties of the Fe Kα and Kβ lines, with the Fe Kα line having an energy 10% higher than that of the Fe Kβ line, and the Fe Kβ having an emissivity of 14% of that of the Fe Kα line. Details may be found in Hölzer et al. (1997).

4.4.3 Emission from quasi-opaque pressure-supported tori

The structured torus has density and temperature stratifications (see Figure 4.4) that give rise to variation in the opacity across the torus and opacity gradients along the line-of-sight for different radiative processes. When the density is sufficiently high, the torus becomes opaque to radiation. Quasi-opaque structured tori have more complex emission properties than their optically thin counterparts and the idealised optically thick rotationally supported tori in the previous sections.

The emission properties of these tori are investigated by employing the covariant radiative transfer formulation introduced in Chapter 3.4. In conducting a full radiative transfer calculation for a model-structured torus, two opacity sources are considered, whose specific emissivities in the rest frame are given by

$$j_{0,1}(E_0) = \mathcal{K}\left(\frac{n_{\rm e}}{\rm cm^{-3}}\right)^2\left(\frac{E_0}{\rm keV}\right)^{-1}\left(\frac{\Theta}{\rm keV}\right)^{-1/2}{\rm e}^{-E_0/\Theta}, \qquad (4.37)$$

$$j_{0,2}(E_0) = C\left(\frac{n_{\rm e}}{\rm cm^{-3}}\right)\left(\frac{E_0}{\rm keV}\right)^{-2.5}, \qquad (4.38)$$

where $\Theta = k_{\rm B}T$ is the relativistic temperature and $\mathcal{K} = 8{\times}10^{-46}{\rm erg\,s^{-1}cm^{-3}Hz^{-1}}$.

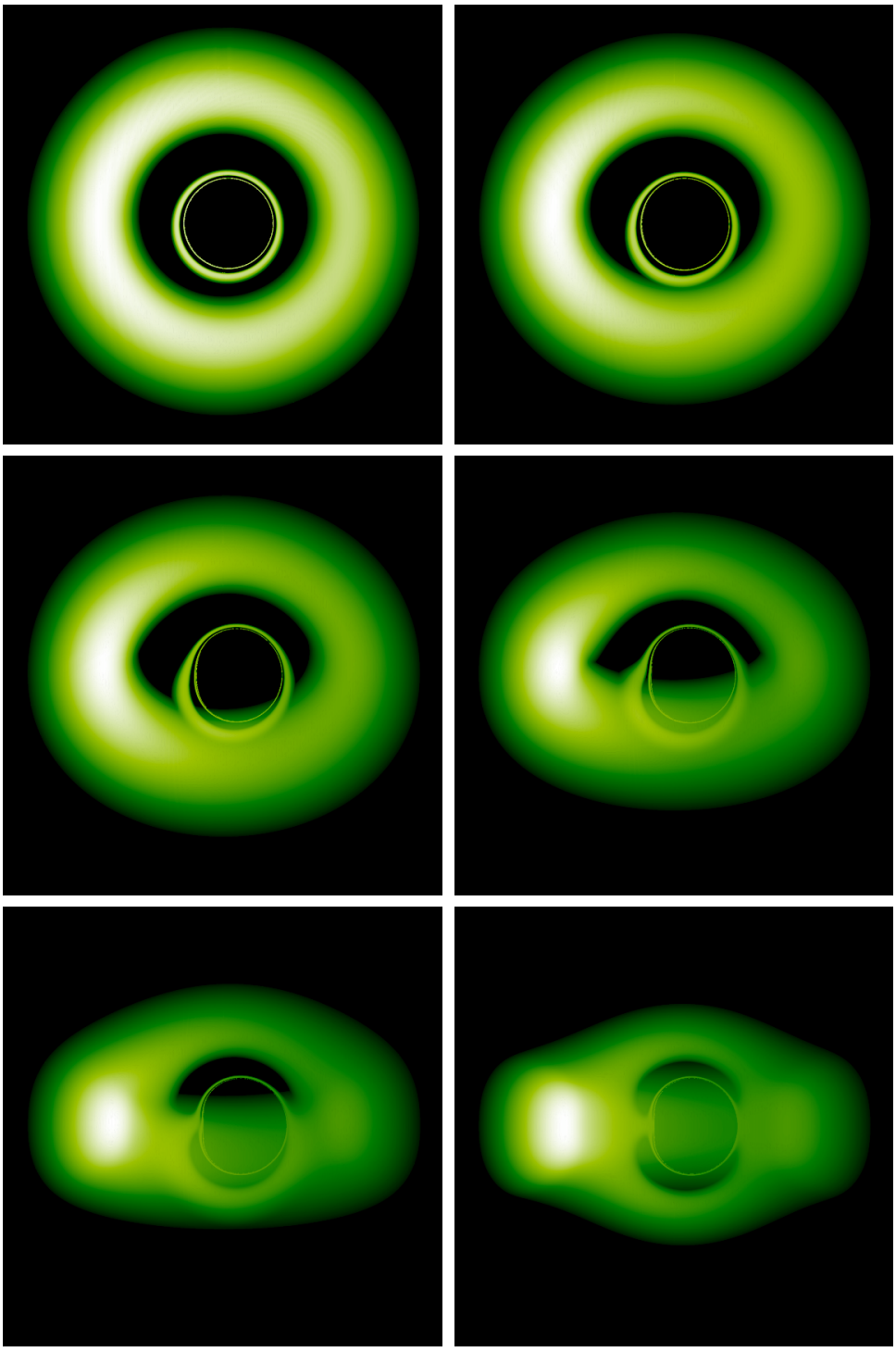

Fig. 4.7: Surface brightness images of optically thin radiative pressure dominated accretion tori, viewed at inclination angles of 15°, 30°, 45°, 60°, 75° and 89° (left to right, top to bottom). The torus parameters are $n = 0.21$, $r_{\rm K} = 12 r_{\rm g}$ and $\beta = 1.235 \times 10^{-5}$. The black-hole spin parameter $a = 0.998$. The brightness of each pixel represents the total intensity integrated over the entire spectrum. The torus brightness is normalised such that the brightness of the brightest pixel in each image is the same.

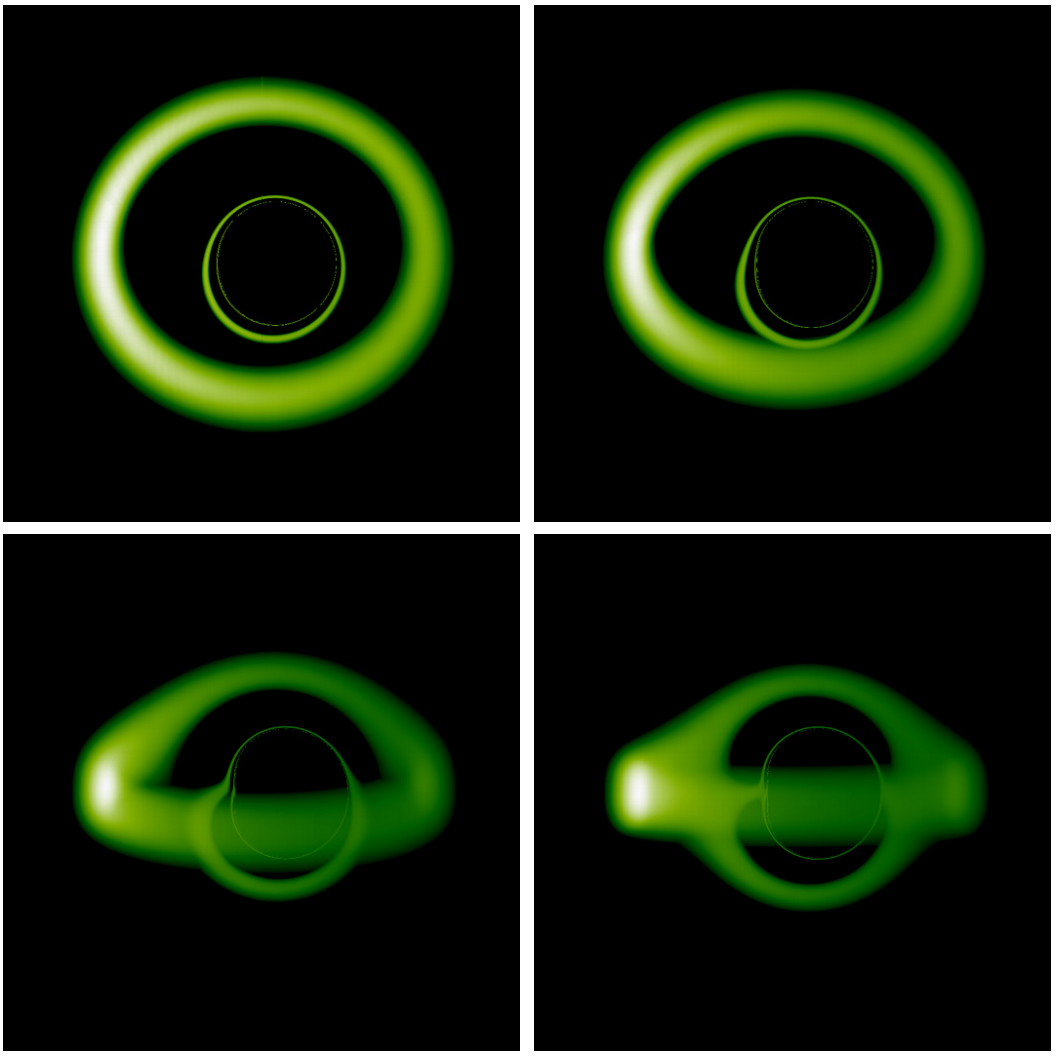

Fig. 4.8: Surface brightness images of optically thin radiation pressure dominated tori viewed at inclination angles of 30°, 45°, 75° and 85° (left to right, top to bottom). The torus parameters are $n = 0.21$, $r_{\rm K} = 12r_{\rm g}$ and $\beta = 5 \times 10^{-5}$. The black-hole spin parameter $a = 0.998$. The brightness of each pixel represents the total intensity integrated over the entire spectrum. The torus brightness is normalised such that the brightness of the brightest pixel in each image is the same.

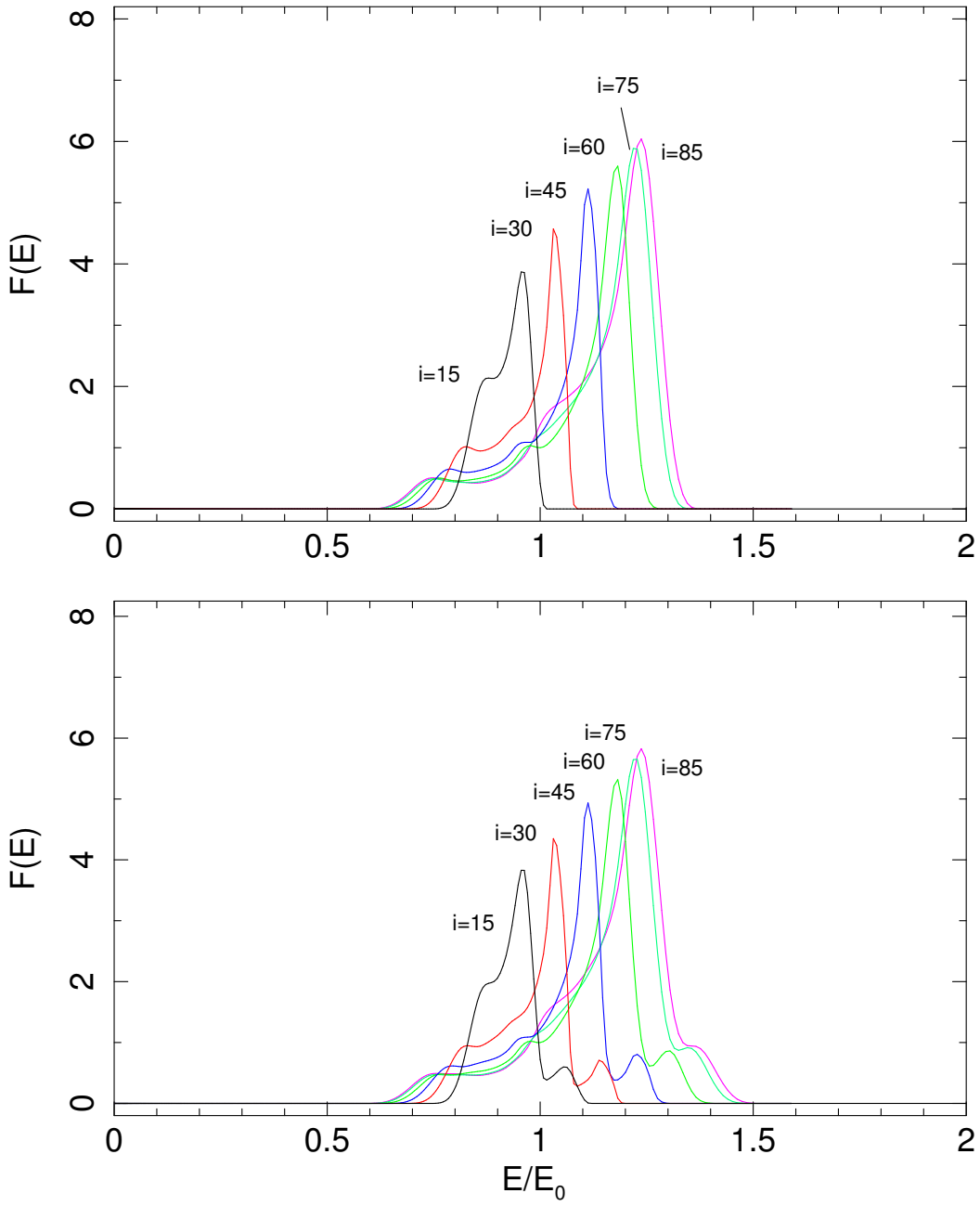

Fig. 4.9: (Top panel) Profiles of an emission line from an optically thin pressure supported structured accretion torus viewed at different inclinations i. The dynamical parameters of the torus are $n = 0.21$ and $r_{\rm K} = 12\ r_{\rm g}$. The black-hole spin parameter $a = 0.998$. The ratio of the gas thermal pressure to the total pressure $\beta = 1.235 \times 10^{-5}$. The radius of the inner boundary $r_{\rm inner} = 8.528 r_g$ and the radius of the outer boundary $r_{\rm outer} = 20.246\ r_{\rm g}$. The line emissivity is proportional to the density ρ. These line profiles are normalised such that the line flux $F(E_0) = 1$ when the torus is viewed at $i = 60°$. (Bottom panel) Profiles of composite profiles from two emission lines. The torus and black hole parameters are the same as those for the lines in the top panel. The line energies are such that one line has an energy 10% higher than the other line and the emissivity of the line with the higher line centre energy is 14% of that of the line with the lower line centre energy (cf. analogous to the relative properties of the Fe Kα and Kβ lines (Hölzer et al. 1997)).

C is a normalisation, dependent on β, chosen such that both $j_{0,1}$ and $j_{0,2}$ are equal at $E_0 = 0.1$ keV, at the torus centre. For $\beta = 1.235 \times 10^{-5}$, $C = 2.162 \times 10^{-45}$ erg s^{-1}cm^{-3} Hz^{-1}, whereas for $\beta = 5 \times 10^{-5}$, $C = 2.681 \times 10^{-45}$ erg s^{-1}cm^{-3} Hz^{-1}. The electron number density is defined as $n_{\rm e} = \rho/\mu m_{\rm H}$. The corresponding specific absorption coefficients are

$$\alpha_{0,1}(E_0) = B_1 \left(\frac{n_{\rm e}}{\rm cm^{-3}}\right)^2 \sigma_T f_1(E_0) \ {\rm cm}^{-1} \ , \tag{4.39}$$

$$\alpha_{0,2}(E_0) = B_2 \left(\frac{n_{\rm e}}{\rm cm^{-3}}\right) \sigma_T f_2(E_0) \ {\rm cm}^{-1} \ , \tag{4.40}$$

where $f_1(E_0)$ and $f_2(E_0)$ are functions of photon energy. The torus is optically thin to the first process, but is partially opaque to the second process, therefore B_1 is set to zero for simplicity. Without loss of generality an energy independent absorption is considered, which implies $f_2(E_0) = 1$. The normalisation constant B_2 is chosen such that $\alpha_{0,2} r_{\rm outer} \sim 1 - 5$ across the torus. Note that the first process has a similar density and temperature dependence to thermal free-free emission. The second process mimics a free-electron scattering-like process that converts photons with different energies indiscriminately into a power-law energy distribution.

Figures 4.10 and 4.11 show intensity images of opaque radiative pressure dominated tori using the aforementioned spectral parameters. These tori differ from the optically thin case in that the emissivity and opacity have changed in the radiative transport calculations, causing significant differences in the intensity images. Towards the outer-edges of the tori there is now obvious limb darkening (dark red). There is now an additional temperature dependence on the emission that is caused by the temperature stratification of the torus, with nearly tangential rays sampling only the cooler surface layers of the torus. However, rays almost perpendicular to the torus surface have a much higher probability of traversing the hotter layers deep beneath the torus surface. Consequently, surfaces viewed face-on by an observer will appear to be much brighter than those viewed at higher inclination angles. For these tori we have assumed $\tau \gg 1$.

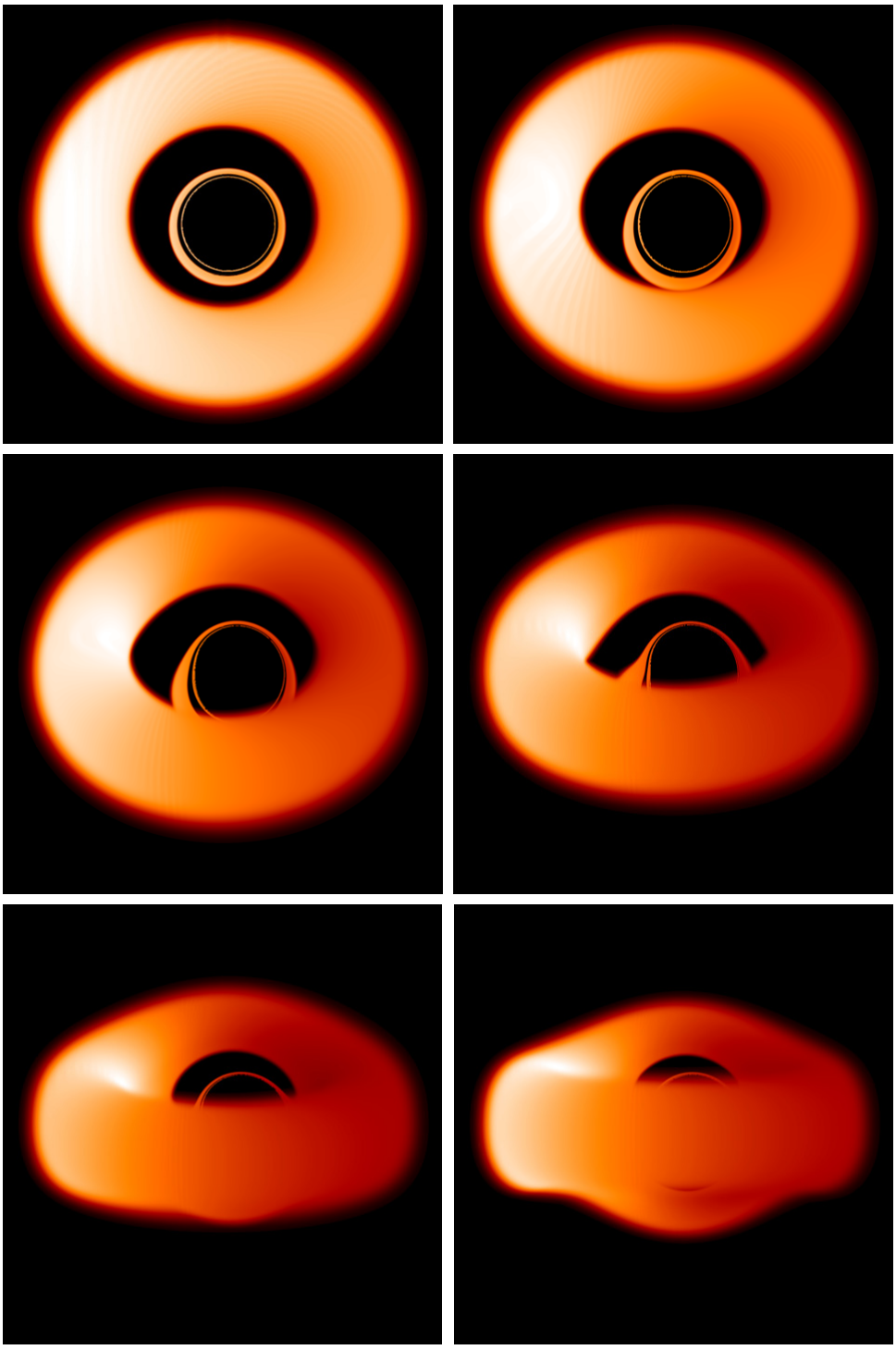

Fig. 4.10: Surface brightness images of opaque radiative pressure dominated accretion tori viewed at inclination angles of 15°, 30°, 45°, 60°, 75° and 85° (left to right, top to bottom). The torus parameters are $n = 0.21$, $r_{\rm K} = 12r_{\rm g}$ and $\beta = 1.235 \times 10^{-5}$. The black-hole spin parameter $a = 0.998$. The emissivity is provided by emission from two spectral lines, and the two opacity sources given in equations (59) and (60). Absorption is provided through the Thomson cross-section in equation (62). The brightness of each pixel represents the total intensity integrated over the entire spectrum. The torus brightness is normalised such that the brightness of the brightest pixel in each image is the same.

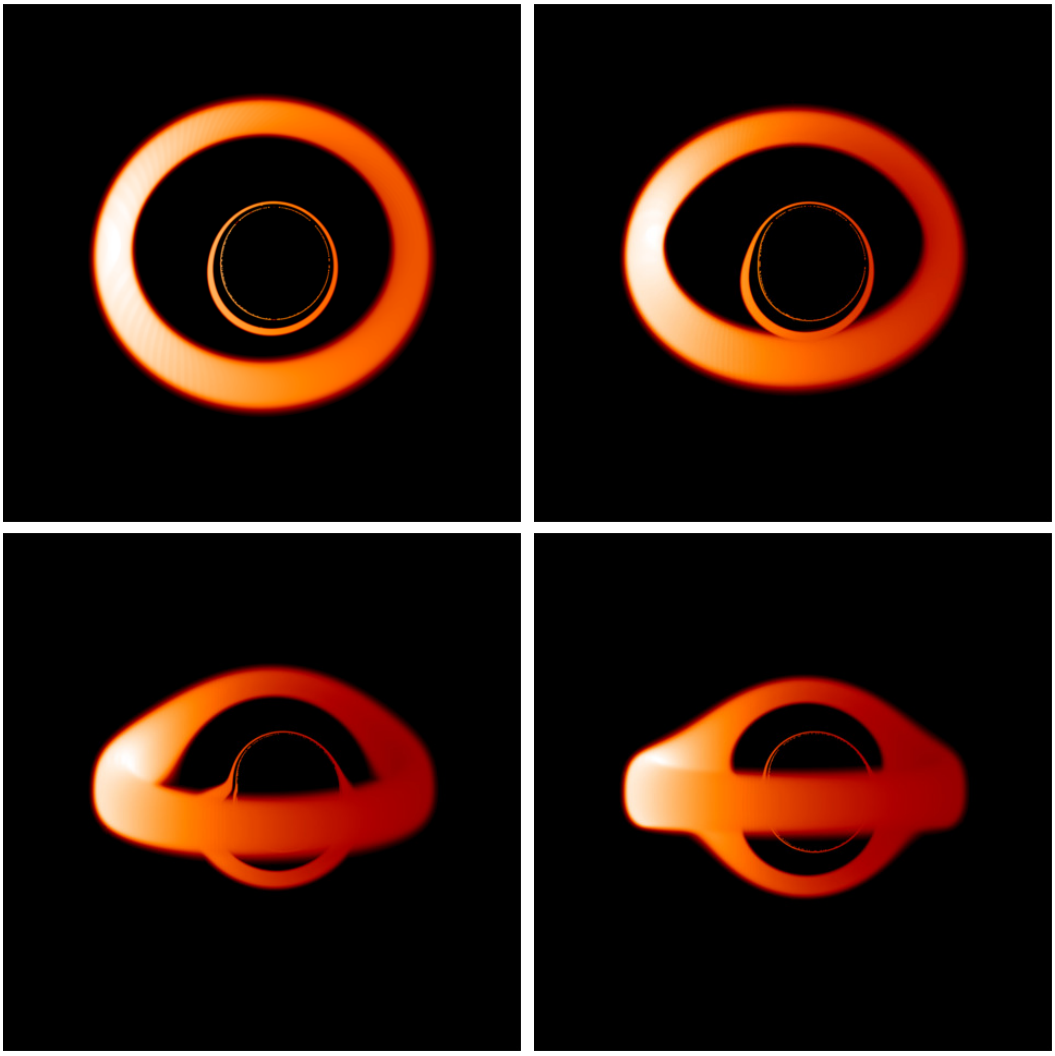

Fig. 4.11: Surface brightness images of quasi-opaque accretion tori around extreme Kerr (a=0.998) black holes, viewed from left to right, top to bottom, at observer inclination angles of 30°, 45°, 75° and 85°. Same parameters as Figure 4.10, but now $\beta = 5 \times 10^{-5}$. Line emission and continuum emission are included. These tori also self-occlude and higher-order emission is greatly suppressed at high inclination angles. The images are normalised such that the brightest pixel in each image is of the same intensity.

4.5 Optically thin vs optically thick emission

For the optically thin tori in Figures 4.7 and 4.8, the low optical depth means that these tori are almost transparent, allowing the entire torus volume to contribute to the emission. The emission from the approaching side of the torus is much stronger due to Doppler boosting, which causes an increase in the projected velocity of the gas along the line of sight towards the observer. The receding limb's projected velocity is decreased and consequently dimmed. At higher viewing inclination angles, geodesics travel through more emissive material than at lower inclinations. Since the fast-moving gas in the inner region of the torus is visible, blueshifting and beaming are very strong and emission from the approaching side of the torus dominates these images. The overall brightness of the optically thin tori at high inclination angles is much greater than at lower inclinations, because at high inclinations geodesics may sample significantly more emissive material in the limbs.

For the rotationally supported opaque tori, emission comes from the surface of the torus only. Since the opaque torus models are optically thick, the front limb of the torus obscures the fast-moving inner regions of these tori at higher inclination angles. The obscuring of the inner regions by the front limb is exhibited in the corresponding torus emission spectra in Figure 4.6, where for $i \geq 45°$ the observed flux decreases rapidly. For the optically thin torus model, emission is observed from the entire volume of the torus, not just the surface. Since the fast-moving gas from the inner-region contributes to the observed emission line profile (Figure 4.9), this gives rise to the more pronounced red and blue wings, which are observed even at high inclination angles. Additionally, for optically thin tori the observed line profiles appear to be roughly monotonically increasing with observer inclination angle. This is in contrast to the line profiles from optically thick accretion disks and tori in Figure 4.6, which decrease in amplitude and appear wedge-shaped for inclination angles beyond 45° (Kojima (1991), Beckwith and Done (2004b), Fuerst and Wu (2004)). As was found in Fuerst (2006), altering the black hole spin does not affect the observed torus images or emission line profiles significantly. The inner edges of the tori presented in this thesis do not extend as close to the

event horizon as thin disks. Consequently, the red wing of their line profiles is not as extended. The shape of these tori, as well as the location of their inner edges, is much more sensitive to the distribution of pressure forces within the tori themselves. If these models are realistic, it would prove difficult to derive the central black hole spin from the observed spectral information.

The emission from quasi-opaque tori is restricted to a thin surface skin layer that is similar to cases of the opaque accretion tori and disks. However, the quasi-opaque torus is distinguishable from the fully opaque accretion tori and accretion disks by the effects arising from gradients in the optical depth. This effect is particularly noticeable near the edges of the quasi-opaque tori, where significant limb darkening occurs (Figure 4.10). These limb effects are a manifestation of the temperature and density stratification within the tori. When looking at the edge of a torus, for a given optical depth, cooler, less dense material is observed than when looking towards the torus centre. Just above the surface of the quasi-opaque torus is an optically thin photosphere. As can be seen in Figures 4.10 and 4.11, photons traversing only the edges of the limb of the torus are weakly attenuated by the cool material and so appear significantly darker than the rest of the torus surface, i.e. only line photons are observed. Hotter neighbouring regions appear to be much brighter because continuum photons are attenuated by the local emission and absorption properties of the medium, as detailed in equations (4.37)–(4.40).

Consider a simple phenomenological model of an emitting and absorbing medium, in local thermodynamic equilibrium (LTE), at a uniform temperature T, with a background source of intensity $\mathcal{I}(0)$. In the absence of scattering, taking $\tau_0 = 0$ at the outer edge of the limb, equation (3.83) implies

$$\mathcal{I}(\tau_\nu) = \mathcal{I}(0)\mathrm{e}^{-\tau_\nu} + \mathcal{B}(T)(1 - \mathrm{e}^{-\tau_\nu}),$$

where $\mathcal{B}(T)$ is the Planck function. For low optical depths, $\tau_\nu \to 0$ and so $\mathcal{I}(\tau_\nu) \to \mathcal{I}(0)$, i.e. the observed intensity of the limb tends towards the background intensity, is independent of temperature, and emission from regions deeper within the torus becomes negligible. In all calculations presented it was assumed that $\mathcal{I}(0) \ll 1$ and so the limb darkening effect is obvious, and

in strong contrast to the rest of the torus image.

4.5.1 Gravitationally induced line resonance in 3D flows

Consider a two-level atomic system. Absorption of a photon causes the excitation of an electron from a lower energy state to a higher energy state. Conversely, a photon is emitted when an electron is de-excited from a higher energy state to a lower energy state. The energy of the absorbed and the emitted photon is the same as the energy difference between the two states. Such a system can be considered an oscillator. Under general conditions, two oscillators with different intrinsic frequencies at different locations would not be resonantly coupled, and two lines from different atomic transitions would not exhibit resonant behaviour without coupling to either other lines or an optical pump.

However, in the vicinity of black holes, where relativistic effects are severe and gravity is extreme, lines from different atomic transitions can couple and exhibit resonance phenomena. As shown in numerous publications (e.g. Cunningham 1975; Fabian et al. 1989; Stella 1990; Fanton et al. 1997; Reynolds et al. 1999; Fabian et al. 2000; Fuerst and Wu 2004), the gravitational frequency shifts of lines from relativistic accretion disks around black holes can be severe. Photons propagating upwards, out of the gravitational well of the black hole, are subject to energy redshifts, whereas photons propagating in the opposite direction, deeper into the gravitational well, are blueshifted.

Consider a radiative transition process occurring in a medium at a radial distance r_1 from the black hole, which consequently emits a photon of energy E_1. The photon propagates outward, and its energy is redshifted. When the photon reaches a distance r_2, its energy becomes E_2, lower than E_1, the energy at its point of emission. Suppose that the photon encounters a bound electron in an atom or ion and is absorbed. The electron is excited to a higher energy state. The electron is then de-excited and returns to its original state, emitting a photon of energy E_2. This photon, however, propagates inward. When it reaches r_1, its energy has been gravitationally blueshifted and is now E_1. Again suppose that this photon encounters another bound electron, is absorbed, and causes the electron to be excited to a higher energy level. This

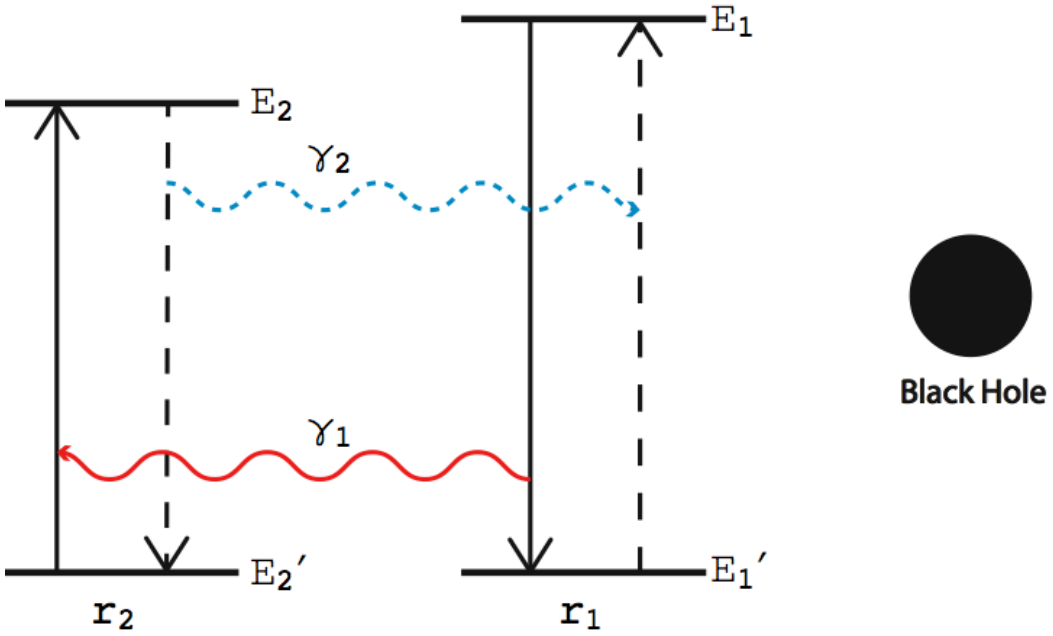

Fig. 4.12: Schematic illustration of the resonance between two lines with E_1 and E_2, emitted at radial distances r_1 and r_2 from a black hole, where $r_2 > r_1$. In the rest frames $E_1 > E_2$.

electron is subsequently de-excited, and again emits a photon of energy E_1. The photon propagates outward once more, is absorbed by a bound electron, and causes another excitation. The later de-excitation of the electron leads to the emission of another photon of energy E_2, and the photon propagates inward again... This process would persist, forming a resonant feedback cycle between the transitions of the two lines with different rest-frame energies (see Figure 4.12).

Such a line resonance occurs easily in 3D flows but not in geometrically thin accretion disks or 2D flows. This can be understood as follows. In the Schwarzschild space time, for a photon with an energy E_1 located at r_1, one can also find a closed surface corresponding to an energy redshift of ΔE, such that the photon energy becomes $E_2 = E_1 - \Delta E$, located at $r_2 > r_1$. The converse also holds, and a photon of energy E_2 located at r_2 always finds a closed surface corresponding to a blueshift of ΔE, such that the photon energy increases to $E_1 = E_2 + \Delta E$. A photon emitted from the vicinity of a black hole must pass through the closed surface with a specific energy shift

before reaching infinity, and in 3D radial flows the entire surface is in principle embedded completely in the flow. A 2D flow cannot completely contain such a surface and hence the photon can escape to infinity, passing through the surface with a specific energy shift at a location not inside the flow. The situation is similar in the Kerr space-time. A detailed quantitative analysis of such a line resonance, and relativistic radiative transfer calculations including these masing effects warrants further investigation.

4.6 Conclusions

Demonstrative numerical general relativistic radiative transfer calculations with a ray-tracing algorithm constructed from the formulation in Chapter 3 were performed for three different models of accretion tori around rotating black holes. Different geometrical aspects, physical structures, emission properties, and optical depth variations of these tori were considered. It was demonstrated that radiative transfer calculations based on the formulation are able to deal with the complexity in the various combinations and convolution of relativistic, geometrical, physical and optical effects. These calculations clearly showed the significant role that structures and optical depth, and their gradients, together with geometrical and relativistic factors, play in shaping the emission properties of these relativistic flows in the vicinity of rotating black holes. The calculations also showed the presence of limb effects in objects with finite optical depths.

It was also found that gravitationally induced line resonance can occur in accretion onto a compact object. This phenomenon is not present in planar objects, such as geometrically thin accretion disks, where the radiation can escape from the disk surface to free space without additional absorption or re-emission.

Chapter 5

General Relativistic Compton Scattering

A covariant scattering kernel is a core component in any self-consistent general relativistic radiative transfer formulation in scattering media. An explicit closed-form expression for a covariant Compton scattering kernel with a good dynamical energy range is as of yet unavailable. Such an expression is essential to obtain numerical solutions to the general relativistic radiative transfer equations in complicated astrophysical settings where strong scattering effects are coupled with highly relativistic flows and steep gravitational gradients. In deriving such an expression, detailed calculations must be performed in a systematic and efficient manner, owing to the complexity of the underlying mathematics and physics.

The derivation of the covariant scattering kernel for Compton scattering in a general relativistic setting is demonstrated explicitly in this Chapter. First the covariant radiative transfer equation in the presence of scattering is introduced and methods for its solution are discussed. The covariant Klein-Nishina cross-section for relativistic Compton scattering is derived. Several methods for computing angular moments of this cross-section are introduced and compared. An analytic result for moments of the Klein-Nishina cross-section is then obtained and from this angular moments of the Compton scattering Kernel are calculated.

5.1 Compton Scattering in Astrophysics

Compton scattering of photons by relativistic electrons is an efficient process in the production of high-energy cosmic X-rays and γ-rays. Compton scattering plays an important role in determining spectral formation and in regulating energy transport in a variety of astrophysical systems, e.g. accretion disks of black hole systems (Sunyaev and Titarchuk 1985; Dermer and Liang 1989; Haardt 1993; Poutanen and Vilhu 1993; Titarchuk 1994a; Hua and Titarchuk 1995; Stern et al. 1995), relativistic AGN jets (Begelman and Sikora 1987; McNamara et al. 2009; Krawczynski 2012), neutron-star X-ray bursts (Titarchuk 1988; Madej 1991; Titarchuk 1994b; Madej et al. 2004), and in some accreting white dwarfs (Kylafis and Lamb 1982; Matt 2004; McNamara et al. 2008b,a; Titarchuk et al. 2009). Compton scattering of cosmic microwave background (CMB) photons by hot gases trapped inside the potential wells of large gravitating systems, such as galaxy clusters, also leads to Sunyaev-Zel'dovich effects (Sunyaev and Zel'dovich 1980; Rephaeli 1995; Dolgov et al. 2001; Colafrancesco et al. 2003), through which various aspects of cosmology and the evolution of large-scale structures in the Universe may be investigated.

In astrophysical plasmas, Compton scattering is often investigated using Monte-Carlo simulations (e.g. Pozdnyakov et al. 1983; Hua and Titarchuk 1995). The Monte-Carlo approach is an approximation scheme to proper radiative transfer calculations, where the radiative transfer equation is derived from the laws of conservation (see Rybicki and Lightman 1979; Chandrasekhar 1960; Peraiah 2001). It has the advantage of being able to handle complicated system geometries, as well as the flexibility to incorporate relevant additional physics, such as absorption and pair production, into the system. However, it is not straightforward to implement the usual Monte-Carlo method in certain extreme astrophysical environments, such as systems with steep density gradients, fractal-like inhomogeneities, or ultra-relativistic flows near the event-horizon of a black hole. In the vicinity of a black hole, relativistic and space-time curvature effects are important, and radiative transfer in these systems requires a covariant formulation (e.g. Lindquist 1966; Baschek et al. 1997; Fuerst and Wu 2004; Younsi et al. 2012).

In the absence of scattering, the covariant radiative transfer equation can be solved along the null geodesic (see Viergutz 1993; Reynolds et al. 1999; Dexter and Agol 2009) using a ray-tracing technique (e.g. Fuerst and Wu 2004; Vincent et al. 2011). However, in the presence of scattering, the covariant radiative transfer equation is much more complicated. The radiative transfer equation becomes an integro-differential equation which is far from trivial to solve. The scattering kernel is a key ingredient in the radiative transfer formulation, describing how photons interact with electrons. The moment expansion (Thorne 1981; Turolla and Nobili 1988; Wu et al. 2008; Shibata et al. 2011) of this kernel is essential in deriving a practical (numerical) scheme to solve the integro-differential radiative transfer equation (see Fuerst 2006; Farris et al. 2008; Zanotti et al. 2011).

5.2 Radiative Transfer With Scattering

In flat space the radiative transfer equation in a medium reads

$$\left(\frac{1}{c}\frac{\partial}{\partial t}+\hat{\mathbf{\Omega}}\cdot\nabla\right)I_\nu(\hat{\mathbf{\Omega}})=j_\nu(\hat{\mathbf{\Omega}})-\kappa_\nu I_\nu(\hat{\mathbf{\Omega}})+\iint \mathrm{d}\Omega'\,\mathrm{d}\nu'\,\sigma(\nu,\hat{\mathbf{\Omega}};\nu',\hat{\mathbf{\Omega}}')I_{\nu'}(\hat{\mathbf{\Omega}}')\,, \tag{5.1}$$

(see Mihalas and Mihalas 1984; Peraiah 2001) where $I_\nu(\hat{\mathbf{\Omega}})$ is the intensity of the radiation at a frequency ν propagating in the $\hat{\mathbf{\Omega}}$-direction, j_ν and κ_ν are the emission and absorption coefficient respectively, and $\sigma(\nu,\hat{\mathbf{\Omega}};\nu',\hat{\mathbf{\Omega}}')$ is the scattering kernel which determines the amount of radiation intensity at a frequency ν' in a direction $\hat{\mathbf{\Omega}}'$ being scattered into the intensity $I_{\nu'}(\hat{\mathbf{\Omega}}')$. For instance, in the photon-electron scattering process, the scattering kernel is determined by the momentum distribution of the electrons and the differential scattering cross-section, the Klein-Nishina (Klein and Nishina 1929) differential cross-section

$$\begin{aligned}\left(\frac{\mathrm{d}\sigma}{\mathrm{d}\Omega}\right)_{\mathrm{KN}} &= \left(\frac{e^2}{m_\mathrm{e}c^2}\right)^2\left(\frac{k_f}{k_i}\right)^2 f(k_f,\hat{\boldsymbol{\epsilon}}_f;k_i,\hat{\boldsymbol{\epsilon}}_i)\\ &= \frac{3\sigma_\mathrm{T}}{8\pi}\left(\frac{k_f}{k_i}\right)^2 f(k_f,\hat{\boldsymbol{\epsilon}}_f;k_i,\hat{\boldsymbol{\epsilon}}_i)\,,\end{aligned} \tag{5.2}$$

where e is the electron charge, m_e is the electron mass, σ_T is the Thomson cross-section, k_i and k_f are the wave numbers of the photon before and after scattering respectively, and $\hat{\boldsymbol{\epsilon}}_i$ and $\hat{\boldsymbol{\epsilon}}_f$ are the corresponding polarisation

vectors of the photon. The function $f(k_f, \hat{\boldsymbol{\epsilon}}_f; k_i, \hat{\boldsymbol{\epsilon}}_i)$ is given by

$$f(k_f, \hat{\boldsymbol{\epsilon}}_f; k_i, \hat{\boldsymbol{\epsilon}}_i) = \left|\hat{\boldsymbol{\epsilon}}_f^* \cdot \hat{\boldsymbol{\epsilon}}_i\right|^2 + \frac{(k_f - k_i)^2}{4\ k_f k_i}\left[1 + \left(\hat{\boldsymbol{\epsilon}}_f^* \times \hat{\boldsymbol{\epsilon}}_f\right) \cdot \left(\hat{\boldsymbol{\epsilon}}_i \times \hat{\boldsymbol{\epsilon}}_i^*\right)\right] \ , \qquad (5.3)$$

(see Jackson 1975).

The ray is specified by choosing an initial position $x^\alpha(\lambda_0)$ and an initial direction of propagation $k^\alpha(\lambda_0)$. The total derivative of the invariant intensity along the world line of the ray is therefore

$$\begin{aligned} \frac{\mathrm{d}\mathcal{I}}{\mathrm{d}\lambda} &= \frac{\partial \mathcal{I}}{\partial x^\alpha}\frac{\mathrm{d}x^\alpha}{\mathrm{d}\lambda} + \frac{\partial \mathcal{I}}{\partial k^\alpha}\frac{\mathrm{d}k^\alpha}{\mathrm{d}\lambda} \\ &= k^\alpha \frac{\partial \mathcal{I}}{\partial x^\alpha} - \Gamma^\alpha{}_{\beta\gamma} k^\beta k^\gamma \frac{\partial \mathcal{I}}{\partial k^\alpha} \ , \end{aligned} \qquad (5.4)$$

where the second term on the second line of equation (5.4) follows from the geodesic equation of motion. Consequently, in the absence of scattering, the covariant form of the radiative transfer equation may be written as

$$\begin{aligned} \frac{\mathrm{d}\mathcal{I}}{\mathrm{d}\lambda} &= k_\alpha \frac{\partial \mathcal{I}}{\partial x^\alpha} - \Gamma^\alpha{}_{\beta\gamma} k^\beta k^\gamma \frac{\partial \mathcal{I}}{\partial k^\alpha} \\ &= -k^\alpha u_\alpha\big|_\lambda \left(\ \eta_0 - \chi_0 \mathcal{I}\ \right) \ , \end{aligned} \qquad (5.5)$$

which is obtained from equation (3.80) through substitution of the invariant absorption and emission coefficients derived in Chapter 3.4 ($\chi = \nu\ \alpha_\nu$, $\eta = j_\nu/\nu^2$), where $\mathcal{I}$ is the invariant intensity of the radiation, x^α is a position 4-vector, η_0 and χ_0 are the invariant emission and absorption coefficients respectively (evaluated in a local inertial frame), λ is the affine parameter, k^α is the propagation (wave number) 4-vector of the radiation, and u^α is the 4-velocity of the medium interacting with the radiation. Equation (5.5) is similar in form to equation (5.1) without the scattering term. The term $k^\alpha u_\alpha|_\lambda$ is a correction factor for the aberration and energy shift in the transformation between any two reference frames. For covariant transfer of radiation in the presence of scattering, the radiative transfer equation is of the form (see Jackson 1975)

$$\begin{aligned} \frac{\mathrm{d}\mathcal{I}(x^\beta, k^\beta)}{\mathrm{d}\lambda} = \ & -k^\alpha u_\alpha\big|_\lambda \Big[\eta_0(x^\beta, k^\beta) - \chi_0(x^\beta, k^\beta)\mathcal{I}(x^\beta, k^\beta) \\ & + \int \mathrm{d}^4 k'^\beta\ \sigma(x^\beta; k^\beta, k'^\beta)\mathcal{I}(x^\beta, k'^\beta)\Big] \ , \end{aligned} \qquad (5.6)$$

analogous to equation (5.1). Several methods have been proposed to solve the above equation or to obtain an approximate solution. For instance, one could transform the integro-differential radiative transfer equation into a set of differential equations using a moment expansion (Thorne 1980, 1981; Fuerst 2006; Wu et al. 2008; Shibata et al. 2011). Nevertheless, one needs to specify the properties of the medium spanning the space-time. In addition to the global flow dynamics, one also needs to know how the radiation interacts with the medium (via the emission coefficient, absorption coefficient and the scattering kernel), at least in the local inertial frame. The invariant emission and absorption coefficients can be easily derived from the conventional emission and absorption coefficients (see Fuerst and Wu 2004, 2007). The derivation of the scattering kernel is more complicated. Some attempts have been made (e.g. Shestakov et al. 1988), but only numerical results were obtained due to the complexity of the underlying mathematics. To date a closed-form expression for the corresponding scattering kernel is not available. The lack of a closed-form scattering kernel hinders the development of fast and accurate numerical algorithms to solve the covariant radiative transfer equation, which itself can be numerically intensive.

5.3 Covariant Compton Scattering

Energy-momentum conservation implies that

$$k^\alpha + p^\alpha = k'^\alpha + p'^\alpha \ , \tag{5.7}$$

in a photon-electron scattering process. Here unprimed and primed variables denote, respectively, variables evaluated before and after scattering. The 4-momentum of a photon k^α and the 4-momentum of an electron p^α satisfy $k^\alpha k_\alpha = k'^\alpha k'_\alpha = 0$ and $p^\alpha p_\alpha = p'^\alpha p'_\alpha = -m_\mathrm{e}^2$, respectively. Energy-momentum conservation also leads to the invariance relation

$$k^\alpha p_\alpha = k'^\alpha p'_\alpha \ , \tag{5.8}$$

and a covariant generalised energy-shift formula for the scattered photon,

$$k'^\alpha (k_\alpha + p_\alpha) = k^\alpha p_\alpha \ . \tag{5.9}$$

As the scattering process occurs in a relativistic fluid, the derivation of the scattering opacity due to ensembles of photons and electrons requires expressing the scattering variables of the particles in the local reference rest-frame (co-moving with the fluid 4-velocity), as well as specifying the transformation between the fluid rest-frame and the observer's frame. The fluid 4-velocity is denoted by u^α. The transverse component of the electron's 4-velocity, orthogonal to u^α in the fluid rest frame, is denoted by v^α. The directional unit 4-vector of the photon in the fluid rest frame may be specified as n^α, which is given by

$$n^\alpha = \frac{P^{\alpha\beta}k_\beta}{||P^{\alpha\beta}k_\beta||} \ . \tag{5.10}$$

Defining the variable

$$\begin{aligned} \gamma &= \frac{h\nu}{m_\mathrm{e}c^2} \\ &\equiv -\frac{k^\alpha u_\alpha}{m_\mathrm{e}} \ , \end{aligned} \tag{5.11}$$

which is the incoming photon energy (in units of the electron rest energy $m_\mathrm{e}c^2$), n^α may be expressed as

$$n^\alpha = \frac{k^\alpha}{m_\mathrm{e}\gamma} - u^\alpha \ . \tag{5.12}$$

Hence, it follows the photon 4-momentum may be expressed as

$$k^\alpha = m_\mathrm{e}\gamma(n^\alpha + u^\alpha) \ . \tag{5.13}$$

Similarly, for the electrons,

$$\lambda \equiv -\frac{p^\alpha u_\alpha}{m_\mathrm{e}} \ . \tag{5.14}$$

Clearly $\lambda = 1/\sqrt{1-v^2}$, which is simply the Lorentz factor of the electron and $\hat{v}^\alpha$ in the fluid frame rest frame is therefore

$$\hat{v}^\alpha = \frac{P^{\alpha\beta}p_\beta}{||P^{\alpha\beta}p_\beta||} = \frac{p^\alpha - m_\mathrm{e}\lambda u^\alpha}{m_\mathrm{e}\lambda v} \ , \tag{5.15}$$

from whence it follows that

$$v^\alpha = \frac{p^\alpha}{m_\mathrm{e}\lambda} - u^\alpha \ , \tag{5.16}$$

and

$$p^\alpha = m_\mathrm{e}\lambda(v^\alpha + u^\alpha) \ . \tag{5.17}$$

Note that the photon 4-momentum after the scattering event is

$$k'^{\alpha} = m_{\mathrm{e}}\gamma'(n'^{\alpha} + u^{\alpha}) \ . \tag{5.18}$$

Thus, the following expressions are obtained:

$$k^{\alpha}k'_{\alpha} = m_{\mathrm{e}}^2\gamma\gamma'(\zeta - 1) \ , \tag{5.19}$$

$$p^{\alpha}k_{\alpha} = m_{\mathrm{e}}^2\lambda\gamma(v^{\alpha}n_{\alpha} - 1) \ , \tag{5.20}$$

$$p^{\alpha}k'_{\alpha} = m_{\mathrm{e}}^2\lambda\gamma'(v^{\alpha}n'_{\alpha} - 1) \ , \tag{5.21}$$

where $\zeta = n^{\alpha}n'_{\alpha}$ is the direction cosine of the angle between the incident and scattered photon. Hence energy-momentum conservation, equation (5.9), may be expressed as:

$$m_{\mathrm{e}}^2\gamma\gamma'\left[\zeta - 1 + \lambda\left(\frac{1 - v^{\alpha}n_{\alpha}}{\gamma'} - \frac{1 - v^{\alpha}n'_{\alpha}}{\gamma}\right)\right] = 0 \ . \tag{5.22}$$

The cross-section for scattering of a photon by an electron is given in Kershaw et al. (1986) as:

$$\begin{aligned}\sigma(\gamma \to \gamma', \hat{\mathbf{\Omega}} \to \hat{\mathbf{\Omega}}', \mathbf{v}) &= \frac{3\sigma_{\mathrm{T}}}{16\pi\gamma\nu\lambda}\left[1 + \left(1 - \frac{1-\zeta}{\lambda^2 DD'}\right)^2 + \frac{(1-\zeta)^2\gamma\gamma'}{\lambda^2 DD'}\right] \\ &\quad \times \delta\left[\zeta - 1 + \lambda\left(\frac{D}{\gamma'} - \frac{D'}{\gamma}\right)\right] \ ,\end{aligned} \tag{5.23}$$

where $D \equiv 1 - \hat{\mathbf{\Omega}}\cdot\mathbf{v}/c = 1 - v^{\alpha}n_{\alpha}$, and similarly for D'. Using equations (5.19)–(5.21), the photon-electron scattering cross-section, equation (5.23), may be expressed in the following covariant form:

$$\begin{aligned}\sigma(\gamma \to \gamma', n^{\alpha} \to n'^{\alpha}, v^{\alpha}) &= \frac{3\sigma_{\mathrm{T}}}{16\pi\gamma\nu\lambda}\left[1 + \left(1 + \frac{m_{\mathrm{e}}^2\mathcal{T}}{k^{\alpha}k'_{\alpha}}\right)^2 + \mathcal{T}\right] \\ &\quad \times \delta\left(\frac{\mathcal{P}}{m_{\mathrm{e}}^2\gamma\gamma'}\right) \ ,\end{aligned} \tag{5.24}$$

where δ denotes the Dirac delta function, and $\mathcal{T}$, $\mathcal{P}$ are defined respectively as

$$\mathcal{T} = \frac{(k^{\alpha}k'_{\alpha})^2}{(p^{\alpha}k_{\alpha})(p^{\beta}p'_{\beta})} \ , \tag{5.25}$$

$$\mathcal{P} = k^{\alpha}k'_{\alpha} + p^{\alpha}k'_{\alpha} - p^{\alpha}k_{\alpha} \ . \tag{5.26}$$

It follows that $\mathcal{P}$ represents energy and momentum conservation of the scattering process. The delta function enforces the conservation of energy and

momentum in the scattering process, by weighting the scattering cross-section such that it is zero if energy and momentum are not conserved. Integrating this cross-section, equation (5.24), over a relativistic electron distribution function yields the kernel for Compton scattering.

5.4 Electron Distribution Function

A distribution function for relativistic electrons, $f(\lambda)$, must be specified in order to calculate the Compton scattering kernel. The energy of an electron is $E = \lambda\, m_{\rm e} c^2$, and its linear momentum is given by $p = \lambda\, m_{\rm e} v$, from which it follows that

$$\frac{{\rm d}p}{{\rm d}v} = m_{\rm e}\frac{\rm d}{{\rm d}v}(\lambda v) = m_{\rm e}\lambda^3 \ . \tag{5.27}$$

As an example, consider an ensemble of relativistic electrons with isotropic momenta for which the distribution function is given by the pseudo-Maxwellian

$$\Psi(\mathbf{p}) = {\rm C}\, e^{-E(\mathbf{p})/k_{\rm B}T_{\rm e}} \ , \tag{5.28}$$

where E is the electron energy, $T_{\rm e}$ the electron temperature, $k_{\rm B}$ the Boltzmann constant and C is a normalisation constant. Note that the distributions of electrons in momentum space and in velocity space are related via

$$f(\mathbf{v})v^2{\rm d}v = \Psi(\mathbf{p})p^2{\rm d}p \ , \tag{5.29}$$

which may be expressed as

$$f(\mathbf{v}) = \frac{p^2}{v^2}\frac{{\rm d}p}{{\rm d}v}\Psi(\mathbf{p}) \ . \tag{5.30}$$

It immediately follows that

$$f(\mathbf{v}) = {\rm C}'\lambda(v)^5 e^{-\lambda(v)/\tau} \ , \tag{5.31}$$

where ${\rm C}' = m_{\rm e}^3{\rm C}$ is a constant and $\tau = k_{\rm B}T_{\rm e}/m_{\rm e}$. The normalisation of the distribution function $f(\mathbf{v})$ to unity, i.e.

$$\int {\rm d}\mathbf{v} f(\mathbf{v}) = 4\pi \int_0^1 {\rm d}v\, v^2 f(\mathbf{v}) = 1 \ , \tag{5.32}$$

yields the familiar relativistic Maxwellian form,

$$f(\lambda) = \frac{\lambda^5 e^{-\lambda/\tau}}{4\pi\tau K_2(1/\tau)} \ , \tag{5.33}$$

where K_2 denotes the modified Bessel function of the second kind of order 2.

5.5 Compton Scattering Kernel

The Compton scattering kernel is essential in solving the radiative transfer equation. It is defined by the convolution of the photon-electron scattering cross-section with the electron velocity distribution, i.e.

$$\sigma_{\rm s}(\gamma \to \gamma', \zeta, \tau) = \frac{3\rho\sigma_{\rm T}}{16\pi\gamma^2} \int {\rm d}\mathbf{v}\ \frac{f(\lambda)}{\lambda} \left[1 + \left(1 + \frac{m_{\rm e}^2 \mathcal{T}}{k^\alpha k'_\alpha}\right)^2 + \mathcal{T}\right]\ \delta\left(\frac{\mathcal{P}}{m_{\rm e}^2\gamma\gamma'}\right)\ , \tag{5.34}$$

where ρ is the electron density. To evaluate the above integral, first consider the argument of the delta function

$$y \equiv \frac{\mathcal{P}}{m_{\rm e}^2\gamma\gamma'}\ . \tag{5.35}$$

Rewriting (5.35) in terms of a linear combination of a scalar and an inner product of two unit vectors is a succinct way of expressing the energy-momentum conservation. More importantly, aside from the more compact notation, the inner product of two unit vectors (the magnitude of which never exceeds unity) provides constraints on the electron energy. This makes the subsequent integrals easier to solve, and is the most natural way of proceeding with the problem. Substituting equations (5.19)–(5.21) into (5.35) yields

$$\begin{aligned} y &= \left[\zeta - 1 + \lambda\left(\gamma'^{-1} - \gamma^{-1}\right) + \frac{\lambda}{\gamma\gamma'} v^\alpha \left(\gamma' n'_\alpha - \gamma n_\alpha\right)\right]\ , \\ &= \Gamma + \hat{v}^\alpha w_\alpha\ , \end{aligned} \tag{5.36}$$

where

$$\Gamma = \zeta - 1 + \lambda\left(\gamma'^{-1} - \gamma^{-1}\right)\ , \tag{5.37}$$

$$w_\alpha = \frac{\lambda v}{\gamma\gamma'}\left(\gamma' n'_\alpha - \gamma n_\alpha\right)\ , \tag{5.38}$$

and hence (5.36) is split into a scalar and vector component. It immediately follows that y may be rewritten as

$$y = w\left(\frac{\Gamma}{w} + \hat{v}^\alpha \hat{w}_\alpha\right)\ , \tag{5.39}$$

where

$$\hat{w}_\alpha = \frac{\gamma' n'_\alpha - \gamma n_\alpha}{q}\ , \tag{5.40}$$

$$w = \frac{\lambda v}{\gamma\gamma'} q\ , \tag{5.41}$$

and q is defined as

$$q = \sqrt{\gamma^2 + \gamma'^2 - 2\gamma\gamma'\zeta} \ . \tag{5.42}$$

Therefore $\hat{w}_\alpha$ represents a unit vector along the direction of photon momentum transfer and $\hat{v}^\alpha \hat{w}_\alpha$ is simply the projection of the electron velocity onto this preferred direction. Under integration, the delta function can be rewritten as $\delta\left(\Gamma/w + \hat{v}^\alpha \hat{w}_\alpha\right)/w$, and the energy-momentum conservation may be rewritten as

$$\hat{v}^\alpha \hat{w}_\alpha = -\frac{\Gamma}{w} \ . \tag{5.43}$$

From this it immediately follows $|| - \Gamma/w|| \leq 1$ and therefore

$$(1-\zeta) + \lambda(\gamma^{-1} - \gamma'^{-1}) \leq \frac{\lambda v q}{\gamma\gamma'} \ , \tag{5.44}$$

which is akin to solving the quadratic equation $\mathrm{a}_2\lambda^2 + \mathrm{a}_1\lambda - \mathrm{a}_0 = 0$, with the coefficients a_2, a_1 and a_0 given by:

$$\mathrm{a}_2 = 2\gamma\gamma'(1-\zeta) \ , \tag{5.45}$$

$$\mathrm{a}_1 = (\gamma' - \gamma)\mathrm{a}_2 \ , \tag{5.46}$$

$$\mathrm{a}_0 = q^2 + \frac{\mathrm{a}_2^2}{4} \ . \tag{5.47}$$

Taking the positive solution to (5.44) yields, upon employing the identity $\mathrm{a}_2 = q^2 - (\gamma' - \gamma)^2$,

$$\lambda_+ = \left(\frac{\gamma' - \gamma}{2}\right) + \frac{q}{2}\sqrt{1 + \frac{2}{\gamma\gamma'(1-\zeta)}} \ , \tag{5.48}$$

which is essentially the minimum electron energy in the Compton scattering process. The form of λ as a function of ζ is crucial in later calculations involving integrations over λ and ζ. The integral in equation (5.34) may now be rewritten (see Kershaw et al. 1986) as

$$\int \mathrm{d}\mathbf{v} = \int_0^1 \mathrm{d}v \ v^2 \int_{-1}^1 \mathrm{d}(\hat{v}^\alpha \hat{w}_\alpha) \int_0^{2\pi} \mathrm{d}\phi \ . \tag{5.49}$$

Hence it follows that the delta function fixes this preferred direction naturally (Prasad et al. 1986; Beason et al. 1991), and this is clearly the most straightforward approach. Note, as in Kershaw et al. (1986), the angular addition formula:

$$\hat{v}^\alpha \hat{m}_\alpha = (\hat{n}^\alpha \hat{m}_\alpha)(\hat{v}^\alpha \hat{n}_\alpha) + \sqrt{1 - (\hat{n}^\alpha \hat{m}_\alpha)^2}\sqrt{1 - (\hat{v}^\alpha \hat{n}_\alpha)^2}\cos\phi, \tag{5.50}$$

where $\hat{m}_\alpha$ is equal to $\hat{w}_\alpha$ or $\hat{w}'_\alpha$, the unit vector of the photon velocity before or after collision, respectively. It is easily verified that

$$n^\alpha \hat{w}_\alpha = \frac{\gamma'\zeta - \gamma}{q} , \tag{5.51}$$

$$n'^\alpha \hat{w}_\alpha = \frac{\gamma' - \gamma\zeta}{q} , \tag{5.52}$$

$$\hat{v}^\alpha \hat{w}_\alpha = -\frac{\gamma\gamma'\Gamma}{q\lambda v} . \tag{5.53}$$

As such, in equation (5.49) only the ϕ integral must be evaluated explicitly. The square-bracketed term in the kernel may be rewritten (e.g. Kershaw et al. 1986) as

$$\left[1 + \left(1 + \frac{m_e^2 \mathcal{T}}{k^\alpha k'_\alpha}\right)^2 + \mathcal{T}\right] = 2 + (\lambda\gamma' D')^{-2} + (\lambda\gamma D)^{-2}\left[(\lambda\gamma' D')^{-1} - (\lambda\gamma D)^{-1}\right] \times \left[\gamma\gamma'(1-\zeta) - 2 - \frac{2}{\gamma\gamma'(1-\zeta)}\right] , \tag{5.54}$$

which must be integrated term-by-term over ϕ. The integrals to evaluate have the forms:

$$I_1 = \int_0^{2\pi} \frac{\mathrm{d}\phi}{\alpha + \beta\cos\phi} , \tag{5.55}$$

$$I_2 = \int_0^{2\pi} \frac{\mathrm{d}\phi}{(\alpha + \beta\cos\phi)^2} , \tag{5.56}$$

where

$$\alpha = 1 - v(\hat{w}^\alpha n_\alpha)(\hat{w}^\alpha \hat{v}_\alpha) , \tag{5.57}$$

$$\beta = -v\sqrt{1 - (\hat{w}^\alpha n_\alpha)^2}\sqrt{1 - (\hat{w}^\alpha \hat{v}_\alpha)^2} . \tag{5.58}$$

Clearly, the two integrals are related, via $I_2 = -\mathrm{d}I_1/\mathrm{d}\alpha$ and therefore only I_1 need be evaluated, yielding

$$I_1 = \frac{2\pi}{(\alpha^2 - \beta^2)^{1/2}} , \tag{5.59}$$

$$I_2 = \frac{2\pi\alpha}{(\alpha^2 - \beta^2)^{3/2}} , \tag{5.60}$$

where the coefficients $\alpha(x)$, β and $\alpha^2 - \beta^2$ are given by

$$\alpha(x) = \frac{\gamma'}{\lambda q^2}\left[x\left(\gamma^{-1}+\gamma'^{-1}\right)-(1+\zeta)\,\gamma\gamma'\right] , \tag{5.61}$$

$$\alpha'(x) = \frac{\gamma}{\gamma'}\alpha(x) , \tag{5.62}$$

$$\beta = \frac{\gamma'\omega(\zeta-1)}{\lambda q^2}\sqrt{\mathrm{a}_2\lambda^2+\mathrm{a}_1\lambda-\mathrm{a}_0} , \tag{5.63}$$

$$\beta' = \frac{\gamma}{\gamma'}\,\beta , \tag{5.64}$$

$$\alpha(x)^2-\beta^2 = \frac{\gamma'^2\,(1-\zeta)^2\,(x^2+\omega^2)}{\lambda^2 q^2} , \tag{5.65}$$

$$\alpha'(x)^2-\beta'^2 = \left(\frac{\gamma}{\gamma'}\right)^2\left[\alpha(x)^2-\beta^2\right] , \tag{5.66}$$

where $x \equiv (\gamma+\lambda)$ prior to collision and $x \equiv (\gamma'-\lambda)$ after collision. Additionally, $\omega^2 \equiv (1+\zeta)/(1-\zeta)$. The ϕ-integrals immediately follow, yielding

$$\int_0^{2\pi}\mathrm{d}\phi\; D^{-1} = \frac{2\pi\lambda q}{\gamma'}\frac{(1-\zeta)^{-1}}{(x^2+\omega^2)^{1/2}} , \tag{5.67}$$

$$\int_0^{2\pi}\mathrm{d}\phi\; D'^{-1} = \frac{\gamma'}{\gamma}\int_0^{2\pi}\mathrm{d}\phi\; D^{-1} , \tag{5.68}$$

$$\int_0^{2\pi}\mathrm{d}\phi\; D^{-2} = \frac{2\pi\gamma\lambda^2 q}{\gamma'\,(1-\zeta)^2}\frac{\left[x\left(\gamma^{-1}+\gamma'^{-1}\right)-(1+\zeta)\right]}{(x^2+\omega^2)^{3/2}} , \tag{5.69}$$

$$\int_0^{2\pi}\mathrm{d}\phi\; D'^{-2} = \frac{\gamma'}{\gamma}\int_0^{2\pi}\mathrm{d}\phi\; D^{-2} . \tag{5.70}$$

The Compton scattering kernel in equation (5.34) may now be rewritten as

$$\sigma_\mathrm{s}\left(\gamma\rightarrow\gamma',\zeta,\tau\right) = \frac{3\rho\sigma_\mathrm{T}}{8\gamma^2}\int_{\lambda_+}^{\infty}\mathrm{d}\lambda\;\frac{f(\lambda)}{\lambda^5}\mathcal{S}\left(\gamma,\gamma',\zeta,\lambda\right) , \tag{5.71}$$

where

$$\mathcal{S}\left(\gamma,\gamma',\zeta,\lambda\right) = \left[\frac{2\gamma\gamma'}{q}+R\left(\gamma+\lambda\right)-R\left(\gamma'-\lambda\right)\right] , \tag{5.72}$$

contains the photon-electron scattering information, with the function $R(x)$ defined as

$$R(x) = \frac{w-\zeta}{(1-\zeta)^2(x^2+\omega^2)^{3/2}}+\left[-\gamma\gamma'+\frac{2}{1-\zeta}+\frac{2}{\gamma\gamma'(1-\zeta)^2}\right]\frac{1}{(x^2+\omega^2)^{1/2}} , \tag{5.73}$$

where $w \equiv w(x) = [x\,(\gamma^{-1}+\gamma'^{-1})-1]$. The scattering kernel, as it is written in equation (5.71), is the sum of three terms: the first is independent of electron energy, and the second and third terms represent the photon-electron interaction immediately before and immediately after collision, respectively. The interaction term is defined in equation (5.73).

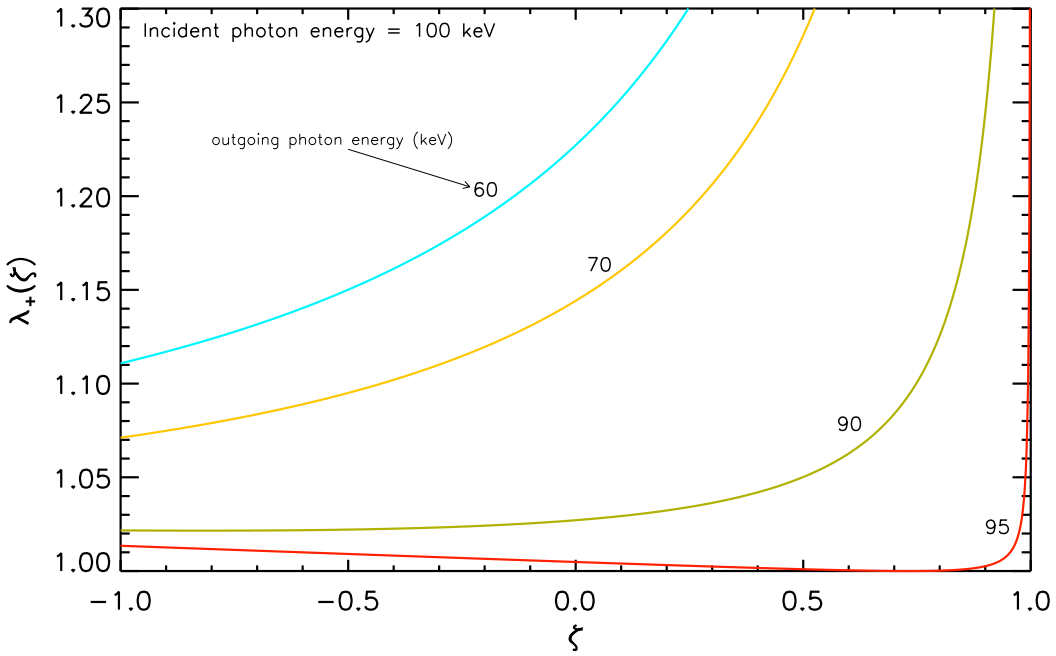

Fig. 5.1: Plot of λ_+ as a function of ζ for an incident photon of energy 100 keV. For outgoing photon energies of 95 keV and 90 keV, λ_+ has a minimum and thus the integration over λ must be divided into two regions. For outgoing photon energies of 60 keV and 70 keV, λ_+ does not have a minimum value between $\lambda_+(-1)$ and $\lambda_+(1)$, hence the integration over λ is simply taken between λ_L and infinity.

5.6 Angular Moments of the Compton Cross Section

In solving the full radiative transfer equation with Compton scattering, a generalised Eddington approximation (Eddington 1926; Rybicki and Lightman 1979) to evaluate successive angular moment integrals of σ_s may be employed (Thorne 1981; Fuerst 2006; Wu et al. 2008). In this section, angular moments of the form ζ^n (e.g. Shestakov et al. 1988, and references therein) are used to define the moment expansion of the Compton scattering kernel. This requires evaluating integrals of the form

$$\int \mathrm{d}\zeta\ \zeta^n \sigma_\mathrm{s}\left(\gamma \rightarrow \gamma', \zeta, \tau\right) = \frac{3\rho\sigma_\mathrm{T}}{8\gamma^2} \int_{-1}^{1} \mathrm{d}\zeta\, \zeta^n \int_{\lambda_+}^{\infty} \mathrm{d}\lambda\ \frac{f(\lambda)}{\lambda^5} \mathcal{S}\left(\gamma, \gamma', \zeta, \lambda\right)\ . \quad (5.74)$$

However, as equation (5.74) stands, integrating over $f(\lambda)$ is analytically impossible. Rather than perform the λ integration first, it is more straightforward to switch the order of integration. Not only does this enable the derivation of analytic results, performing the λ integration after the ζ integration affords the method greater generality, since the ζ integral is independent of the as-

sumed electron distribution function (in the isotropic case). To change the order of integration, first consider $\lambda_+(\zeta)$, which must be inverted (i.e. $\zeta(\lambda_+)$ found) to change the order of integration. Since $|\zeta| \leq 1$, the left boundary λ_L of integration over λ is found as

$$\lambda_+(-1) \equiv \lambda_\mathrm{L} = \frac{\gamma' - \gamma}{2} + \frac{\gamma' + \gamma}{2}\sqrt{1 + \frac{1}{\gamma\gamma'}} \ , \tag{5.75}$$

whereas

$$\lim_{\zeta \to 1} \lambda_+(\zeta) = +\infty \ , \tag{5.76}$$

is the right boundary. Since λ_+ is a function of ζ, the minimum value of λ is found at

$$\zeta_{1,2} = 1 \pm \left(\gamma^{-1} - \gamma'^{-1}\right) \ , \tag{5.77}$$

which upon substitution into equation (5.48) yields

$$\lambda_\mathrm{min} = 1 + \frac{1}{2}\left[(\gamma' - \gamma) + |\gamma' - \gamma|\right] \ . \tag{5.78}$$

Normally $\lambda_\mathrm{min} < \lambda_\mathrm{L}$ by definition. However, $\lambda_\mathrm{L} \leq \lambda_\mathrm{min}$ if the following condition is satisfied:

$$\left|\gamma^{-1} - \gamma'^{-1}\right| \geq 2. \tag{5.79}$$

Rearranging λ_+ to find ζ as a function of λ yields

$$\zeta_\pm = \frac{1}{\gamma\gamma'}\left[1 + (\gamma + \lambda)(\gamma' - \lambda) \pm \sqrt{\lambda^2 - 1}\sqrt{(\lambda + \gamma - \gamma')^2 - 1}\right] \ . \tag{5.80}$$

It immediately follows that the order of integration may be reversed as

$$\int_{-1}^{1} \mathrm{d}\zeta \int_{\lambda_+}^{\infty} \mathrm{d}\lambda = \int_{\lambda_\mathrm{L}}^{\infty} \mathrm{d}\lambda \int_{-1}^{\zeta_+} \mathrm{d}\zeta + \int_{\lambda_\mathrm{min}}^{\lambda_\mathrm{L}} \mathrm{d}\lambda \int_{\zeta_-}^{\zeta_+} \mathrm{d}\zeta \ , \tag{5.81}$$

at the expense of evaluating two different integrals. However, if $\lambda_\mathrm{L} \leq \lambda_\mathrm{min}$ then $\lambda_\mathrm{min} = \lambda_\mathrm{L}$ and the second term in equation (5.81) vanishes, necessitating evaluation of the first double integral only (see Figure 5.1).

5.7 Performing the Angular Moment Integrals

In evaluating equation (5.74) with (5.81), three different types of moment integral arise, namely

$$Q_n(\gamma,\gamma') = \int \mathrm{d}\zeta\ \frac{\zeta^n}{q}\ , \tag{5.82}$$

$$R_n(x) = \int \frac{\mathrm{d}\zeta\ \zeta^n}{(1-\zeta)^2\left(x^2+\frac{1+\zeta}{1-\zeta}\right)^{3/2}}\ , \tag{5.83}$$

$$S_{n,m}(x) = \int \frac{\mathrm{d}\zeta\ \zeta^n}{(1-\zeta)^m\left(x^2+\frac{1+\zeta}{1-\zeta}\right)^{1/2}}\ , \quad m=0,\ 1,\ 2\ . \tag{5.84}$$

Note the identity $\mathrm{d}S_{n,2}/\mathrm{d}x \equiv -xR_n$. With the aforementioned definitions the angular moment function of order n, $\mathcal{M}_n$, may be written as

$$\begin{aligned}\mathcal{M}_n &= \int \mathrm{d}\zeta\ \zeta^n\,\mathcal{S}\left(\gamma,\gamma',\zeta,\lambda\right)\\ &= A_n(\gamma,\gamma') + B_n\left(\gamma+\lambda\right) - B_n\left(\gamma'-\lambda\right)\ ,\end{aligned} \tag{5.85}$$

where

$$A_n(\gamma,\gamma') = 2\gamma\gamma' Q_n\ , \tag{5.86}$$

is independent of x and

$$B_n(x) = \left[w\,R_n(x) - R_{n+1}(x)\right] + \left[2S_{n,1}(x) + \frac{2}{\gamma\gamma'}S_{n,2}(x) - \gamma\gamma' S_{n,0}(x)\right]\ . \tag{5.87}$$

In equations (5.83) and (5.84), the integrals have an x-dependence which is crucial to their evaluation. The evaluation of these integrals yields different results depending on whether $x^2<1$, $x^2=1$ or $x^2>1$.

The moment integrals may be integrated analytically, although the resultant expressions are algebraically cumbersome. The $n=0,1,2$ moments for A_n are as follows:

$$A_0 = -2q\ , \tag{5.88}$$

$$A_1 = \frac{A_0}{3\gamma\gamma'}\left(q^2+3\gamma\gamma'\zeta\right)\ , \tag{5.89}$$

$$A_2 = \frac{A_0}{5}\left[\zeta^2 - 2\left(\frac{A_1}{A_0}\right)\zeta + 6\left(\frac{A_1}{A_0}\right)^2\right]\ . \tag{5.90}$$

Similarly, the $n = 0, 1, 2$ moments for B_n are given by

$$\begin{aligned} B_0 &= b\left[2 - x\left(\gamma^{-1} + \gamma'^{-1}\right) + \frac{2\left(1+\gamma\gamma'\right)}{x^2-1} + \gamma\gamma'\left(1-\zeta\right) + \frac{2}{\gamma\gamma'}\left(x^2+\omega^2\right)\right] \\ &\quad + \frac{2\left(2x^2+\gamma\gamma'-1\right)}{1-x^2}\mathtt{C}\left(x\right) \ , \end{aligned} \tag{5.91}$$

$$\begin{aligned} B_1 &= \frac{b}{1-x^2}\Bigg\{x\left(1+x^2\right)\left(\gamma^{-1}+\gamma'^{-1}\right) - \left(7+\zeta\right) + 2x^2\left(\zeta-2\right) \\ &\quad + \left[\left(1+x^2\right) + \left(1-x^2\right)\zeta\right]\left[\frac{4\left(1-x^2\right) - \gamma^2\gamma'^2\left(1-\zeta^2\right)}{2\gamma\gamma'\left(1-\zeta\right)}\right]\Bigg\} \\ &\quad + \left[\frac{2\left(w-2x^2\right)}{x^2-1} + \frac{\left(2-\gamma\gamma'\right)\left(2x^2+1\right)}{\left(x^2-1\right)^2} + \frac{4}{\gamma\gamma'}\right]\mathtt{C}\left(x\right) \ , \end{aligned} \tag{5.92}$$

$$\begin{aligned} B_2 &= \frac{b}{(1-x^2)^2}\Bigg\{-w\left[2+\zeta+x^2\left(3-\zeta\right)+x^4\right] \\ &\quad + \left[1+\zeta+x^2\left(1-\zeta\right)\right]\left[x^2\left(3+\zeta\right)-\zeta\right] \\ &\quad + \frac{6}{x^2-1}\Big\{\left(4+9x+2x^4\right)\left(3+3x^2+\gamma\gamma'\right) \\ &\quad + \left(x^2-1\right)\left[3\left(\gamma\gamma'-1\right)+2x^2\left(\gamma\gamma'-6\right)\right]\zeta \\ &\quad + \left(x^2-1\right)^2\left(2\gamma\gamma'-3\right)\zeta^2\Big\} \\ &\quad + \frac{2\left(1-x^2\right)\left[\left(1+\zeta\right)+x^2\left(1-\zeta\right)\right]\left(2-x^2-\zeta\right)}{\gamma\gamma'\left(1-\zeta\right)}\Bigg\} \\ &\quad + \frac{1}{1-x^2}\Bigg\{\frac{2\left[w\left(2x^2+1\right)-\left(2x^4+1\right)\right]}{1-x^2} \\ &\quad + \frac{3+\gamma\gamma'\left[5+6\left(x^2-1\right)+2\left(x^2-1\right)^2\right]}{\left(1-x^2\right)^2} \qquad (5.93) \\ &\quad + \frac{4\left(1-2x^2\right)}{\gamma\gamma'}\Bigg\}\mathtt{C}\left(x\right) \ , \qquad (5.94) \end{aligned}$$

where

$$b = \frac{1}{\sqrt{\omega^2+x^2}} \ , \tag{5.95}$$

and the function $\mathtt{C}\left(x\right)$ is defined as

$$\mathtt{C}(x) = \begin{cases} \frac{1}{\sqrt{1-x^2}}\ \arctan\left(b\sqrt{1-x^2}\right) \ , & \text{if } x^2 < 1 \ ; \\ \frac{1}{\sqrt{1-x^2}}\ \operatorname{arcsinh}\left(\frac{\sqrt{x^2-1}\sqrt{1-\zeta}}{\sqrt{2}}\right) \ , & \text{if } x^2 > 1 \ . \end{cases} \tag{5.96}$$

In the special case $x^2 = 1$ the expressions for B_n are considerably simpler

$$B_0 = \sqrt{\frac{1-\zeta}{2}}\left[\frac{4}{\gamma\gamma'(1-\zeta)} - 4 - w + \frac{2\gamma\gamma'(1-\zeta)}{3} + \frac{2+\zeta}{3}\right] , \quad (5.97)$$

$$B_1 = \sqrt{\frac{1-\zeta}{2}}\left[\frac{4(2-\zeta)}{\gamma\gamma'}(1-\zeta) - \frac{4}{3}(2+\zeta) - \frac{w(2+\zeta)}{3} + \frac{2\gamma\gamma'(1-\zeta)(2+3\zeta)}{15} + \frac{8+4\zeta+3\zeta^2}{15}\right] , \quad (5.98)$$

$$B_2 = \sqrt{\frac{1-\zeta}{2}}\left[\frac{4(8-4\zeta-\zeta^2)}{3\gamma\gamma'(1-\zeta)} - \frac{(4+w)(8+4\zeta+3\zeta^2)}{15} + \frac{2\gamma\gamma'(1-\zeta)(8+12\zeta+15\zeta^2)}{105} + \frac{16+8\zeta+6\zeta^2+5\zeta^3}{35}\right] . \quad (5.99)$$

In principle equations (5.82)–(5.84) may be integrated for arbitrary n, but, as seen in equations (5.88)–(5.99), the resultant algebraic expressions become extremely cumbersome. Moreover, the expressions for A_n must be evaluated either two or four times per scattering event, and B_n either four or eight times per scattering event. Given the inherent algebraic complexity, and the number of calls required per scattering event, this will lead to significant loss of precision, in particular between cancellations of terms of similar value or of particular smallness (e.g. Poutanen and Vurm 2010).

Using equations (5.85)–(5.87) the n-th angular moment expansion of the Compton scattering kernel may be written more compactly as

$$\sigma_{sn}(\gamma \to \gamma', \tau) = \frac{3\rho\sigma_T}{8\gamma^2}\left(\int_{\lambda_L}^{\infty} d\lambda\ \frac{f(\lambda)}{\lambda^5}\mathcal{M}_n\Big|_{-1}^{\zeta_+} + \int_{\lambda_{min}}^{\lambda_L} d\lambda\ \frac{f(\lambda)}{\lambda^5}\mathcal{M}_n\Big|_{\zeta_-}^{\zeta_+}\right) , \quad (5.100)$$

where, as noted before, the second term in brackets in (5.100) vanishes when $\lambda_L \leq \lambda_{min}$, saving significant computational expense. In the case of $x^2 = 1$, the moment integrals simplify significantly. This is as far as it proves possible to proceed analytically. Integrations over λ need to be performed with an appropriate numerical scheme.

Naturally, the question arises as to whether the integrals in equation (5.100) can be evaluated analytically. As it stands, the method presented thus far would require arbitrary precision arithmetic to evaluate, and therefore be computationally expensive and time consuming. In the following section, the evaluation of integrals (5.82)–(5.84) is demonstrated analytically and in closed

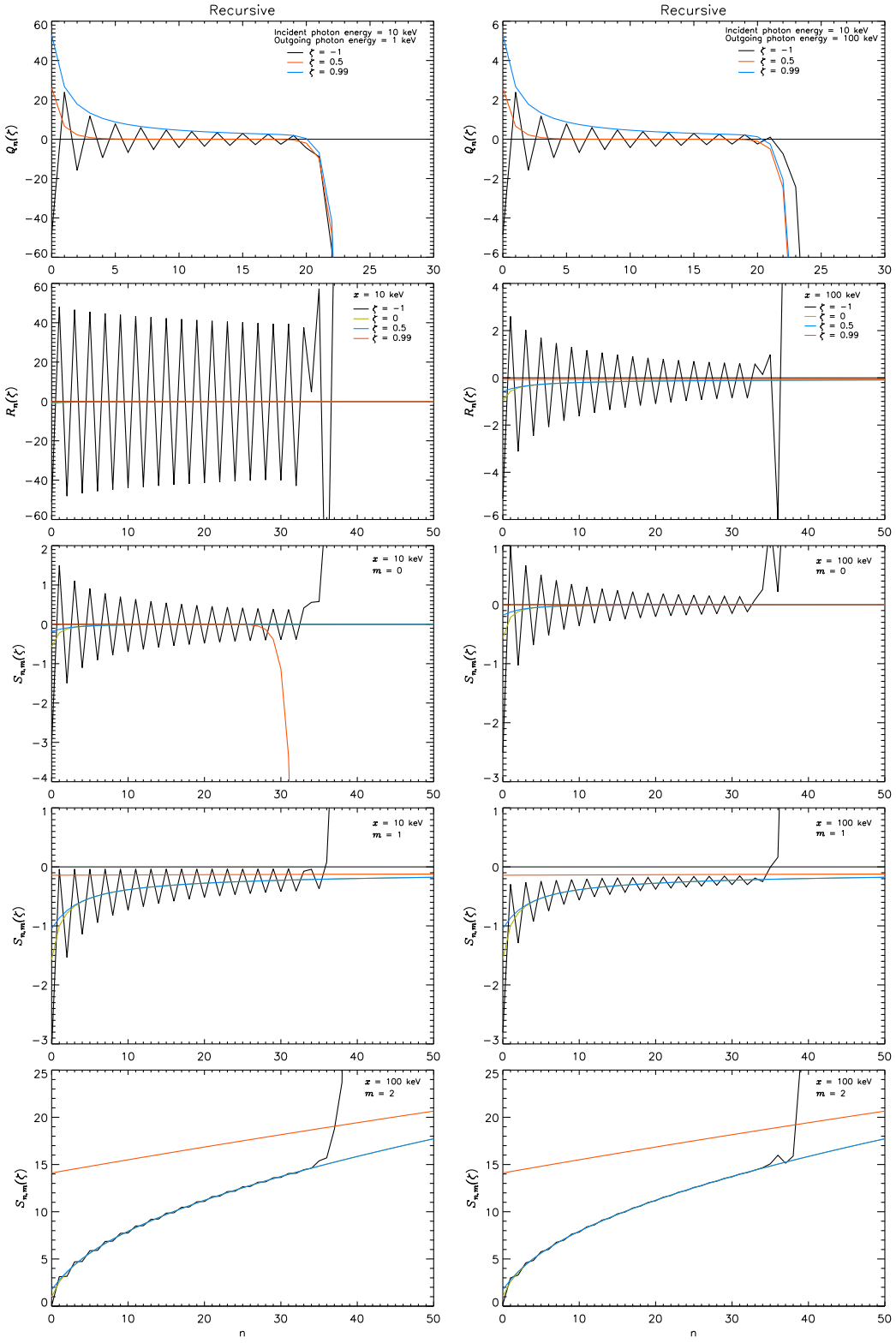

Fig. 5.2: Numerical FORTRAN evaluation (in double precision) of the moment integrals Q_n, R_n and $S_{n,m}$, through recursion, for $x = 10$ keV (left) and $x = 100$ keV (right). The same colour scheme is employed for R_n and $S_{n,m}$. For Q_n numerical round-off errors occur beyond $n = 20$. For R_n and $S_{n,m}$ numerical round-off errors dominate beyond $n = 30$.

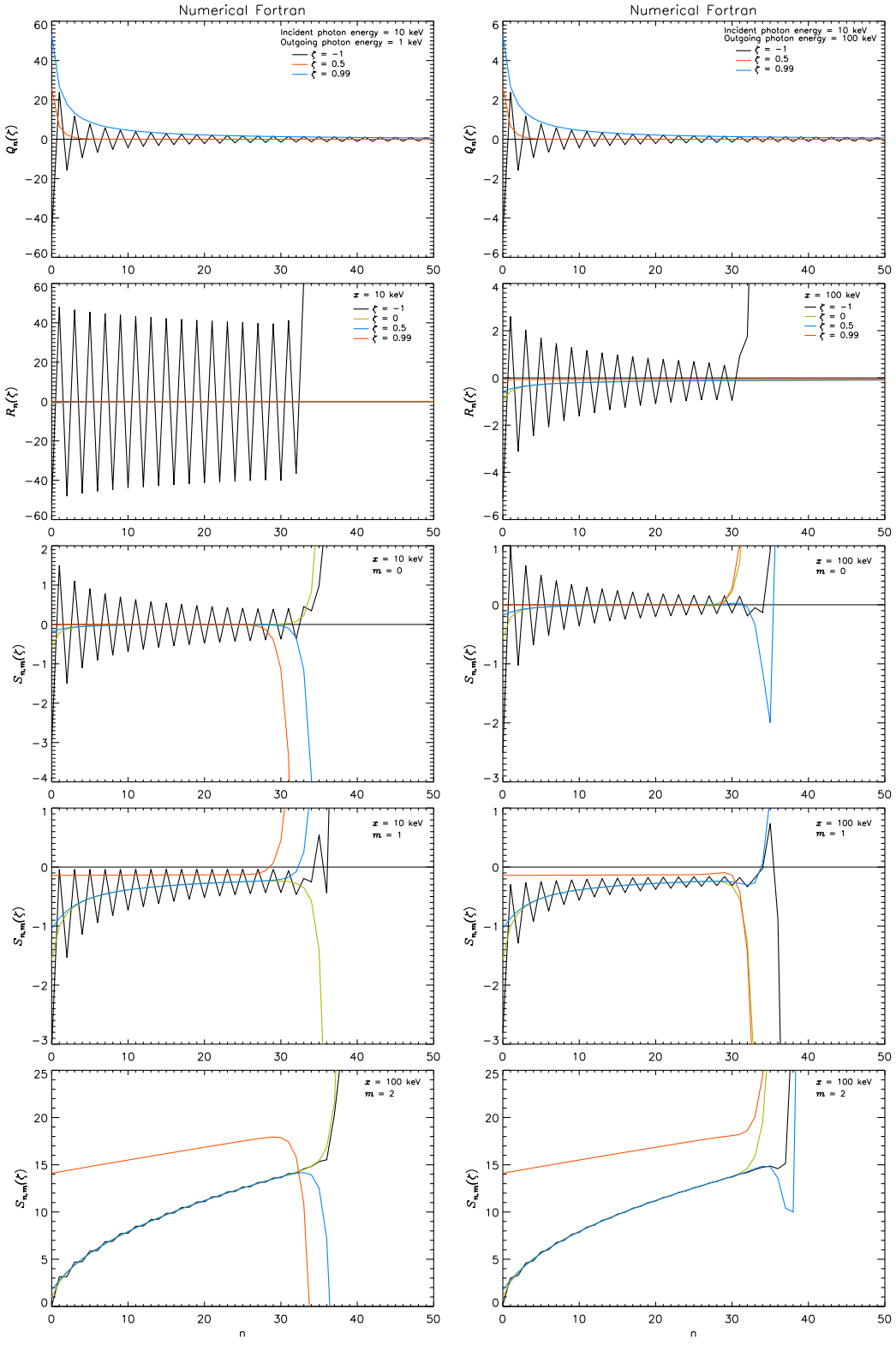

Fig. 5.3: As in Figure 5.2, but now with Q_n, R_n and $S_{n,m}$ evaluated directly through the numerical hypergeometric function method, for $x = 10$ keV (left) and $x = 100$ keV (right). Q_n is now numerically very stable, even beyond $n = 100$ (not shown). However, for R_n and $S_{n,m}$ there is no improvement compared to the recurrence relation method.

form, for arbitrary moment order.

5.8 Evaluating Moment Integrals for Arbitrary Order

The previous section derived analytic expressions for the first three moments of the Compton scattering kernel. As the moment order increases, the algebraic complexity of the resultant expression grows rapidly. Clearly the method, as it stands, does not lend itself readily to the evaluation of higher-order moments. These are necessary for a more accurate treatment of radiation transport problems. A much faster method is to evaluate equations (5.82)–(5.84) recursively. Firstly, consider equation (5.82) for Q_n. By employing the identity

$$\frac{\mathrm{d}q}{\mathrm{d}\zeta} = -\frac{\gamma\gamma'}{\zeta} \ , \tag{5.101}$$

upon integrating Q_n by parts, the following recurrence relation immediately follows

$$\gamma\gamma' \left(2n+1\right) Q_n = \left(\gamma^2 + \gamma'^2\right) n \, Q_{n-1} - q \, \zeta^n \ . \tag{5.102}$$

With the seed $Q_0 = \left(\sqrt{\gamma^2 + \gamma'^2} - q\right) / \gamma\gamma'$, Q_n may be evaluated for arbitrary n. Next consider equation (5.83) in the form

$$R_n = -\frac{1}{2\sqrt{2}} \int \mathrm{d}u \, u^{-1/2} \left(1-u\right)^n \left(1 - c\,u\right)^{-3/2} \ , \tag{5.103}$$

where the substitution $u = 1 - \zeta$ has been employed, and $c \equiv (1 - x^2)/2$. By expanding in series the term $(1-u)^n = \sum_{k=0}^{n} (-1)^k \binom{n}{k} u^k$, equation (5.103) may be written as

$$R_n = \frac{\sqrt{2}}{4} \sum_{k=0}^{n} \left(-1\right)^{k+1} \binom{n}{k} \int \mathrm{d}u \frac{u^{k-1/2}}{\left(1 - c\,u\right)^{3/2}} \ . \tag{5.104}$$

Defining the integral

$$I_{_R}\left(k\right) = \int \mathrm{d}u \frac{u^{k-1/2}}{\left(1 - c\,u\right)^{3/2}} \ , \tag{5.105}$$

a recursion relation for equation (5.105) may be found by integrating by parts

$$2\left(k-1\right) c \, I_{_R}(k) = \left(2k-1\right) I_{_R}\left(k-1\right) - \frac{2u^{k-1/2}}{\sqrt{1 - c\,u}} \ . \tag{5.106}$$

The value $I_{R}(0)$ immediately follows, but to perform recursively the seed value $I_{R}(1)$ is also needed

$$I_{R}(1) = \frac{2\sqrt{u}}{c\sqrt{1-c\,u}} - \frac{2}{c^{3/2}}\arcsin\left(\sqrt{c\,u}\right) \ . \tag{5.107}$$

Therefore R_n may now be defined as

$$R_n = \frac{\sqrt{2}}{4}\sum_{k=0}^{n}(-1)^{k+1}\binom{n}{k}I_{R}(k) \ , \tag{5.108}$$

which can be solved for arbitrary n. Similarly, for $S_{n,m}$

$$S_{n,m} = \frac{\sqrt{2}}{2}\sum_{k=0}^{n}(-1)^{k+1}\binom{n}{k}I_{S}\left(k,m\right) \ , \tag{5.109}$$

where

$$I_{S}(k,m) = \int \mathrm{d}u \frac{u^{k-m+1/2}}{\sqrt{1-c\,u}} \ . \tag{5.110}$$

After some working, the recursion relation for $I_{S}(k,m)$ is obtained as

$$(k-m+1)\,c\,I_{S}\left(k,m\right) = (k-m+1/2)\,I_{S}\left(k-1,m\right) - u^{k-m+1/2}\sqrt{1-c\,u} \ . \tag{5.111}$$

This identity requires four different seed values for the cases $m = 0$, 1 and 2:

$$I_{S}(0,0) = \frac{u}{2c}I_{S}(0,2) + \frac{1}{2c}I_{S}(0,1) \ , \tag{5.112}$$

$$I_{S}(0,1) = \frac{2\arcsin\left(\sqrt{c\,u}\right)}{\sqrt{c}} \ , \tag{5.113}$$

$$I_{S}(0,2) = -\frac{2\sqrt{1-c\,u}}{\sqrt{u}} \ , \tag{5.114}$$

$$I_{S}(1,2) = I_{S}(0,1) \ . \tag{5.115}$$

The numerical evaluation of these recursion relations in FORTRAN95 is shown in Figure 5.2 for Q_n, R_n and $S_{n,m}$. For Q_n it is clear the method is inaccurate for $n > 20$, regardless of the cosine of the scattering angle, ζ. For R_n the method is numerically unstable for $n > 30$ for $\zeta = -1$, as well as slowly convergent, regardless of the value of x. However, for $\zeta > -1$ the method appears both numerically stable and rapidly convergent, even for $n = 50$. Similar results are obtained for $S_{n,m}$ as for R_n, with the exception that for lower energies, $S_{n,0}$ is numerically unstable both for extreme backward scattering and extreme forward scattering beyond $n = 30$. More accurate evaluation would

require the implementation of arithmetic precision beyond that of standard double precision.

Thus equations (5.102), (5.108) and (5.109) enable (5.85) to be solved iteratively. In computing angular moments of the Klein-Nishina cross-section this will greatly reduce the computational time and resources required. Each moment integral can be computed recursively using the stored numerical value of the previous moment. Unfortunately, as the order increases, there will inevitably be loss of numerical precision through differences between terms in the recursion relations. Further, it is impossible to perform the final integral over the electron distribution function without either an algebraic expression for each moment, or an appropriate closed-form expression for each moment in terms of more generalised functions. The following sections detail a method based on such a closed-form representation of each moment.

5.9 Evaluating Moment Integrals - Hypergeometric Functions

In this section the moment integrals in equations (5.82)–(5.84) are evaluated in terms of ordinary hypergeometric functions. In terms of these functions, the problem of relativistic Compton scattering is greatly simplified (see Aharonian and Atoyan 1981). Hypergeometric functions are a very general class of functions which contain many of the known mathematical functions as special or limiting cases.

The ordinary hypergeometric function of one variable, or Gauss hypergeometric function, is defined by the following infinite series

$$ {}_2F_1\left(a,b;c;z\right) = \sum_{n=0}^{\infty} \frac{\left(a\right)_n \left(b\right)_n}{\left(c\right)_n \, n!} z^n \ , \tag{5.116} $$

where the notation

$$ \left(a\right)_n \equiv \frac{\Gamma(a+n)}{\Gamma(a)} \ , \tag{5.117} $$

is the rising factorial or Pochhammer symbol. The series is absolutely convergent for $|z| < 1$, and terminates after a finite number of terms if either a or b is a negative integer. The case $|z| \geq 1$ may be solved by analytic continuation (Zhang and Jin 1996). Although z may take complex values, in the Compton

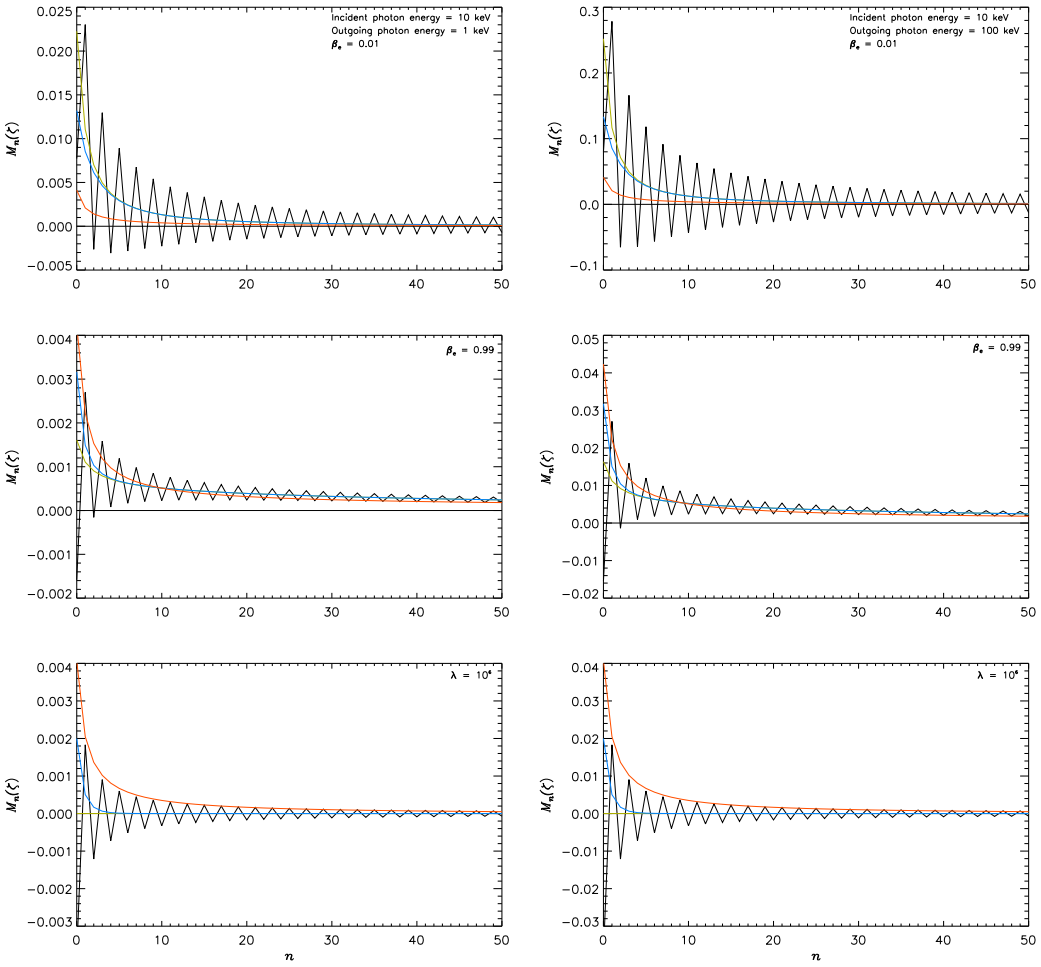

Fig. 5.4: Numerical evaluation of the moment integral $\mathcal{M}_n$ as a function of n. Same colour scheme as R_n and $S_{n,m}$ in Figures 5.2 and 5.3. In all plots the incident photon energy is 10 keV. Left plots show Compton scattering resulting in an outgoing photon energy of 1 keV, for (top to bottom) electron velocities of $\beta_e = 0.01$, $\beta_e = 0.99$ and $\lambda = 10^6$ ($\beta_e \simeq 0.9999999999995$) respectively. Right plots show inverse Compton scattering for an outgoing photon of energy 100 keV.

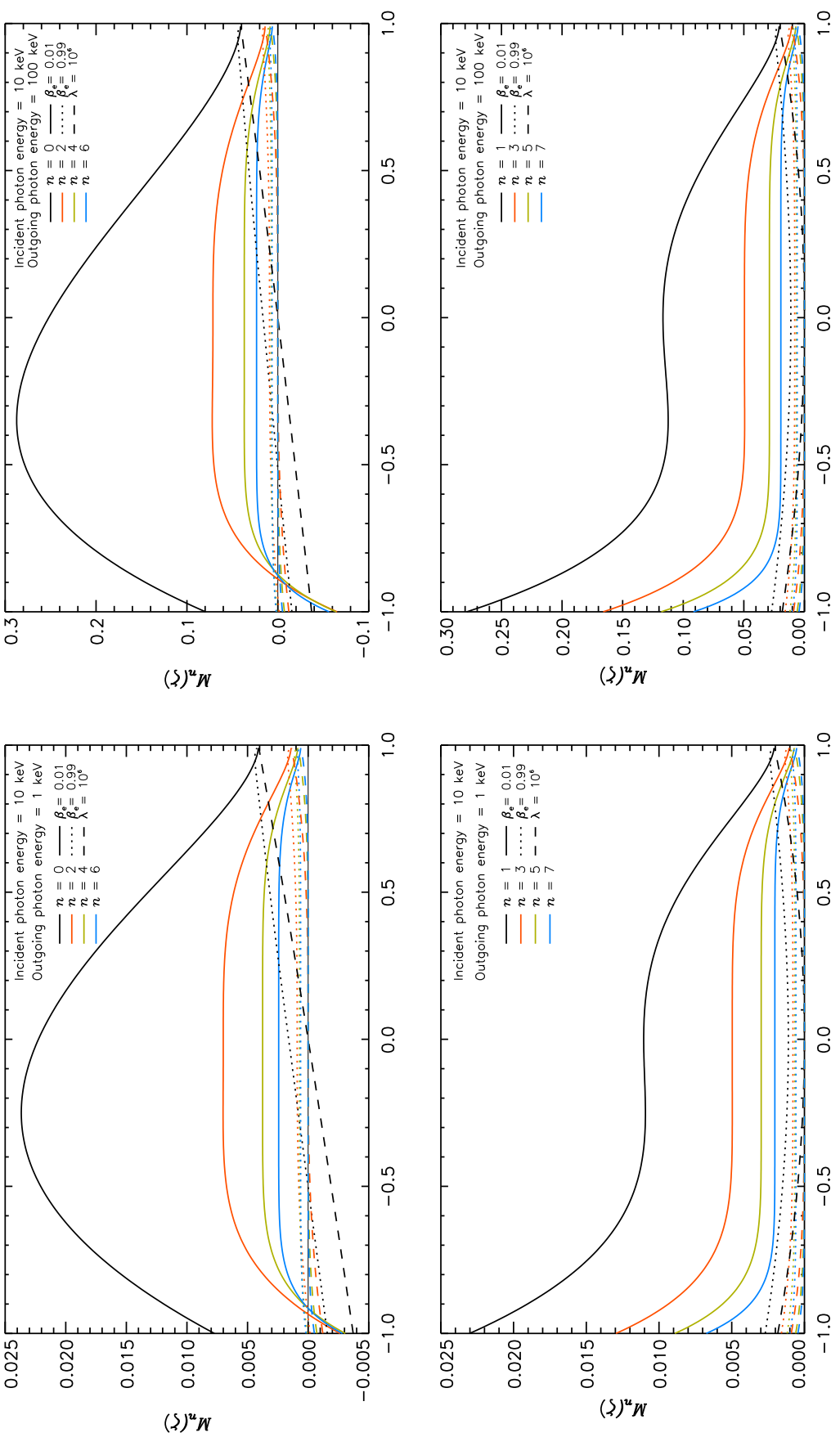

Fig. 5.5: Plots of the moment integral $\mathcal{M}_n$ as a function of ζ for an incident photon energy of 10 keV. Plots on the left show an outgoing photon energy of 1 keV, plots on the right an outgoing photon energy of 100 keV (i.e. inverse Compton scattering). Left and right columns show, from top to bottom, $\mathcal{M}_n$ evaluated for $n = 0$, 2, 4 and 6, and $n = 1$, 3, 5 and 7, respectively. Solid, dotted, and dashed lines denote electron velocities of $\beta_e = 0.01$, $\beta_e = 0.99$ and $\lambda = 10^6$ respectively. As n increases, the angular moments become increasingly insensitive to a wider range of ζ. The angular moments are strongly dependent on electron velocity.

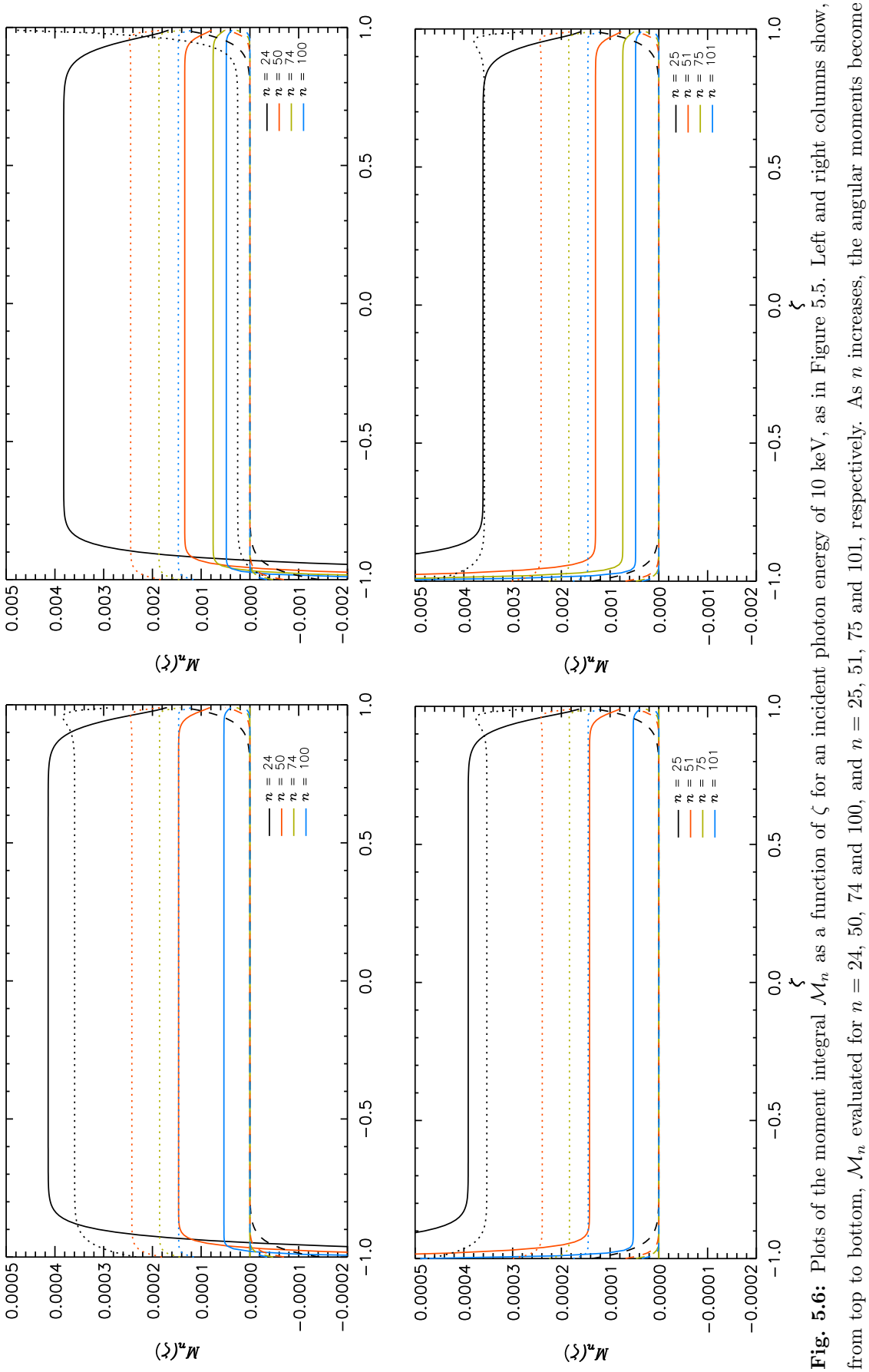

Fig. 5.6: Plots of the moment integral $\mathcal{M}_n$ as a function of ζ for an incident photon energy of 10 keV, as in Figure 5.5. Left and right columns show, from top to bottom, $\mathcal{M}_n$ evaluated for $n = 24$, 50, 74 and 100, and $n = 25$, 51, 75 and 101, respectively. As n increases, the angular moments become increasingly insensitive to a wider range of ζ. The angular moments are strongly dependent on electron velocity.

scattering problem z is always real. With this definition the integrals Q_n, R_n and $S_{n,m}$ may be evaluated. Having written R_n and $S_{n,m}$ in summation form in equations (5.108) and (5.109) simplifies things considerably. Using the series expansion of $(1-u)^n$ and equation (5.116), the following expressions for (5.82)–(5.84) are found

$$Q_n = \frac{\zeta^{n+1}}{(n+1)\sqrt{\gamma^2+\gamma'^2}^2}\mathfrak{F}\left(\frac{1}{2}, n+1, x_1\right), \tag{5.118}$$

$$R_n = -\frac{(1-\zeta)^{1/2}}{\sqrt{2}}\sum_{k=0}^{n}\frac{\binom{n}{k}(\zeta-1)^k}{2k+1}\mathfrak{F}\left(\frac{3}{2}, k+\frac{1}{2}, x_2\right), \tag{5.119}$$

$$S_{n,m} = -\frac{(1-\zeta)^{\frac{3}{2}-m}}{\sqrt{2}}\sum_{k=0}^{n}\frac{\binom{n}{k}(\zeta-1)^k}{k-m+3/2}\mathfrak{F}\left(\frac{1}{2}, k-m+\frac{3}{2}, x_2\right), \tag{5.120}$$

where

$$\mathfrak{F}(a_1, a_2, x) = {}_2\mathrm{F}_1\left[a_1, a_2; a_2+1; x\right], \tag{5.121}$$

and

$$x_1 \equiv \frac{2\gamma\gamma'}{\gamma^2+\gamma'^2}\zeta, \tag{5.122}$$

$$x_2 \equiv \frac{1}{2}\left(1-x^2\right)(1-\zeta). \tag{5.123}$$

The continuity of expressions (5.118)–(5.120) is of paramount importance in accurate numerical calculation of the moments. Q_n is always within the convergence region, and only lies on the boundary in the case of a perfectly elastic collision i.e. Thomson scattering. Equations (5.119) and (5.120) can be divided into two cases: those which lie within the convergence region ($|z|<1$) and those that lie on the boundary or outside it ($z \leq -1$). The case $z \leq -1$, i.e. $\zeta \geq (x^2+1)/(x^2-1)$, may be solved by analytic extension with the following expression

$${}_2\mathrm{F}_1\left[a, b; b+1; z\right] = (1-z)^{-a}{}_2\mathrm{F}_1\left[a, 1; b+1; \frac{z}{z-1}\right], \tag{5.124}$$

which brings R_n and $S_{n,m}$ into the convergence region. The Gauss hypergeometric function is well documented in the literature and there exist several codes in FORTRAN which can evaluate it both accurately and rapidly (e.g. Forrey 1997; Zhang and Jin 1996), in addition to handling all cases of differences of parameters and values which can give rise to numerical problems (e.g. Zhang and Jin 1996).

In the special case $x^2 = 1$ the expressions for R_n and $S_{n,m}$ reduce to

$$R_n = -\frac{(1-\zeta)^{1/2}}{\sqrt{2}}\mathfrak{F}\left(-n, \frac{1}{2}, 1-\zeta\right) , \tag{5.125}$$

$$S_{n,m} = -\frac{\sqrt{2}\,(1-\zeta)^{\frac{3}{2}-m}}{3-2m}\mathfrak{F}\left(-n, \frac{3}{2}-m, 1-\zeta\right) , \tag{5.126}$$

which are detailed in Appendix B.

Thus the moment integrals for all values of x have been defined in closed-form. Results of the direct numerical evaluation of the moment integrals Q_n, R_n and $S_{n,m}$ are presented in Figure 5.3. For Q_n the direct hypergeometric function method is a significant improvement. This is obvious since, in closed-form, Q_n only ever requires one function evaluation, irrespective of the moment order. However, for R_n and $S_{n,m}$ this method fares no better. This is due to oscillating sums in the corresponding expressions. However, the closed-form nature of these expressions is necessary to define the scattering kernel analytically. Plots of the numerical evaluation of the moment integral $\mathcal{M}_n$ as a function of n, evaluated in PYTHON to high numerical precision, are shown in Figure 5.4. For very low scattering angles the angular moments are oscillatory, as can be seen in the $\zeta = -1$ case. However, this is not a numerical issue, but rather an issue inherent to the form of the Compton scattering kernel itself. Recall equation (5.42), which was derived in taking the direction of photon momentum transfer as the z-axis of integration. This choice fixes q to be uniquely defined by equation (5.42) and so the method is innately oscillatory for ζ close to -1, i.e. scattering angles close to 0.

In Figures 5.5 and 5.6, $\mathcal{M}_n$ is plotted as a function of ζ for low order and high order, odd and even moments n. Odd and even moments are plotted separately to emphasise the change in shape and decrease in size of $\mathcal{M}_n$ as the order increases. Odd and even moments have a distinct shape which flattens and decreases in magnitude as the order increases. Clearly as the moment order increases, $\mathcal{M}_n$ becomes less sensitive to moderate scattering angles and remains unchanged over an increasingly large range of ζ. The effect of increasing electron velocity is to shift the maximum of $\mathcal{M}_n$ towards $\zeta = 1$, i.e. back scattering, as well as reducing the absolute magnitude of $\mathcal{M}_n$.

In subsequent sections the hypergeometric function method is employed, with the aforementioned numerical considerations in mind. The final step in computing the Compton scattering cross-section is evaluating the integral over the relativistic electron distribution function.

5.10 Computing the Scattering Kernel

In the general case, in all of the literature at present, only integration over ζ or λ has been performed analytically — generally a choice must be made between performing integrals of the angular moments or integrating over the electron distribution function. The sixth and final integration over photon energy can be performed numerically during the radiative transfer calculations at each point along a ray. Regardless, with the methods at present, one is left with at best two further sets of integrals to evaluate. Further, the problem as formulated in the current literature (Prasad et al. 1986; Nagirner and Poutanen 1993; Poutanen and Vurm 2010) is algebraically cumbersome. It is common to resort to Monte-Carlo methods to solve the multi-dimensional integrals. To have a closed-form solution to the first five integrals, including the electron distribution function, would eliminate the need for evaluating multi-dimensional integrals and entail solving only the photon frequency integral along the ray, as is common in ray-tracing.

5.10.1 Integrating over the electron distribution function

To evaluate the full Compton scattering kernel, in full generality, there are two expressions of importance, namely equations (5.86) and (5.87). Computing the Compton scattering kernel involves evaluating the following expression:

$$T = T_1 + T_2 \ , \tag{5.127}$$

where

$$T_1 = \int_{\lambda_\mathrm{L}}^{\infty} \mathrm{d}\lambda \, \mathrm{e}^{-\lambda/\tau} \left[A_n + B_n(\gamma + \lambda) - B_n(\gamma' - \lambda) \right] \Big|_{-1}^{\zeta_+} \ , \tag{5.128}$$

$$T_2 = \int_{\lambda_\mathrm{min}}^{\lambda_\mathrm{L}} \mathrm{d}\lambda \, \mathrm{e}^{-\lambda/\tau} \left[A_n + B_n(\gamma + \lambda) - B_n(\gamma' - \lambda) \right] \Big|_{\zeta_-}^{\zeta_+} \ . \tag{5.129}$$

The second term in equation (5.127), namely equation (5.129), vanishes if the condition given by equation (5.79) is satisfied, as mentioned previously.

Solving for T_1 and T_2 in equation (5.127) necessitates the definition of the following seven integrals

$$I_{1,n}(\zeta,\lambda_1,\lambda_2) = 2\gamma\gamma'\int_{\lambda_1}^{\lambda_2} \mathrm{d}\lambda\, \mathrm{e}^{-\lambda/\tau}\, Q_n(\zeta)\ , \tag{5.130}$$

$$I_{2,n}(\zeta,x,\lambda_1,\lambda_2) = \int_{\lambda_1}^{\lambda_2} \mathrm{d}\lambda\, \mathrm{e}^{-\lambda/\tau}\, R_n(\zeta,x)\ , \tag{5.131}$$

$$I_{3,n}(\zeta,x,\lambda_1,\lambda_2) = (\gamma^{-1}+\gamma'^{-1})\int_{\lambda_1}^{\lambda_2} \mathrm{d}\lambda\, \mathrm{e}^{-\lambda/\tau}\, \lambda\, R_n(\zeta,x)\ , \tag{5.132}$$

$$I_{4,n}(\zeta,x,\lambda_1,\lambda_2) = \int_{\lambda_1}^{\lambda_2} \mathrm{d}\lambda\, \mathrm{e}^{-\lambda/\tau}\, R_{n+1}(\zeta,x)\ , \tag{5.133}$$

$$I_{5,n}(\zeta,x,\lambda_1,\lambda_2) = \gamma\gamma'\int_{\lambda_1}^{\lambda_2} \mathrm{d}\lambda\, \mathrm{e}^{-\lambda/\tau}\, S_{n,0}(\zeta,x)\ , \tag{5.134}$$

$$I_{6,n}(\zeta,x,\lambda_1,\lambda_2) = 2\int_{\lambda_1}^{\lambda_2} \mathrm{d}\lambda\, \mathrm{e}^{-\lambda/\tau}\, S_{n,1}(\zeta,x)\ , \tag{5.135}$$

$$I_{7,n}(\zeta,x,\lambda_1,\lambda_2) = \frac{2}{\gamma\gamma'}\int_{\lambda_1}^{\lambda_2} \mathrm{d}\lambda\, \mathrm{e}^{-\lambda/\tau}\, S_{n,2}(\zeta,x)\ , \tag{5.136}$$

where the dependence of ζ and x on λ has not been explicitly shown, i.e. $\zeta \equiv \zeta(\lambda)$ and $x \equiv x(\lambda)$, for the sake of brevity. Consider the functions

$$f(\zeta,x,\lambda_1,\lambda_2) = \frac{\gamma}{\gamma'}I_{2,n} + I_{3,n} - I_{4,n} - I_{5,n} + I_{6,n} + I_{7,n}\ , \tag{5.137}$$

$$\begin{aligned} g(\zeta,x,\lambda_1,\lambda_2) &= \frac{\gamma'}{\gamma}I_{2,n} - I_{3,n} - I_{4,n} - I_{5,n} + I_{6,n} + I_{7,n} \\ &= f(\zeta,x,\lambda_1,\lambda_2) - \left[\left(\frac{\gamma}{\gamma'} - \frac{\gamma'}{\gamma}\right) I_{2,n} + 2I_{3,n}\right]\ . \end{aligned} \tag{5.138}$$

where the dependence of I on ζ, x, λ_1 and λ_2 has been suppressed for the sake of brevity. The Compton scattering kernel may then be expressed as the composition of the following ten terms:

$$t_1 = I_{1,n}(\zeta_+,\lambda_\mathrm{L},\infty) - 2\gamma\gamma'\tau\, Q_n(-1)\,\mathrm{e}^{-\lambda_\mathrm{L}/\tau}\ , \tag{5.139}$$

$$t_2 = I_{1,n}(\zeta_+,\lambda_\mathrm{min},\lambda_\mathrm{L}) - I_{1,n}(\zeta_-,\lambda_\mathrm{min},\lambda_\mathrm{L})\ , \tag{5.140}$$

$$t_3 = f(\zeta_+,\gamma+\lambda,\lambda_\mathrm{L},\infty)\ , \tag{5.141}$$

$$t_4 = f(-1,\gamma+\lambda,\lambda_\mathrm{L},\infty)\ , \tag{5.142}$$

$$t_5 = g(\zeta_+,\gamma'-\lambda,\lambda_\mathrm{L},\infty)\ , \tag{5.143}$$

$$t_6 = g(-1, \gamma' - \lambda, \lambda_{\rm L}, \infty) \ , \tag{5.144}$$

$$t_7 = f(\zeta_+, \gamma + \lambda, \lambda_{\rm min}, \lambda_{\rm L}) \ , \tag{5.145}$$

$$t_8 = f(\zeta_-, \gamma + \lambda, \lambda_{\rm min}, \lambda_{\rm L}) \ , \tag{5.146}$$

$$t_9 = g(\zeta_+, \gamma' - \lambda, \lambda_{\rm min}, \lambda_{\rm L}) \ , \tag{5.147}$$

$$t_{10} = g(\zeta_-, \gamma' - \lambda, \lambda_{\rm min}, \lambda_{\rm L}) \ , \tag{5.148}$$

where $Q_n(-1)$ is equivalent to Q_n evaluated at $\zeta = -1$. Recall $\zeta_\pm \equiv \zeta_\pm(\lambda)$, as given in equation (5.80). Terms t_1 (pre-collisional) and t_2 (post-collisional) are independent of x. With the above ten terms T_1 and T_2 may now be written as

$$T_1 = t_1 + t_3 - t_4 - t_5 + t_6 \ , \tag{5.149}$$

$$T_2 = t_2 + t_7 - t_8 - t_9 + t_{10} \ , \tag{5.150}$$

where, as noted before, T_2 vanishes if condition (5.79) is satisfied. With T_1 and T_2 expressed as shown, one may now evaluate equation (5.127) numerically. It is easily shown that the number of numerical integrals scales linearly with the moment order n and is given by $48n + 51$ or $24n + 25$, depending on whether T_2 need be evaluated. However, this is assuming the independent evaluation of each moment. In reality, in evaluating a moment n, all lower-order moments must also have been evaluated, and so the order of the method at each order n is given by $(n + 1)(24n + 51)$ or $(n + 1)(12n + 25)$.

The angular moments of the full Klein-Nishina Compton scattering kernel may now finally be written as:

$$\begin{aligned} \sigma_{\rm KN}(\gamma \rightarrow \gamma', \tau) &= \int {\rm d}\zeta \, \zeta^n \, \sigma_{sn}(\gamma \rightarrow \gamma', \zeta, \tau) \\ &= \frac{\mathcal{C}}{\gamma^2 \, \tau \, {\rm K}_2(1/\tau)} T(\gamma, \gamma', \tau) \ , \end{aligned} \tag{5.151}$$

where $T(\gamma, \gamma', \tau) \equiv T$, as given in equation (5.127) and $\mathcal{C} = 3\rho\sigma_{\rm T}/32\pi m_{\rm e}$.

5.10.2 Numerical implementation

In implementing the formulation in the previous subsection numerically, several considerations and modifications of the formulae need to be employed. A prominent problem is the magnitude of the $\tau^{-1}/{\rm K}_2(\tau^{-1})$ term in the expression for the scattering kernel at electron temperatures below 10 keV. For an

electron temperature of 10 keV its value is 4.378×10^{24}, at 1 keV its value is 7.717×10^{225} and moving down to temperatures of 1 meV, the lower-end of temperatures we will investigate numerically, the corresponding value is $1.649 \times 10^{221924493}$. On this basis alone, any numerical computation of the scattering kernel would immediately require very high numerical precision indeed, particularly at temperatures below 1 keV. Accordingly, all of the numerical integrals in equations (134)–(140), particularly in the case of nearly elastic collisions, will be of corresponding numerical smallness so as to cancel such large terms, since the value of the scattering kernel in this case is generally of the order of unity. Consequently, these numerical integrals will also require substantial numerical precision in memory storage alone.

Another issue is the need to define an efficient algorithm which computes the integrals and sums in equations (5.130)–(5.136) with the minimum of computational overhead. Some integrals are repeated and consequently we introduce a new notation to make the formulation and its numerical implementation more transparent. Consider the following integral definition:

$$\mathcal{F}_k(a,b,\alpha) = \int_{\lambda_1}^{\lambda_2} \mathrm{d}\lambda\, \mathrm{e}^{-(\lambda-1)/\tau}\, \lambda^{\alpha}\, (1-\zeta)^b {}_2\mathrm{F}_1\left[a,b;b+1;x_2\right] \ . \tag{5.152}$$

We may now rewrite equations (5.130)–(5.136) as follows

$$I_{1,n} = \frac{2\gamma\gamma'(n+1)^{-1}}{\sqrt{\gamma^2+\gamma'^2}} \int_{\lambda_1}^{\lambda_2} \mathrm{d}\lambda\, \mathrm{e}^{-(\lambda-1)/\tau}\, \zeta^{n+1}\, \mathfrak{F}\left(\frac{1}{2}, n+1, x_1\right) \ , \tag{5.153}$$

$$I_{2,n} = \frac{1}{\sqrt{2}} \sum_{k=0}^{n} \mathcal{D}(n,k,1)\, \mathcal{F}_k\left(\frac{3}{2}, k+\frac{1}{2}, 0\right) \ , \tag{5.154}$$

$$I_{3,n} = \frac{(\gamma^{-1}+\gamma'^{-1})}{\sqrt{2}} \sum_{k=0}^{n} \mathcal{D}(n,k,1)\, \mathcal{F}_k\left(\frac{3}{2}, k+\frac{1}{2}, 1\right) \ , \tag{5.155}$$

$$I_{4,n} = \frac{1}{\sqrt{2}} \sum_{k=0}^{n+1} \mathcal{D}(n+1,k,1)\, \mathcal{F}_k\left(\frac{3}{2}, k+\frac{1}{2}, 0\right) \ , \tag{5.156}$$

$$I_{5,n} = \sqrt{2}\gamma\gamma' \sum_{k=0}^{n} \mathcal{D}(n,k,2)\, \mathcal{F}_k\left(\frac{1}{2}, k+\frac{3}{2}, 0\right) \ , \tag{5.157}$$

$$I_{6,n} = 2\sqrt{2} \sum_{k=0}^{n} \mathcal{D}(n,k,1)\, \mathcal{F}_k\left(\frac{1}{2}, k+\frac{1}{2}, 0\right) \ , \tag{5.158}$$

$$I_{7,n} = \frac{2\sqrt{2}}{\gamma\gamma'} \sum_{k=0}^{n} \mathcal{D}(n,k,0)\, \mathcal{F}_k\left(\frac{1}{2}, k-\frac{1}{2}, 0\right) \ , \tag{5.159}$$

where,

$$\mathcal{D}\left(n,k,l\right)=\frac{(-1)^{k+1}}{2k+2l-1}\binom{n}{k}. \tag{5.160}$$

Note that the integrals in equations (5.154) and (5.156) are identical, thus only the integral $\mathcal{F}_{n+1}\left(3/2,n+3/2,0\right)$ need be computed in $I_{4,n}$. With this, the scattering kernel may be written as

$$\sigma_{\mathrm{KN}}(\gamma\rightarrow\gamma',\tau)=\frac{\mathcal{C}\,\mathrm{e}^{-1/\tau}}{\gamma^2\,\tau\,\mathrm{K}_2(1/\tau)}T(\gamma,\gamma',\tau)\ , \tag{5.161}$$

where $T(\gamma,\gamma',\tau)$ is now defined in terms of equations (5.153)–(5.159), which is far less expensive to compute numerically. Now, the modified term $\tau^{-1}\mathrm{e}^{-\tau^{-1}}/\mathrm{K}_2(\tau^{-1})$, at an electron temperature of 10 keV has the value of 2.811×10^2, at 1 keV its value is 9.183×10^3 and at 1 meV its value is now 9.217×10^{12}. This method is readily parallelised, with each integral, or group of integrals, performed per CPU. Additionally, if the array $\mathcal{D}\left(n,k,l\right)$ is populated prior to runtime, and care is taken to handle positive and negative terms, then just one subtraction need be performed at the end. This method can be made very accurate. In the following subsection a numerical investigation of a code written in PYTHON to evaluate angular moments of the Compton scattering kernel is detailed.

Table 5.1: Relative errors for the first 6 moments of the Compton scattering kernel, evaluated at an electron temperature of 1 meV. Numbers between brackets denote multiplicative powers of 10. Absence of a double precision value indicates a relative error at double precision of greater than unity.

γ	δ	Precision	$\varepsilon_{n=0}$	$\varepsilon_{n=1}$	$\varepsilon_{n=2}$	$\varepsilon_{n=3}$	$\varepsilon_{n=4}$	$\varepsilon_{n=5}$
1 meV	10^{-6}	DD	1.11[-04]	2.39[-04]	3.95[-04]	8.94[-05]	2.68[-04]	3.55[-03]
		TD	1.80[-20]	6.13[-20]	5.64[-20]	8.14[-20]	5.33[-20]	6.37[-21]
	10^{-4}	DD	1.25[-06]	3.22[-05]	8.43[-05]	8.13[-05]	1.17[-04]	3.38[-04]
		TD	2.10[-21]	4.80[-21]	4.77[-21]	1.33[-20]	1.52[-20]	4.04[-19]
1 eV	10^{-6}	DD	7.35[-14]	2.94[-14]	2.06[-14]	7.74[-13]	2.01[-13]	7.24[-13]
		DD	7.35[-14]	2.94[-14]	2.06[-14]	7.74[-13]	2.01[-13]	7.24[-13]
		TD	1.17[-30]	4.60[-30]	8.05[-29]	1.39[-29]	3.92[-29]	3.62[-29]
	10^{-4}	DD	6.63[-15]	2.25[-14]	8.62[-14]	6.66[-14]	1.30[-13]	3.40[-13]
		TD	1.40[-30]	6.21[-30]	4.73[-30]	1.28[-29]	1.89[-29]	3.38[-29]
1 keV	10^{-6}	D	4.97[-05]	6.77[-05]	4.27[-06]	4.71[-04]	1.27[-03]	3.09[-03]
		DD	4.90[-21]	1.99[-21]	7.07[-21]	1.18[-21]	6.33[-21]	1.27[-20]
	10^{-4}	D	2.76[-03]	2.89[-03]	3.01[-03]	3.12[-03]	3.23[-03]	3.32[-03]
		DD	2.76[-03]	2.89[-03]	3.01[-03]	3.12[-03]	3.23[-03]	3.32[-03]
		TD	2.76[-03]	2.89[-03]	3.01[-03]	3.12[-03]	3.23[-03]	3.32[-03]
		QD	8.52[-31]	3.15[-18]	1.01[-10]	3.20[-10]	6.78[-10]	1.20[-09]

Table 5.2: As in Table 5.1, but now evaluated at an electron temperature of 1 keV.

γ	δ	Precision	$\varepsilon_{n=0}$	$\varepsilon_{n=1}$	$\varepsilon_{n=2}$	$\varepsilon_{n=3}$	$\varepsilon_{n=4}$	$\varepsilon_{n=5}$
1 meV	10^{-6}	DD	4.18[-02]	2.42[-01]	6.15[-02]	5.40[-01]	9.72[-01]	5.24[-01]
		TD	9.27[-18]	5.83[-17]	2.12[-17]	1.97[-17]	6.83[-18]	1.46[-16]
	10^{-4}	DD	1.47[-02]	3.75[-02]	2.48[-02]	4.83[-02]	3.08[-02]	5.19[-02]
		TD	1.24[-18]	3.22[-18]	2.27[-18]	3.25[-18]	2.53[-18]	3.85[-18]
	10^{-2}	DD	3.53[-04]	1.32[-03]	7.55[-04]	1.86[-03]	1.13[-03]	2.42[-03]
		TD	8.67[-21]	1.31[-20]	4.06[-21]	4.40[-20]	1.88[-20]	5.94[-20]
	1	DD	5.47[-06]	1.12[-04]	1.18[-04]	5.39[-05]	1.08[-04]	9.49[-04]
		TD	6.25[-21]	7.72[-21]	3.13[-21]	6.42[-21]	9.38[-21]	4.30[-20]
1 eV	10^{-6}	DD	9.24[-11]	3.06[-10]	7.12[-11]	4.13[-10]	1.61[-10]	7.85[-11]
	10^{-4}	DD	2.35[-12]	2.78[-12]	1.27[-12]	6.32[-12]	2.89[-12]	9.84[-12]
	10^{-2}	DD	2.37[-14]	2.05[-14]	1.54[-14]	3.02[-14]	1.04[-13]	4.93[-14]
	1	DD	4.39[-13]	1.23[-14]	2.77[-14]	4.07[-13]	3.44[-13]	3.88[-14]
1 keV	10^{-6}	D	1.75[-03]	5.55[-03]	2.98[-03]	1.80[-03]	2.40[-03]	7.01[-03]
		DD	7.19[-20]	4.63[-19]	5.24[-19]	7.15[-19]	1.85[-19]	7.73[-19]
	10^{-4}	D	1.65[-05]	2.15[-05]	2.30[-05]	3.74[-05]	1.07[-05]	3.07[-05]
		DD	2.35[-12]	2.78[-12]	1.27[-12]	6.32[-12]	2.89[-12]	9.84[-12]
	10^{-2}	D	1.71[-07]	4.90[-07]	7.27[-08]	2.18[-07]	6.10[-07]	1.34[-07]
		DD	2.00[-24]	1.31[-23]	2.81[-23]	1.29[-22]	1.80[-23]	1.17[-22]
	1	DD	8.16[-25]	3.83[-23]	8.84[-23]	1.92[-22]	2.66[-22]	6.29[-22]
1 MeV	10^{-6}	D	6.15[-11]	1.17[-11]	5.47[-11]	2.94[-11]	7.44[-11]	5.20[-11]
		DD	1.25[-27]	4.58[-27]	6.01[-27]	9.13[-27]	4.43[-27]	9.32[-27]
	10^{-4}	D	3.47[-13]	5.52[-13]	3.74[-13]	1.56[-13]	1.94[-13]	2.49[-13]
		DD	2.10[-28]	2.01[-28]	2.44[-28]	2.11[-28]	1.97[-28]	2.59[-28]
	10^{-2}	D	4.24[-14]	5.83[-14]	5.84[-13]	6.21[-12]	2.84[-11]	7.30[-11]
		DD	4.52[-30]	3.25[-30]	4.36[-30]	5.11[-30]	4.25[-30]	3.95[-30]
1 GeV	10^{-6}	D	5.70[-09]	5.70[-09]	5.70[-09]	5.70[-09]	5.70[-09]	5.70[-09]
		DD	1.22[-23]	1.22[-23]	1.22[-23]	1.22[-23]	1.22[-23]	1.22[-23]
	10^{-4}	D	2.81[-01]	2.81[-01]	2.81[-01]	2.81[-01]	2.81[-01]	2.81[-01]
		DD	2.81[-01]	2.81[-01]	2.81[-01]	2.81[-01]	2.81[-01]	2.81[-01]
		TD	5.99[-08]	5.99[-08]	5.99[-08]	5.99[-08]	5.99[-08]	5.99[-08]
		QD	1.25[-30]	1.02[-17]	2.04[-17]	3.06[-17]	4.08[-17]	5.10[-17]

5.10.3 Numerical tests

The computation of the angular moments of the Compton scattering kernel is based on the solution of many integrals of the form given in equations (5.152) and (5.153). I have written a code using the arbitrary-precision mathematics package MPMATH in PYTHON 2.7.3 from the Enthought PYTHON Distribution 7.3-1 (64 bit). All calculations were performed on a Mid-2009 MacBook Pro with a 3.06GHz Intel Core 2 Duo CPU with 8GB of 1067 MHz DDR3 RAM - no computer-specific optimisations were performed. The code was designed and tested on Mac OSX 10.8.2, compatible with any OS with PYTHON and MPMATH installed.

To illustrate the functionality of the method and its accuracy in numerical computations, the relative error, ε, is calculated for the first six angular moments of the Compton scattering kernel. This is done for a broad range of photon energies, from $\gamma = 1$ meV to $\gamma = 1$ GeV. The relative error is calculated with respect to an arbitrary precision code written in MATHEMATICA. Consequently, ε is defined with respect to the exact numerical value. Values of σ_{KN} of magnitude less than 10^{-100} are neglected. The code is evaluated first with 53 bits of numerical precision (double precision - D). If the relative error is not less than 10^{-12} then σ_{KN} is evaluated with 106 bit precision (double-double - DD), 159 bit precision (triple-double - TD) and, if necessary, with 212 bits of precision (quad-double - QD). Two electron temperatures are chosen for numerical testing, 1 meV and 1 keV. The outgoing photon energy, γ', is iterated as $\gamma' = (1 + \delta)\gamma$, with δ taking the values 10^{-6}, 10^{-4} and 10^{-2} (for $\delta \gtrsim 1$, σ_{KN} is negligibly small).

There are no freely available codes in the literature which can compute successive angular moments of the Compton scattering kernel. Consequently, I have written a code in MATHEMATICA 9 which computes the angular moments to arbitrary order. The results from MATHEMATICA are compared with those obtained from the arbitrary precision PYTHON code, evaluating the relative error ε between the two.

In Table 1 the relative errors are computed for an electron temperature of 1 meV. It is clear that at low incident photon energies, namely 1 meV and

1 eV, double precision arithmetic is insufficient. Further, at $\gamma = 1$ meV, even the errors at double-double precision are not sufficiently small, so the result for triple-double precision is displayed. By photon energies of $\gamma = 1$ keV double precision results become no worse than a few parts in 10^3.

In Table 2 the relative errors are computed for an electron temperature of 1 keV. As before, at sub-keV double-double, and even triple-double arithmetic precision becomes necessary. However, by photon energies of 1 keV, double precision arithmetic is again sufficient. In those regions where γ is large and the relative error at double precision is of the order of 10^{-3} or greater, the value of the scattering kernel is significantly less than unity, generally of the order of 10^{-50} or less. As the electron temperature increases still higher the results become even more accurate at double precision, following the same underlying trends.

Clearly the method presented does not fare so well at low photon energies ($\gamma,\ \gamma' \ll 1$), as well as in regions where $|\gamma - \gamma'| \ll 1$ and $\tau \ll 1$ and so we must resort to numerical precision greater than that of standard double precision. Regarding computation time, at double precision the numerical results can take from a few tenths of seconds to a few tens of seconds. Computation time increases drastically with increased numerical precision. It is important to stress that the system architecture these calculations were performed on was a laptop, and there is tremendous scope to improve the implementation of the method itself.

Central to the method is the solution of specific definite integrals, allowing straightforward parallelisation of the numerical scheme. Further, by careful consideration of positive and negative terms, only one subtraction need be performed per moment evaluation, greatly reducing round-off error (since the integral in equation (5.152) is always positive). The terms $\mathcal{D}(n, k, l)$ may be tabulated prior to runtime and all values of $\mathcal{F}_k$ can be stored in an appropriate array. In addition, the integrals themselves could be pre-calculated on a standard grid of cases, with interpolation performed on this grid at run-time. In the regions where double precision accuracy is insufficient, asymptotic series expansions may be employed, particularly where $\tau \to 0$, $(\gamma, \gamma') \to 0$, $\gamma/\gamma' \to 1$

and γ fixed with $\gamma' \to 0$ (and vice-versa). The aforementioned refinements would make the Compton scattering code very robust across a much broader energy range, specifically at lower energies (in the eV range and below).

However, in most regions of astrophysical interest, particularly in the situations investigated in this thesis, electron and photon energies are of the order of keV energies or greater. In this energy range the numerical scheme presented performs well at standard double precision and becomes more accurate as energy increases. Whilst this method is already applicable in high-energy astrophysical situations, the aforementioned refinements will not only make it more reliable in the $\gtrsim$ keV range investigated in this thesis, but also extend its application to the eV range and below.

5.11 Numerical Results

The method presented in this Chapter can easily be generalised to include the evaluation of moments of the cross-section in terms of more general functions of ζ, such as Legendre polynomials. This is shown in Appendix C.

The computed moments of the Compton scattering kernel (in arbitrary units, i.e. $\mathcal{C} = 1$) are plotted as a function of scattered photon energy in Figures 5.7–5.11. Figures 5.7 and 5.8 illustrate the dependence of the zeroth moment of the scattering kernel on the electron temperature, for various incident photon energies. Figure 5.9 shows the dependence of the 1st, 2nd, 3rd, 4th and 5th moments of the scattering kernel for an incident photon energy of 40 keV and an electron temperature of 1 keV (top) and 20 keV (bottom). Figure 5.10 is similar to Figure 5.9, except that the incident photon energy is 100 keV. Figure 5.11 is as in Figure 5.10, except the incident photon energy is now 300 keV.

The parameters for the plots in these figures were chosen to enable comparison with previous numerical calculations by Pomraning (1972, 1973) in which the angular moments are expanded in terms of Legendre polynomials $P_n(\zeta)$. Without a closed-form expression for the scattering kernel, Pomraning (1972, 1973) employed a fully numerical approach in his calculations. Although Pomraning employed a Legendre polynomial moment expansion, different functions

for the moment expansions have been considered in this work. In the classical limit, the zeroth order terms in both calculations are identical, enabling direct comparison.

Figures 5.7 and 5.8 indeed show that the zeroth order moments obtained by the closed-form expression I derived are the same as those obtained by the Legendre polynomial expansion of Pomraning (1972). The zeroth order moments of the kernel that were computed for various electron temperatures are consistent with Monte-Carlo simulations of Compton scattering of monochromic emission lines shown in Pozdniakov et al. (1979) and Pozdnyakov et al. (1983).

In practical radiative transfer calculations, the full radiative transfer equation with scattering can in principle be decoupled, in a truncated moment expansion, into a series of coupled ordinary differential equations (Thorne 1981; Fuerst 2006; Wu et al. 2008). In solving the full radiative transfer equation in curved space-times, a covariant generalisation of the Eddington approximation may be employed. Coupled with the aforementioned closed-form expressions for the angular moments, this yields a semi-analytic approach, necessitating the evaluation of two numerical integrals over λ and γ (or γ', by detailed balance). The inclusion of this formulation into a truncated moment expansion, as well as its subsequent solution, is left for future study. The work presented in this Chapter has been published in Younsi and Wu (2013).

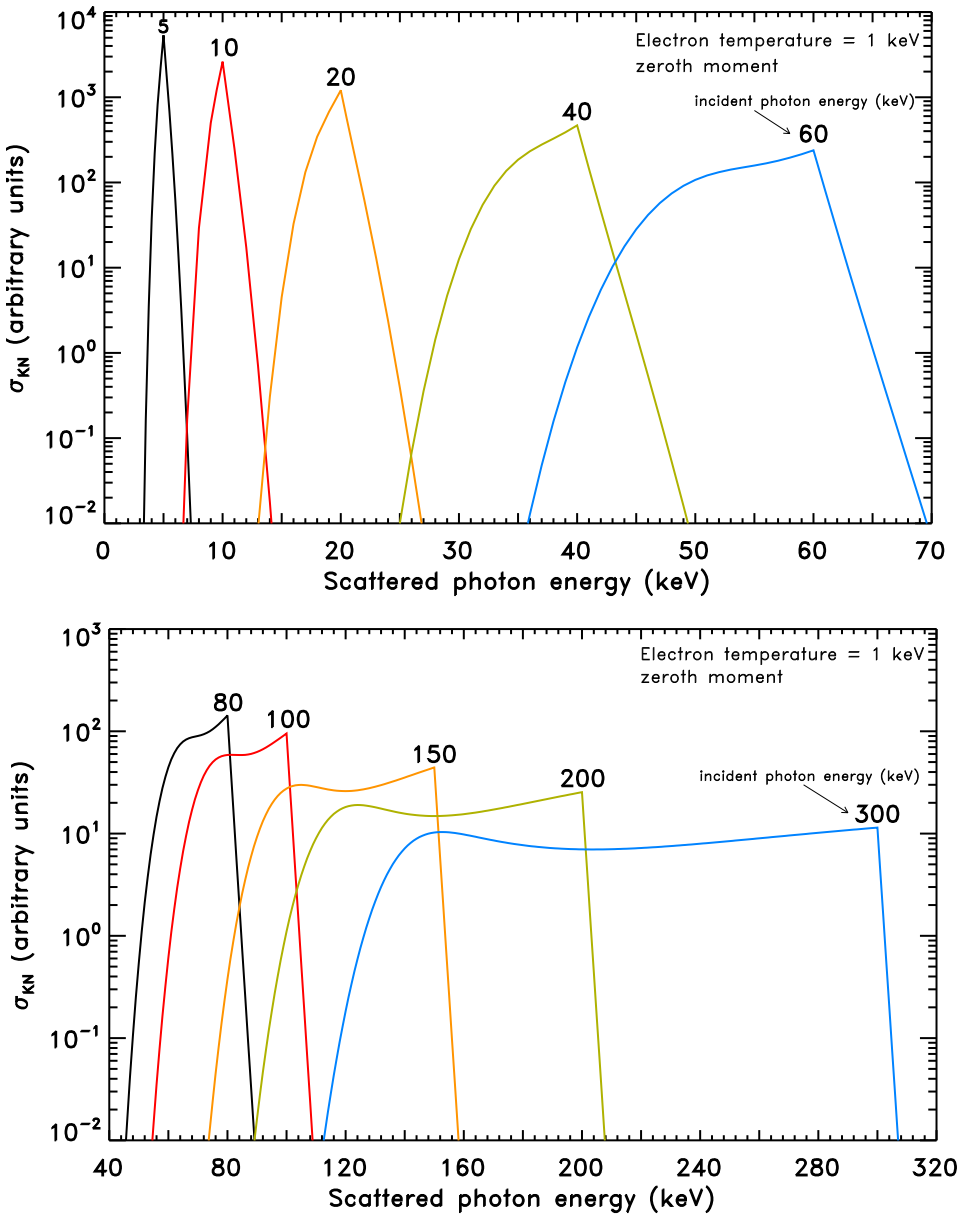

Fig. 5.7: Zeroth moment of the Compton scattering kernel (as a function of scattered photon energy) evaluated at an electron temperature of 1 keV. Top: incident photon energies of 5 keV, 10 keV, 20 keV, 40 keV and 60 keV. Bottom: incident photon energies of 80 keV, 100 keV, 150 keV, 200 keV and 300 keV.

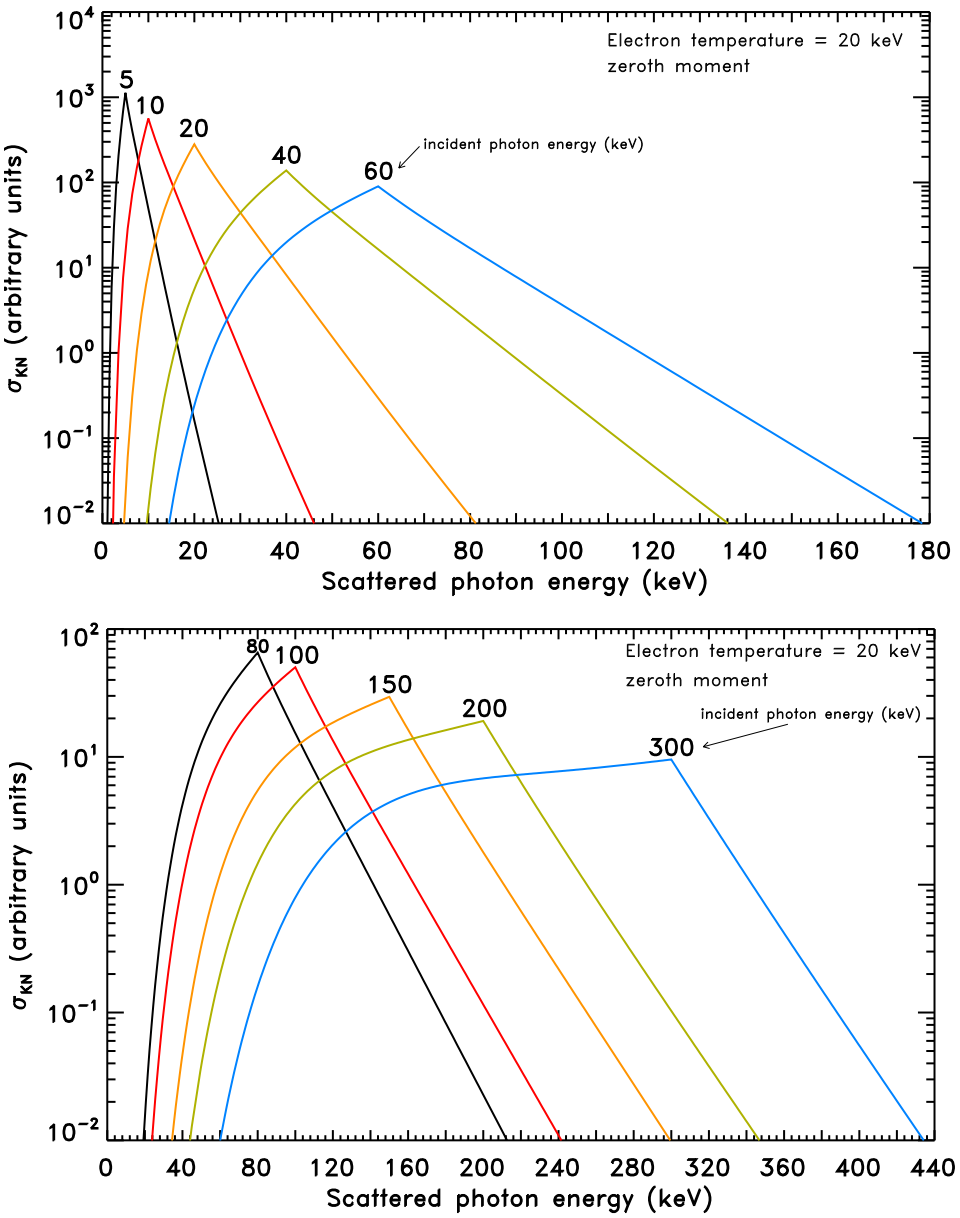

Fig. 5.8: Zeroth moment of the Compton scattering kernel (as a function of scattered photon energy) evaluated at an electron temperature of 20 keV. Top: incident photon energies of 5 keV, 10 keV, 20 keV, 40 keV and 60 keV. Bottom: incident photon energies of 80 keV, 100 keV, 150 keV, 200 keV and 300 keV.

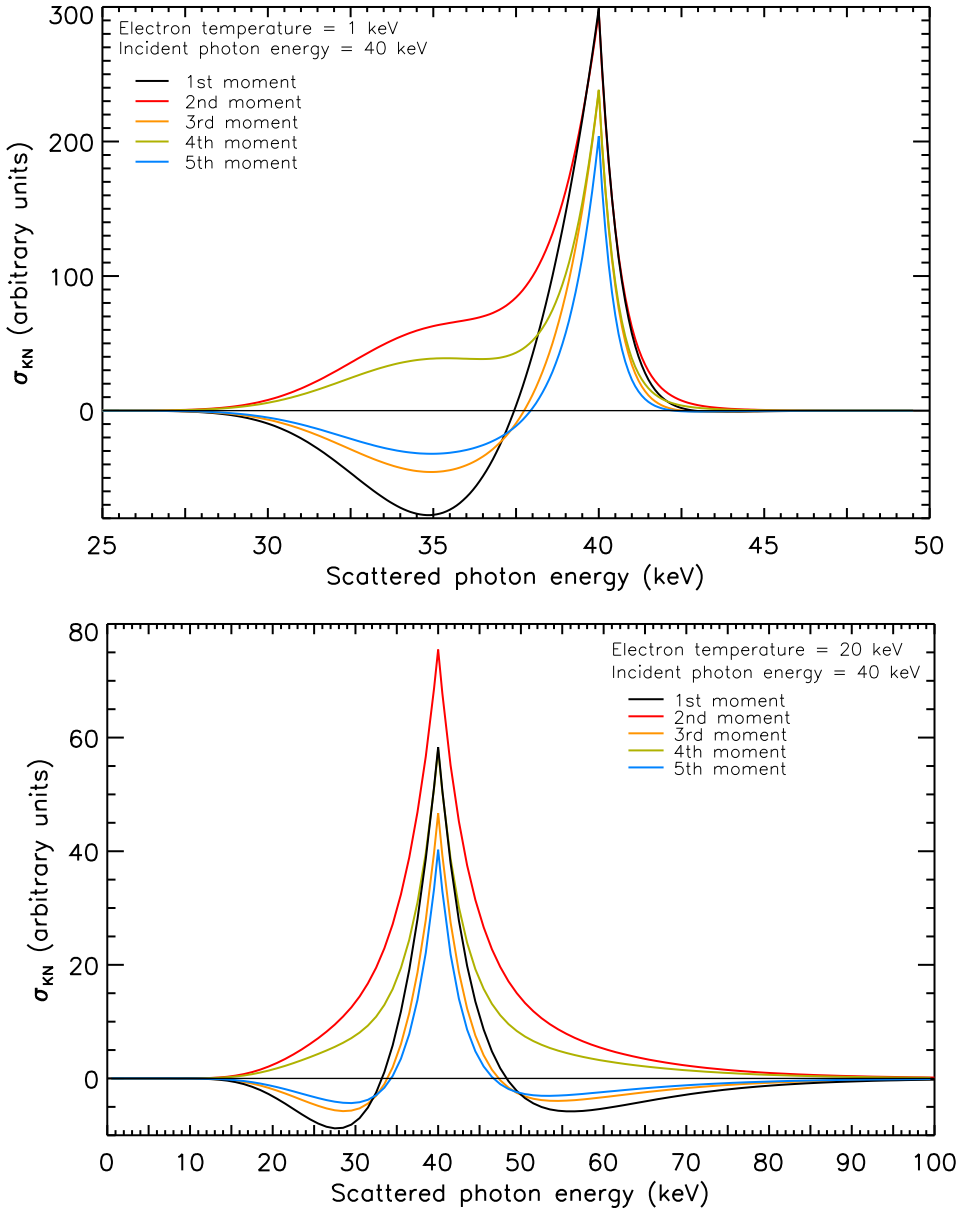

Fig. 5.9: The 1st, 2nd, 3rd, 4th and 5th moments of the Compton scattering kernel (as a function of scattered photon energy) evaluated at an incident photon of energy of 40 keV. Top: electron temperature of 1 keV. Bottom: electron temperature of 20 keV.

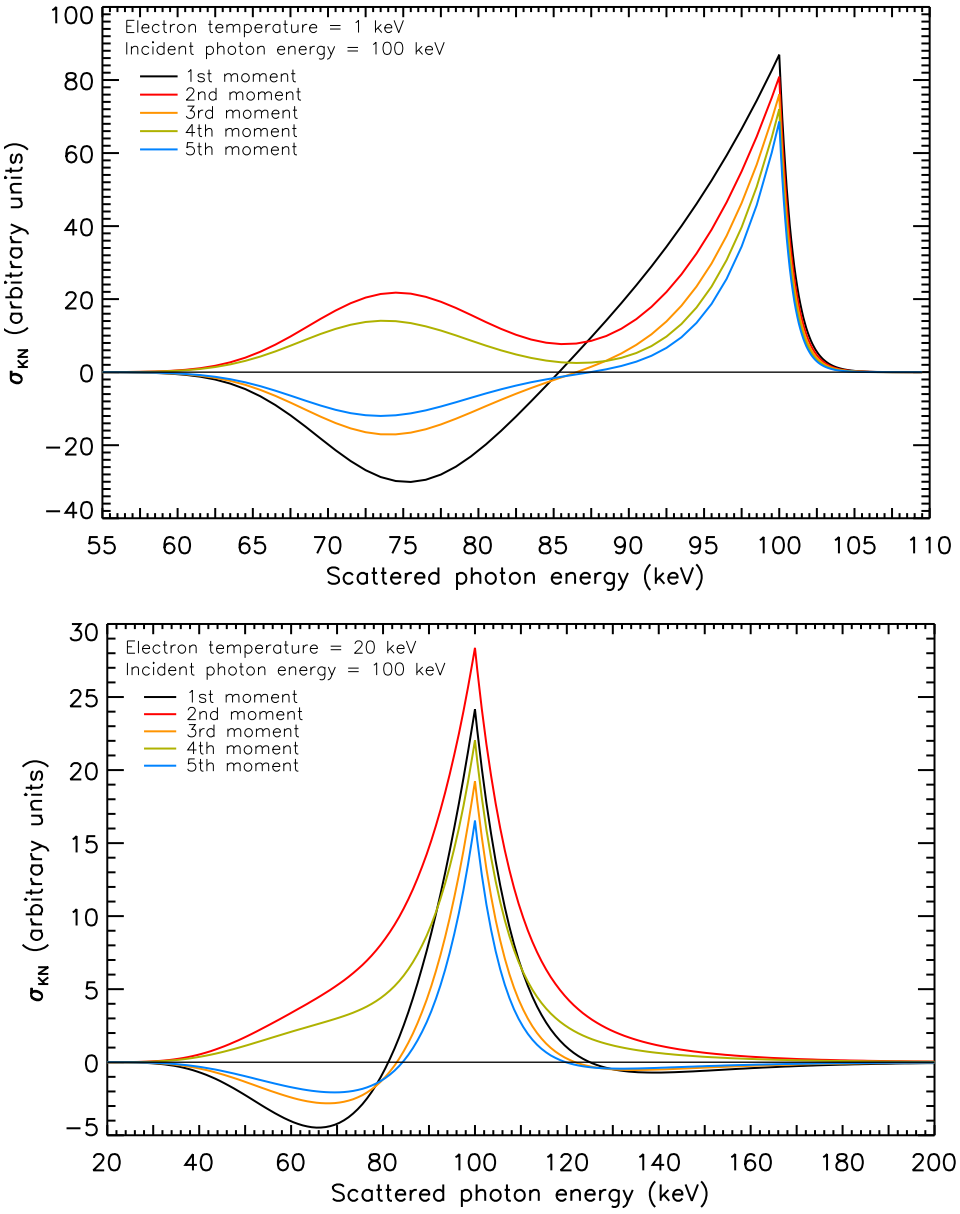

Fig. 5.10: The 1st, 2nd, 3rd, 4th and 5th moments of the Compton scattering kernel (as a function of scattered photon energy) evaluated at an incident photon of energy of 100 keV. Top: electron temperature of 1 keV. Bottom: electron temperature of 20 keV.

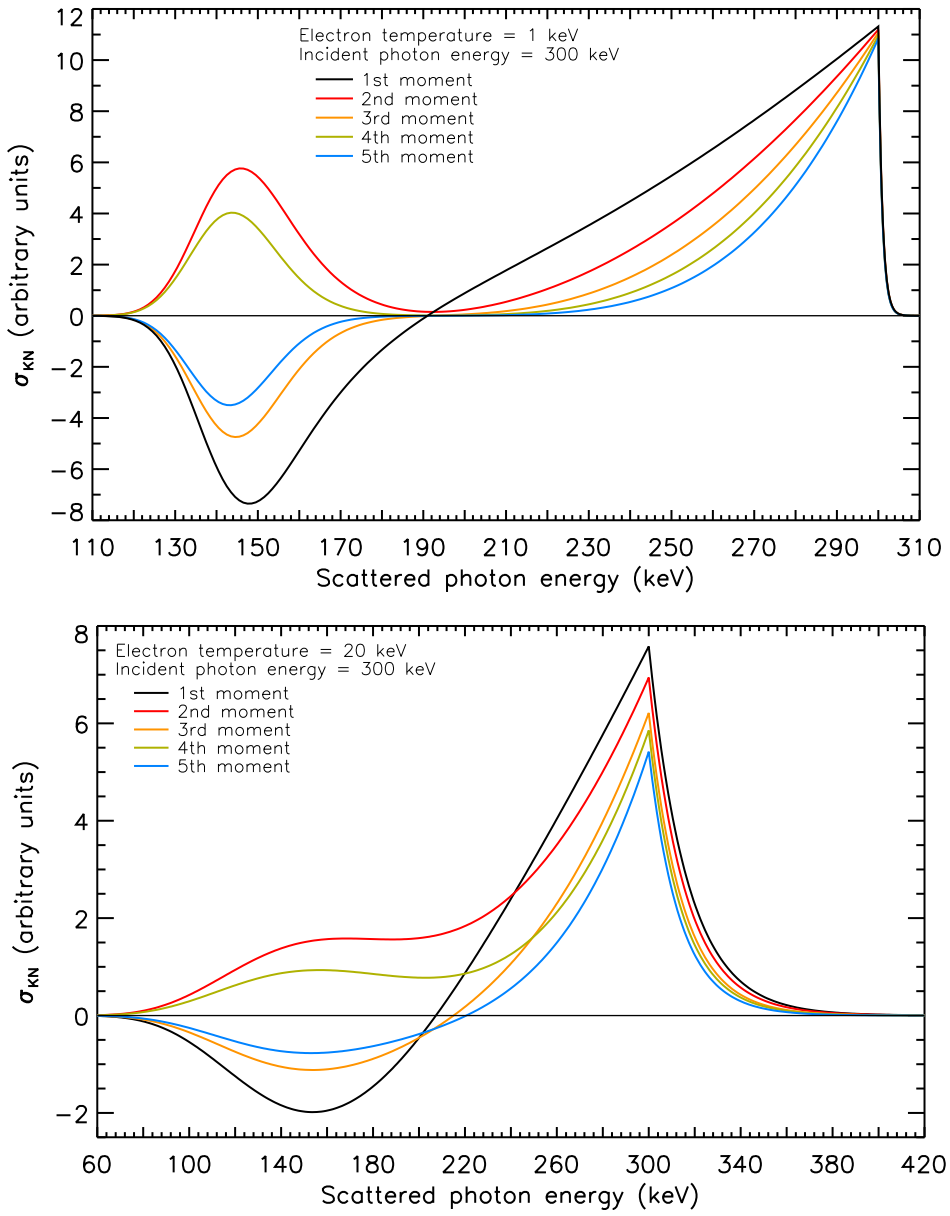

Fig. 5.11: The 1st, 2nd, 3rd, 4th and 5th moments of the Compton scattering kernel (as a function of scattered photon energy) evaluated at an incident photon of energy of 300 keV. Top: electron temperature of 1 keV. Bottom: electron temperature of 20 keV.

Chapter 6

Time-Dependent Radiative Transfer

Previous calculations presented in Chapter 4 of the emission from accretion disks and accretion tori assumed that variability in the source emission was sufficiently low to calculate an image of the entire emitting region, as well as its corresponding spectra. Changes in the size and shape of the emitting region, as well as its emission properties, were neglected as a first approximation. In reality, particularly close to the event horizon of a rapidly spinning Kerr black hole, dynamical timescales can become very short indeed. For example, the orbital period of a material particle in an accretion disk at 2 $r_{\rm g}$ around a Kerr black hole is roughly 24 $r_{\rm g}/c$. For a $\sim 10^6 M_\odot$ black hole (e.g. Sgr A*) this would correspond to an orbital period of roughly 8 minutes, which is very short (compared to the integrated observation times of current telescopes). However for a $\sim 10^9 M_\odot$ black hole (e.g. the SMBH in M87), this corresponds to an orbital period of over five-and-a-half days. Observations of variability in black hole systems therefore depend strongly on the mass of the central object.

Black holes show variability across multiple bands, and it is known that much information is contained in this time-varying emission, particlularly close to the black hole event horizon where the inner-edge of the accretion disk is determined by the spin of the black hole alone. Fundamental information about the black hole is lost through degeneracy (i.e. smeared out) in observed and calculated spectral profiles. A time-dependent spectrum, or spectrogram, must instead be constructed. This spectrogram may be integrated at the relevant points in time to give spectra similar to those seen in Chapter 4. By

integrating over photon energy, the net flux may be obtained as a function of time, i.e. a light curve. It is of practical interest to study light curves of time-varying features as they are an important probe of dynamical features in these systems and very sensitive to key black hole parameters like the mass and spin, as well as the inclination angle.

In this Chapter, I extend the formalism developed in Chapters 3 and 4 to perform radiative transfer calculations where variability is high and both the spatial distribution and radiative properties of the emitting medium fluctuate rapidly.

6.1 Calculating Time-Delayed Emission

A first step in calculating time-dependent emission is accounting for the differences in photon arrival times from different locations on an emission source at a particular observer time. Consider an observer making an observation of a time-varying source. In numerical computations the observer effectively observes all photons instantaneously and the observation time window is zero. In reality a source is observed over a certain time interval, with the detector having a particular time resolution. In time-dependent radiative transfer calculations, an observation is made for a particular time window. Photon arrival times must be binned, with the fineness of temporal bins corresponding to the time resolution of the observation.

The observation time $t_{\rm total}$ ($\sim$ 1 orbital period in all calculations) is divided into n (typically 100) equally spaced time intervals. At each interval $t_{{\rm obs},i}$, where i denotes the i-th such interval ($i \in [0, n]$), the spatial position of the plasmoid, along with its emissivity profile, is specified. Ray-tracing is then performed and for all rays which originate from the plasmoid, their 4-momentum, redshift and time delay are recorded and the emissivity of each ray is calculated. Thus $n + 1$ images of the plasmoid's position as it performs one full orbital period are calculated.

Since the observer image plane is located considerably far from the black hole, there are two time delays to account for: the time delay for photon travel time from the point of emission to the point it is received at the observer, and

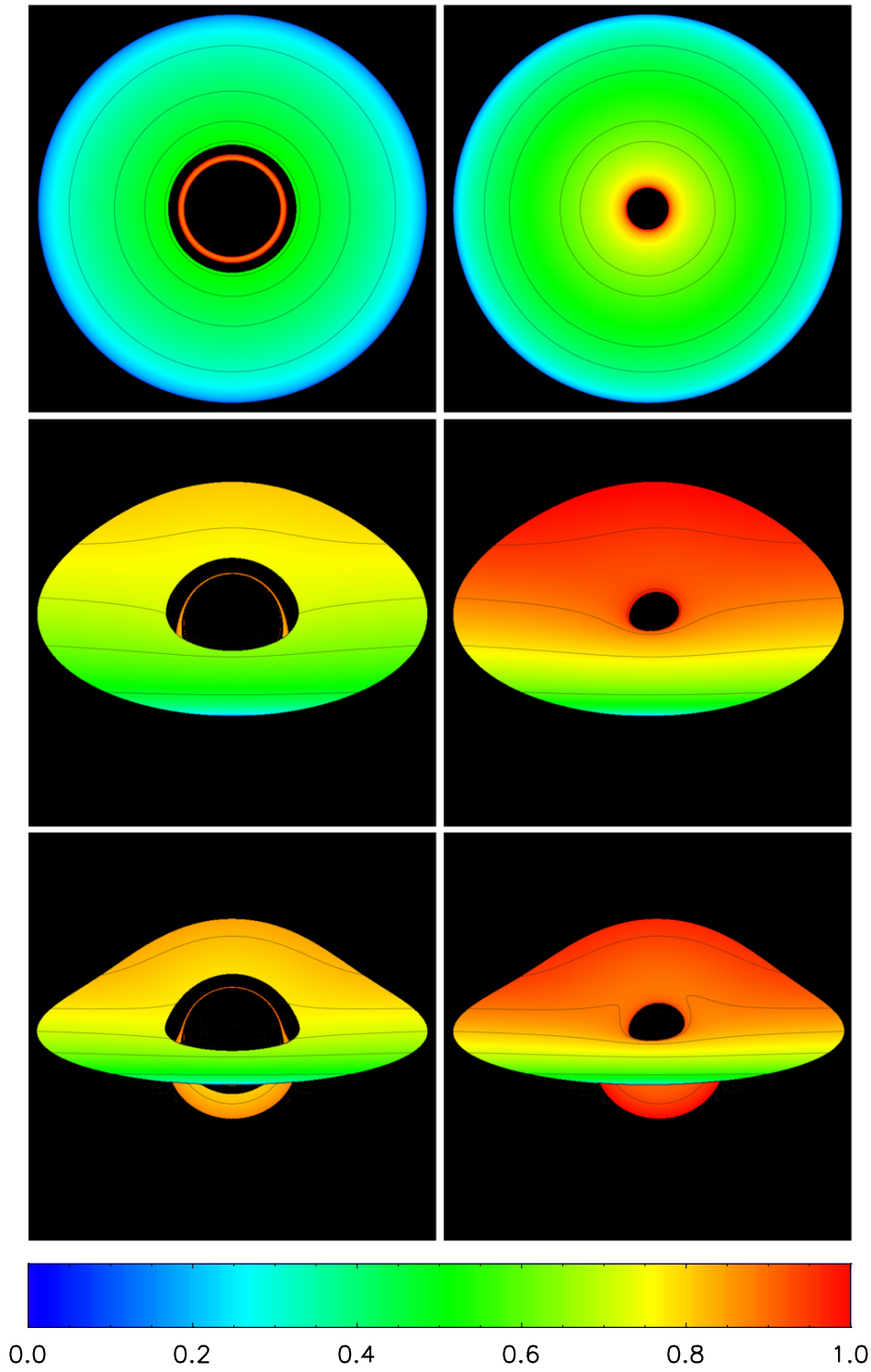

Fig. 6.1: Time delay images of geometrically thin, optically thick accretion disks viewed at inclination angles of $i = 0°$ (top), $i = 60°$ (middle) and $i = 75°$ (bottom). The black hole spin parameters are $a = 0$ (left) and $a = 0.998$ (right). The inner and outer radii of the disk are the ISCO and 20 r_g respectively. Solid black lines indicate constant-time contours. Contours of equal time have different radial locations in different spin black holes viewed at the same inclination angle, due to the differing Keplerian rotational velocities in the disk. The effects of frame-dragging can be seen in the innermost time contour of the bottom right ($a = 0.998$, $i = 75°$) image. The images are normalised such that the brightness of the brightest pixel in each image is the same (see accompanying text).

the relative time delay between neighbouring photons as a consequence of the differing gravitational redshifts they experience. In order to remove the effects of photon arrival time delay between the emitter and the observer, in the first image ($t_{\rm obs,0}$) the photons are sorted by arrival time and stored in an array $\mathbf{t}_i$. The arrival time of the first photon to be received is then subtracted from all other photon arrival times for that image, i.e. $\mathbf{t}_0 - \mathrm{MIN}\{\mathbf{t}_0\}$. In this way, only the relative time delay between photons in the image is considered, and the distance of the observer from the black hole has a negligible effect on the observed emission. This process is then repeated for all subsequent images, with the time between each interval $t_{\rm obs,i}$ added to every pixel in the corresponding i-th image. Thus, the recorded arrival time for each photon, $\mathbf{t}_{{\rm rec},i}$, is calculated as

$$\mathbf{t}_{{\rm rec},i} = \mathbf{t}_i - \mathrm{MIN}\{\mathbf{t}_i\} + t_{{\rm obs},i} \ . \tag{6.1}$$

Received photons are then binned by time, with those received after a time $t_{\rm total}$ (typically ~ 1 orbital period) omitted from further calculations.

The basic algorithm is demonstrated in Figure 6.1, which shows plots of steady geometrically thin, optically thick accretion disks coloured by the time delay of each photon relative to its neighbours. All arrival times $\mathbf{t}_{{\rm rec},i}$ are normalised into the range $[0,1]$ by evaluating $(\mathbf{t}_{{\rm rec},i} - \mathrm{MIN}\{\mathbf{t}_{{\rm rec},i}\})/\Delta t$, where $\Delta t \equiv \mathrm{MAX}\{\mathbf{t}_{{\rm rec},i}\} - \mathrm{MIN}\{\mathbf{t}_{{\rm rec},i}\}$. This is indicated by the accompanying colour bar in Figure 6.1. This normalisation is applied to all calculated images in this Chapter.

6.2 Orbiting Plasmoid

The orbiting plasmoid/hot spot/blob model had been employed by several authors in the context of Sgr A* (e.g. Broderick and Loeb 2005; Meyer et al. 2006; Doviak et al. 2006; Noble et al. 2007; Zamaninasab et al. 2011). It is shown here as a test of the new formulation, and to discuss qualitatively the important features of time-dependent emission from black hole systems.

Ray-tracing from the image plane to the accretion disk, each ray bundle is labeled with a distinct position, 4-momentum and time delay. Using this information, time-dependent images of the disk are constructed from time-

varying emission models. The plasmoid is modelled as a spheroidal overdensity of non-thermal electrons centered at a point on the accretion disk orbiting at the local Keplerian velocity. Since $x^2 + y^2 + z^2 = r^2 + a^2 \sin^2\theta$, for high black hole spins the plasmoid becomes oblate spheroidal in shape (i.e. compressed in the z-direction). The plasmoid is taken to be optically thick and the emissivity on its surface is modelled as a Gaussian in the z-direction, given by

$$j_\nu\left(z,t\right) \propto \exp\left\{-\frac{\left[z - z_{\rm p}(t)\right]^2}{r_{\rm p}^2}\right\} \ , \tag{6.2}$$

where $z_{\rm p}\left(t\right)$ is the plasmoid position at time t and $r_{\rm p}$ is the plasmoid radius. The position $z \equiv r\cos\theta$ in BL co-ordinates. In all subsequent calculations, emission that is located outside of 5 $r_{\rm p}$ of the initial geodesic trajectory (i.e. the first ray to reach the observer) is truncated. In all subsequent calculations the plasmoid radius is fixed as $r_{\rm p} = 0.5\ r_{\rm g}$. The resultant normalised lightcurves and spectrograms are weakly dependent on the plasmoid radius.

All matter in the plasmoid is assumed to be moving at the same 4-velocity as the initial trajectory. Tabulating the plasmoid trajectory as a function of time, the observing region is divided into n equally spaced time intervals, with $n = 100$ taken for all calculations. Employing the prescription in equation (6.1), static images of the plasmoid at each time interval are ray-traced. This is done for one full orbit of the plasmoid.

Two different cases are considered: a plasmoid orbiting a non-rotating ($a = 0$) black hole, at a distance of $r_{\rm c} = 6.5\ r_{\rm g}$[1] (i.e. at the ISCO). The second case places the plasmoid in orbit around an $a = 0.998$ Kerr black hole at a distance of $r_{\rm c} = 2.5\ r_{\rm g}$, i.e. within 0.8 $r_{\rm g}$ of the ISCO. The plasmoid is orbiting in an anticlockwise direction (as seen from above) with a Keplerian angular velocity.

Time delay images of a plasmoid orbiting a black hole with spin parameter $a = 0$ (left panels) and a black hole with spin parameter $a = 0.998$ (right panels) are illustrated in Figures 6.2–6.5. When viewed from directly above ($i = 0°$), there is no change in apparent shape as the plasmoid orbits the black hole. The ultra-relativistic velocities close to the event horizon (in the right

[1]This distance is chosen so that the inner radius of the plasmoid coincides with the ISCO

Fig. 6.2: Snapshot images of a plasmoid orbiting black holes with spins of $a = 0$ (left) and $a = 0.998$ (right). The plasmoid is orbiting in the e_ϕ-direction, i.e. anticlockwise as viewed from above. From top to bottom: orbital phases $\phi = 0°$, $\phi = 90°$, $\phi = 180°$ and $\phi = 270°$. The observer inclination angle $i = 0°$ in all images. For $a = 0$, the plasmoid deviates only slightly from its spherical shape, as Doppler effects are moderate at $r_c = 6.5\ r_g$. For $a = 0.998$, at $r_c = 2.5\ r_g$ gravitational lensing is significant and the plasmoid appears elongated in its direction of propagation. Arcs of emission are higher-order images from the plasmoid that orbit the black hole multiple times before reaching the observer. Same colour coding as Figure 6.1.

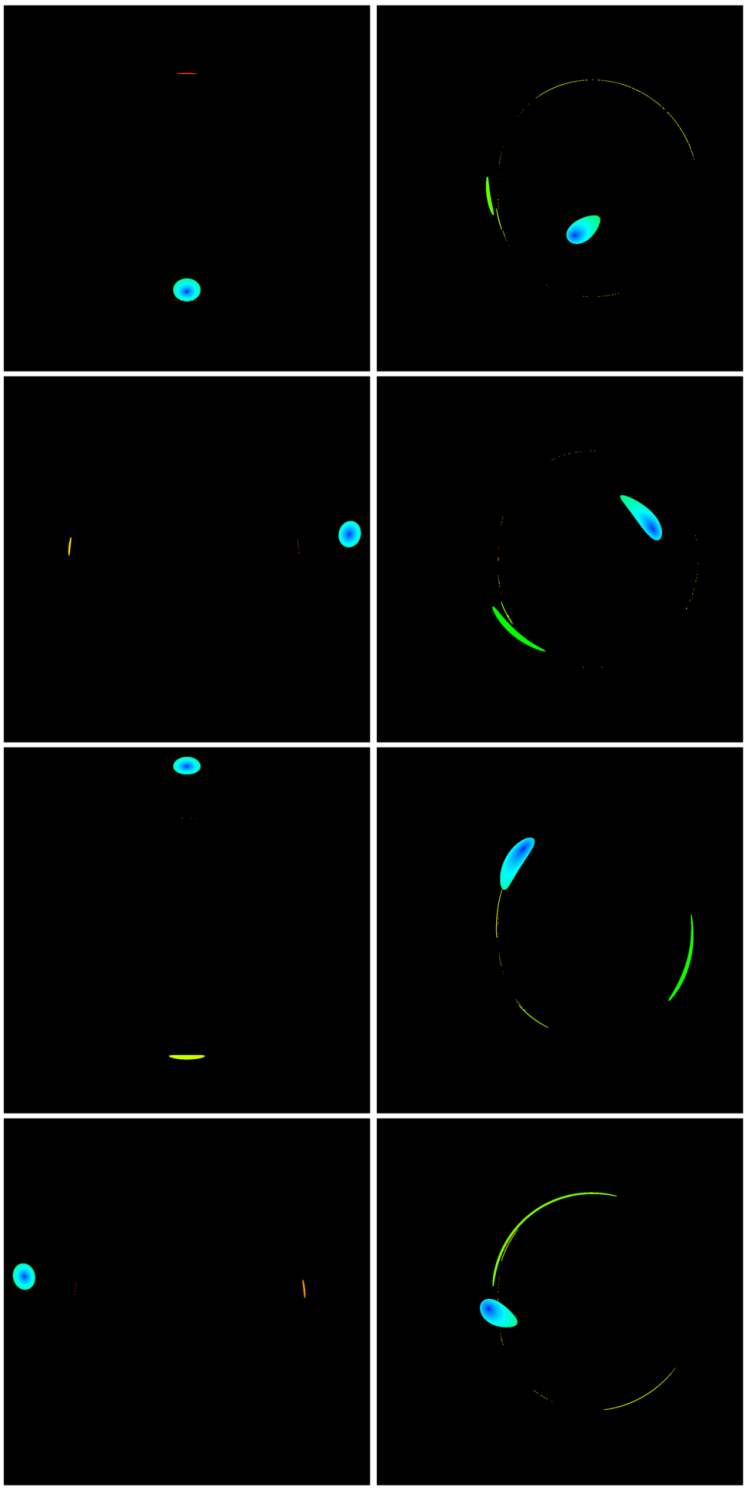

Fig. 6.3: As in Figure 6.2, but now viewed at an observer inclination angle $i = 45°$. At $\phi = 180°$, i.e. when the plasmoid is directly behind the black hole, the direct image and opposite first-order images are more elongated and larger in surface area.

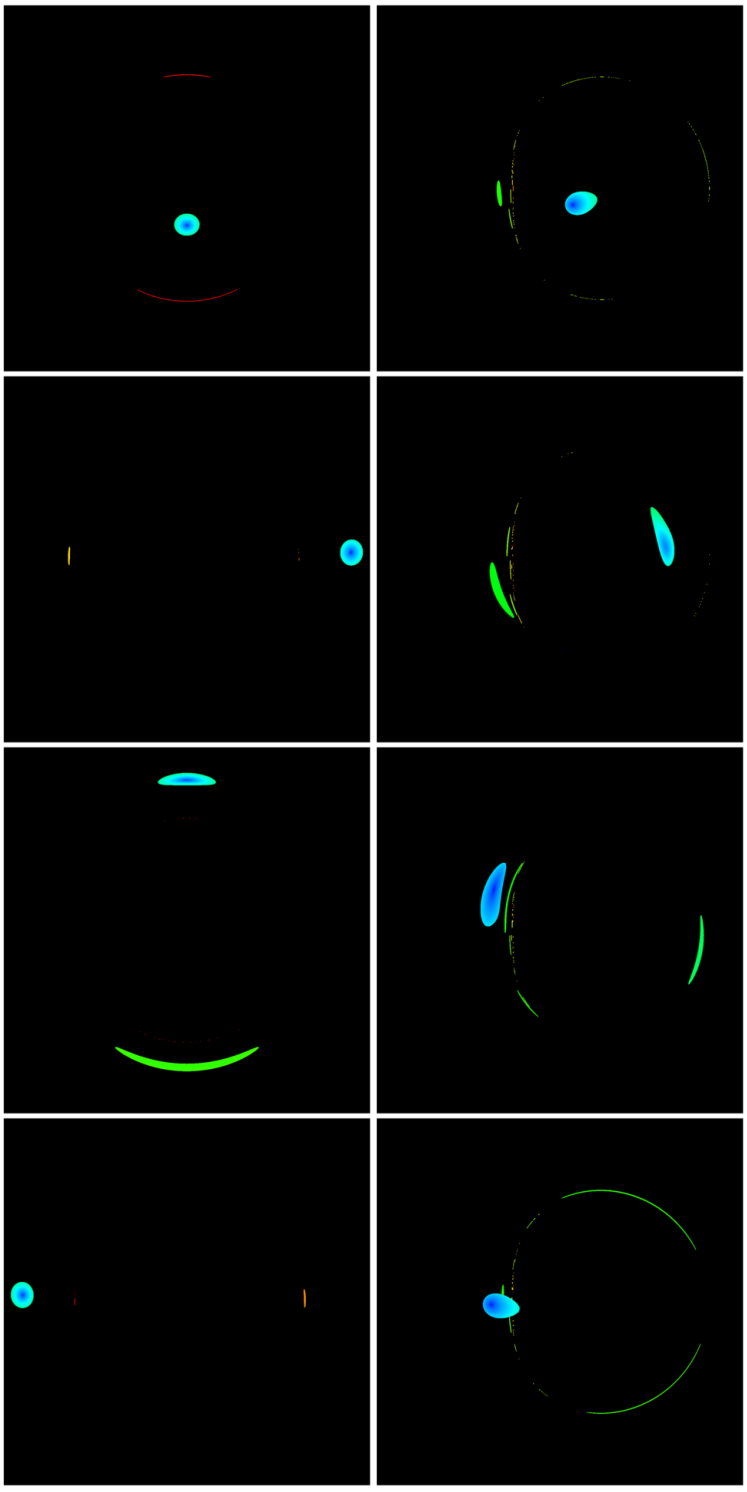

Fig. 6.4: As in Figure 6.3, but now viewed at an observer inclination angle $i = 75°$. Now when the plasmoid is directly behind the black hole, the direct image and opposite first-order images are even more pronounced as gravitational lensing starts to dominate.

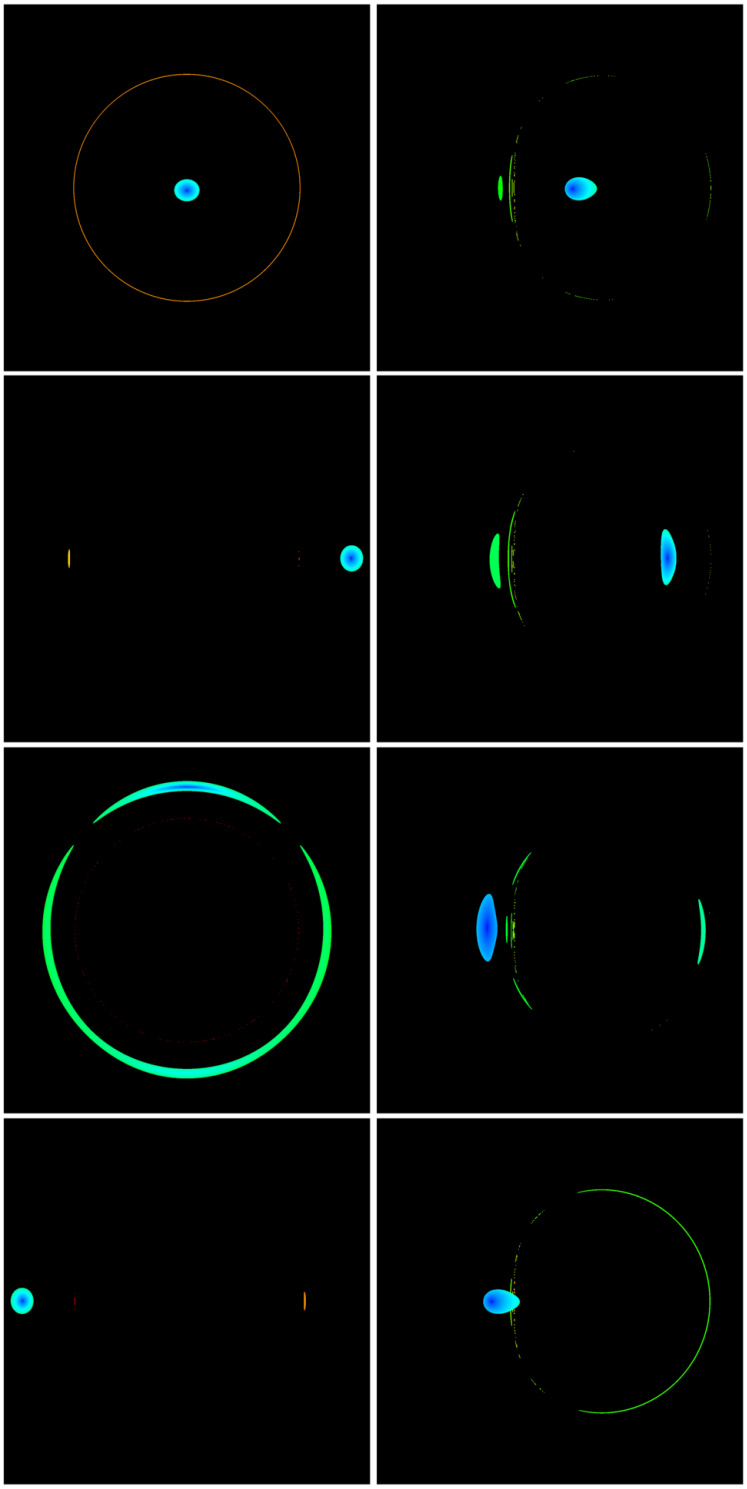

Fig. 6.5: As in Figure 6.4, but now viewed at an observer inclination angle $i = 89°$. When the plasmoid is directly behind the black hole, in the case of an $a = 0$ black hole a near-complete Einstein ring forms (this would be complete at $i = 90°$). The direct image and opposite first-order image merge into one bright ring of emission. At the highest inclination angles, gravitational lensing is the dominant effect. No corresponding Einstein ring is observed for the $a = 0.998$ black hole when the plasmoid is directly behind. This is because the point of maximum blueshift has been shifted away from $\phi = 180°$ by the frame-dragging of the Kerr black hole.

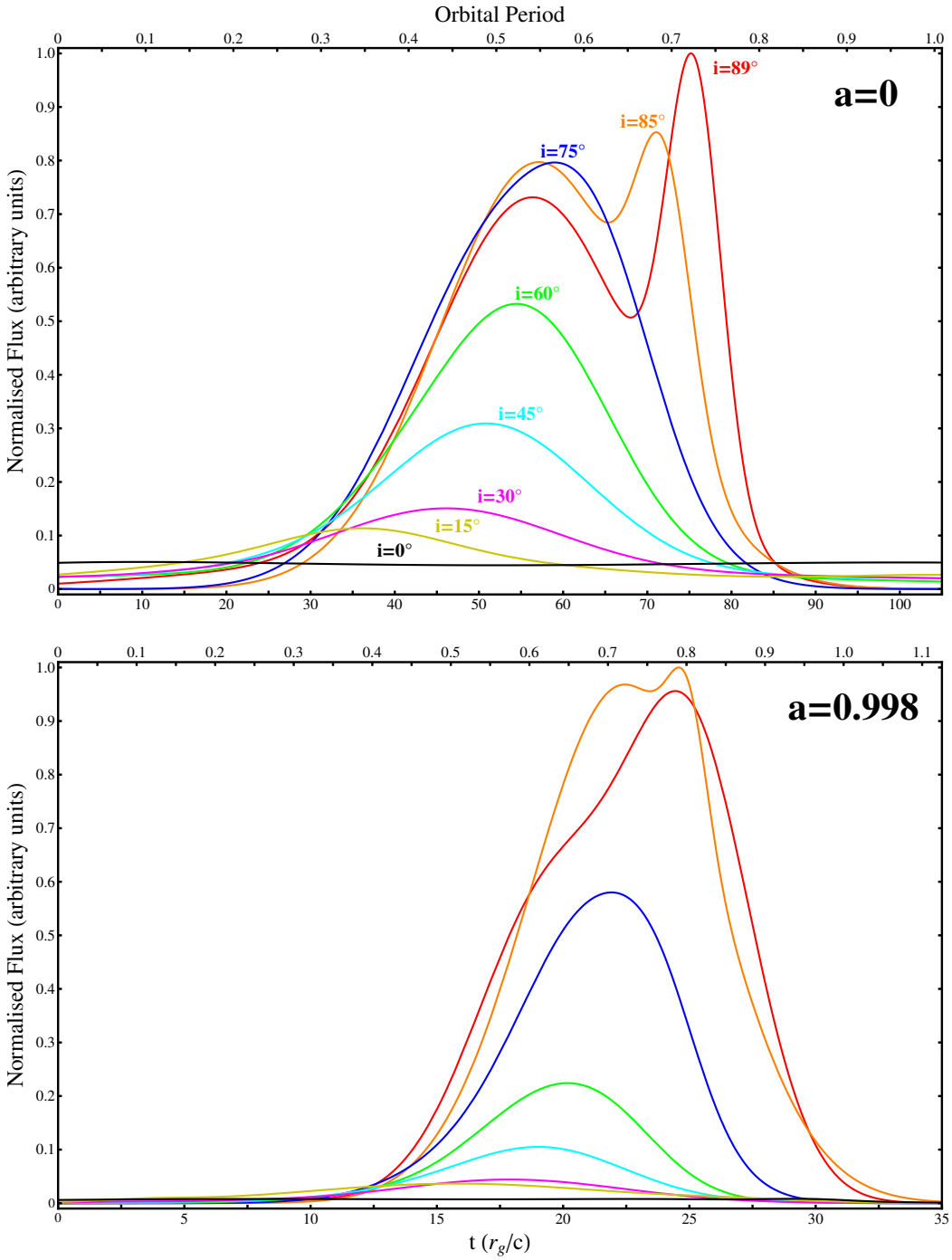

Fig. 6.6: Smoothed frequency-integrated lightcurves of a plasmoid orbiting a black hole for different observer inclination angles: $i = 0°$ (black), $i = 15°$ (yellow), $i = 30°$ (magenta), $i = 45°$ (cyan), $i = 60°$ (green), $i = 75°$ (blue), $i = 85°$ (orange) and $i = 89°$ (red). Roughly one period of emission is shown (top axis). The plasmoid is initially at $\phi_{\rm i} = 90°$ and is orbiting in the e_ϕ-direction, i.e. anticlockwise as viewed from above. Top: plasmoid orbiting an $a = 0$ black hole at $r_{\rm c} = 6.5r_{\rm g}$. Bottom: plasmoid orbiting an $a = 0.998$ Kerr black hole at $r_{\rm c} = 2.5r_{\rm g}$. At high inclination angles relativistic beaming causes the light curves to become sharply peaked as the plasmoid approaches the observer. Beyond inclination angles of 80° gravitational lensing creates an Einstein ring when the plasmoid moves behind the black hole. The lightcurves become asymmetrical due to time delays from ring images, the spin of the black hole, and the Doppler shift of the plasmoid itself.

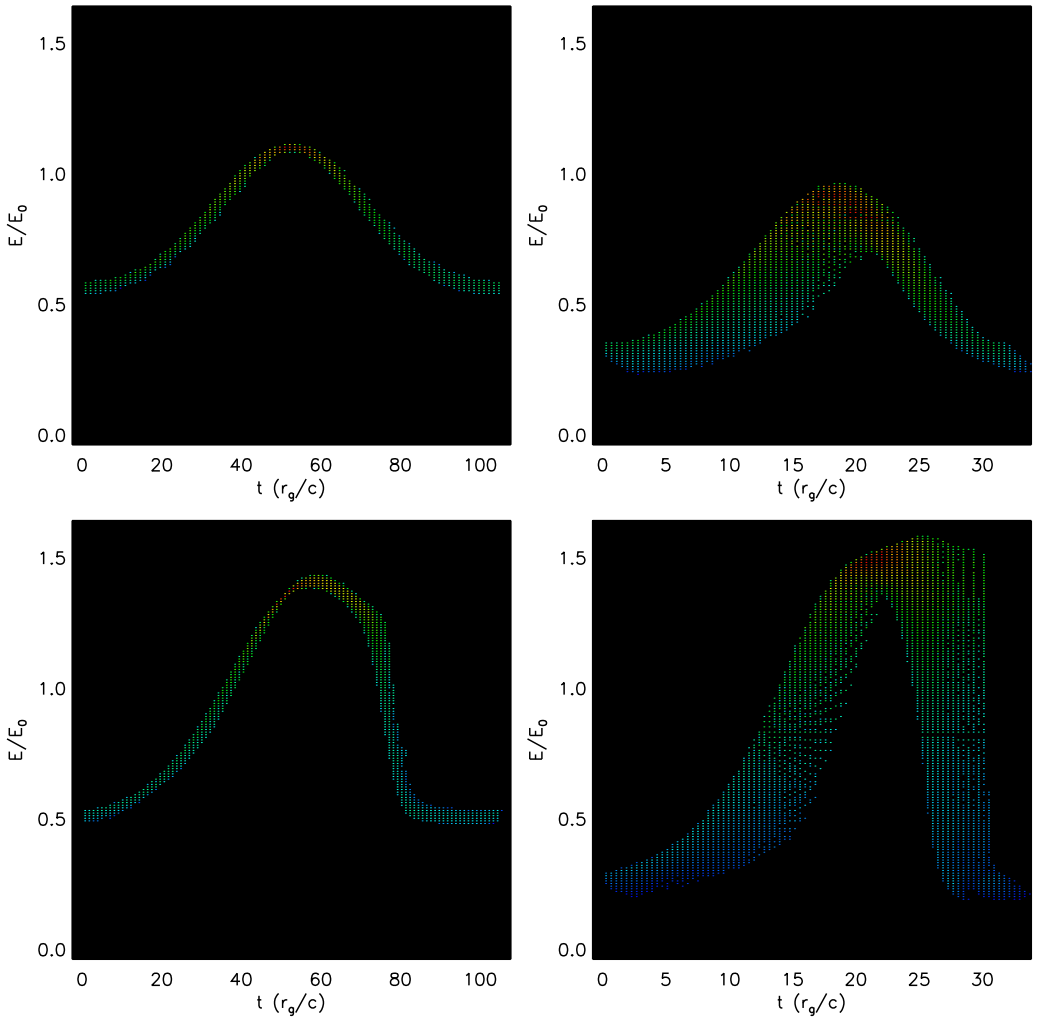

Fig. 6.7: Time-dependent lightcurves (spectrograms) of orbiting plasmoids around spin $a = 0$ black holes (left) and spin $a = 0.998$ black holes (right). Top panels: observer inclination $i = 45°$. Bottom panels: observer inclination $i = 85°$. The plasmoid is initially at $\phi_{\rm i} = 90°$. The spectrogram profile shape is very sensitive to both inclination angle and spin. Black hole spin serves to increase the energy width of each temporal bin (i.e. gravitational redshift/blueshift). Observer inclination angle affects the absolute amplitude of the spectrograms, due to the Doppler beaming effects becoming more powerful at higher inclinations. Each pixel is coloured by the total flux for that photon, normalised as in Figure 6.1.

panels) cause significant gravitational lensing of the primary plasmoid image, appearing elongated in the direction of propagation. The gravitational lensing effect becomes more severe as the observer's inclination angle increases. Arcs of emission from multiple images form, and at high inclinations even trace the shadow of the black hole event horizon. The effect of black hole spin is pronounced, shifting the point of maximum blueshift.

For a Newtonian plasmoid, the point of maximum blueshift as seen by an observer would correspond to $\phi = 270°$. In Figure 6.5 for $a = 0.998$ and $\phi = 270°$ an Einstein ring is not observed, unlike in the corresponding image for the non-rotating black hole. The plasmoid appears to be located at an azimuthal position beyond 270°, owing to severe gravitational lensing and Doppler effects.

The primary distinction between plasmoids located at different radii is the variability time-scale of the total flux. This is illustrated through the normalised frequency-integrated lightcurves in Figure 6.6. These lightcurves are smoothed to remove numerical noise, owing to the finite number of numerical photons available for calculations. Emission from the disk is subtracted in all calculations so only the variable component is presented. Emission from higher-order lensed images of the plasmoids are also neglected. Such higher-order photons orbit the black hole multiple times, with the image order specifying the number of orbits of the photon before escaping to reach the observer. These photons arrive much later than neighbouring photons, distorting the shape of the calculated spectrograms and lightcurves by contributing extra emission in time bins where the observed flux form the primary image is negligible. In the numerical scheme these photons are neglected since in a real physical situation such photons traverse vast distances through the accretion flow close to the event horizon and are highly redshifted. They are likely to be strongly attenuated and absorbed by the surrounding medium and their flux contribution to the observed spectrograms and lightcurves is negligible, if they escape at all.

The top panel of Figure 6.6 shows the frequency-integrated lightcurves for a plasmoid orbiting a black hole with a spin parameter of $a = 0$. At a

distance of $r_c = 6.5\ r_g$ the orbital period $\approx 104\ r_g/c$. At $i = 0°$ the observer is looking directly down the black hole spin axis, implying an absence of transverse Doppler shifts. This is reflected in the flatness of the corresponding lightcurve. As inclination angle increases, the peaks in the lightcurves become much stronger. Relativistic Doppler beaming shifts the peaks of the lightcurves as the location of the point of maximum blueshift moves. Beyond inclinations of 80° the light curve becomes double peaked. This occurs when the flux emitted from the Einstein ring overpowers the flux from the region of maximum blueshift. As the observer inclination angle moves to 89° the azimuthal positions of the maximum blueshift region and the Einstein ring formation region increase in separation, giving two distinct peaks. This means that at the highest inclinations the effects of gravitational lensing dominate over relativistic effects. That is to say, at large inclinations general relativistic effects overpower special relativistic effects.

Similar features appear in the bottom panel of Figure 6.6, for a plasmoid orbiting an $a = 0.998$ Kerr black hole. At this distance the plasmoid orbital period is $\approx 31\ r_g/c$. Observational features are qualitatively similar at low to moderate inclination angles to those observed for the non-rotating black hole. In this case the formation of the Einstein ring does not affect the observed integrated flux so strongly. This is because the orbital period of the plasmoid is much shorter and the magnification/de-magnification of the plasmoid image which causes the shift in the two peaks is much faster. The presence of separated double peaks could potentially distinguish between black holes of differing spins.

In Figure 6.7, time-dependent spectra (spectrograms) are plotted for black hole spins of $a = 0$ and $a = 0.998$, and observer inclinations $i = 45°$ and $i = 85°$. Spectrogram profile shape is very sensitive to black hole spin and observer inclination angle.

6.3 Plasmoid Ejection

As discussed in Chapter 1, jets are ubiquitous in accreting AGN. Intermittent, episodic outflows associated with flare emission are also observed in these

systems. Such flaring has been observed in Sgr A* in the X-ray, IR and radio, with several episodes occurring every day (Eckart et al. 2006; Genzel et al. 2003), showing delays in the peaks of the light curves at different wavebands (Yusef-Zadeh et al. 2006). The observed delays in these peaks, combined with the sharp rise and slow decay in the brightness and polarisation of these flares, are attributed to the ejection and expansion of plasmoids from the accretion flow (e.g. van der Laan 1966; Marrone et al. 2008).

X-ray and radio observations of the active galaxy 3C120 over a three-year period show episodic ejections in the form of bright superluminal knots (Marscher et al. 2002). Knots are very common in radio-loud AGN like M87, and are sometimes interpreted as decollimation shocks. Similar plasmoid ejecta have been observed in microquasars, e.g. GRS 1915+105 (Mirabel and Rodríguez 1994; Mirabel et al. 1998). Short but powerful radio flares, along with X-ray flares (and in the case of GRS 1915+105 IR flares also), are observed in the hard to soft X-ray spectral state transition. Such flares have also been associated with plasmoid ejection. Observations of Sgr A* show multiple simultaneous light curves at different wavebands, from which plasmoid ejecta are inferred.

GRMHD simulations of the accretion flow near the black hole event horizon show, even under the assumption of a weak initial magnetic field, that rapid mass ejections embedded within continuous jet-like outflows can occur (Machida et al. 2000; De Villiers et al. 2003). In these simulations, the time interval between successive episodes was found to be $\sim 1600 r_{\rm g}/c$.

In solar physics, two-component magnetic outflows and ejections are well-known and understood in terms of rapid solar winds and coronal mass ejections (CMEs). The similar morphologies and attributes found in the outflow components of accreting black holes as well as the Sun hint at a common underlying physical mechanism. To this extent, a solar CME-like outflow model for the accretion flow is employed, as in Yuan et al. (2009).

Observational implications aside, there are many compelling theoretical reasons as to why the magnetic processes operating in black hole environments and in the Solar corona are morphologically similar. Numerous GRMHD simu-

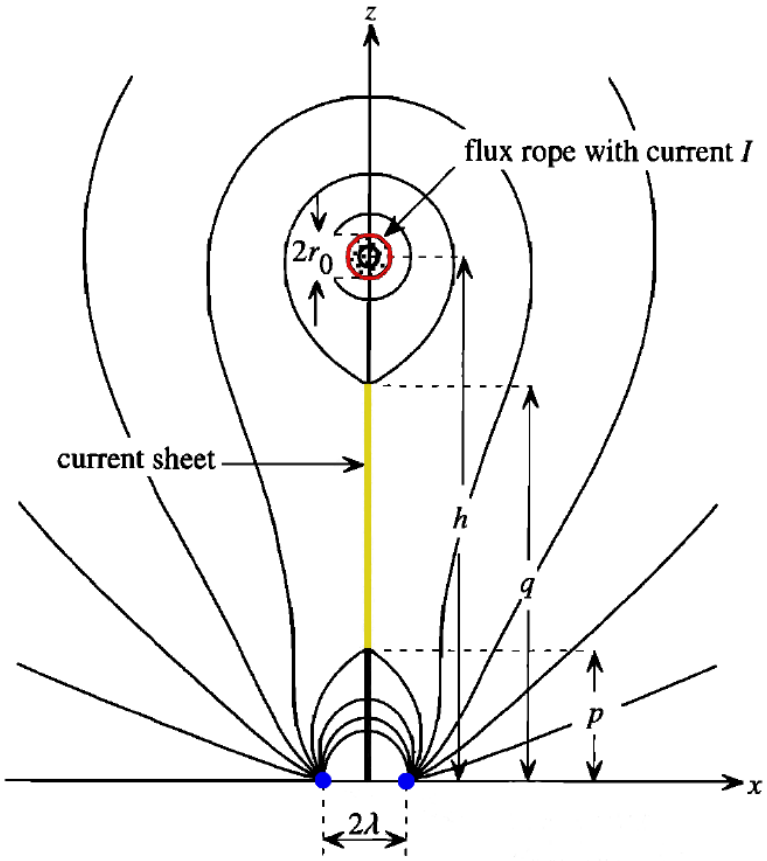

Fig. 6.8: Diagram of plasmoid configuration. The plasmoid (flux rope) is indicated by the red circle. The current sheet is denoted by the yellow line. The footprints of the magnetic field are indicated by a pair of blue circles. The x-axis indicates the accretion disk surface. The key parameters in the model are the flux rope starting position $p(t)$, end position $q(t)$ and the plasmoid height above the accretion disk surface, $h(t)$. A fourth quantity, namely the plasmoid mass, $m(t)$, is also of importance. Adapted from Lin and Forbes (2000).

lations of hot accretion flows demonstrate remarkable similarity with the solar atmosphere. An accreting black hole is essentially a dense disk enveloped by a corona (De Villiers et al. 2005).

Accretion disks are permeated by magnetic fields, with their angular momentum transport regulated by magneto-rotational instability (MRI). Consequently, accretion disks are highly turbulent (Balbus 2003; Balbus and Hawley 2003). Magnetic field loops emerge from the accretion disk into the corona, their footprints fixed in place in the disk. Differential rotation and turbulence within the disk means that magnetic reconnection (and shortly thereafter flar-

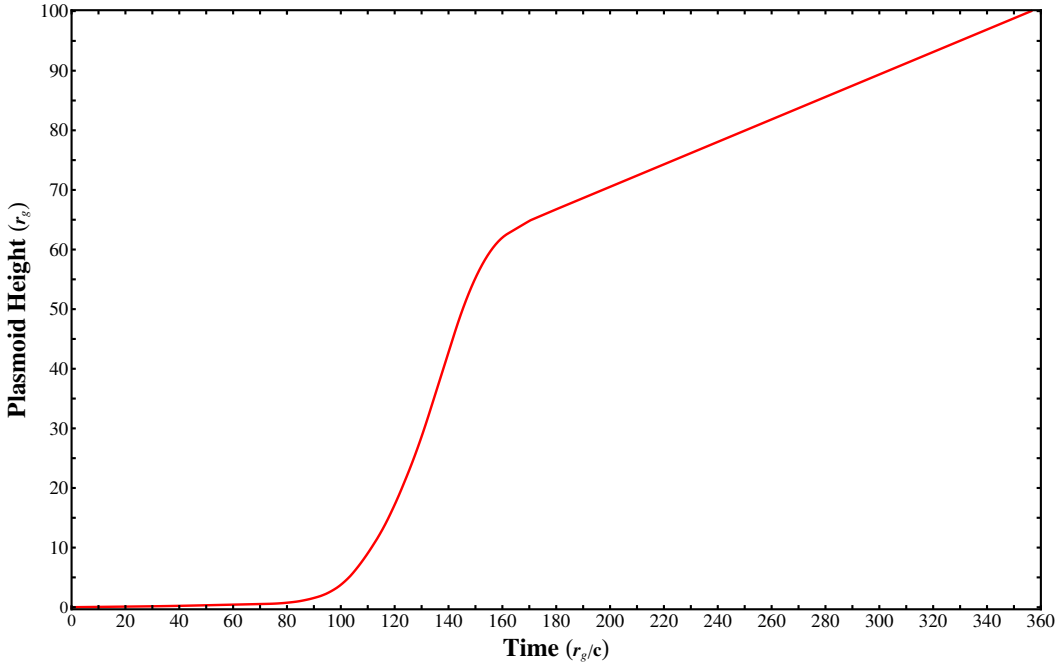

Fig. 6.9: Plot of calculated plasmoid height as a function of time. These values are normalised from the data in Yuan et al. (2009) to units of $r_{\rm g}$. The plasmoid does not accelerate immediately after loss of equilibrium, taking $\sim 100 r_{\rm g}/c$ to accelerate from rest to $\sim 0.02c$. Shortly thereafter, magnetic reconnection in the form of a huge Lorentz force feeds current into the plasmoid, accelerating it to $\gtrsim 0.8c$ in $\sim 50 r_{\rm g}/c$, reaching a height of $\sim 60 r_{\rm g}$. Thereafter the plasmoid decelerates, tending to a roughly constant velocity.

ing through CMEs) can occur. Reconnection alters the topology of the magnetic field, redistributing helicity, of which most is stored in the corona in a flux rope (essentially a plasmoid prior to ejection). The magnetic field continues to evolve after forming a current sheet and eventually loss of equilibrium occurs, rapidly expelling the plasmoid, whilst still connected by a current sheet. Meanwhile, magnetic reconnection occurs in the current sheet, and the powerful Lorentz force accelerates the plasmoid away from the disk. In principle, this process should be more prominent, and violent, closer to the black hole.

I consider the data from the MHD model from Yuan et al. (2009). In their model the upward motion of the plasmoid is governed, to first order, by the following approximation

$$m\frac{{\rm d}^2 h}{{\rm d}t^2} = |\mathbf{I} \times \mathbf{B}_{\rm ext}| - F_{\rm g} \ , \tag{6.3}$$

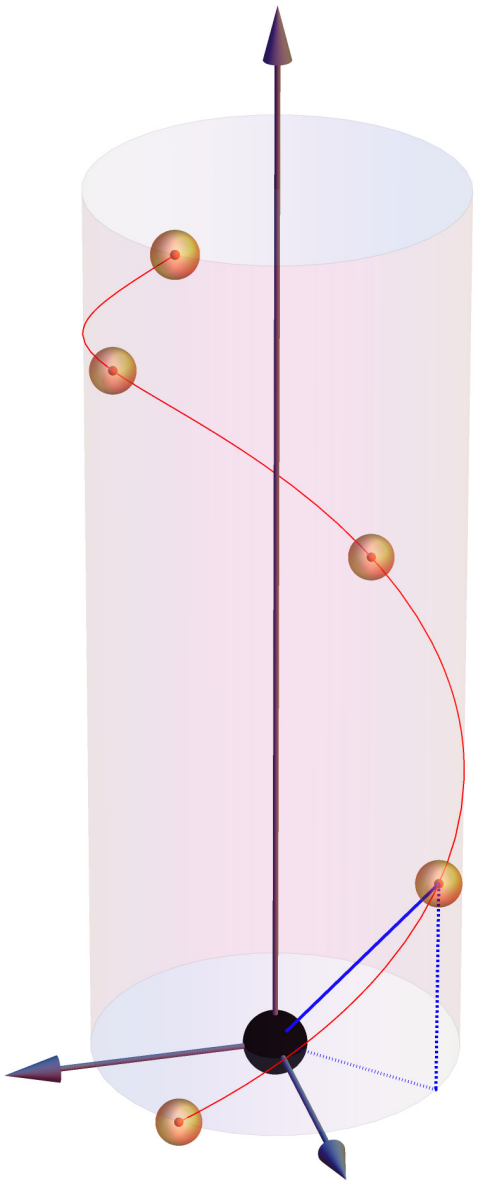

Fig. 6.10: Illustration of the ejected plasmoid motion (orange spheres) at different times (not to scale) around a black hole (black sphere). The plasmoid follows a helical trajectory (red curve) on the surface of a cylinder of radius r_c. The plasmoid height (vertical dashed blue line), $h(t)$, is interpolated from Figure 6.9. At each time step the plasmoid radial distance (solid blue line) is calculated as a function of time. Subsequently the change in azimuth is calculated from equation (6.8).

where $m(t)$ is the total mass within the plasmoid, $h(t)$ is the height of the plasmoid above the accretion disk, $F_{\rm g}$ is the gravitational force, $\mathbf{I}$ is the integrated current density $\mathbf{j}$ inside the plasmoid, and $\mathbf{B}_{\rm ext}$ is the total magnetic field from all sources except $\mathbf{I}$. The current and magnetic field interior to and outside of the plasmoid satisfy the following conditions (at zeroth order):

$$\mathbf{j} \times \mathbf{B} = 0 \,, \tag{6.4}$$

$$\mathbf{j} = \frac{c}{4\pi} \nabla \times \mathbf{B} \,. \tag{6.5}$$

To determine the plasmoid velocity as a function of time, equation (6.3) must be solved, along with three other parameters. In total, five coupled ODEs must be solved (for h, $\dot{h}$, p, q and m). Details may be found in Yuan et al. (2009).

The plasmoid is initially located at $r_{\rm c} = 5\ r_{\rm g}$ from the black hole, with the density with the plasmoid $\rho_0 = 10^5$ cm^{-3} and the initial magnetic field set to $B_0 = 16$ G. The initial configuration of the plasmoid is illustrated in Figure 6.8. The density and magnetic field distributions within the corona are poorly understood. For simplicity, they are assumed to be similar to those found in the solar corona. This is an acceptable approximation since results will not change very much unless the local Alfvén speed near the current sheet decreases drastically with height within the plasmoid ejection region (Lin et al. 2006). This is unlikely given the planar configuration of the accretion disk corona. The solution of equation (6.3) for the aforementioned initial conditions is plotted in Figure 6.9 as a function of time.

The model presented is two-dimensional and accounts neither for the variation in azimuthal position of the plasmoid, nor for changes in distance from the spin axis of the disk. In reality, it is expected that the plasmoid will follow helical field lines, and turbulence and shocks will also cause the plasmoid to deviate from motion just in the z-direction. This second effect is harder to treat, so as a first approximation only azimuthal motion is considered. This is modelled as a relativistic particle under the influence of the black hole's gravitational field. The initial x-position of the plasmoid ($r_{\rm c}$) remains fixed, with the plasmoid motion confined to the surface of a cylinder (Figure 6.10)

Particle motion in the Kerr space-time was discussed in Chapter 3.2, where expressions for $\dot{t}$ and $\dot{\phi}$ were given in equations (3.48)–(3.49). From these, the orbital velocity of a particle in the flow is given by

$$\begin{aligned} v_\phi\left(r,\theta\right) &= \frac{\dot{\phi}}{\dot{t}} \\ &= \frac{\sqrt{2r^2-\Sigma}}{\left(\Sigma\sqrt{r}+a\sin\theta\sqrt{2r^2-\Sigma}\right)\sin\theta} \ . \end{aligned} \tag{6.6}$$

The plasmoid is initially centred on the equatorial plane. Assuming a helical magnetic field, and remaining a fixed radial distance $r_{\rm c}$ from the black hole, the plasmoid velocity may be parameterised as a function of r

$$v_\phi(r) = \frac{r^2+a^2}{r_{\rm c}}\left\{\sqrt{r}\left[\frac{\left(r^2+a^2\right)^2-a^2r_{\rm c}^2}{\sqrt{r^4+a^2r_{\rm c}^2-a^4}}\right]-ar_{\rm c}\right\}^{-1} \ . \tag{6.7}$$

The change in azimuth for the plasmoid may now be calculated by integrating equation (6.7) between its initial and final radial position

$$\Delta\phi = \int_{r(t_i)}^{r(t_{i+1})} {\rm d}r\, v_\phi\left(r\right) \ , \tag{6.8}$$

where $r(t_i)^2 = {\rm R}+\sqrt{{\rm R}^2+a^2h(t_i)^2}$, $2{\rm R} = (r_{\rm c}^2+h(t_i)^2-a^2)$ and $h(t_i)$ is the height of the plasmoid as a function of time. It follows from equation (6.8) that the change in ϕ is weakly-dependent on black hole spin, but depends strongly on $r_{\rm c}$. Plasmoids ejected close to the black hole event horizon experience much stronger gravitational forces, since a particle orbiting in the equatorial plane has a velocity $v_\phi \propto 1/\left(a+r^{3/2}\right)$.

As for the orbiting plasmoid calculations in the previous subsection, two cases are investigated, namely $r_{\rm c} = 6.5\ r_{\rm g}$ for a non-rotating black hole and $r_{\rm c} = 2.5\ r_{\rm g}$ for an $a = 0.998$ Kerr black hole. For $a = 0$ the corresponding value for $\Delta\phi = 131.5°$, whereas for $a = 0.998$, $\Delta\phi = 387.5°$. At each time-step the (r,θ,ϕ,t)-location of the plasmoid is determined. This is used to specify its location for the ray-traing calculation, exactly as in Chapter 6.2. As such, light curves and spectrograms of the ejected plasmoid may be calculated.

Figures 6.11–6.14 show the un-smoothed calculated lightcurves for magnetically-driven plasmoid ejection. The spurious oscillations at longer times are due to the finite number of photons used in calculations. These may

be smoothed by increasing the resolution at each time step in the numerical algorithm and applying an appropriate noise filter to the data. Regardless, the qualitative features of the lightcurves are not compromised, and several conclusions can be drawn from the data.

In Figure 6.11 the sharp rise in flux is attributable to the rapid plasmoid acceleration phase at $t \approx 100\ r_{\rm g}/c$, lasting until $t \approx 150\ r_{\rm g}/c$. For the $a = 0$ lightcurves, the flux increases monotonically with inclination angle, steadily decaying once the acceleration phase is over. For the $a = 0.998$ lightcurves, the flux rises and falls rapidly during the plasmoid acceleration phase. This is because of the rapid change in ϕ over the same time period, corresponding to the plasmoid's transition from the blueshifted region to the redshifted region. At late times, the lightcurves slightly increase in flux due to the plasmoid again approaching the observer along the line-of-sight.

Lightcurves in Figure 6.12 are qualitatively similar to those in Figure 6.11. For $a = 0$ the acceleration phase of the plasmoid is less rapid, whereas for $a = 0.998$ it is more pronounced, but the subsequent dip in observed flux at $t \approx 125\ r_{\rm g}/c$ is less sharp.

For an initial plasmoid position of $\phi = 180^\circ$ in Figure 6.13, the lightcurves are now drastically different. In both panels, at high inclination angles the flux drops sharply. For the spin $a = 0.998$ black hole the drop in flux is more pronounced due to stronger transverse Doppler shifts away from the line-of-sight and the shorter orbital period of the plasmoid. For $a = 0$ the rapid acceleration phase is almost completely suppressed, and strongly suppressed for $a = 0.998$, particularly at lower inclination angles. The initial rapid drop in flux dominates the emission from both models.

In Figure 6.14 both sets of lightcurves show a steady emission of flux for the first 80–100 $r_{\rm g}/c$. For $a = 0$ a sharp drop in flux is seen, corresponding to the rapid acceleration phase. Thereafter the emitted flux shows little variability. For the $a = 0.998$ black hole there is an increase in flux at $t \approx 80\ r_{\rm g}/c$, as the plasmoid passes through the region of maximum blueshift. At $t \approx 100\ r_{\rm g}/c$ the sharp drop in flux again corresponds to redhshifted emission as the plasmoid accelerates away from the observer. After this, the flux

from plasmoids viewed at higher inclination angles increases at a nearly linear rate until $t \sim 165\ r_{\rm g}/c$, due to strong transverse Doppler shifts.

6.4 Discussion

The radiative transfer formulation in Chapters 3 and 4 was extended to properly account for the differences in photon arrival times, to investigate time-dependent emission and dynamical effects in the accretion flow around a black hole. As a simple first test of how well the code accounts for time delay, images of accretion disks overlaid with constant photon arrival time contours were presented (Figure 6.1), showing the effects of black hole spin and observer inclination angle.

As a second test of the formulation, images of a plasmoid orbiting close to the ISCO for black holes with spin parameters of $a = 0$ and $a = 0.998$ in Figures 6.2–6.5 were calculated. For $a = 0.998$ the gravitational lensing effect is strong, and emission from the plasmoid is smeared and beamed forward in the direction of propagation. The effects of gravitational lensing are also much stronger closer to the black hole, magnifying all images of the plasmoid and resulting in a greater projected surface area. At very high inclinations the effects of gravitational lensing are so pronounced that an Einstein ring forms, magnifying the projected emission surface of the plasmoid by a factor of $\sim$ 10–100 as the inclination angle approaches 90°.

The frequency-integrated lightcurves of plasmoids orbiting a black hole for one orbital period were then computed. In all cases the plasmoid was initially located at $\phi_{\rm i} = 90°$, i.e. the point of maximum redshift. At low inclination angles the lightcurves are symmetrical and not strongly peaked. As inclination angle increases the lightcurves become more sharply peaked and skewed. These results are in strong qualitative agreement with previous calculations with different orbital parameters (e.g. Schnittman and Bertschinger 2004; Schnittman and Rezzolla 2006; Broderick and Loeb 2005, 2006; Dexter and Agol 2009).

At inclination angles above $i = 80°$, gravitational lensing through the amplified emission from an Einstein ring dominates, causing the light curves to

become double-peaked. This effect is less marked for the rapidly rotating black hole due to the much shorter orbital period of the plasmoid, limiting the time this effect can manifest and therefore dominate over the total observed flux. These effects at inclination angles above $i = 80°$ have not been demonstrated previously in the literature. Variability in the plasmoid spectra was also characterised in the spectrograms in Figure 6.7. Unlike the spectra in Chapter 4, these spectrograms are easily distinguishable in terms of the black hole spin and inclination angle, which are also visible in the frequency-integrated lightcurves of Figure 6.6.

Finally, a more physically realistic dynamical model of episodic outflows from the accretion disk was considered. Since the vertical motion of the plasmoid is governed through magnetic turbulence in the flow, a solar CME flaring model from Yuan et al. (2009) was employed. This is a suitable first approximation because the accretion disk is linear to first order and the solar corona and accretion disk corona are morphologically similar. The ejected plasmoid height was then calculated as a function of time. For the azimuthal motion, the magnetic field was assumed to be helical, confining the plasmoid motion to the surface of a cylinder[2]. A parameterised form for the plasmoid velocity was derived, allowing its change in azimuth to be calculated as a function of its height.

With the plasmoid dynamics specified, light curves of the plasmoid for the first 100 $r_{\rm g}$ of its vertical motion were calculated. Aside from varying the spin parameter of the black hole, azimuthal position of the plasmoid was also considered. The corresponding light curves (Figures 6.11–6.14) are completely different to those in Figure 6.6. Ejected plasmoid lightcurves are qualitatively similar across all inclination angles, in contrast to the case of an orbiting plasmoid. However, they are far more sensitive to the black hole spin than their orbiting counterparts, exhibiting completely different profiles between $a = 0$ and $a = 0.998$. Azimuthal position also significantly affects the observed lightcurves, with those ejected at $\phi_{\rm i} = 180°$ demonstrating significantly

[2]The assumption of a helical magnetic field is supported by polarisation observations and jet-launching models.

suppressed emission, most notably during the rapid ejection phase of the plasmoid. The rapid acceleration at $\sim 100\ r_{\rm g}$ is almost universally prominent and consistent in duration. Since this is essentially dependent on the assumed initial magnetic field in the accretion disk, measurements of this timescale also offer insight into magnetic activity in the corona, as well as kinematic and dynamical properties of the flow itself.

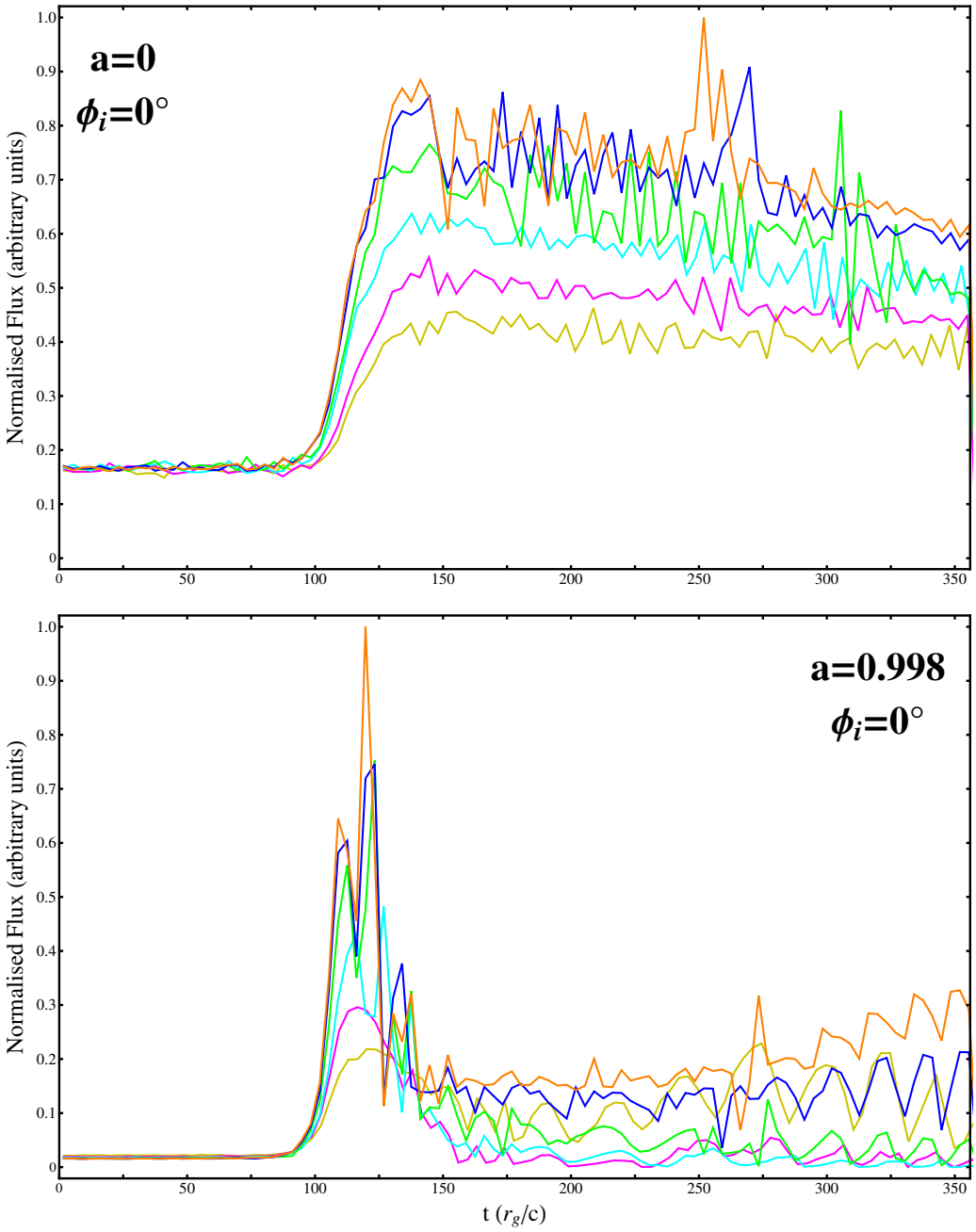

Fig. 6.11: Frequency-integrated lightcurves of magnetically-driven plasmoid ejection from a black hole accretion disk. Only flux associated with variability is considered: all lightcurves are disk emission subtracted. Viewed at inclination angles: $i = 15°$ (yellow), $i = 30°$ (magenta), $i = 45°$ (cyan), $i = 60°$ (green), $i = 75°$ (blue) and $i = 85°$ (orange). The plasmoid is initially at $\phi_{\rm i} = 0°$ and is orbiting in the e_ϕ-direction, i.e. anticlockwise as viewed from above. Top: plasmoid ejection from an $a = 0$ black hole at $r_{\rm c} = 6.5 r_{\rm g}$. Bottom: plasmoid ejection from an $a = 0.998$ Kerr black hole at $r_{\rm c} = 2.5 r_{\rm g}$. The rapid increase in flux at $t \approx 100\ r_{\rm g}/c$ corresponds to the rapid acceleration phase of the plasmoid (cf. Figure 6.9), ending when $t \approx 150\ r_{\rm g}/c$.

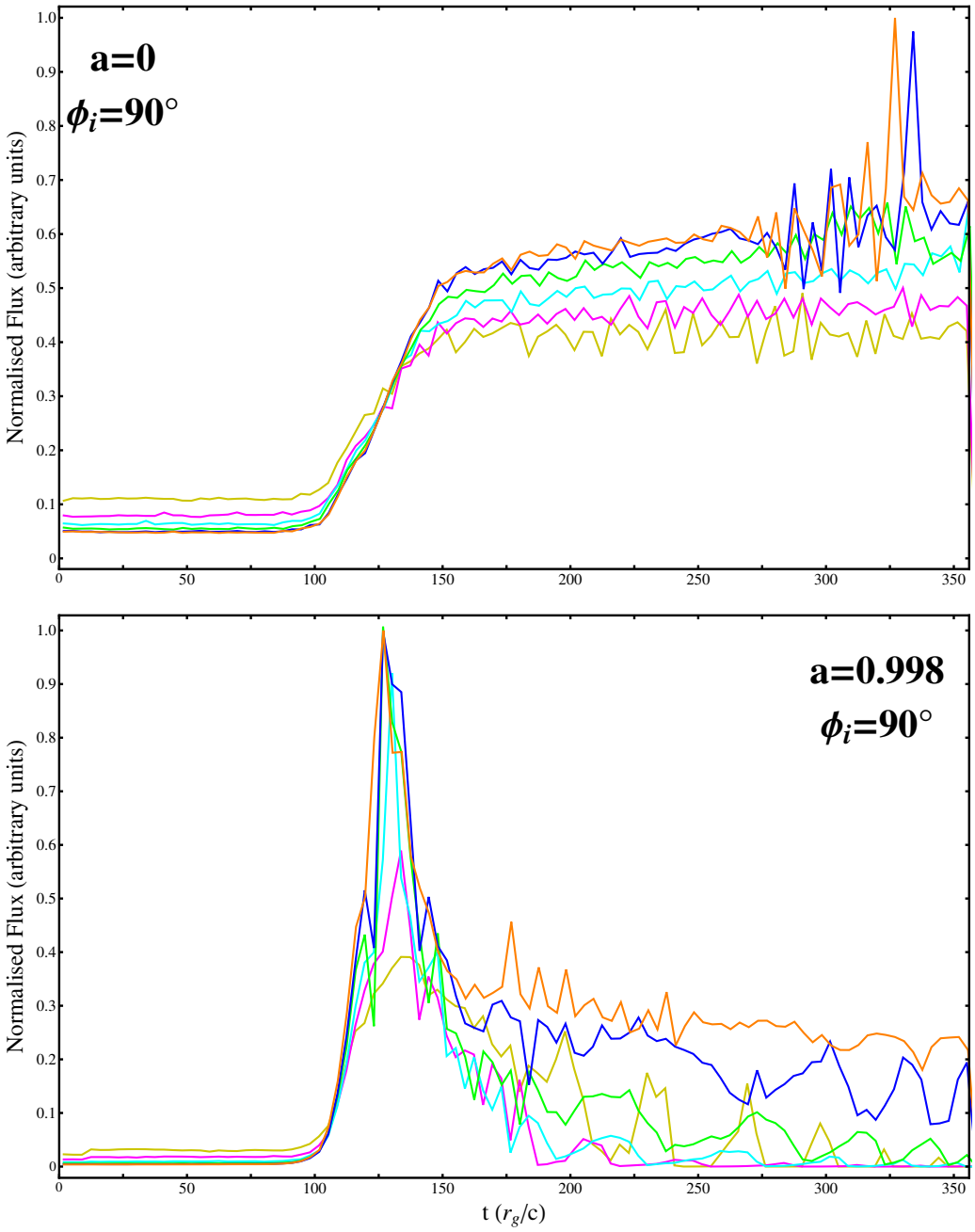

Fig. 6.12: As in Figure 6.11, but now with initial azimuth $\phi_{\rm i} = 90°$. As seen for $\phi_{\rm i} = 0°$, the black hole spin strongly affects the observed lightcurves, increasing the amplitude and duration of the observed flux during the acceleration phase.

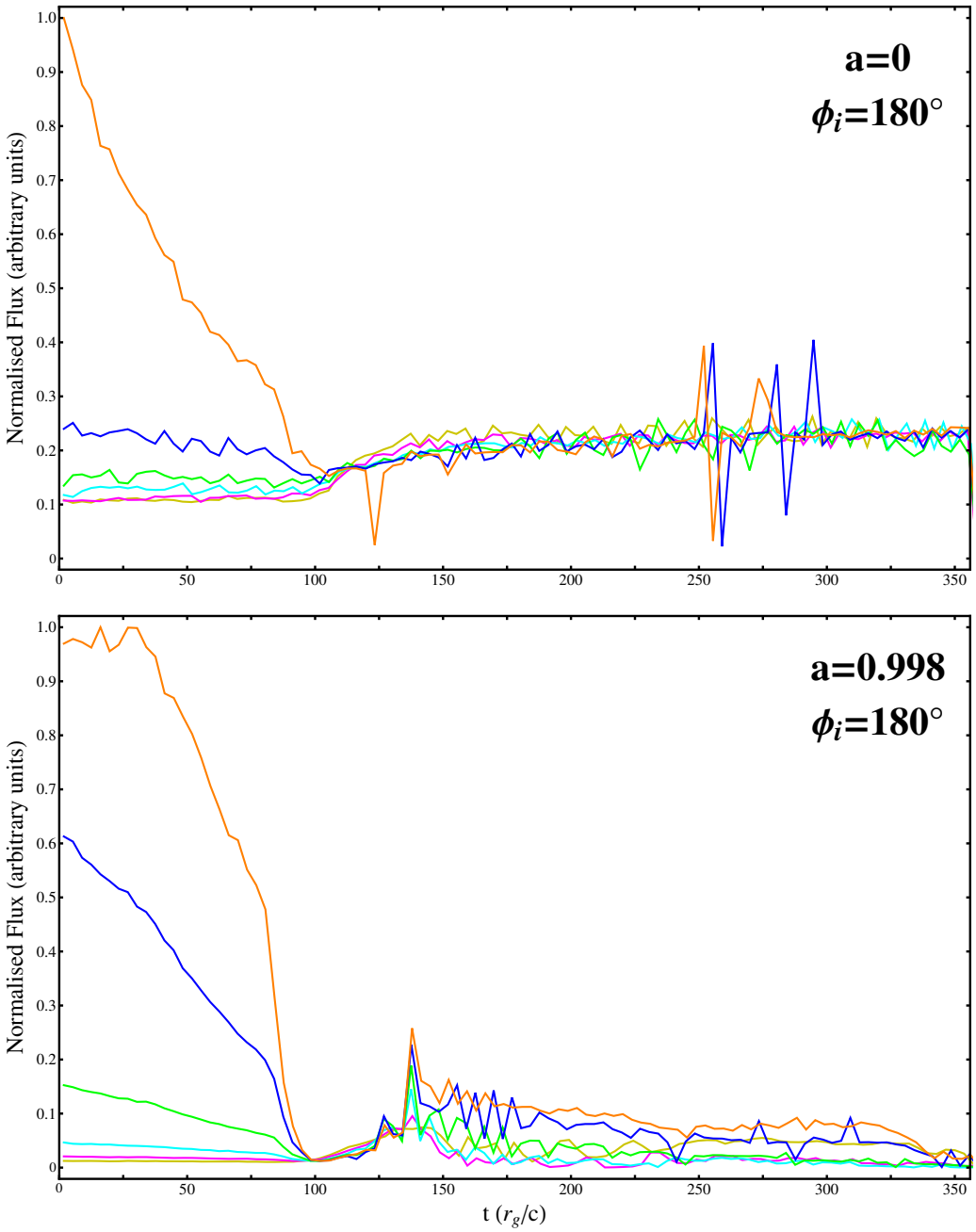

Fig. 6.13: As in Figure 6.12, but now with initial azimuth $\phi_{\rm i} = 180°$. The plasmoid is initially moving towards the region of maximum blueshift, but its vertical motion overpowers this, leading to a rapid decrease in flux until $t \approx 100\ r_{\rm g}/c$. For $a = 0$ the rapid acceleration phase is almost completely suppressed. For $a = 0.998$ a modest increase in flux is seen for $i = 60°$, $i = 75°$ and $i = 85°$ at $t \approx 135\ r_{\rm g}/c$.

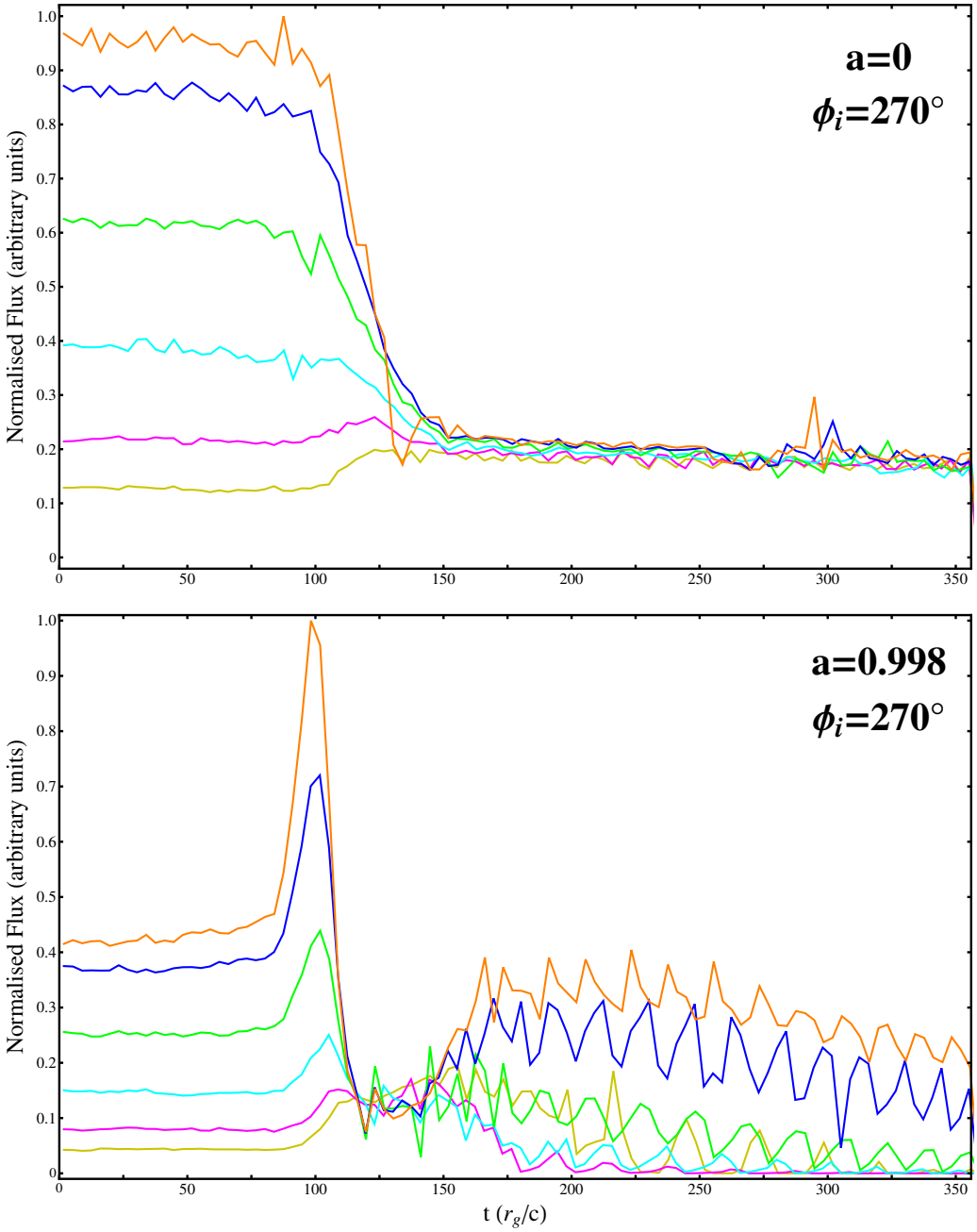

Fig. 6.14: As in Figure 6.13, but now with initial azimuth $\phi_{\rm i} = 270°$. In both panels the observed flux remains steady for the first $\sim 100\ r_{\rm g}/c$ for $a = 0$ and for the first $\sim 80\ r_{\rm g}/c$ for $a = 0.998$. Again, this is due to the relatively weak Doppler boosting as the plasmoid exits the region of maximum blueshift at $\phi \sim 270°$. Due to the location of the plasmoid during the rapid acceleration phase, its emission is strongly redshifted for $a = 0$, and redshifted followed by blueshift at high inclination angles for $a = 0.998$.

Chapter 7

Conclusions and Implications

In this thesis I have developed a numerical radiative transfer formulation to calculate the emission from accretion and outflows around a black hole self-consistently. I have used this formulation to investigate three different aspects of AGN physics: calculating the emission from different models of the accretion flow; deriving a formalism to calculate Compton scattering in strong gravity correctly and self-consistently; and investigating variability in the flow by studying the time-dependent emission properties of sporadic jets in the form of plasmoid outflows.

7.1 Equations of Motion and Radiative Transfer

In Chapter 3, a covariant radiative transfer formulation was derived. This formulation also incorporates the effects of particle mass into the flux propagation. It is completely general, incorporating all relativistic and general relativistic effects self-consistently, and is applicable to studies of radiation transport and spectral formation in AGN environments where the effects of space-time curvature may be important. The equations of motion for particles with and without mass in the vicinity of a spinning black hole were also derived. These are used to determine the kinematic properties of the accretion flow, as well as to calculate the trajectories emitted radiation follows.

The derived relativistic form of the radiative transfer equation is a generalisation of the classical version. It includes a Lorentz transformation factor and replaces the specific intensity and opacity with their corresponding Lorentz-invariant forms. The presence of particle mass is also included, manifesting

as an additional multiplicative abberation factor. The ray-tracing algorithm follows individual ray trajectories along their paths from observer to emitter. Using the equations of motion, these trajectories are determined from the Euler-Lagrange equations of motion for the Kerr metric.

The equations of motion for particles that orbit outside of the equatorial plane were also derived, describing the motions of three-dimensional flows like the accretion tori discussed in Chapter 4 and the orbiting and ejected plasmoids studied in Chapter 6. These equations of motion were used to derive key critical surfaces for the Kerr black hole, including the location of the marginally stable orbits for material particles as a function of r and θ. These critical surfaces were used to specify the inner and outer radii of the accretion disks and tori investigated in Chapter 4.

7.2 Emission from Translucent Tori

In Chapter 4, a model for an optically thick accretion torus was constructed. The 4-acceleration coupled with a parametric velocity field was used to derive a pair of coupled ODEs describing the torus surface as a function of r and θ. After solving for the torus surface, ray-tracing was employed to calculate images of these tori, as well as using radiative transfer to calculate their emission lines.

The line profiles from these optically thick accretion tori were compared with line profiles from thin accretion disks with the same inner and outer radii. There were significant differences between both models. As the torus is not geometrically thin, at high inclinations its inner surface is obscured, rendering emission from the fastest moving matter closest to the event horizon unobservable. As a consequence, torus emission spectra have narrower red and blue wings compared to thin disks. Torus spectra resemble broad humps centred around the line rest frequency, whereas disk spectra have sharply-defined red wings. It is very hard to determine the geometry of the flow and key black hole parameters from these profiles, as both disks and optically thick tori are capable of reproducing the observed red and blue wings.

With this in mind, accretion tori with internal structure were constructed.

Using the general relativistic hydrodynamic equations with a relativistic polytropic equation of state, the density distribution within the torus, including the effects of radiation pressure forces was derived. Two different scenarios were presented.

The first scenario considered only density-driven line emission from an optically thin torus. Surface brightness images of these tori were generated and their emission line profiles were calculated. These lines were found to be quite dissimilar to opaque accretion tori, as the entire emitting volume of the torus contributes to the emission and is unobscured. However, these lines still bear resemblance to the lines from thin disks. Optically thick and optically thin torus images show several differences. Optically thin tori are translucent, meaning higher-order images are not obscured and merge with the primary image to form a more intricate emission structure.

Emission line profiles from optically thin tori for two adjacent emission lines were also calculated. As an illustrative example, the lines were taken to have the same relative emissivities as Fe Kα and Fe Kβ lines, finding that while the two lines are still discernible, their wings are entangled. The optically thin torus line profiles also differ from both thin disks and optically thick tori in that the observed emission originates from the entire volume of the torus. This adds considerably more flux to the red and blue wings of the line profiles since the inner edge of the torus is not obscured. These profiles resemble those from disks. The presence of a second emission line added an extra peak to the profile, to the right of the blue wing. The red wing and most of the rest of the line remained unchanged. Relativistic Doppler smearing was not powerful enough to blend these lines together and they remained distinct even at the highest inclination angles.

In the second scenario, a model for the continuum was incorporated, including a thermal Bremsstrahlung-like component and a free-electron scattering-like process that converts photons with different energies indiscriminately into a power-law energy distribution, mimicking electron scattering. This was in addition to density-driven multiple emission lines. Surface brightness images of these quasi-opaque tori were then calculated. Limb-darkening

is clearly visible towards the edges of these tori. The Bremmstrahlung emission is dominant, being proportional to ρ^2 as well as $T^{1/2}$. Tori viewed at low inclination angles appear brighter as incident rays penetrate deeper into the hotter sub-surface layers. In these tori, self-occultation is apparent due to their high optical depth, and higher-order images are almost completely obscured.

The possibility of gravitationally induced line resonance was also demonstrated. In the extreme gravitational field around black holes, radiation experiences strong gravitational redshifts and blueshifts. Resonant feedback cycles may form between neighbouring lines with different rest-frame energies. Although this resonant phenomenon cannot occur in 2D flows like accretion disks, it can occur easily in 3D flows like the accretion tori discussed in this thesis. This is a uniquely general relativistic effect.

7.3 General Relativistic Compton Scattering

In Chapter 5, a new formulation to evaluate the general relativistic Compton scattering kernel and its angular moments for arbitrary moment order was derived. This is crucial for a proper treatment of general relativistic radiative transfer that incorporates the effects of scattering, such as close to the event horizon where the flow may become optically thick.

This is the first derivation of a closed-form expression for the general relativistic Compton scattering kernel. This method has the following advantages: (i) it is fast and highly parallelisable; (ii) it is accurate and able to handle arbitrary electron distributions as no underlying assumptions are made; (iii) it is not restricted by energy range, and is especially fast and accurate over keV energy ranges and above, as is found in most astrophysically relevant situations, including in AGN.

The general relativistic Compton scattering kernel was first expressed in covariant form. Convolving this with a relativistic electron distribution function, an expression for angular moments of this kernel was derived. The resultant multi-dimensional nested integrals required to calculate the kernel were reduced to a double integral over electron velocity and scattering angle. This

was then simplified further and re-expressed in terms of three different types of integral. These integrals are readily represented in terms of Gauss hypergeometric functions, which are rapidly convergent (and for which many accurate numerical routines already exist). Angular moments of the kernel in terms of finite sums of integrals over these hypergeometric functions were then expressed, essentially reducing the problem to one of quadratures (Chapter 5.10.2).

No freely-available codes exist to compute angular moments of the general relativistic Compton scattering kernel. To test the accuracy of the formulation and the numerical scheme a code was written in MATHEMATICA to compute angular moments of the scattering kernel with arbitrary numerical precision. The numerical scheme presented in Chapter 5, written in PYTHON, was tested at four different numerical precisions ranging from double to quad-double. It was found that quad-double precision was always sufficient. At the meV[1] energies where this was necessary a simple non-relativistic treatment would have been sufficient. For the keV energies and greater (where relativistic effects become relevant), double precision arithmetic was almost always sufficient. Several ways to solve regions of particular numerical difficulty were also described.

These results were found to be identical to semi-analytic calculations and Monte-Carlo simulations of Compton scattering of monochromatic emission lines by various other authors.

7.4 Time-Dependent Radiative Transfer

In Chapter 6, the radiative transfer formalism derived in Chapter 3 was extended to include the effects of photon time delay. An algorithm was developed to assign a proper relative arrival time for each photon and sort the corresponding times and associated positions and four-momenta. This algorithm was first tested by plotting images of accretion disks coloured by normalised photon arrival time and overlaid with contours of constant time.

A simple model of variability in the accretion flow given by a plasmoid

[1]Such low temperatures may occur in the intergalactic medium. The principal reason for choosing such a low temperature was to test the energy range of the code. In practice, a non-relativistic treatment of Compton scattering would suffice.

sphere on a Keplerian orbit around the black hole was considered. Background emission from the accretion disk was subtracted, and only time-varying emission was considered. This plasmoid was prescribed a Gaussian emissivity profile in the z-direction. Images of the plasmoid at various stages in its orbital motion were calculated, varying the black hole spin parameter, plasmoid radial position and observer inclination angle. For plasmoids closer to the black hole, the emission is smeared over the sky due to gravitational lensing. At high inclination angles, gravitational lensing can produce an Einstein ring, magnifying the emission from the plasmoid by factors of $\sim 10 - 100$.

In the corresponding frequency-integrated lightcurves, as inclination angle increases the emission becomes sharply peaked due to relativistic beaming and gravitational lensing. This also causes the lightcurves to be skewed towards later times. At the highest inclinations, gravitational lensing dominates over relativistic beaming, and the lightcurves becomes double-peaked. The lightcurves are very sensitive to the orbital period of the plasmoid, and hence the spin of the black hole, as well as inclination angle, much more so than the emission line profiles for accretion disks and tori in Chapter 4. The presence of separated double peaks in the observed lightcurves could potentially distinguish between black holes of differing spins.

A dynamical and kinematic model of accretion disk outflows in the form of magnetically-driven plasmoid ejection was then considered. A solar CME model is a good first approximation for the dynamical formation and acceleration of episodic jets from the accretion disk. Using this model, the motion of the ejected plasmoid as a function of time was calculated and used to calculate the observed time-dependent emission. For simplicity, a helical magnetic field was assumed, centred around the spin axis.

Using these data, the plasmoid position and momentum at each point in time was then specified, and the observed lightcurves during the first 100 $r_{\rm g}$ of its vertical motion were calculated. In these synthetic lightcurves, in addition to spin and inclination angle, the effects of azimuthal position of the plasmoid at the time of ejection were also investigated. These lightcurves were completely different to those of orbiting plasmoids, and found to be even

more sensitive to black hole spin, since this determines the amount of azimuthal precession the plasmoid experiences during its vertical motion, causing rapid changes in redshift and blueshift and enhancing variability further. These lightcurves were also extremely sensitive to initial azimuthal position, either greatly enhancing or suppressing the appearance of the rapid acceleration phase of the plasmoid. The rapid acceleration phase timescale was found to be consistent across all lightcurves and independent of intrinsic black hole parameters. Measurements of this timescale can potentially be used as an independent probe of magnetic activity in the corona and dynamical properties of the accretion flow.

Chapter 8

Future Work

The general relativistic Compton scattering kernel derived in this thesis is straightforward to implement numerically and massively parallelisable, along with the ray-tracing formulation. The mathematical formalism derived to calculate the kernel is not limited by energy ranges, and as such is extremely general in its applicability. Compared to previous methods for relativistic Compton scattering, this is a significant advance.

I propose incorporating this new formulation into a general relativistic moment formalism. This moment formalism can decompose the integral general relativistic radiative transfer equations into a set of decoupled ODEs which describe the intensity evolution along the ray. This will enable proper calculations of the emission from scattering-dominated accretion flows in AGN. Combining emission, absorption and scattering self-consistently will enable the production of proper continuum spectra, permitting direct comparison with observations.

I have already derived a radiative transfer formulation that incorporates particle mass. The remnant neutron torus formed after neutron star-neutron star or neutron star-black hole mergers is a powerful source of neutrino flux. By applying my formulation to calculate the emission from these objects, the relationship between the black hole mass and spin, and that of its progenitors may be investigated.

As already mentioned, synchrotron emission in relativistic jets and IC emission from the accretion disk are highly polarised. Polarisation gives addi-

tional information about the geometry, the flow structure and the magnetism in the intervening medium. The general relativistic radiative transfer formulation presented in this thesis may be generalised to include polarisation. By parallel-propagating the polarisation vector as a new variable (in addition to the intensity) this may be accomplished. The calculated polarisation can constrain the vectorial quantities of the flow, probing jet dynamics and composition, magnetic fields, and radiative processes.

In order to study the global physics as well as the detailed microphysics near the black hole event horizon, general relativistic absorption, emission and scattering must be treated properly. The formalism presented in this thesis is completely modular and additional radiation processes are easily incorporated as additional modules within the numerical scheme.

Through the combination of all of these approaches, I plan to address the following fundamental questions concerning the physics of astrophysical black holes:

i. How big is a massive black hole and what shadow will its event horizon cast on the sky?

ii. What are the properties of the accretion flow when approaching the event horizon: what are the observational signatures?

iii. How do the disk and jet *and* event horizon interact with one another?

Through my collaboration on the Greenland telescope (GLT) for submm-VLBI, along with other projects including the Event Horizon Telescope (EHT), the black hole shadows of the SMBHs in M87, Centaurus A and Sgr A* will be imaged. These projects also possess enough angular resolution to image the base of the jet, if present, in these black holes. Data from future X-ray observatories including the Large Observatory for X-ray Timing (LOFT) and ATHENA+ can be combined with radio data to address these questions.

I also propose developing an interface for my general relativistic radiative transfer code with the GRMHD and GRPIC codes of my collaborators. This is the only way to treat the complex dynamics near the event horizon properly, as well as answering key questions regarding jet formation and content.

The results of these simulations are essential input in general relativistic radiative transfer calculations. This interface must properly correct for photon propagation from aberration, geometry and frequency shifts. It will treat all relativistic aspects properly and self-consistently. As such, I can make reliable predictions, enabling meaningful comparison with observations.

Further challenges include generalising to the case where the geometric optics approximation breaks down (discussed in Chapter 2.1.1), incorporating atomic processes, and deriving the correct plasma response tensor for the different radiation processes being considered. This latter challenge is necessary for polarised radiative transfer: in order to obtain the correct absorption and emission coefficients, as well as the Faraday rotation and conversion coefficients.

Appendix A

Christoffel Symbol Components

The Christoffel symbol components for the Kerr metric are as follows

$$\Gamma^{t}{}_{tr} = \frac{M\left(r^2+a^2\right)\left(2r^2-\Sigma\right)}{\Sigma^2\Delta}\,, \tag{A.1}$$

$$\Gamma^{t}{}_{t\theta} = -\frac{a^2 Mr\sin 2\theta}{\Sigma^2}\,, \tag{A.2}$$

$$\Gamma^{t}{}_{r\phi} = -\frac{aM\left[4r^4-\left(r^2-a^2\right)\Sigma\right]\sin^2\theta}{\Sigma^2\Delta}\,, \tag{A.3}$$

$$\Gamma^{t}{}_{\theta\phi} = \frac{2a^3 Mr\sin^3\theta\cos\theta}{\Sigma^2}\,, \tag{A.4}$$

$$\Gamma^{r}{}_{tt} = \frac{M\Delta\left(2r^2-\Sigma\right)}{\Sigma^3}\,, \tag{A.5}$$

$$\Gamma^{r}{}_{t\phi} = -\frac{aM\Delta\left(2r^2-\Sigma\right)\sin^2\theta}{\Sigma^3}\,, \tag{A.6}$$

$$\Gamma^{r}{}_{rr} = \frac{\left(1+\Delta/\Sigma\right)r-M}{\Delta}\,, \tag{A.7}$$

$$\Gamma^{r}{}_{r\theta} = -\frac{a^2\sin 2\theta}{2\Sigma} = \Gamma^{\theta}{}_{\theta\theta} = -\frac{\Gamma^{\theta}{}_{rr}}{\Delta}\,, \tag{A.8}$$

$$\Gamma^{r}{}_{\theta\theta} = -\frac{r\Delta}{\Sigma} = \Delta\Gamma^{\theta}{}_{r\theta}\,, \tag{A.9}$$

$$\Gamma^{r}{}_{\phi\phi} = -\frac{\Delta\left[r\Sigma^2-a^2M\left(2r^2-\Sigma\right)\right]\sin^2\theta}{\Sigma^3}\,, \tag{A.10}$$

$$\Gamma^{\theta}{}_{tt} = -\frac{a^2Mr\sin 2\theta}{\Sigma^3}\,, \tag{A.11}$$

$$\Gamma^{\theta}{}_{t\phi} = \frac{aMr\left(r^2+a^2\right)\sin 2\theta}{\Sigma^3}\,, \tag{A.12}$$

$$\Gamma^{\theta}{}_{\phi\phi} = -\frac{\sin 2\theta}{2\Sigma^3}\left\{\left(r^2+a^2\right)\Sigma^2+2a^2Mr\left[\Sigma+\left(r^2+a^2\right)\right]\sin^2\theta\right\}, \tag{A.13}$$

$$\Gamma^{\phi}{}_{tr} = \frac{aM\left(2r^2-\Sigma\right)}{\Delta\Sigma^2}\,, \tag{A.14}$$

$$\Gamma^{\phi}_{t\theta} = -\frac{2aMr\cot\theta}{\Sigma^2}\,, \tag{A.15}$$

$$\Gamma^{\phi}_{r\phi} = \frac{r\Sigma^2 - M\left[2r^2\Sigma - (2r^2-\Sigma)\,a^2\sin^2\theta\right]}{\Delta\Sigma^2}\,, \tag{A.16}$$

$$\Gamma^{\phi}_{\theta\phi} = \cot\theta + \frac{a^2Mr\sin 2\theta}{\Sigma^2}\,. \tag{A.17}$$

In the limit of non-rotating flat space ($a = 0$ and $M = 0$) it is clear these components reduce to the Christoffel symbols for the Minkowski metric in spherical polar co-ordinates.

Appendix B

Appell Hypergeometric Functions

The Appell F_1 hypergeometric function is one of a set of four hypergeometric series of two variables (Appell 1880; Appell and Kampé de Fériet 1926). It is a very general class of special function, containing many other special functions as particular or limiting cases, including hypergeometric functions of one variable like the Gauss ${}_2\mathrm{F}_1$. The Appell F_1 function is defined by the series expansion

$$\mathrm{F}_1\left(a; b_1, b_2; c; z_1, z_2\right) = \sum_{k=0}^{\infty}\sum_{l=0}^{\infty} \frac{(a)_{k+l}(b_1)_k(b_2)_l}{(c)_{k+l}\,k!\,l!} z_1^k\, z_2^l \;, \tag{B.1}$$

This series is absolutely convergent for $|z_1| < 1$, $|z_2| < 1$. Cases outside of the unit disc of convergence can be calculated through analytic extension (Olsson 1964), hence an algorithm can be constructed to evaluate the function numerically (e.g. Colavecchia et al. 2001; Colavecchia and Gasaneo 2004).

Consider R_n and $S_{n,m}$ in Chapter 5, as given in equations (5.103) and (5.109). After an appropriate substitution, R_n may be expanded into a double infinite series as

$$\begin{aligned}
\mathrm{R}_n &= \alpha^{-3/2} \int \mathrm{d}\zeta\, \zeta^n (1-\zeta)^{-1/2} \left(1 + \frac{\beta}{\alpha}\zeta\right)^{-3/2} \\
&= -\frac{1}{2\sqrt{2}} \int \mathrm{d}u\, u^{-1/2} \left[\sum_{k=0}^{\infty} \frac{(-n)_k}{k!} u^k\right] \left[\sum_{l=0}^{\infty} \frac{\left(\frac{3}{2}\right)_l}{l!} \left(\frac{\beta}{2}\right)^l u^l\right] \\
&= -\frac{1}{2\sqrt{2}} \sum_{k,l=0}^{\infty} \frac{(-n)_k \left(\frac{3}{2}\right)_l}{k!\,l!} \left(\frac{\beta}{2}\right)^l \int \mathrm{d}u\, u^{k+l-1/2} \\
&= -\frac{\sqrt{u}}{\sqrt{2}} \sum_{k,l=0}^{\infty} \frac{(-n)_k \left(\frac{3}{2}\right)_l}{k!\,l!(2k+2l+1)!} u^k \left(\frac{\beta}{2}u\right)^l \;,
\end{aligned} \tag{B.2}$$

where $\alpha \equiv 1+x^2$, $\beta \equiv 1-x^2$ and $u \equiv 1-\zeta$. Performing the integral over u and using the identity $(2k+2l+1)! = (3/2)_{k+l}/(1/2)_{k+l}$ the following closed-form expression for the moment integral R_n is obtained:

$$\begin{aligned} R_n &= -\frac{u^{1/2}}{\sqrt{2}} \sum_{k=0}^{\infty} \sum_{l=0}^{\infty} \frac{\left(\frac{1}{2}\right)_{k+l} (-n)_k \left(\frac{3}{2}\right)_l}{\left(\frac{3}{2}\right)_{k+l} k!\, l!} u^k \left(\frac{\beta}{2} u\right)^l \\ &= -\frac{(1-\zeta)^{1/2}}{\sqrt{2}} \mathrm{F}_1 \left[\frac{1}{2}; -n, \frac{3}{2}; \frac{3}{2}; 1-\zeta, \frac{1}{2}(1-x^2)(1-\zeta)\right] . \end{aligned} \quad \text{(B.3)}$$

By the same process, a closed-form expression for the moment integral $S_{n,m}$ also follows

$$\mathrm{S}_{n,m} = -\frac{(1-\zeta)^{\frac{3}{2}-m}}{(\frac{3}{2}-m)\sqrt{2}} \mathrm{F}_1 \left[\frac{3}{2}-m; -n, \frac{1}{2}; \frac{5}{2}-m; 1-\zeta, \frac{1}{2}(1-x^2)(1-\zeta)\right] . \quad \text{(B.4)}$$

In the case $x^2 = 1$ these expressions simplify to Gauss hypergeometric functions of one variable through the following identity:

$$\mathrm{F}_1 \left(a; b_1, b_2; c; x, 0\right) = {}_2\mathrm{F}_1 \left(a, b_1; c; x\right) . \quad \text{(B.5)}$$

As expected from the integral expressions for the moment integrals in equations (5.83) and (5.84), equations (B.3) and (B.4) are identical in argument and differ only in their parameters (a, b_2, c). For both of these expressions the parameter $b_1 = -n$, and are hence absolutely convergent, since $(-n)_k = 0$ for $k \geq n$. That is to say, by writing the Appell hypergeometric function as a single sum over Gauss hypergeometric functions (Srivastava and Karlsson 1985) the series always converges in $n+1$ terms.

Although it may appear profitable to compute the scattering kernel in terms of Appell hypergeometric functions, since these simplify to finite sums of Gauss hypergeometric functions, it is not computationally cheaper and so the results in Chapter 5.9 are expressed in terms of the latter.

Appendix C

Generalised Moment Expansion

As has already been observed (see Figure 4.6), a moment expansion in terms of ζ^n, although convenient, is not strongly convergent for very small scattering angles. The expansion is inherently oscillatory in this instance, since even moments will always yield strictly positive results for the Compton scattering kernel, and odd moments are both positive and negative. The question naturally arises as to how the behaviour changes if a different moment formalism is chosen. This method can also be applied if the electron distribution is no longer isotropic, introducing a ζ–dependence in the electron distribution function. Consider a generalised function of ζ, $\mathcal{F}(\zeta)$, which can be represented as a Taylor series:

$$\mathcal{F}_n(\zeta) = \sum_{k=0}^{n} c(n,k)\,\zeta^k. \tag{C.1}$$

Defining tilde variables as those which represent a moment expansion in terms of $\mathcal{F}_n(\zeta)$, it is readily shown that the generalised moment integrals may be written in terms of the usual Q_n, R_n and $S_{n,m}$ as

$$\begin{aligned} \widetilde{Q}_n &= \int \mathrm{d}\zeta\ \frac{\mathcal{F}_n(\zeta)}{q} \\ &= \sum_{k=0}^{n} c(n,k)\,Q_k\ , \end{aligned} \tag{C.2}$$

$$\begin{aligned} \widetilde{R}_n &= \int \frac{\mathrm{d}\zeta\ \mathcal{F}_n(\zeta)}{(1-\zeta)^2\left(x^2+\frac{1+\zeta}{1-\zeta}\right)^{3/2}} \\ &= \sum_{k=0}^{n} c(n,k)\,R_k\ , \end{aligned} \tag{C.3}$$

$$\begin{aligned}\widetilde{S}_{n,m} &= \int \frac{\mathrm{d}\zeta\ \mathcal{F}_n(\zeta)}{(1-\zeta)^m \left(x^2 + \frac{1+\zeta}{1-\zeta}\right)^{1/2}} \\ &= \sum_{k=0}^{n} c\,(n,k)\, S_{k,m}\ , \end{aligned} \tag{C.4}$$

from whence it follows

$$\widetilde{\mathcal{M}}_n = \sum_{k=0}^{n} c\,(n,k)\, \mathcal{M}_k\ . \tag{C.5}$$

Therefore

$$\begin{aligned}\widetilde{\sigma}_{\mathrm{KN}}(\gamma \to \gamma', \tau) &= \int \mathrm{d}\zeta\, \mathcal{F}_n(\zeta)\, \sigma_{\mathrm{S}}(\gamma \to \gamma', \zeta, \tau) \\ &= \frac{\mathcal{C}}{\gamma^2\, \tau\, \mathrm{K}_2(1/\tau)} \sum_{k=0}^{n} c\,(n,k)\, T(\gamma, \gamma', \tau)\ . \end{aligned} \tag{C.6}$$

List of Acronyms

AGN	active galactic nuclei
BL	Boyer-Lindquist
BLRG	broad-line radio galaxy
BZ	Blandford-Znajeck
CCD	charged-coupled device
CME	coronal mass ejection
EHT	Event Horizon Telescope
FR	Fanaroff and Riley
FSRQ	flat spectrum radio quasar
FWHM	full-width-half-maximum
GLT	Greenland telescope
GRB	gamma-ray burst
GRMHD	general relativistic magnetohydrodynamics
GRPIC	general relativistic particle-in-cell
IC	inverse Compton scattering
ISCO	innermost stable circular orbit
ISM	interstellar medium
LOFT	Large Observatory for X-ray Timing
LTE	local thermodynamic equilibrium
MRI	magnetorotational instability
NLRG	narrow-line radio galaxy
ODE	ordinary differential equation
OVV	optically violent variable quasar
QSO	quasi-stellar object
Sgr A*	Saggitarius A*

SMBH	supermassive black hole
SSC	synchrotron self-Compton
SSRQ	steep-spectrum radio quasar
VLBI	very-long-baseline interferometry
ZAMO	zero angular momentum observer

Bibliography

Abramowicz, M. A. (2005), Super-Eddington black hole accretion: Polish doughnuts and slim disks, *in* A. Merloni, S. Nayakshin, & R. A. Sunyaev (ed.), *Growing Black Holes: Accretion in a Cosmological Context*, pp.257–273.

Abramowicz, M. A., Calvani, M. and Nobili, L. (1980), Thick accretion disks with super-Eddington luminosities, *ApJ* **242**, 772–788.

Abramowicz, M. A., Czerny, B., Lasota, J. P. and Szuszkiewicz, E. (1988), Slim accretion disks, *ApJ* **332**, 646–658.

Abramowicz, M., Jaroszynski, M. and Sikora, M. (1978), Relativistic, accreting disks, *A&A* **63**, 221–224.

Adams, T. F. (1977), A Survey of the Seyfert Galaxies Based on Large-Scale Image-Tube Plates, *ApJS* **33**, 19.

Aharonian, F. A. and Atoyan, A. M. (1981), Compton scattering of relativistic electrons in compact X-ray sources, *Ap&SS* **79**, 321–336.

Anderson, J. M., Ulvestad, J. S. and Ho, L. C. (2004), Low-Luminosity Active Galactic Nuclei at the Highest Resolution: Jets or Accretion Flows?, *ApJ* **603**, 42–50.

Anderson, M., Lehner, L., Megevand, M. and Neilsen, D. (2010), Post-merger electromagnetic emissions from disks perturbed by binary black holes, *Phys. Rev. D* **81**(4), 044004.

Antonucci, R. (1993), Unified models for active galactic nuclei and quasars, *ARA&A* **31**, 473–521.

Appell, P. (1880), Sur une classe de polynomes, *Ann. Sci. Ecole Norm. Sup. 9 (2), 119* .

Appell, P. and Kampé de Fériet, J. (1926), *Fonctions hypergomtriques et hypersphriques: polynomes d'Hermite, Gauthier-Villars: Paris.*

Baiotti, L., Giacomazzo, B. and Rezzolla, L. (2008), Accurate evolutions of inspiralling neutron-star binaries: Prompt and delayed collapse to a black hole, *Phys. Rev. D* **78**(8), 084033.

Balbus, S. A. (2003), Enhanced Angular Momentum Transport in Accretion Disks, *ARA&A* **41**, 555–597.

Balbus, S. A. and Hawley, J. F. (2003), Numerical Simulations of MHD Turbulence in Accretion Disks, *in* E. Falgarone and T. Passot (eds.), *Turbulence and Magnetic Fields in Astrophysics*, Vol. 614 of *Lecture Notes in Physics, Berlin Springer Verlag*, pp.329–348.

Bao, G. (1992), The signature of corotating spots in accretion disks, *A&A* **257**, 594–598.

Bao, G., Hadrava, P. and Ostgaard, E. (1994), Emission-line profiles from a relativistic accretion disk and the role of its multiple images, *ApJ* **435**, 55–65.

Bardeen, J. M., Press, W. H. and Teukolsky, S. A. (1972), Rotating Black Holes: Locally Nonrotating Frames, Energy Extraction, and Scalar Synchrotron Radiation, *ApJ* **178**, 347–370.

Baschek, B., Efimov, G. V., von Waldenfels, W. and Wehrse, R. (1997), Radiative transfer in moving spherical atmospheres. II. Analytical solution for fully relativistic radial motions., *A&A* **317**, 630–635.

Beason, J. D., Kershaw, D. S. and Prasad, M. K. (1991), Using physical insight - The relativistic Compton scattering kernel for radiative transfer, *Journal of Computational Physics* **95**, 497–504.

Beck, R. (2005), Magnetic Fields in Galaxies, *in* R. Wielebinski and R. Beck (eds.), *Cosmic Magnetic Fields*, Vol. 664 of *Lecture Notes in Physics, Berlin Springer Verlag*, p.41.

Beckmann, V. and Shrader, C. R. (2012), *Active Galactic Nuclei*.

Beckwith, K. and Done, C. (2004a), Accurate Modelling of Relativistic Iron Lines from Accretion Discs, *Progress of Theoretical Physics Supplement* **155**, 259–262.

Beckwith, K. and Done, C. (2004b), Iron line profiles in strong gravity, *MNRAS* **352**, 353–362.

Beckwith, K. and Done, C. (2005), Extreme gravitational lensing near rotating black holes, *MNRAS* **359**, 1217–1228.

Begelman, M. C., Blandford, R. D. and Rees, M. J. (1984), Theory of extragalactic radio sources, *Reviews of Modern Physics* **56**, 255–351.

Begelman, M. C. and Sikora, M. (1987), Inverse Compton scattering of ambient radiation by a cold relativistic jet - A source of beamed, polarized continuum in blazars?, *ApJ* **322**, 650–661.

Birkinshaw, M. and Worrall, D. M. (1994), ROSAT Observations of Three Galaxies with Prominent Radio Jets, *in American Astronomical Society Meeting Abstracts*, Vol. 26 of *Bulletin of the American Astronomical Society*, p.109.07.

Blaes, O. M. and Hawley, J. F. (1988), Nonaxisymmetric disk instabilities - A linear and nonlinear synthesis, *ApJ* **326**, 277–291.

Blandford, R. D. and McKee, C. F. (1982), Reverberation mapping of the emission line regions of Seyfert galaxies and quasars, *ApJ* **255**, 419–439.

Blandford, R. D. and Rees, M. J. (1974), A 'twin-exhaust' model for double radio sources, *MNRAS* **169**, 395–415.

Blandford, R. D. and Znajek, R. L. (1977), Electromagnetic extraction of energy from Kerr black holes, *MNRAS* **179**, 433–456.

Blumenthal, G. R. and Gould, R. J. (1970), Bremsstrahlung, Synchrotron Radiation, and Compton Scattering of High-Energy Electrons Traversing Dilute Gases, *Reviews of Modern Physics* **42**, 237–271.

Boettcher, M., Harris, D. E. and Krawczynski, H. (2012), *Relativistic Jets from Active Galactic Nuclei*.

Boyer, R. H. and Lindquist, R. W. (1967), Maximal Analytic Extension of the Kerr Metric, *Journal of Mathematical Physics* **8**, 265–281.

Bridle, A. H. and Perley, R. A. (1984), Extragalactic Radio Jets, *ARA&A* **22**, 319–358.

Broderick, A. E. and Loeb, A. (2005), Imaging bright-spots in the accretion flow near the black hole horizon of Sgr A*, *MNRAS* **363**, 353–362.

Broderick, A. E. and Loeb, A. (2006), Imaging optically-thin hotspots near the black hole horizon of Sgr A* at radio and near-infrared wavelengths, *MNRAS* **367**, 905–916.

Carter, B. (1968), Global Structure of the Kerr Family of Gravitational Fields, *Physical Review* **174**, 1559–1571.

Chakrabarti, S. K. (1985), The natural angular momentum distribution in the study of thick disks around black holes, *ApJ* **288**, 1–6.

Chandrasekhar, S. (1960), *Radiative transfer, New York: Dover*.

Chandrasekhar, S. (1964), The Dynamical Instability of Gaseous Masses Approaching the Schwarzschild Limit in General Relativity., *ApJ* **140**, 417.

Chandrasekhar, S. (1983), *The mathematical theory of black holes*.

Chartas, G., Worrall, D. M., Birkinshaw, M., Cresitello-Dittmar, M., Cui, W., Ghosh, K. K., Harris, D. E., Hooper, E. J., Jauncey, D. L., Kim, D.-W., Lovell, J., Mathur, S., Schwartz, D. A., Tingay, S. J., Virani, S. N. and Wilkes, B. J. (2000), The Chandra X-Ray Observatory Resolves the X-Ray Morphology and Spectra of a Jet in PKS 0637-752, *ApJ* **542**, 655–666.

Colafrancesco, S., Marchegiani, P. and Palladino, E. (2003), The non-thermal Sunyaev-Zel'dovich effect in clusters of galaxies, *A&A* **397**, 27–52.

Colavecchia, F. D., Gasaneo, G. and Miraglia, J. E. (2001), Numerical evaluation of Appell's F_1 hypergeometric function, *Computer Physics Communications* **138**, 29–43.

Colavecchia, F. D. and Gasaneo, G. (2004), f1: a code to compute Appell's F_1 hypergeometric function, *Computer Physics Communications* **157**, 32–38.

Compton, A. H. (1923), A Quantum Theory of the Scattering of X-rays by Light Elements, *Phys. Rev.* **21**, 483–502.

Cunningham, C. T. (1975), The effects of redshifts and focusing on the spectrum of an accretion disk around a Kerr black hole, *ApJ* **202**, 788–802.

Curtis, H. D. (1918), Descriptions of 762 Nebulae and Clusters Photographed with the Crossley Reflector, *Publications of Lick Observatory* **13**, 9–42.

Dahari, O. (1984), Companions of Seyfert galaxies - A statistical survey, *AJ* **89**, 966–974.

De Villiers, J.-P., Hawley, J. F. and Krolik, J. H. (2003), Magnetically Driven Accretion Flows in the Kerr Metric. I. Models and Overall Structure, *ApJ* **599**, 1238–1253.

De Villiers, J.-P., Hawley, J. F., Krolik, J. H. and Hirose, S. (2005), Magnetically Driven Accretion in the Kerr Metric. III. Unbound Outflows, *ApJ* **620**, 878–888.

Dermer, C. D. and Liang, E. P. (1989), Electron thermalization and heating in relativistic plasmas, *ApJ* **339**, 512–528.

Dexter, J. and Agol, E. (2009), A Fast New Public Code for Computing Photon Orbits in a Kerr Spacetime, *ApJ* **696**, 1616–1629.

Dolence, J. C., Gammie, C. F., Mościbrodzka, M. and Leung, P. K. (2009), grmonty: A Monte Carlo Code for Relativistic Radiative Transport, *ApJS* **184**, 387–397.

Dolgov, A. D., Hansen, S. H., Pastor, S. and Semikoz, D. V. (2001), Spectral Distortion of Cosmic Microwave Background Radiation by Scattering on Hot Electrons: Exact Calculations, *ApJ* **554**, 74–84.

Doviak, M., Karas, V. and Matt, G. (2006), X-ray spectra and polarization from accreting black holes: polarization from an orbiting spot, *Astronomische Nachrichten* **327**(10), 993–996.

Drappeau, S., Dibi, S., Dexter, J., Markoff, S. and Fragile, P. C. (2013), Self-consistent spectra from radiative GRMHD simulations of accretion on to Sgr A*, *MNRAS* **431**, 2872–2884.

Eckart, A., Baganoff, F. K., Schödel, R., Morris, M., Genzel, R., Bower, G. C., Marrone, D., Moran, J. M., Viehmann, T., Bautz, M. W., Brandt, W. N., Garmire, G. P., Ott, T., Trippe, S., Ricker, G. R., Straubmeier, C., Roberts, D. A., Yusef-Zadeh, F., Zhao, J. H. and Rao, R. (2006), The flare activity of Sagittarius A*. New coordinated mm to X-ray observations, *A&A* **450**, 535–555.

Eddington, A. S. (1926), *The Internal Constitution of the Stars, Cambridge University Press: Cambridge.*

Eracleous, M. and Halpern, J. P. (2003), Completion of a Survey and Detailed Study of Double-peaked Emission Lines in Radio-loud Active Galactic Nuclei, *ApJ* **599**, 886–908.

Fabian, A. C., Iwasawa, K., Reynolds, C. S. and Young, A. J. (2000), Broad Iron Lines in Active Galactic Nuclei, *PASP* **112**, 1145–1161.

Fabian, A. C., Rees, M. J., Stella, L. and White, N. E. (1989), X-ray fluorescence from the inner disc in Cygnus X-1, *MNRAS* **238**, 729–736.

Falcke, H. and Biermann, P. L. (1999), The jet/disk symbiosis. III. What the radio cores in GRS 1915+105, NGC 4258, M 81 and SGR A* tell us about accreting black holes, *A&A* **342**, 49–56.

Fanaroff, B. L. and Riley, J. M. (1974), The morphology of extragalactic radio sources of high and low luminosity, *MNRAS* **167**, 31P–36P.

Fanton, C., Calvani, M., de Felice, F. and Cadez, A. (1997), Detecting Accretion Disks in Active Galactic Nuclei, *PASJ* **49**, 159–169.

Farris, B. D., Li, T. K., Liu, Y. T. and Shapiro, S. L. (2008), Relativistic radiation magnetohydrodynamics in dynamical spacetimes: Numerical methods and tests, *Phys. Rev. D* **78**(2), 024023.

Fishman, G. J. and Meegan, C. A. (1995), Gamma-Ray Bursts, *ARA&A* **33**, 415–458.

Forrey, R. (1997), Computing the Hypergeometric Function, *Journal of Computational Physics* **137**, 79–100.

Fowler, W. A. (1964), Massive Stars, Relativistic Polytropes, and Gravitational Radiation, *Reviews of Modern Physics* **36**, 545–554.

Fowler, W. A. (1966), The Stability of Supermassive Stars, *ApJ* **144**, 180.

Frank, J. and Rees, M. J. (1976), Effects of massive central black holes on dense stellar systems, *MNRAS* **176**, 633–647.

Frank, J., King, A. and Raine, D. J. (2002), *Accretion Power in Astrophysics: Third Edition*, Cambridge: Cambridge University Press.

Fuerst, S. V. (2006), General Relativistic Radiative Transfer, PhD thesis, University College London.

Fuerst, S. V. and Wu, K. (2004), Radiation transfer of emission lines in curved space-time, *A&A* **424**, 733–746.

Fuerst, S. V. and Wu, K. (2007), Line emission from optically thick relativistic accretion tori, *A&A* **474**, 55–66.

Fuerst, S. V., Mizuno, Y., Nishikawa, K.-I. and Wu, K. (2007), General relativistic radiative transfer and general relativistic mhd simulations of accretion and outflows of black holes, *Astrophys.J.* .

Galama, T. J., Vreeswijk, P. M., van Paradijs, J., Kouveliotou, C., Augusteijn, T., Böhnhardt, H., Brewer, J. P., Doublier, V., Gonzalez, J.-F., Leibundgut,

B., Lidman, C., Hainaut, O. R., Patat, F., Heise, J., in't Zand, J., Hurley, K., Groot, P. J., Strom, R. G., Mazzali, P. A., Iwamoto, K., Nomoto, K., Umeda, H., Nakamura, T., Young, T. R., Suzuki, T., Shigeyama, T., Koshut, T., Kippen, M., Robinson, C., de Wildt, P., Wijers, R. A. M. J., Tanvir, N., Greiner, J., Pian, E., Palazzi, E., Frontera, F., Masetti, N., Nicastro, L., Feroci, M., Costa, E., Piro, L., Peterson, B. A., Tinney, C., Boyle, B., Cannon, R., Stathakis, R., Sadler, E., Begam, M. C. and Ianna, P. (1998), An unusual supernova in the error box of the γ-ray burst of 25 April 1998, *Nature* **395**, 670–672.

Gammie, C. F. and Leung, P. K. (2012), A Formalism for Covariant Polarized Radiative Transport by Ray Tracing, *ApJ* **752**, 123.

Gammie, C. F., McKinney, J. C. and Tóth, G. (2003), HARM: A Numerical Scheme for General Relativistic Magnetohydrodynamics, *ApJ* **589**, 444–457.

Garrington, S. T., Leahy, J. P., Conway, R. G. and Laing, R. A. (1988), A systematic asymmetry in the polarization properties of double radio sources with one jet, *Nature* **331**, 147–149.

Genzel, R., Schödel, R., Ott, T., Eckart, A., Alexander, T., Lacombe, F., Rouan, D. and Aschenbach, B. (2003), Near-infrared flares from accreting gas around the supermassive black hole at the Galactic Centre, *Nature* **425**, 934–937.

Gerbal, D. and Pelat, D. (1981), Profile of a line emitted by an accretion disk - Influence of the geometry upon its shape parameters, *A&A* **95**, 18–23.

Ginzburg, V. L. and Syrovatskii, S. I. (1965), Cosmic Magnetobremsstrahlung (synchrotron Radiation), *ARA&A* **3**, 297.

Greenstein, J. L. and Schmidt, M. (1964), The Quasi-Stellar Radio Sources 3c 48 and 3c 273., *ApJ* **140**, 1.

Griem, H. R. (1974), *Spectral line broadening by plasmas*.

Haardt, F. (1993), Anisotropic Comptonization in thermal plasmas - Spectral distribution in plane-parallel geometry, *ApJ* **413**, 680–693.

Hawley, J. F. (2000), Global Magnetohydrodynamical Simulations of Accretion Tori, *ApJ* **528**, 462–479.

Heinzeller, D. and Duschl, W. J. (2007), On the Eddington limit in accretion discs, *MNRAS* **374**, 1146–1154.

Hills, J. G. (1975), Possible power source of Seyfert galaxies and QSOs, *Nature* **254**, 295–298.

Ho, L. C., Filippenko, A. V. and Sargent, W. L. W. (1992), HST Observations of NGC 4395: The Least Luminous Seyfert 1 Nucleus, *in American Astronomical Society Meeting Abstracts*, Vol. 24 of *Bulletin of the American Astronomical Society*, p.1208.

Hölzer, G., Fritsch, M., Deutsch, M., Härtwig, J. and Förster, E. (1997), K$\alpha_{1,2}$ and K$\beta_{1,3}$ x-ray emission lines of the 3d transition metals, *Phys. Rev. A* **56**, 4554–4568.

Horne, K. and Marsh, T. R. (1986), Emission line formation in accretion discs, *MNRAS* **218**, 761–773.

Hoyle, F. and Fowler, W. A. (1963), Nature of Strong Radio Sources, *Nature* **197**, 533–535.

Hua, X.-M. and Titarchuk, L. (1995), Comptonization Models and Spectroscopy of X-Ray and Gamma-Ray Sources: A Combined Study by Monte Carlo and Analytical Methods, *ApJ* **449**, 188.

Itoh, N., Kawana, Y. and Nozawa, S. (2002), Nonrelativistic electron-electron thermal bremsstrahlung Gaunt factor, *Nuovo Cimento B Serie* **117**, 359.

Jackson, J. D. (1975), *Classical Electrodynamics, 2nd ed., Wiley: New York.*

Jaroszynski, M., Abramowicz, M. A. and Paczynski, B. (1980), Supercritical accretion disks around black holes, *Acta Astron.* **30**, 1–34.

Jester, S. (2008), Retardation magnification and the appearance of relativistic jets, *MNRAS* **389**, 1507–1520.

Johnston, H. M., Kulkarni, S. R. and Oke, J. B. (1989), The black hole A0620-00 and its accretion disk, *ApJ* **345**, 492–497.

Kerr, R. P. (1963), Gravitational Field of a Spinning Mass as an Example of Algebraically Special Metrics, *Physical Review Letters* **11**, 237–238.

Kershaw, D. S., Prasad, M. K. and Beason, J. D. (1986), A simple and fast method for computing the relativistic Compton Scattering Kernel for radiative transfer, *J. Quant. Spec. Radiat. Transf.* **36**, 273–282.

Klein, O. and Nishina, T. (1929), ber die Streuung von Strahlung durch freie Elektronen nach der neuen relativistischen Quantendynamik von Dirac, *Zeitschrift fr Physik A Hadrons and Nuclei* **52**, 853–868. 10.1007/BF01366453.

Kojima, Y. (1991), The effects of black hole rotation on line profiles from accretion discs, *MNRAS* **250**, 629–632.

Komissarov, S. S. (2004), Electrodynamics of black hole magnetospheres, *MNRAS* **350**, 427–448.

Komissarov, S. S., Barkov, M. V., Vlahakis, N. and Königl, A. (2007), Magnetic acceleration of relativistic active galactic nucleus jets, *MNRAS* **380**, 51–70.

Komissarov, S. S. and Barkov, M. V. (2009), Activation of the Blandford-Znajek mechanism in collapsing stars, *MNRAS* **397**, 1153–1168.

Kontar, E. P., Emslie, A. G., Massone, A. M., Piana, M., Brown, J. C. and Prato, M. (2007), Electron-Electron Bremsstrahlung Emission and the Inference of Electron Flux Spectra in Solar Flares, *ApJ* **670**, 857–861.

Kozlowski, M., Jaroszynski, M. and Abramowicz, M. A. (1978), The analytic theory of fluid disks orbiting the Kerr black hole, *A&A* **63**, 209–220.

Krawczynski, H. (2012), The Polarization Properties of Inverse Compton Emission and Implications for Blazar Observations with the GEMS X-Ray Polarimeter, *ApJ* **744**, 30.

Krolik, J. H. (1999), *Active galactic nuclei : from the central black hole to the galactic environment.*

Kylafis, N. D. and Lamb, D. Q. (1982), X-ray and UV radiation from accreting nonmagnetic degenerate dwarfs. II, *ApJS* **48**, 239–272.

Laing, R. A. (1988), The sidedness of jets and depolarization in powerful extragalactic radio sources, *Nature* **331**, 149–151.

Lawrence, A., Watson, M. G., Pounds, K. A. and Elvis, M. (1987), Low-frequency divergent X-ray variability in the Seyfert galaxy NGC4051, *Nature* **325**, 694–696.

Lea, S. M., Mushotzky, R. and Holt, S. S. (1982), Einstein Observatory solid state spectrometer observations of M87 and the Virgo cluster, *ApJ* **262**, 24–32.

Lin, J. and Forbes, T. G. (2000), Effects of reconnection on the coronal mass ejection process, *J. Geophys. Res.* **105**, 2375–2392.

Lin, J., Mancuso, S. and Vourlidas, A. (2006), Theoretical Investigation of the Onsets of Type II Radio Bursts during Solar Eruptions, *ApJ* **649**, 1110–1123.

Lindquist, R. W. (1966), Relativistic transport theory, *Annals of Physics* **37**, 487–518.

Longair, M. S. (1992), *High energy astrophysics. Vol.1: Particles, photons and their detection.*

Lynden-Bell, D. (1969), Galactic Nuclei as Collapsed Old Quasars, *Nature* **223**, 690–694.

Machida, M., Hayashi, M. R. and Matsumoto, R. (2000), Global Simulations of Differentially Rotating Magnetized Disks: Formation of Low-β Filaments and Structured Coronae, *ApJ* **532**, L67–L70.

Madej, J. (1991), Model atmospheres and X-ray spectra of bursting neutron stars, *ApJ* **376**, 161–176.

Madej, J., Joss, P. C. and Różańska, A. (2004), Model Atmospheres and X-Ray Spectra of Bursting Neutron Stars: Hydrogen-Helium Comptonized Spectra, *ApJ* **602**, 904–912.

Marrone, D. P., Baganoff, F. K., Morris, M. R., Moran, J. M., Ghez, A. M., Hornstein, S. D., Dowell, C. D., Muñoz, D. J., Bautz, M. W., Ricker, G. R., Brandt, W. N., Garmire, G. P., Lu, J. R., Matthews, K., Zhao, J.-H., Rao, R. and Bower, G. C. (2008), An X-Ray, Infrared, and Submillimeter Flare of Sagittarius A*, *ApJ* **682**, 373–383.

Marscher, A. P., Jorstad, S. G., Gómez, J.-L., Aller, M. F., Teräsranta, H., Lister, M. L. and Stirling, A. M. (2002), Observational evidence for the accretion-disk origin for a radio jet in an active galaxy, *Nature* **417**, 625–627.

Marsh, T. R., Robinson, E. L. and Wood, J. H. (1994), Spectroscopy of A0620-00 - the Mass of the Black-Hole and an Image of its Accretion Disc, *MNRAS* **266**, 137.

Matt, G. (2004), X-ray polarization properties of the accretion column in magnetic CVs, *A&A* **423**, 495–500.

McClintock, J. E., Shafee, R., Narayan, R., Remillard, R. A., Davis, S. W. and Li, L.-X. (2006), The Spin of the Near-Extreme Kerr Black Hole GRS 1915+105, *ApJ* **652**, 518–539.

McHardy, I. and Czerny, B. (1987), Fractal X-ray time variability and spectral invariance of the Seyfert galaxy NGC5506, *Nature* **325**, 696–698.

McKinney, J. C., Tchekhovskoy, A. and Blandford, R. D. (2012), General relativistic magnetohydrodynamic simulations of magnetically choked accretion flows around black holes, *MNRAS* **423**, 3083–3117.

McNamara, A. L., Kuncic, Z. and Wu, K. (2008a), X-ray polarization signatures of Compton scattering in magnetic cataclysmic variables, *MNRAS* **386**, 2167–2172.

McNamara, A. L., Kuncic, Z. and Wu, K. (2009), X-ray polarization in relativistic jets, *MNRAS* **395**, 1507–1514.

McNamara, A. L., Kuncic, Z., Wu, K., Galloway, D. K. and Cullen, J. G. (2008b), Compton scattering of Fe Kα lines in magnetic cataclysmic variables, *MNRAS* **383**, 962–970.

Meszaros, P. and Rees, M. J. (1997), Optical and Long-Wavelength Afterglow from Gamma-Ray Bursts, *ApJ* **476**, 232.

Meyer, L., Eckart, A., Schödel, R., Duschl, W. J., Mužić, K., Dovčiak, M. and Karas, V. (2006), Near-infrared polarimetry setting constraints on the orbiting spot model for Sgr A* flares, *A&A* **460**, 15–21.

Mihalas, D. and Mihalas, B. W. (1984), *Foundations of Radiation Hydrodynamics, Oxford University Press: Oxford* .

Mirabel, I. F., Dhawan, V., Chaty, S., Rodriguez, L. F., Marti, J., Robinson, C. R., Swank, J. and Geballe, T. (1998), Accretion instabilities and jet formation in GRS 1915+105, *A&A* **330**, L9–L12.

Mirabel, I. F. and Rodríguez, L. F. (1994), A superluminal source in the Galaxy, *Nature* **371**, 46–48.

Misner, C. W., Thorne, K. S. and Wheeler, J. A. (1973), *Gravitation, W.H. Freeman: San Francisco.*

Mortlock, D. J., Warren, S. J., Venemans, B. P., Patel, M., Hewett, P. C., McMahon, R. G., Simpson, C., Theuns, T., Gonzáles-Solares, E. A., Adamson, A., Dye, S., Hambly, N. C., Hirst, P., Irwin, M. J., Kuiper, E., Lawrence, A. and Röttgering, H. J. A. (2011), A luminous quasar at a redshift of z = 7.085, *Nature* **474**, 616–619.

Nagirner, D. I. and Poutanen, Y. J. (1993), Compton scattering by Maxwellian electrons - Redistribution of radiation according to frequencies and directions, *Astronomy Letters* **19**, 262–267.

Narayan, R. and McClintock, J. E. (2012), Observational evidence for a correlation between jet power and black hole spin, *MNRAS* **419**, L69–L73.

Nishikawa, K.-I., Niemiec, J., Medvedev, M., Zhang, B., Hardee, P., Nordlund, A., Frederiksen, J., Mizuno, Y., Sol, H., Pohl, M., Hartmann, D. H., Oka, M. and Fishman, G. J. (2011), Radiation from relativistic shocks in turbulent magnetic fields, *Advances in Space Research* **47**, 1434–1440.

Noble, S. C., Leung, P. K., Gammie, C. F. and Book, L. G. (2007), Simulating the emission and outflows from accretion discs, *Classical and Quantum Gravity* **24**, 259.

Novikov, I. D. and Thorne, K. S. (1973), Astrophysics of black holes., *in* C. Dewitt & B. S. Dewitt (New York: Gordon and Breach) (ed.), *Black Holes (Les Astres Occlus)*, p.343.

Novotny, E. (1973), *Introduction to stellar atmospheres and interiors*.

Olivero, J. and Longbothum, R. (1977), Empirical fits to the Voigt line width: A brief review, *Journal of Quantitative Spectroscopy and Radiative Transfer* **17**(2), 233 – 236.

Olsson, P. O. M. (1964), Integration of the Partial Differential Equations for the Hypergeometric Functions F[sub 1] and F[sub D] of Two and More Variables, *Journal of Mathematical Physics* **5**(3), 420–430.

Osterbrock, D. E. and Ferland, G. J. (2006), *Astrophysics of gaseous nebulae and active galactic nuclei*.

Outram, P. J., Carswell, R. F. and Theuns, T. (2000), Non-Voigt Lyα Absorption Line Profiles, *ApJ* **529**, L73–L76.

Pedlar, A., Kukula, M. J., Longley, D. P. T., Muxlow, T. W. B., Axon, D. J., Baum, S., O'Dea, C. and Unger, S. W. (1993), The Radio Nucleus of NGC4151 at 5-GHZ and 8-GHZ, *MNRAS* **263**, 471.

Penston, M. V. and Cannon, R. D. (1970), Optical monitoring of radio sources. I. The brighter quasars., *Royal Greenwich Observatory Bulletins* **159**, 83–109.

Peraiah, A. (2001), *An Introduction to Radiative Transfer, Cambridge University Press: Cambridge* .

Piran, T. (2005), The physics of gamma-ray bursts, *Rev. Mod. Phys.* **76**, 1143–1210.

Pomraning, G. C. (1972), Compton and inverse Compton scattering., *J. Quant. Spec. Radiat. Transf.* **12**, 1047–1061.

Pomraning, G. C. (1973), *The equations of radiation hydrodynamics, Pergamon Press: Oxford*.

Poutanen, J. and Vilhu, O. (1993), Compton scattering of polarized light in two-phase accretion discs, *A&A* **275**, 337.

Poutanen, J. and Vurm, I. (2010), Theory of Compton Scattering by Anisotropic Electrons, *ApJS* **189**, 286–308.

Pozdniakov, L. A., Sobol, I. M. and Sunyaev, R. A. (1979), The profile evolution of X-ray spectral lines due to Comptonization - Monte Carlo computations, *A&A* **75**, 214–222.

Pozdnyakov, L. A., Sobol, I. M. and Syunyaev, R. A. (1983), Comptonization and the shaping of X-ray source spectra - Monte Carlo calculations, *Astrophysics and Space Physics Reviews* **2**, 189–331.

Prasad, M. K., Kershaw, D. S. and Beason, J. D. (1986), A simple method for computing the relativistic Compton scattering kernel for radiative transfer, *Applied Physics Letters* **48**, 1193–1195.

Puchnarewicz, E. M., Mason, K. O. and Carrera, F. J. (1996), Double-peaked Balmer line emission in the radio-quiet AGN RX J1042+1212, *MNRAS* **283**, 1311–1321.

Rees, M. J. (1971), New Interpretation of Extragalactic Radio Sources, *Nature* **229**, 312–317.

Rees, M. J. (1984), Black Hole Models for Active Galactic Nuclei, *ARA&A* **22**, 471–506.

Rees, M. J. and Meszaros, P. (1992), Relativistic fireballs - Energy conversion and time-scales, *MNRAS* **258**, 41P–43P.

Rees, M. J. and Meszaros, P. (1994), Unsteady outflow models for cosmological gamma-ray bursts, *ApJ* **430**, L93–L96.

Rephaeli, Y. (1995), Cosmic microwave background comptonization by hot intracluster gas, *ApJ* **445**, 33–36.

Reynolds, C. S., Young, A. J., Begelman, M. C. and Fabian, A. C. (1999), X-Ray Iron Line Reverberation from Black Hole Accretion Disks, *ApJ* **514**, 164–179.

Rezzolla, L., Baiotti, L., Giacomazzo, B., Link, D. and Font, J. A. (2010), Accurate evolutions of unequal-mass neutron-star binaries: properties of the torus and short GRB engines, *Classical and Quantum Gravity* **27**(11), 114105.

Rybicki, G. B. and Lightman, A. P. (1979), *Radiative Processes in Astrophysics, Wiley-Interscience: New York* .

Salpeter, E. E. (1964), Accretion of Interstellar Matter by Massive Objects., *ApJ* **140**, 796–800.

Sambruna, R. M., Maraschi, L. and Urry, C. M. (1996), On the Spectral Energy Distributions of Blazars, *in* H. R. Miller, J. R. Webb and J. C. Noble (eds.), *Blazar Continuum Variability*, Vol. 110 of *Astronomical Society of the Pacific Conference Series*, p.450.

Sandage, A. (1965), The Existence of a Major New Constituent of the Universe: the Quasistellar Galaxies., *ApJ* **141**, 1560.

Scheuer, P. A. G. (1974), Models of extragalactic radio sources with a continuous energy supply from a central object, *MNRAS* **166**, 513–528.

Schmidt, M. (1963), 3C 273 : A Star-Like Object with Large Red-Shift, *Nature* **197**, 1040.

Schmidt, M. (1972), Statistical Studies of the Evolution of Extragalactic Radio Sources. I. Quasars., *ApJ* **176**, 273.

Schnittman, J. D. and Bertschinger, E. (2004), The Harmonic Structure of High-Frequency Quasi-periodic Oscillations in Accreting Black Holes, *ApJ* **606**, 1098–1111.

Schnittman, J. D. and Rezzolla, L. (2006), Quasi-periodic Oscillations in the X-Ray Light Curves from Relativistic Tori, *ApJ* **637**, L113–L116.

Seyfert, C. K. (1943), Nuclear Emission in Spiral Nebulae., *ApJ* **97**, 28.

Shajn, G. and Struve, O. (1929), On the rotation of the stars, *MNRAS* **89**, 222–239.

Shakura, N. I. and Sunyaev, R. A. (1973), Black holes in binary systems. Observational appearance., *A&A* **24**, 337–355.

Shestakov, A. I., Kershaw, D. S. and Prasad, M. K. (1988), Evaluation of integrals of the Compton scattering cross-section., *J. Quant. Spec. Radiat. Transf.* **40**, 577–589.

Shibata, M., Kiuchi, K., Sekiguchi, Y. and Suwa, Y. (2011), Truncated Moment Formalism for Radiation Hydrodynamics in Numerical Relativity, *Progress of Theoretical Physics* **125**, 1255–1287.

Shibata, M., Taniguchi, K. and Uryū, K. (2003), Merger of binary neutron stars of unequal mass in full general relativity, *Phys. Rev. D* **68**(8), 084020.

Shields, G. A. (1978), Thermal continuum from acretion disks in quasars, *Nature* **272**, 706–708.

Smak, J. (1969), On the Rotational Velocities of Gaseous Rings in Close Binary Systems, *Acta Astron.* **19**, 155–+.

Sochora, V., Karas, V., Svoboda, J. and Dovčiak, M. (2011), Black hole accretion rings revealed by future X-ray spectroscopy, *MNRAS* **418**, 276–283.

Soria, R., Wu, K. and Johnston, H. M. (1999), Optical spectroscopy of GX 339-4 during the high-soft and low-hard states - I, *MNRAS* **310**, 71–77.

Srivastava, H. M. and Karlsson, P. W. (1985), *Multiple Gaussian Hypergeometric Series, Ellis Horwood: Chichester*.

Stella, L. (1990), Measuring black hole mass through variable line profiles from accretion disks, *Nature* **344**, 747–749.

Stern, B. E., Begelman, M. C., Sikora, M. and Svensson, R. (1995), A large-particle Monte Carlo code for simulating non- linear high-energy processes near compact objects, *MNRAS* **272**, 291–307.

Strateva, I. V., Brandt, W. N., Eracleous, M., Schneider, D. P. and Chartas, G. (2006), The X-Ray Properties of Active Galactic Nuclei with Double-peaked Balmer Lines, *ApJ* **651**, 749–766.

Strittmatter, P. A., Serkowski, K., Carswell, R., Stein, W. A., Merrill, K. M. and Burbidge, E. M. (1972), Compact Extragalactic Nonthermal Sources, *ApJ* **175**, L7.

Sunyaev, R. A. and Titarchuk, L. G. (1985), Comptonization of low-frequency radiation in accretion disks Angular distribution and polarization of hard radiation, *A&A* **143**, 374–388.

Sunyaev, R. A. and Zel'dovich, I. B. (1980), Microwave background radiation as a probe of the contemporary structure and history of the universe, *ARA&A* **18**, 537–560.

Tanaka, Y., Nandra, K., Fabian, A. C., Inoue, H., Otani, C., Dotani, T., Hayashida, K., Iwasawa, K., Kii, T., Kunieda, H., Makino, F. and Matsuoka, M. (1995), Gravitationally redshifted emission implying an accretion disk and massive black hole in the active galaxy MCG-6-30-15, *Nature* **375**, 659–661.

Thomson, J. (1906), *Conduction of electricity through gases, Cambridge University Press: Cambridge*.

Thorne, K. S. (1974), Disk-Accretion onto a Black Hole. II. Evolution of the Hole, *ApJ* **191**, 507–520.

Thorne, K. S. (1980), Multipole expansions of gravitational radiation, *Reviews of Modern Physics* **52**, 299–340.

Thorne, K. S. (1981), Relativistic radiative transfer - Moment formalisms, *MNRAS* **194**, 439–473.

Titarchuk, L. (1994a), Generalized Comptonization models and application to the recent high-energy observations, *ApJ* **434**, 570–586.

Titarchuk, L. (1994b), On the specta of X-ray bursters: Expansion and contraction stages, *ApJ* **429**, 340–355.

Titarchuk, L. G. (1988), Comptonization of Bremsstrahlung and X-Ray Burster Spectra, *Soviet Astronomy Letters* **14**, 229.

Titarchuk, L., Laurent, P. and Shaposhnikov, N. (2009), On the Nonrelativistic Origin of Red-skewed Iron Lines in Cataclysmic Variable, Neutron Star, and Black Hole Sources, *ApJ* **700**, 1831–1846.

Tolhoek, H. A. (1956), Electron Polarization, Theory and Experiment, *Reviews of Modern Physics* **28**, 277–298.

Treister, E., Cardamone, C. N., Schawinski, K., Urry, C. M., Gawiser, E., Virani, S., Lira, P., Kartaltepe, J., Damen, M., Taylor, E. N., Le Floc'h, E., Justham, S. and Koekemoer, A. M. (2009), Heavily Obscured AGN in Star-Forming Galaxies at z sime 2, *ApJ* **706**, 535–552.

Tucker, W. (1975), *Radiation processes in astrophysics*.

Turolla, R. and Nobili, L. (1988), General relativistic radiative transfer in spherical flows, *MNRAS* **235**, 1273–1285.

Uchiyama, Y., Urry, C. M., Cheung, C. C., Jester, S., Van Duyne, J., Coppi, P., Sambruna, R. M., Takahashi, T., Tavecchio, F. and Maraschi, L. (2006), Shedding New Light on the 3C 273 Jet with the Spitzer Space Telescope, *ApJ* **648**, 910–921.

Ulvestad, J. S. and Ho, L. C. (2001), The Origin of Radio Emission in Low-Luminosity Active Galactic Nuclei: Jets, Accretion Flows, or Both?, *ApJ* **562**, L133–L136.

Urry, C. M. and Padovani, P. (1995), Unified Schemes for Radio-Loud Active Galactic Nuclei, *PASP* **107**, 803.

Čadež, A. and Calvani, M. (2006), Relativistic emission lines from accretion disks around black holes, *Advances in Space Research* **38**, 1403–1404.

van der Laan, H. (1966), A Model for Variable Extragalactic Radio Sources, *Nature* **211**, 1131.

Viergutz, S. U. (1993), Image generation in Kerr geometry. I. Analytical investigations on the stationary emitter-observer problem, *A&A* **272**, 355.

Vincent, F. H., Paumard, T., Gourgoulhon, E. and Perrin, G. (2011), GYOTO: a new general relativistic ray-tracing code, *Classical and Quantum Gravity* **28**(22), 225011.

Voigt, W. (1912), ber das Gesetz der Intensittsverteilung innerhalb der Linien eines Gasspektrums, *Sitzungsberichte Knigliche Bayerische Akademie der Wissenschaften* **42**, 603–620. cited By (since 1996)12.

Wald, R. M. (ed.) (1998), *Black holes and relativistic stars*.

Wang, Y. and Li, X.-D. (2012), Strong Field Effects on Emission Line Profiles: Kerr Black Holes and Warped Accretion Disks, *ApJ* **744**, 186.

Westfold, K. C. (1959), The Polarization of Synchrotron Radiation., *ApJ* **130**, 241.

Wilson, A. S. and Ulvestad, J. S. (1982), Radio structures of Seyfert galaxies. IV - Jets in NGC 1068 and NGC 4151, *ApJ* **263**, 576–594.

Wilson, A. S. and Ulvestad, J. S. (1983), Radio jets and high velocity gas in the Seyfert Galaxy NGC 1068, *ApJ* **275**, 8–14.

Winkler, K.-H. A. and Norman, M. L. (eds.) (1986), *Astrophysical Radiation Hydrodynamics*.

Wu, K., Fuerst, S. V., Lee, K.-G. and Branduardi-Raymont, G. (2006), General Relativistic Radiative Transfer: Emission from Accreting Black Holes in AGN, *Chinese Journal of Astronomy and Astrophysics Supplement* **6**(1), 010000–220.

Wu, K., Fuerst, S. V., Mizuno, Y., Nishikawa, K.-I., Branduardi-Raymont, G. and Lee, K.-G. (2008), General Relativistic Radiative Transfer: Applications to Black-Hole Systems, *Chinese Journal of Astronomy and Astrophysics Supplement* **8**, 226–236.

Wu, K., Soria, R., Hunstead, R. W. and Johnston, H. M. (2001), Optical spectroscopy of GX 339-4 during the high-soft and low-hard states - II. Line ionization and emission region, *MNRAS* **320**, 177–192.

Yang, X. and Wang, J. (2013), YNOGK: A New Public Code for Calculating Null Geodesics in the Kerr Spacetime, *ApJS* **207**, 6.

Younsi, Z. and Wu, K. (2013), Covariant Compton scattering kernel in general relativistic radiative transfer, *MNRAS* **433**, 1054–1081.

Younsi, Z., Wu, K. and Fuerst, S. V. (2012), General relativistic radiative transfer: formulation and emission from structured tori around black holes, *A&A* **545**, A13.

Yuan, F., Lin, J., Wu, K. and Ho, L. C. (2009), A magnetohydrodynamical model for the formation of episodic jets, *MNRAS* **395**, 2183–2188.

Yusef-Zadeh, F., Roberts, D., Wardle, M., Heinke, C. O. and Bower, G. C. (2006), Flaring Activity of Sagittarius A* at 43 and 22 GHz: Evidence for Expanding Hot Plasma, *ApJ* **650**, 189–194.

Zamaninasab, M., Eckart, A., Dovčiak, M., Karas, V., Schödel, R., Witzel, G., Sabha, N., García-Marín, M., Kunneriath, D., Mužić, K., Straubmeier, C., Valencia-S, M. and Zensus, J. A. (2011), Near-infrared polarimetry as a tool for testing properties of accreting supermassive black holes, *MNRAS* **413**, 322–332.

Zane, S., Turolla, R., Nobili, L. and Erna, M. (1996), General Relativistic Radiative Transfer in Hot Astrophysical Plasmas: A Characteristic Approach, *ApJ* **466**, 871.

Zanotti, O., Roedig, C., Rezzolla, L. and Del Zanna, L. (2011), General relativistic radiation hydrodynamics of accretion flows - I. Bondi-Hoyle accretion, *MNRAS* **417**, 2899–2915.

Zhang, S. and Jin, J. (1996), *Computation of Special Functions, Wiley-Interscience: New York*.

Zhang, S. N., Cui, W. and Chen, W. (1997), Black Hole Spin in X-Ray Binaries: Observational Consequences, *ApJ* **482**, L155.